

© Copyright 2021

Brittany P. Bishop

Synthesis, Surface Functionalization, and Strain-Engineering of Luminescent  
Inorganic Nanostructures

Brittany P. Bishop

A dissertation

submitted in partial fulfillment of the  
requirements for the degree of

Doctor of Philosophy

University of Washington

2021

Reading Committee:

Vincent C. Holmberg, Chair

Elizabeth Nance

Qiuming Yu

Alexandra Velian

Program Authorized to Offer Degree:

Chemical Engineering

University of Washington

**Abstract**

Synthesis, Surface Functionalization, and Strain-Engineering of Luminescent Inorganic Nanostructures

Brittany P. Bishop

Chair of the Supervisory Committee:  
Vincent C. Holmberg  
Chemical Engineering

Quantum dots (QDs) are a class of luminescent materials with nanoscale dimensions and unique optical and photoluminescent properties. Due to the effects of quantum confinement, size-dependent changes to the electronic structure cause the QD band gap to increase in energy as the nanocrystal diameter decreases, resulting in size-tunable absorbance and photoluminescence characteristics. Their tunability and ultra-small size make QDs advantageous for a wide array of applications, including energy conversion, photodetection, biological imaging, and display technologies. Notably, nanocrystals with decreased toxicity and more widely accessible synthetic protocols are two areas that could lead to increases in the availability and continued commercial implementation of quantum dots. This dissertation describes investigations related to the impact of surface functionalization on nanocrystal toxicity, explores strain-engineering strategies in spherical quantum well (SQW) heterostructures, and presents alternate nanocrystal synthesis pathways that may lead toward greater accessibility.

First, cadmium selenide / cadmium sulfide (CdSe/CdS) core-shell QDs are investigated as a model system to understand the impact that the surface functionalization has on toxicity, stability, and cellular uptake in biologically relevant fluids and mouse models. This study demonstrates that functionalizing the QDs with polyethylene glycol decreases toxicity, improves stability, and increases cellular uptake. Furthermore, in addition to surface chemistry, the QD concentration and type of biological model utilized play a large role in the observed QD behavior, which must be taken into consideration when choosing a model system to evaluate QDs for biological applications.

In the next chapter, the sonochemical synthesis of CdSe QDs and magic-sized clusters (MSCs) is examined. The synthesis utilizes ultrasound to generate nanocrystals under atmospheric conditions without the need of a Schlenk line, specialized glassware, or heating equipment. In addition, when nanocrystal precursors are dissolved in a single-phase system and sonicated, ultra-small, white-light-emitting CdSe QDs were generated; however, when nanocrystal precursor were compartmentalized in emulsion droplets in a two-phase ethylene glycol system, atomically precise MSCs were produced. Moreover, since the nucleation and growth processes are entirely dependent on active sonication, this synthesis is highly controllable and can be turned on and off rapidly.

The third chapter focuses on the generation of ZnS nanocrystals using a one-pot solvothermal synthesis with improved scalability relative to commonly used hot-injection syntheses. By utilizing a highly reactive sulfur precursor in combination with coordinating solvents that are liquid at room temperature, we demonstrate a highly reproducible ZnS nanocrystal synthesis with streamlined purification that consistently generates a high yield of monodisperse ZnS nanocrystals. The nanocrystal diameters can also be adjusted via the reaction temperature, allowing for straightforward tunability of the ZnS nanocrystal diameter and bandgap.

Finally, the growth of zinc selenide/indium phosphide/zinc sulfide (ZnSe/InP/ZnS), ZnS/InP/ZnS, and ZnSe/InP/ZnSe core/shell/shell spherical quantum well (SQW) architectures were explored. This strain-engineering strategy has been utilized previously to generate high-quantum-yield cadmium chalcogenide SQWs with narrow emission linewidths and is a promising candidate for application in other semiconductor systems with lower toxicity. Herein, we investigate the impact that precursors and surface chemistry have on the successful epitaxial growth of InP onto zinc chalcogenide cores, while demonstrating the importance that symmetry, band alignment, and lattice match have on the photoluminescent characteristics of the resulting SQWs.

# TABLE OF CONTENTS

List of Figures .....	vi
Chapter 1. Introduction .....	1
1.1 Semiconductor Nanocrystals .....	1
1.1.1 Quantum Confinement.....	1
1.1.2 Properties and Applications .....	2
1.1.3 Toxicity and Earth Abundance .....	3
1.2 Colloidal Nanocrystal Synthesis and Optimization .....	5
1.2.1 Nucleation and Growth Methods of Nanocrystals.....	5
1.2.2 Magic-size Clusters and Intermediates in Nanocrystal Growth .....	7
1.2.3 Shell Growth onto Quantum Dot Cores.....	9
1.2.4 Strain-Engineering in Semiconductor Nanostructures.....	11
1.2.5 Surface Chemistry and Functionalization of Nanocrystals.....	14
1.3 Dissertation Overview .....	16
Chapter 2. Surface Functionalization of Fluorescent Nanocrystals for Biological Imaging .....	19
2.1 Introduction.....	19
2.2 Synthesis and Surface Functionalization of Cadmium Selenide Quantum Dots for Biological Imaging .....	22
2.2.1 Materials .....	22
2.2.2 Synthesis of Cadmium Selenide Quantum Dots.....	23
2.2.3 Growth of Cadmium Sulfide Shells onto Cadmium Selenide Cores.....	23
2.2.4 Surface Functionalization of Cadmium Selenide/Cadmium Sulfide Quantum Dots	25

2.2.5	Quantum Dot Characterization .....	26
2.3	Characterization and Surface Functionalization of Cadmium Selenide/Cadmium Sulfide Quantum Dots .....	27
2.4	Nanocrystal Stability, Toxicity, and Cellular Uptake.....	30
2.4.1	Quantum Dot Photoluminescence Stability .....	30
2.4.2	Quantum Dot Dissolution Stability.....	31
2.4.3	Cadmium Dissolution and Photoluminescence Stability of Quantum Dots in Neurophysiologically Relevant Fluids.....	32
2.4.4	Nanocrystal Stability, Toxicity, and Cellular Uptake.....	32
2.5	Conclusions.....	36
2.6	Author Contributions and Acknowledgements.....	37
2.6.1	Author Contributions .....	37
2.6.2	Acknowledgements.....	38
Chapter 3. Sonochemical Synthesis of Fluorescent Semiconductor Quantum Dots and Magic-size Clusters .....		
		39
3.1	Introduction.....	40
3.2	Materials and Methods.....	43
3.2.1	Materials .....	43
3.2.2	Precursor Preparation.....	43
3.2.3	Sonochemical Quantum Dot and Magic-Size Cluster Synthesis.....	44
3.2.4	UV–Visible (UV–Vis) Absorbance and Photoluminescence (PL) Spectroscopy....	46
3.2.5	Transmission Electron Microscopy (TEM) .....	46
3.3	Results and Discussion .....	46

3.4	Conclusions.....	55
3.5	Acknowledgements.....	56
Chapter 4. Highly Repeatable One-Pot Synthesis of Monodisperse Zinc Sulfide Nanocrystals with Broadband Near-UV and Visible Emission.....		
		57
4.1	Introduction.....	57
4.2	Materials and Methods for ZnS .....	60
4.2.1	Chemicals.....	60
4.2.2	ZnS Nanocrystal Syntheses with Unsaturated Fatty Compounds.....	60
4.2.3	ZnS Nanocrystal Synthesis with Saturated Fatty Compounds and DPP:S .....	62
4.2.4	ZnS Nanocrystal Synthesis with Saturated Fatty Compounds and Sulfur Powder ..	62
4.2.5	Characterization .....	63
4.3	Results and Discussion .....	65
4.4	Conclusions.....	74
4.5	Author Contributions and Acknowledgements.....	75
4.5.1	Author Contributions .....	75
4.5.2	Acknowledgements.....	75
Chapter 5. Impact of Precursors and Surface Chemistry on Indium Phosphide Shell Growth in Strain-Engineered Indium Phosphide Spherical Quantum Wells.....		
		77
5.1	Introduction.....	77
5.2	Materials and Methods.....	80
5.2.1	Chemicals.....	80
5.2.2	InP Syntheses with TMS <sub>3</sub> P and Indium Oleate .....	81

5.2.3	InP Syntheses with TDAP and Indium Oleate.....	82
5.2.4	InP Syntheses with TDAP and Indium Chloride .....	82
5.2.5	Characterization .....	83
5.3	Results and Discussion .....	84
5.4	Conclusions.....	97
5.5	Author Contributions and Acknowledgements.....	98
5.5.1	Author Contributions .....	98
5.5.2	Acknowledgements.....	98
Chapter 6. Conclusions and Future Directions .....		99
6.1	Conclusions.....	99
6.1.1	Surface Functionalization of Fluorescent Nanocrystals for Biological Imaging.....	99
6.1.2	Sonochemical Synthesis of Fluorescent Semiconductor Quantum Dots and Magic-size Clusters .....	100
6.1.3	Highly Repeatable One-Pot Synthesis of Monodisperse Zinc Sulfide Nanocrystals with Broadband Near-UV and Visible Emission.....	101
6.1.4	Impact of Precursors and Surface Chemistry on Indium Phosphide Shell Growth in Strain-Engineered Indium Phosphide Spherical Quantum Wells .....	101
6.2	Future Directions .....	102
6.2.1	Sonochemical Synthesis of Doped Quantum Dots and Magic-Size Clusters.....	102
6.2.2	Optimization and Further Investigation into the Indium Phosphide Spherical Quantum Well.....	103
6.2.3	Extension of the Spherical Quantum Well into New Material Systems.....	104

Appendix A. Chapter 4 Supplemental Information .....	106
Appendix B. Chapter 5 Supplemental Information .....	110
Appendix C. Silver Sulfide as a Spherical and Annular Quantum Well .....	122
Appendix D. A Decade with DYSS: Lessons Learned and Looking Forward.....	139
Bibliography .....	163
Vita.....	189

# LIST OF FIGURES

Figure 1.1. a) Schematic of the quantum confinement effect in semiconductor nanocrystals. b) Emission of colloidal CdSe nanocrystals with different sizes, which blue shift with a decrease in nanocrystal diameter.<sup>1</sup> ..... 1

Figure 1.2. Absorption spectra of CdSe quantum dots with diameters ranging from 12 Å (1.2 nm) to 115 Å (11.5 nm).<sup>2</sup> ..... 2

Figure 1.3. Ranges of photoluminescence emission for various semiconductor materials.<sup>3,3</sup>

Figure 1.4. Range of luminescence wavelengths and relative toxicity and earth abundance of different QD materials.<sup>28</sup> ..... 4

Figure 1.5. Nanoparticle nucleation and growth described through LaMer and Dinegar’s model. The black curve indicates the theoretical concentration of monomers over time.<sup>40</sup> ... 5

Figure 1.6. a) Depiction of the nucleation and growth of nanocrystals via the a) hot-injection method and b) a schematic of the chemical set-up commonly used for the hot-injection method.<sup>41</sup> ..... 5

Figure 1.7. a) Depiction of the nucleation and growth of nanocrystals via the solvothermal method.<sup>49</sup> ..... 6

Figure 1.8. a) Two-step nucleation and growth of InP QDs, with MSCs as an intermediate.<sup>51</sup> b) Multi-step nucleation and growth of CdTe MSCs and QDs.<sup>52</sup> ..... 8

Figure 1.9. Schematic of three different band alignments between core/shell semiconductor nanocrystals. a) Type I: charge carriers are both localized to the core. b) Type 1.5: one charge carrier is localized to the core, while the other is delocalized across the nanocrystal. c) Type II: the charge carriers are specially separated. In this case, the electrons are localized to the core, while the holes are localized to the outer shell.<sup>1</sup> ..... 9

Figure 1.10. Representation of different charge carrier trapping and exciton recombination: a) thermalization via exciton coupling, b) multi-exciton generation via carrier energy transfer, c) radiative recombination, and d) charge carrier ejection into the environment of the nanocrystal.<sup>1</sup> ..... 10

Figure 1.11. Visualization of possible defects in nanocrystals a) before and b) after shell growth in core/shell structures with large lattice mismatch. c) Visualization of trapping in the electronic structure of a semiconductor. ....	11
Figure 1.12. Depiction of strain-engineering techniques in quantum dots: a) gradient cores, b) gradient shells, c) alloyed core/shells, and d) spherical quantum wells. ....	12
Figure 2.1. Absorbance spectra for CdSe quantum dots as they grow in diameter over time. The purple spectrum indicates the smallest nanocrystals, while the light green spectrum indicates the largest. ....	27
Figure 2.2. Surface functionalization and characterization of CdSe–CdS core–shell QDs. (A) Absorbance and photoluminescence of CdSe nanocrystal cores (blue and pink) and final core–shell CdSe/CdS QDs (red and black) with 60% quantum yield. (B) TEM images of final $6.7 \pm 0.5$ nm diameter core–shell QDs and initial $3.4 \pm 0.4$ nm-diameter nanocrystal cores (inset). (C, D) Images of QD dispersions under UV excitation (C) before and (D) after surface functionalization and transfer to aqueous media. (E) Relative emission intensity of initial nanocrystal cores (pink), and final core–shell QDs before (black) and after (green) surface functionalization and transfer to aqueous media. ....	28
Figure 2.3. ATR-FTIR spectra of QD-MPA (orange), QD-PEG-OMe (blue), and QD-PEG-OH (red). The FTIR spectra of the PEGylated QDs show the distinct features of the polyethylene glycol polymer ligand. The peak at $1100\text{ cm}^{-1}$ is characteristic of an ether C-O-C band, while the peaks at $2870$ and $1465\text{ cm}^{-1}$ correspond to $\text{CH}_2$ stretching and scissoring vibrations, respectively. The remaining peaks indicate the presence of a long-chain polyether. The peaks at $1340$ , $1280$ , and $1235\text{ cm}^{-1}$ are indicative of $\text{CH}_2$ wagging, symmetric twisting, and antisymmetric twisting, respectively. The peak at $960\text{ cm}^{-1}$ corresponds to a combination of coupled symmetric $\text{CH}_2$ rocking, C-C stretching, and C-O stretching, while the peak at $840\text{ cm}^{-1}$ corresponds to coupled $\text{CH}_2$ rocking and C-O stretching. The QD-PEG-OH samples show an additional broad O-H stretching band extending from $3300$ to $3560\text{ cm}^{-1}$ , which is indicative of the additional terminal O-H functional group attached to the PEG. The 3-mercaptopropionic acid-functionalized QDs exhibited characteristic antisymmetric and symmetric alkyl $\text{CH}_2$ stretching bands at $2920$ and $2860\text{ cm}^{-1}$ , respectively, along with clear antisymmetric and symmetric carboxylate	

(COO<sup>-</sup>) stretching bands at 1560 and 1410 cm<sup>-1</sup>, respectively. These observations, in combination with the absence of a strong carboxylic acid C=O stretch at 1710 cm<sup>-1</sup>, indicate complete deprotonation of the carboxylic acid groups on the MPA ligands. .... 29

Figure 2.4. (A) Cadmium ion release of 0.1 μM CdSe/CdS QDs with different surface functionalities in aCSF at 37°C after 0 h and 24 h incubation. The level of free Cd<sup>2+</sup> ions in all groups tested was less than 10 parts per billion (ppb). Note that the initial 0-h baseline levels of Cd<sup>2+</sup> are due to a small subset of CdSe particles that pass through the 50-kD filter and are digested to Cd<sup>2+</sup> during ICP-MS sample preparation. When a lower molecular weight cutoff filter (3 kD) was used on identical PEGylated samples, a baseline Cd<sup>2+</sup> ion level of 1 ppb was achieved. The concentration of free Cd<sup>2+</sup> ions remained virtually unchanged (less than 1 ppb change in concentration) for all samples over the 24-hour measurement period. (B) Photoluminescence intensity of QDs incubated in aCSF under physiological conditions as a function of time. .... 31

Figure 2.5. (A) QD hydrodynamic diameter at 37 °C in aCSF at 0, 4, 24 h (n = 3 measurements per particle type). (B) Toxicity of QDs on in vitro BV-2 cells. Treatment of QD-MPA and QD-PEG-OH at 0.01 μM concentration on in vitro BV-2 cells for 1, 2, 4, 6, and 24 h, with reported % cell viability. For each condition, n = 3 wells were evaluated with 10,000 cells per well when plated. (C) Dose-dependent toxicity of QD-PEG-OH and QD-PEG-OMe in ex vivo OWH slices. Treatment of QD-PEG-OH (red) and QD-PEG-OMe (blue) at 1 μM concentrations in P14 rat organotypic brain slices for 24 h. QD toxicity was determined by LDH assay at 0, 1, 2, 4, 8, and 24 h as follows. For each QD concentration, n = 3 slices per QD per concentration condition were evaluated; for NT group (black), n = 5 slices. (D) Time-dependent mRNA profiles of QD-induced proinflammatory and metallothionein markers in OWH slices. Fold-changes in mRNA expression were measured at 1 h, 6 h, and 24 h of QD-MPA (orange), QD-PEG-OH (red), and QD-PEG-OMe (blue) exposure at 0.1 mM concentration in OWH slices. The fold-changes were measured for metallothionein isoform Mt1 and proinflammatory cytokine TNF-α, and compared to NT slices (black). For 1 h, 6 h, and 24 h time points, n = 3 groups and n = 3–6 slices per group were evaluated for each experimental sample (except for the QD-PEG-OMe 6 h proinflammatory sample, where n = 2 groups with n = 6 slices in total were evaluated). All data are reported as

median values with 95% confidence intervals. (E) Iba1+ microglia and lysosome uptake of QDs in ex vivo OWH slices. Representative 40× magnification images of QD-MPA, QD-PEG-OH, and QD-PEG-OMe distribution and Iba1+ cellular uptake in the corpus callosum in P14 Sprague-Dawley (SD) rat OWH slices (300 μm thickness). QDs (red, all images) were found internalized into Iba1+ microglia (green, all images). Representative high-magnification images of QD-MPA, QD-PEG-OH, and QD-PEG-OMe localization inside Iba1+ cells are shown as insets. Cell nuclei were stained with DAPI and display blue luminescence. (F) QD cellular uptake in P7 rats, 4 h post-administration. Representative images of QD-PEG-OH (red, all images) colocalization with Iba1+ microglia cells (green, all images) in the corpus callosum regions in P7 mglur5 WT, 4 h after i.p. administration. 40× magnification images with 4-fold zoom (160×) are presented in the rightmost column to show QD-PEG-OH internalization in cells. Data provided courtesy of Dr. Mengying Zhang, Kate Hildahl, Binh Dang, Olesya Mironchuk, Nina Chen, and Dr. Elizabeth Nance.

.....	33
Figure 3.1. Schematic representation of transient acoustic cavitation. <sup>146</sup> .....	41
Figure 3.2. Schematic of the sonochemical nanoparticle synthesis procedure, along with photos of the final products under UV excitation.....	42
Figure 3.3. Temperature of the mixture tracked with sonication time.....	47
Figure 3.4. (a) Absorbance and (b) PL spectra ( $\lambda_{exc} = 360$ nm) of CdSe QDs synthesized via sonication in the single-phase solvent system. ....	47
Figure 3.5. (a) Absorbance and (b) PL spectra ( $\lambda_{exc} = 420$ nm) of CdSe particles synthesized using sonication in the emulsion-based systems as a function of sonication time. ..	48
Figure 3.6. Quantum yield of samples synthesized in the emulsion system as a function of sonication time. ....	49
Figure 3.7. XRD spectra of CdSe particles synthesized via sonication in (a) single-phase and (b) emulsion-based systems. Red lines represent the expected peak positions for the bulk zincblende CdSe structure.....	50
Figure 3.8. TEM of CdSe nanoparticles formed after 180 min of sonication in single phase at (a) low and (b) high magnifications. (c) MSCs formed after 60 min in emulsion-based systems. (d) CdSe nanoparticles formed after 180 min in emulsion-based systems. ....	51

Figure 3.9. Conversion of Cd and Se precursors in (CdSe) with sonication. .... 52

Figure 3.10. Quantitative absorbance at 420 nm of CdSe MSCs synthesized in the emulsion system with periodic (a) 10 min on–off cycles and (c) 20 min on-off cycles. Blue shades indicate the time period during which sonication is active. (b) Schematic of the sonochemical QD synthesis mechanism, where cavitation provides the energy required for precursors to react, form clusters, and grow into QDs. d) Quantitative absorbance at 420 nm of CdSe MSCs synthesized in the emulsion system with periodic 10-minute and 20-minute on-off cycles normalized by the total active sonication time..... 53

Figure 4.1. a) Extinction, photoluminescence, b) diameter distribution, and c) precursors and solvothermal synthesis conditions of ZnS nanocrystals produced using DPP:S and unsaturated fatty compounds. Inset shows TEM images of the resulting ZnS nanocrystals at low and high resolution. The high-resolution scale bar = 2 nm. d) Extinction, photoluminescence, e) diameter distribution, and f) precursors and solvothermal synthesis conditions of ZnS nanocrystals produced using sulfur powder and saturated fatty compounds. Inset shows TEM images of the resulting ZnS nanocrystals..... 66

Figure 4.2. Extinction spectra of ZnS nanocrystals synthesized with DPP:S and unsaturated fatty compounds (a) at different time points during a single synthesis and (b) across multiple syntheses. .... 68

Figure 4.3. a) TEM at low and high resolution, b) diameter distribution, and c) precursors and conditions of ZnS nanocrystals synthesized with DPP:S and saturated fatty compounds. d) TEM at low and high resolution, e) diameter distribution, and f) precursors and conditions of ZnS nanocrystals synthesized with sulfur powder and unsaturated fatty compounds. g) TEM, h) diameter distribution, and i) precursors and conditions of size-selected ZnS nanocrystals synthesized with sulfur powder and saturated fatty compounds. High resolution scale bar = 2 nm. .... 69

Figure 4.4. a) Extinction spectra, b) PL, and PLE spectra of ZnS nanocrystals synthesized via different solvothermal synthesis protocols. .... 70

Figure 4.5. a) Extinction, b) PL, and PLE spectra of ZnS-Unsaturated-DPP:S nanocrystals synthesized at different reaction temperatures with excess oleic acid added after 5 minutes.

TEM of ZnS nanocrystals synthesized at c) 210°C, d) 230°C, e) 250°C, and f) 270°C. Inset scale bar = 1.5 nm. ....	71
Figure 4.6. SAXS profiles and modeled size distributions for (a and c) ZnS nanocrystals synthesized with DPP:S and unsaturated fatty compounds and (b and d) size-selected ZnS nanocrystals synthesized with sulfur powder and saturated fatty compounds. ....	73
Figure 5.1. Schematic of the maximum possible InP shell thickness for coherently strained InP SQWs grown onto a) ZnS cores and b) ZnSe cores, based on the critical thickness values calculated from Equations 5.1 – 5.4. The zoomed-in sections demonstrate the lattice mismatch between InP and the zinc chalcogenide. c) Band alignment of zinc chalcogenides and indium pnictogens in relation to the ZnS valence band. Interface between d) a hexagonal (HCP) ZnS and cubic (FCC) InP crystal structures and e) two cubic (FCC) ZnS/InP crystal structures. Black dashed lines highlight defects at the interface.....	86
Figure 5.2. PL and PLE spectra of products obtained after attempted SILAR growth of InP/ZnS using a) InO <sub>3</sub> and TMS <sub>3</sub> P and b) InO <sub>3</sub> and TDAP as InP precursors. PL and PLE spectra of c) ZnS/InP/ZnS nanocrystals and d) ZnSe/InP/ZnS nanocrystals using InCl <sub>3</sub> and TDAP as InP precursors. The legends in panels c and d illustrate the structures that were formed in each synthesis. Quantum yield measurements were collected using an excitation wavelength of 390 nm. ....	88
Figure 5.3. TEM of InP SQWs synthesized with TDAP and InCl <sub>3</sub> : a) ZnS, b) ZnS/InP, c) ZnS/InP/ZnS, d) ZnSe, e) ZnSe/1XInP, f) ZnSe/1XInP/ZnS, g) ZnSe, h) ZnSe/3XInP, and i) ZnSe/3XInP/ZnS. Insets show high-resolution images of individual nanocrystals (inset scale bar = 1.5 nm). ....	90
Figure 5.4. a) Shifting of the (220) XRD peak of InP SQWs synthesized with TDAP and InCl <sub>3</sub> . b) Shifting of the (220) XRD peak of attempted InP SQWs synthesized with TMS <sub>3</sub> P and InO <sub>3</sub> . Diagrams show the structures at each step in the synthesis process, from cores to shelled nanostructures. ....	93
Figure 5.5. Schematic of a ZnS nanocrystal with a) oleic acid and b) oleylamine surface functionalization. PL and normalized PLE spectra of ZnS/InP/ZnS synthesized using ZnS cores with c) oleic acid and b) oleylamine surface functionalization. e and f) ATR-FTIR of	

ZnS nanocrystals before (oleic acid, pink) and after (oleylamine, blue) ligand exchange.  
..... 95

## ACKNOWLEDGEMENTS

I would not be where I am today without the inspiration and encouragement of everyone who has supported me throughout my life.

First and foremost, I want to thank my advisor Dr. Vincent Holmberg for his incredible support during my graduate studies. I am truly appreciative of the countless hours of hands-on training and research collaboration that has transformed me into the researcher I am today. In addition to guiding my research, his insight and expertise has improved my writing, teaching, and presentation skills immensely, making me a more confident science communicator. He has also supported me in every fellowship and external activity that I have been involved with, allowing me to explore the breadth of science and engineering outside of academia and the lab. I also want to thank my committee members Dr. Elizabeth Nance, Dr. Qiuming Yu, and Dr. Alexandra Velian for their continued support and guidance throughout my graduate experience. Their feedback and wisdom have shaped my research and helped me grow immensely, both personally and professionally.

I especially want to thank Dr. Elizabeth Nance for the unbelievable sponsorship and mentorship she has provided me. In addition to research and teaching collaborations, she has encouraged me and sponsored me to engage with Women in Chemical Engineering and other inclusivity efforts across campus. Without her and Vince's support, I never would have engaged in the education, diversity, and science policy programs that I have been a part of. I am also thankful to Dan Schwartz, Shaun Taylor, and the entirety of the Clean Energy Institute, who have supported me in various research, education, outreach, and science policy efforts and encouraged me to advocate for clean energy and climate justice.

I am also grateful for the wonderful labmates who have assisted me in research and provided me moral support over the years. I am particularly appreciative of Soohyung Lee's significant contributions to the shaping, characterization and analysis of my research, especially towards the end of my Ph.D. Elena Pandres and Grant Williamson have been incredibly helpful at providing feedback and advice for both my writing and presentation skills and have helped me become a better communicator. I am also thankful to Grant Williamson for encouraging me to become involved and enter science policy at the beginning of my graduate studies. I also want to thank Nicole Thompson, Reyn Aoki, Ashley Mapile, David Ollodart, Gary Boon, Srivathsav Venkatesh, Benjamin Rinn, and Kenny Andre for their collaboration and assistance over the years. And finally, I want to thank all other past and present labmates, including Kevin Lee, Ge Gu, Chih-Wei Hsu, Sabiha Rustam, Yiheng Zhang, and Yao-Yu Li their consistent encouragement and scientific support.

I want to thank all of my collaborators, who have worked with me on exploring exciting and unique areas of research. In particular, I want to thank Dr. Elizabeth Nance, Dr. Mengying Zhang, Dr. Lilo Pozzo, Dr. Ryan Kastilani, and Dr. Caitlyn Wolf for being incredible research partners. I also want to thank the UW Clean Energy Institute, the Molecular Engineering Materials Center, and the Interdisciplinary Center for Exposures, Diseases, Genomics, and Environment for financial support and facilitating collaborations, as well as staff members at the Molecular Analysis Facility for assisting in the characterization of my research, especially at the end of my Ph.D. I am also grateful to my mentors during my undergraduate research experience, Mohan Sankaran and Souvik Ghosh, for introducing me to the world of nanomaterials and encouraging me to pursue a graduate degree.

I cannot be more appreciative of the people in my life who have supported me and become my chosen family. I am so grateful to my friends from Newton, MA and Case Western University—Katy Hennen, Greg Ziegan, Roger Li, Maddie Starr, Bre Glover, Renee Hartney, Anton Spencer, Phil Banaszek, and many more—for the unconditional love and support they have brought to my life. Without the encouragement of my friends from graduate school, I would have never become the person I am today. Thank you to Jon Witt, Gabriella Tosado, Victor Hu, and Caitlyn Wolf for being my champions, going on adventures with me, bringing me food during my times of need, and inspiring me to fight for change in the world. You have all been there for me during the many highs and lows of graduate school, and I don't know how I would've gotten through it without you. I also want to thank Peyton Turner for the unconditional love, friendship, support, and joy you have brought me during the last few years of my Ph.D. I am also grateful for the other members of my Seattle community who have accompanied me on adventures, bonded over campfires, and laughed with me along the way, including Grant Williamson, Tori Hernandez, Laura Dobroski, Brian Gerwe, and Lindsay Blaire.

Finally, I want to thank my family for the many years of love and encouragement. From a young age, you allowed me to explore the world in a way that kept me curious and set me on my path through science and engineering. I am especially grateful for my mom, dad, brother, and sister—Jayne, Robert, Jon, and Lindsay Bishop—for the endless support throughout my childhood and today. You fostered my passions of science, engineering and art, which allows me to see beauty in everyday life.

To every person who has encouraged me during my Ph.D., thank you for embodying the sentiment “lift as you climb.” You have all raised me to be a better version of myself.

# **DEDICATION**

To my sister, Lindsay.

## Chapter 1. INTRODUCTION

### 1.1 SEMICONDUCTOR NANOCRYSTALS

#### 1.1.1 *Quantum Confinement*

Luminescent semiconductor nanocrystals, or quantum dots (QDs), are a subset of spherical nanomaterials with diameters typically between 1 and 100 nanometers (nm). When a semiconductor approaches the size of its innate exciton Bohr radius (*i.e.*, the physical distance between the charge carriers in a Coulombically bound electron-hole pair), the semiconductor begins to experience the effects of quantum confinement. Upon reaching the Bohr radius, which typically ranges between 2 and 50 nm for most materials, the valence and conduction band states

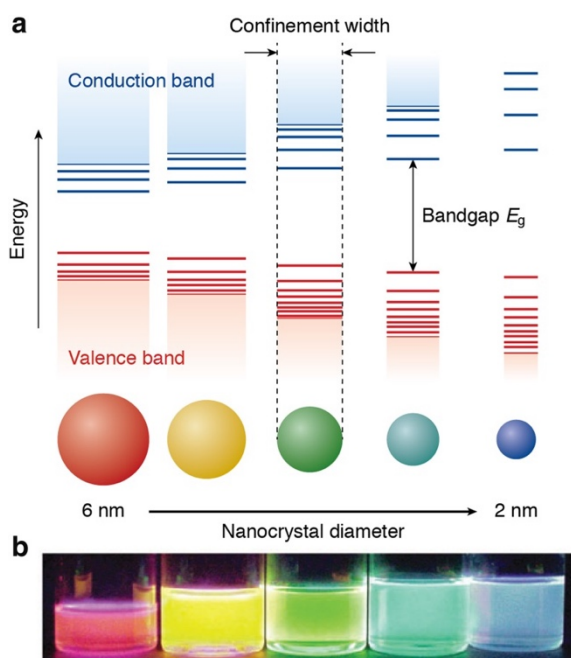


Figure 1.1. a) Schematic of the quantum confinement effect in semiconductor nanocrystals. b) Emission of colloidal CdSe nanocrystals with different sizes, which blue shift with a decrease in nanocrystal diameter.<sup>1</sup>

begin to separate and the bandgap of the semiconductor begins to increase (Figure 1.1a).<sup>1</sup> In addition, discrete energy levels emerge at the band-edge, with the separation between states increasing in energy with a decrease in nanocrystal diameter. With increasing confinement, the photoluminescence (PL) of the semiconductor QDs shifts to lower wavelengths, with materials such as cadmium selenide (CdSe) exhibiting luminescence in the red that blue-shifts and across the visible

spectrum for increasingly smaller nanocrystal diameters (Figure 1.1b).<sup>1</sup> This direct radiative recombination between a band-edge electron-hole

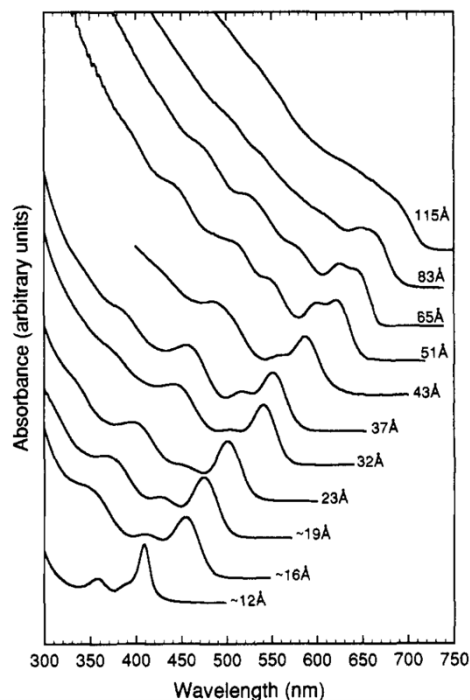


Figure 1.2. Absorption spectra of CdSe quantum dots with diameters ranging from 12 Å (1.2 nm) to 115 Å (11.5 nm).<sup>2</sup>

pair is referred to as band-edge luminescence. In addition to size-dependent PL, the effects of quantum confinement are also evident in the nanocrystal absorption spectra. As seen in Figure 1.2, the peaks in a QD absorption spectrum correspond to the allowed excitonic absorption transitions ( $1S_{3/2}1S_e$ , etc.), where the allowed excitonic transitions shift to higher energy with decreases size. As seen in Figure 1.2, distinct absorption features corresponding to allowed excitonic transitions are observed, where the amount of energy required to generate an exciton increases for smaller, more highly quantum-confined nanocrystals. For example, the lowest-energy  $1S_{3/2}1S_e$  excitonic transition shows a distinct absorbance peak that shifts to higher energies as the nanocrystal size decreases, with the higher-energy excitonic transitions also shifting to shorter wavelengths.<sup>2</sup>

### 1.1.2 Properties and Applications

The tunability of semiconductor quantum dots make them attractive for a variety of applications, and the band gap of the semiconductor plays a large role with respect to the potential applications of a particular semiconductor quantum dot. Figure 1.3 displays several semiconductor materials with bandgaps that are tunable across the visible and near-infrared (NIR).<sup>3</sup> Quantum dots that emit near or within the NIR region between 700 and 2500 nm, such as indium arsenide (InAs) and lead sulfide (PbS), can be advantageous for deep tissue biological imaging,<sup>4,5</sup> solar cells,<sup>6-8</sup>

and NIR photodetectors<sup>9,10</sup>, while quantum dots that emit in the visible range, such CdSe and indium phosphide (InP) can be utilized for display applications<sup>11-13</sup> and multi-color biological imaging.<sup>14,15</sup>

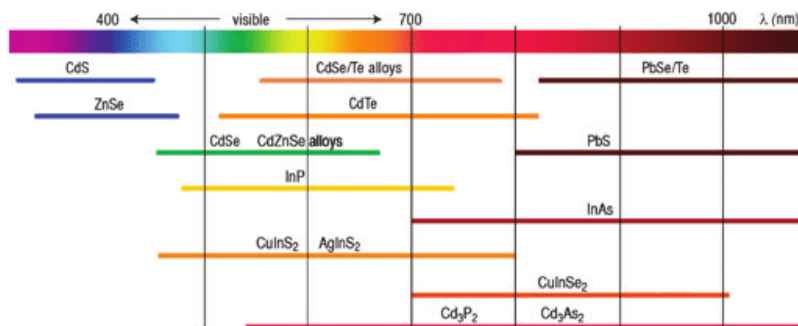


Figure 1.3. Ranges of photoluminescence emission for various semiconductor materials.<sup>3</sup>

Quantum dots have been studied and optimized over the past decades in order to better understand each nanocrystal system and improve their characteristics for the different purposes they serve. For example, nanocrystals have significantly improved photostability relative to fluorescent dyes and their surface chemistry can be readily functionalized for different targeting applications, making them valuable for bioimaging and labeling.<sup>14,16-20</sup> Their large absorption cross-section and broadband absorption capabilities makes them promising for energy conversion applications, including solar cells, solar concentrators, and photodetectors,<sup>21-24</sup> and several semiconductor quantum dot systems have been optimized to have narrow photoluminescence bandwidths and near-perfect photoluminescence quantum yields, making them advantageous for high-efficiency and pure-color LEDs.<sup>16,25,26</sup>

### 1.1.3 Toxicity and Earth Abundance

CdSe and PbS are arguably two of the most well-studied and highly optimized QD material systems. They have been optimized to have high energy conversion efficiencies and have thus been used in LEDs, photovoltaics, photodetectors, photoconductors, biomedical imaging, and photocatalysis.<sup>27</sup> However, both of these materials contain toxic elements, making them less

suitable for biological and commercial applications.<sup>28–31</sup> As alternatives, researchers are interested in developing materials comprised of non-toxic and earth abundant elements, including zinc chalcogenides and indium pnictides (Figure 1.4).<sup>28</sup> For example, InP is significantly less toxic than CdSe and can similarly be tuned throughout the visible spectrum, while silver sulfide (Ag<sub>2</sub>S) and

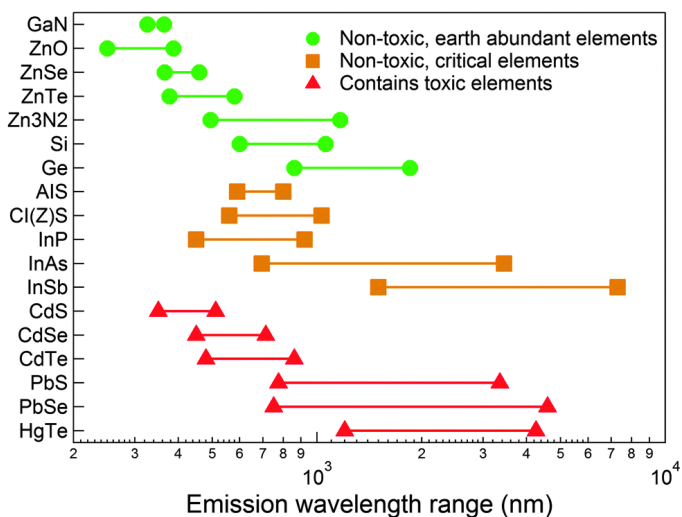


Figure 1.4. Range of luminescence wavelengths and relative toxicity and earth abundance of different QD materials.<sup>28</sup>

InAs are less toxic than PbS and can be similarly tuned throughout the NIR.<sup>28</sup> However, these earth-abundant and non-toxic semiconductor QDs still need further optimization in order to compete with CdSe and PbS. For example, most Ag<sub>2</sub>S nanocrystals exhibit exceedingly low quantum efficiencies and most InAs syntheses utilize dangerous, highly reactive precursors or generate QDs with low quantum efficiencies.<sup>32–35</sup> Similarly, many syntheses of high-quantum-yield InP QDs still utilize highly reactive precursors like tris(trimethylsilyl) phosphine, while InP QDs synthesized with aminophosphines, which are significantly safer, still require further optimization to create nanocrystals with both the high quantum yield photoluminescence and narrow linewidths that are necessary to rival and replace CdSe.<sup>16,25,26,36–38</sup> Thus, significant work is still required to improve the photoluminescent properties of these materials such that they are more viable for commercial use.

## 1.2 COLLOIDAL NANOCRYSTAL SYNTHESIS AND OPTIMIZATION

### 1.2.1 Nucleation and Growth Methods of Nanocrystals

In 1950, LaMer and Dinegar proposed a model for the nucleation and growth of monodisperse colloids.<sup>39</sup> In this model, they described three main phases: (i) decomposition of precursors in

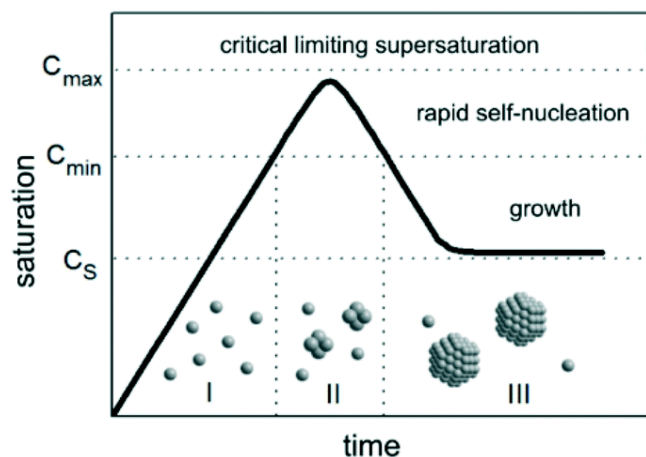


Figure 1.5. Nanoparticle nucleation and growth described through LaMer and Dinegar's model. The black curve indicates the theoretical concentration of monomers over time.<sup>40</sup>

solution until supersaturation is reached, (ii) rapid self-nucleation of the colloidal material, and (iii) growth by diffusion as the concentration of precursors declines to its solubility limit. A depiction of this process can be seen in Figure 1.5.<sup>40</sup>

Since then, this foundational model has been utilized to describe nanocrystal nucleation and growth through common synthesis techniques, including the hot-injection and solvothermal methods. While the overall principal of the nucleation is similar in hot-injection and solvothermal methods, each have their own mechanisms, which result in different advantages and disadvantages for each.

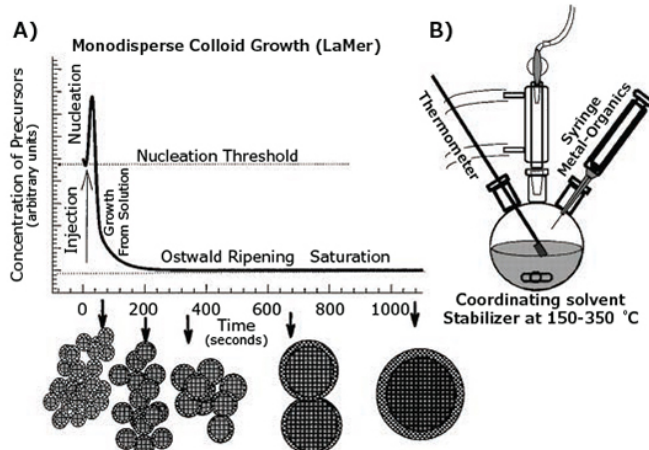


Figure 1.6. a) Depiction of the nucleation and growth of nanocrystals via the a) hot-injection method and b) a schematic of the chemical set-up commonly used for the hot-injection method.<sup>41</sup>

In the hot-injection method, as depicted in Figure 1.6a and b,<sup>41</sup> precursors are rapidly injected into a flask with hot coordinating

solvents, which are commonly fatty acids, fatty amines, or organophosphates heated between 150 and 350°C. These coordinating solvents, which also serve as ligands, are present during synthesis to bond to the surface of the nanocrystal and are typically necessary for nanocrystal stabilization. They can also act as reducing agents, assist with precursor decomposition, and influence surface-related electronic states.<sup>42–45</sup> Since most nanocrystal precursors decompose at elevated temperatures, these coordinating solvents must have high boiling points as well. For compound semiconductors with ionic character, the cation precursor is typically added to the flask along with the coordinating solvents, while excess anion precursor is rapidly injected. Upon injection at increased temperatures, there is rapid precursor decomposition followed by nucleation of nanocrystals and growth via Ostwald ripening, where small nanocrystals coalesce into larger particles.<sup>41</sup> The rapid nature of this injection facilitates near-instantaneous nucleation of nanocrystals and a fast depletion of precursors, resulting in a single rapid nucleation event that generates monodisperse nanocrystals.<sup>41,46,47</sup> While the hot-injection method has been utilized to produce a variety monodisperse nanocrystals, including II-VI, III-V, and IV-VI semiconductors,<sup>48</sup> the nature of the nucleation process makes it difficult to scale and relies on the speed of the injection, which can vary day-to-day or human-to-human and can create batch-to-batch inconsistencies.<sup>46,47</sup>

In contrast, solvothermal syntheses involve the simultaneous heating of all precursors and coordinating solvents in a single temperature ramp. Upon reaching a temperature where all precursors have

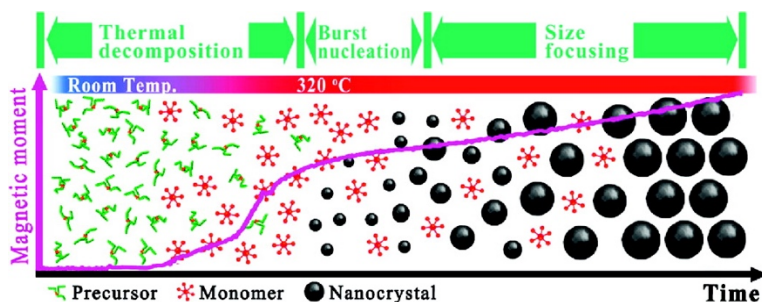


Figure 1.7. a) Depiction of the nucleation and growth of nanocrystals via the solvothermal method.<sup>49</sup>

decomposed, a burst nucleation and subsequent nanocrystal growth will occur, as seen in Figure 1.7.<sup>49</sup> In comparison to hot-injection, the solvothermal method is significantly easier to scale and does not rely on injection speed, decreasing variation and increasing batch-to-batch consistency. However, it is significantly more difficult to separate the nucleation and growth of nanocrystals via the solvothermal method, often resulting in several nucleation bursts and polydisperse samples.<sup>50</sup> To effectively control solvothermal syntheses, precursors, coordinating solvents, and temperature ramps must be chosen carefully such that reaction kinetics are optimized to effectively separate the nucleation and growth of the nanocrystals. It is particularly important to choose precursors that are stable at room temperature but rapidly decompose at higher temperatures in order to ensure a single, rapid nucleation burst for the synthesis of monodisperse nanocrystals.<sup>50</sup>

Given that both of these systems have contrasting advantages and disadvantages, development of nanocrystal syntheses that can produce monodisperse nanocrystals and can also be easily scaled is desired. In addition, for many nanocrystal systems, typical hot-injection and solvothermal syntheses require inert conditions, which necessitates expensive equipment like glove boxes or a Schlenk line, which further inhibits the scalability of these syntheses. Thus, developing systems that can generate high-quality nanocrystals, be run in atmospheric conditions, are easily scalable, and utilize common equipment is greatly desired in order to facilitate the integration of nanomaterials into commercial products.

### 1.2.2 *Magic-size Clusters and Intermediates in Nanocrystal Growth*

Recently investigations into the nucleation and growth of semiconductor nanocrystals, have unearthed systems with growth pathways that diverge from LaMer and Dinegar's model. In 2015, Gary, *et al.* monitored the nucleation and growth of InP quantum dots using a combination of

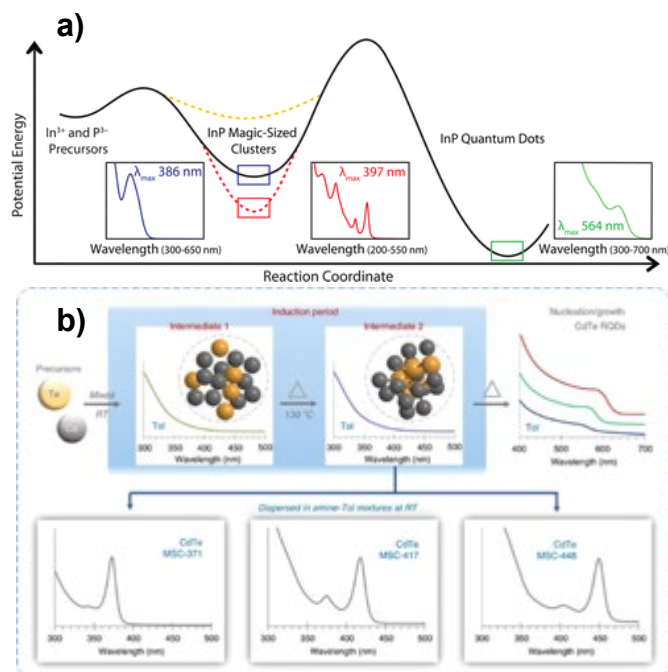


Figure 1.8. a) Two-step nucleation and growth of InP QDs, with MSCs as an intermediate.<sup>51</sup> b) Multi-step nucleation and growth of CdTe MSCs and QDs.<sup>52</sup>

ultraviolet-visible (UV-vis) absorbance spectra, X-ray diffraction (XRD), and nuclear magnetic resonance (NMR) spectroscopy. In this system, they found that the growth of InP QDs did not follow the classic nucleation theory and that instead, there was an intermediate phase where InP magic-sized clusters (MSCs), ultrasmall nanostructures with a discrete, precisely defined number of atoms, were formed before being converted into larger nanocrystals, as depicted in Figure 1.8a.<sup>51</sup> In

2017, Liu, *et al.* showed similar nucleation pathways for cadmium telluride (CdTe) QDs, where two intermediates, both  $\sim 1$  nm in size, were observed prior to the nucleation and growth of the nanocrystals (Figure 1.8b).<sup>52</sup> Based on their findings, they hypothesized a three-step process: the assembly of Cd and Te precursors held together by noncovalent interactions, the formation of Cd-Te bonds at higher temperatures, and finally, the formation of MSCs when dispersed into solvents at room temperature or QDs when the solution was continuously heated. Additional studies have shown that MSCs are common intermediates in the formation of CdSe QDs as well, with a hypothesized multi-step nucleation and growth process that is similar to the InP QDs.<sup>53–55</sup>

Researchers have also been able to isolate MSCs and utilize them as building blocks for larger nanostructures, including 2D and 3D superstructures,<sup>56,57</sup> nanoplatelets,<sup>58,59</sup> nanorods,<sup>53</sup> quantum dots,<sup>51,60,61</sup> and nanowires.<sup>62</sup> In addition to acting as intermediates or building blocks, MSCs are

useful for a variety of applications. Most notably, their photoluminescence spectra is dominated by broadband emission deriving from their large surface area and large fraction of surface states, making them promising for efficient white-light LEDs.<sup>11,63</sup> Their ultrasmall size also makes them advantageous for biological imaging and labeling since the body can easily clear them through the renal system.<sup>60,64,65</sup>

### 1.2.3 Shell Growth onto Quantum Dot Cores

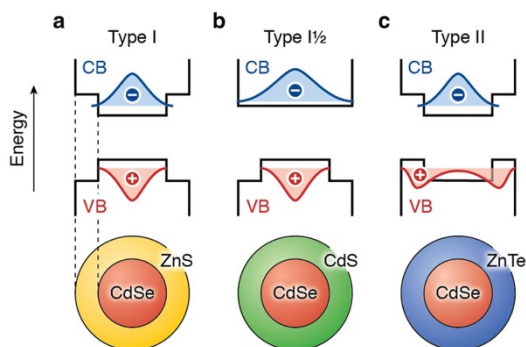


Figure 1.9. Schematic of three different band alignments between core/shell semiconductor nanocrystals. a) Type I: charge carriers are both localized to the core. b) Type I.5: one charge carrier is localized to the core, while the other is delocalized across the nanocrystal. c) Type II: the charge carriers are specially separated. In this case, the electrons are localized to the core, while the holes are localized to the outer shell.<sup>1</sup>

The addition of an epitaxial inorganic shell onto a semiconductor nanocrystal is an important strategy that has been used to facilitate the localization and protection of the electron-hole pairs, or excitons, in the quantum dot emitter. The presence of this protective shell has shown to result in increased radiative recombination, where excitons recombine and generate a photon, rather than recombining via competing nonradiative pathways, thereby improving the photoluminescence quantum efficiency of the system. In particular, this shell must be able to

localize the exciton enough to prevent trapping of charge carriers in lower energy electronic states that exist due to surface defects or by species present in solution, which can effectively “steal” a charge carrier and prevent exciton recombination. Examples of defects that can lead to electronic trap states include atomic vacancies and unbound surface atoms with poor ligand passivation and

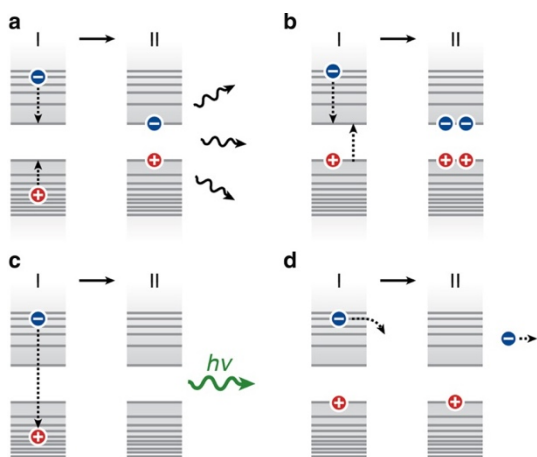


Figure 1.10. Representation of different charge carrier trapping and exciton recombination: a) thermalization via exciton coupling, b) multi-exciton generation via carrier energy transfer, c) radiative recombination, and d) charge carrier ejection into the environment of the nanocrystal.<sup>1</sup>

incomplete valence or dangling bonds. Sufficient exciton localization can be achieved through proper band alignment between the core and shell.<sup>66</sup> In particular, a type 1 or 1.5 band alignment is typically utilized for efficient localization of the charge carriers to the nanocrystal, as shown in Figure 1.9.<sup>1</sup> This structure has been utilized for a

library of inorganic semiconductor quantum dots, including cadmium selenide/cadmium sulfide (CdSe/CdS), zinc selenide/zinc sulfide (ZnSe/ZnS), indium phosphide/zinc sulfide (InP/ZnS), and many more.<sup>16,25,67,68</sup> In addition to improved

quantum efficiencies, carefully engineered shells have been able to suppress PL “blinking”, or emission intermittency, making single nanocrystals viable for single-dot biological tracking.<sup>16,69</sup> Studies have shown that blinking can derive from thermal ejection, surface-state trapping, and auger recombination—or transfer of energy from one charge carrier to another, as seen in Figure 1.10.<sup>1,70</sup> While the presence of defects or trap states often enhances unwanted nonradiative recombination pathways, they can also lead to radiative recombination. If the observed luminescence is derived from surface-state-based recombination, this is sometimes referred to as surface-state emission, which manifests as wideband luminescence at lower energies (longer wavelengths) than the band-edge luminescence. However, growth of a protective shell that can suppress charge carrier trapping and nonradiative recombination pathways will increase band-edge luminescence quantum yields, decrease surface-state emission, and decrease blinking.<sup>16,70</sup>

Two common strategies for the addition of this epitaxial protective shell are through a syringe-pump-aided slow-drip method, where shell precursors are slowly added to a heated mixture of quantum dot cores, and successive ion layer adsorption and reaction (SILAR), where individual monolayers of each element in a compound semiconductor are sequentially added until the desired shell thickness is achieved.<sup>16,71</sup> Both methods have been successful at generating CdSe/CdS and CdSe/ZnS nanocrystals with high quantum yields, narrow bandwidth, and suppressed blinking.<sup>16,72,73</sup>

#### 1.2.4 Strain-Engineering in Semiconductor Nanostructures

While growing a carefully engineered shell can protect a nanocrystal core from and surface traps and the surrounding environment, lattice mismatch between a core and shell often results in strain at the core/shell interface. This strain can result in dislocations in the lattice, which leads to the formation of defects, such as vacancies and dangling bonds,<sup>74,75</sup> as seen in Figure 1.11. Similar

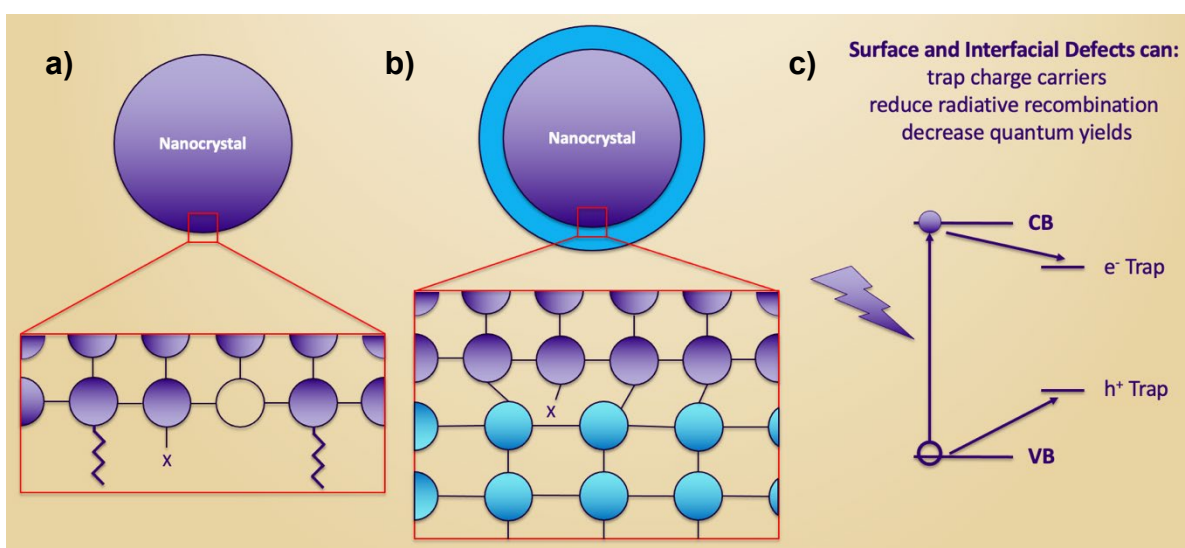


Figure 1.11. Visualization of possible defects in nanocrystals a) before and b) after shell growth in core/shell structures with large lattice mismatch. c) Visualization of trapping in the electronic structure of a semiconductor.

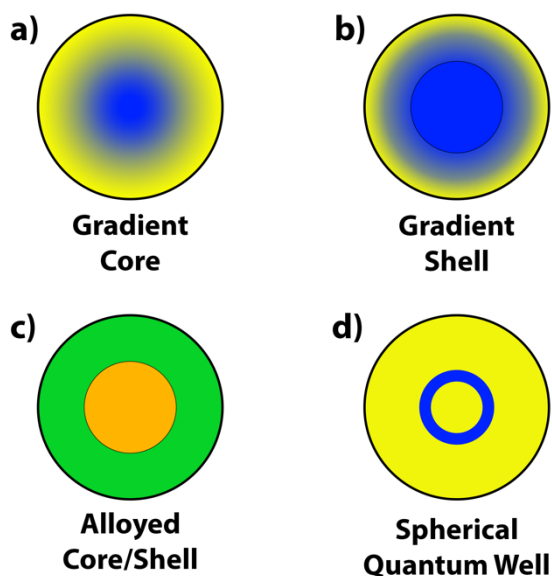


Figure 1.12. Depiction of strain-engineering techniques in quantum dots: a) gradient cores, b) gradient shells, c) alloyed core/shells, and d) spherical quantum wells.

to surface defects, these interfacial defects can also result in charge carrier trapping and non-radiative recombination, decreasing the band-edge luminescence efficiency of the nanocrystals.

In attempts to combat lattice mismatch and the resulting interfacial defects, a variety of strain engineering strategies have been employed in quantum dot systems. One technique utilizes graded cores, which slowly

transitions from core material to shell material instead of having a distinct interface between the two, as seen in Figure 1.12a. For example, in 2003, Bailey and Nie demonstrated that  $\text{CdTe}_x\text{Se}_{1-x}$  nanocrystals that slowly transition radially from CdTe to CdSe exhibit quantum yields up to 60% with narrow photoluminescence spectra.<sup>76</sup>  $\text{CdSe}_x\text{S}_{1-x}$  QDs have also been synthesized that exhibited 50-80% quantum yields and significantly reduced blinking.<sup>77,78</sup>

Similarly, gradient shells (Figure 1.12b) have been grown onto CdSe and InP nanocrystal cores. In 2017, Cho, *et al.* synthesized  $\text{CdSe}/\text{CdSe}_x\text{S}_{1-x}/\text{ZnSe}_y\text{S}_{1-y}/\text{ZnS}$  QDs with quantum yields of 90%.<sup>79</sup> However, while the quantum yield was high, the nanocrystals exhibited wider-band PL spectra, making them less useful for pure color LEDs compared to other QD architectures. Interestingly, in 2019, Lee, *et al.* compared  $\text{InP}/\text{ZnSe}_x\text{S}_{1-x}/\text{ZnS}$  and  $\text{InP}/\text{ZnSe}/\text{ZnS}$  nanocrystals and found that the nanocrystals with discrete shells ( $\text{InP}/\text{ZnS}/\text{ZnS}$ ) had a higher quantum yield, narrower emission spectrum, and lower photoluminescent blinking than the corresponding

nanocrystals with a gradient shell.<sup>80</sup> Surprisingly, their analysis indicated that there was actually larger lattice mismatch in the gradient-shelled nanostructures, explaining the less desirable photoluminescence properties.

Another strategy employs the use of both an alloyed core and shell to minimize the lattice mismatch between the two (Figure 1.12c). In 2016, Pietra, *et al.* generated  $\text{In}_x\text{Zn}_y\text{P}/\text{ZnSe}_z\text{S}_{1-z}$  with maximum photoluminescence quantum yields up to 60%, but also exhibiting wideband emission.<sup>81</sup> More recently, in 2020, Mulder, *et al.* synthesized alloyed  $\text{InZnP}/\text{ZnMgSe}/\text{ZnS}$  nanocrystals with quantum yields up to 60% and similar wideband emission that narrowed with increased magnesium (Mg) content.<sup>82</sup>

Lastly, another approach to strain engineering high quantum yield emitters is through two-dimensional layered heterostructures, also known as quantum wells, where the small band-gap emitter is layered between two or more wider band-gap substrates in order to alleviate strain and improve the device performance. These structures were first developed in the 1960s, where these two-dimensional quantum wells were engineered at Bell Labs for improved lasers and LEDs.<sup>83–85</sup> In these systems, if the emitting material is very thin—below a critical thickness value—and is equally and oppositely strained by a substrate on both sides, the quantum well's lattice structure will remain coherent with the substrate, reducing strain at the interfaces between the two materials and enhancing the photoluminescent properties.<sup>86–89</sup> Extending this technique further, the spherical quantum well (SQW) combines the concepts of a traditional quantum well and strain engineering within a colloidal semiconductor nanocrystal. In this system, the emissive material is sandwiched between a wider bandgap core and outer shell (Figure 1.12d) in order to reduce interfacial strain between each layer and improve the photoluminescent properties.<sup>87,89</sup> The SQW was first developed in 1994 with mercury sulfide (HgS), when Mews, *et al.* investigated a  $\text{CdS}/\text{HgS}/\text{CdS}$

“quantum dot quantum well.”<sup>89</sup> In 2016, Jeong *et al.* synthesized CdS/CdSe/CdS structures with an ultrathin CdSe shell and large CdS shell.<sup>87</sup> When the CdSe shell was small enough, it became coherently strained, reducing lattice mismatch between the CdSe and CdS. Upon growing a large enough shell, they were able to generate CdS/CdSe/CdS nanocrystals with quantum yields approaching 100% and low PL blinking without compromising narrow bandwidths. Based on these results, the spherical quantum well seems to be a promising architecture that could be utilized to increase quantum yields, photoluminescence stability, and color purity in other semiconductor systems.

### 1.2.5 *Surface Chemistry and Functionalization of Nanocrystals*

The surfaces of quantum dots can be functionalized with different chemistries in order to improve biological targeting and stability,<sup>90–93</sup> induce self-assembly of nanocrystals,<sup>94–97</sup> and facilitate charge transfer in solar cells and photocatalysis.<sup>94,98–100</sup> In particular, within biological targeting, nanoparticles conjugated with polyethylene glycol (PEG) have been found to result in decreased nanocrystal aggregation, increased circulation time in the body, increased penetration into the brain, and reduced toxicity, making PEGylated nanoparticles a promising option for biological applications.<sup>101,102</sup>

Furthermore, the choice of surface chemistry can greatly impact the quantum yield and photoluminescent properties of quantum dots. Since shorter ligands can enhance charge transfer, they are ideal when developing solar cells and photodetectors, but increase dot-to-dot coupling and interactions with the environment, thereby decreasing nanocrystal quantum yields.<sup>99,100,103,104</sup> For example, in nanocrystals functionalized with fatty acids with different carbon chain lengths, those with shorter carbon chains (C4-C8) exhibited significantly lower quantum yields than those

with long carbon chains (C12 – C18).<sup>105</sup> In particular, aliphatic long chain amines and carboxylic acids have proven to enhance quantum yields due to their ability to pack tightly on the surface of the nanocrystal, passivating a large fraction of surface trap sites and sufficiently insulating nanoparticles from the environment.<sup>104</sup>

In addition to chain length, the electronegativity of a ligand's functional group can greatly influence the density of hole traps at the surface of the nanocrystal. For instance, in CdSe nanocrystals, the terminal oxygen of trioctylphosphine oxide (TOPO) forms a strong complex with surface Cd sites due to the high electronegativity of oxygen, thereby effectively passivating surface sites and increasing quantum efficiencies.<sup>104,106</sup> Conversely, a terminal sulfur is less electronegative and exhibits two lone pairs of electrons after bonding with the cadmium at the nanocrystal surface, introducing deep hole traps, decreasing band-edge luminescence, and increasing surface-state emission.<sup>106</sup> Manipulating the elemental density at the surface of CdSe nanocrystals, creating either Cd-rich or Se-rich surface chemistry, has also shown to impact the quantum efficiencies. In 2007, Jasieniak and Mulvaney showed that Se-rich CdSe reached ~50% quantum yields with TOP passivation and were much less sensitive to the presence of typical metal-binding ligands, while Cd-rich CdSe had lower quantum yields but exhibited significantly better PL stability in both oxygen-free and ambient air conditions.<sup>107</sup>

Compared to CdSe, InP nanocrystals are extremely sensitive to the presence of oxygen and water, which can easily react at the InP surface at elevated reaction temperatures (100-300 °C) or after long exposure to oxygen under atmospheric conditions.<sup>108–112</sup> In 2010, Cros-Gagneux, *et al.* demonstrated that using carboxylate-containing precursors and coordinating solvents in the synthesis of InP NCs can result in ketonization of the carboxylic acids, leading to the formation of water and oxidation at the surface of the nanocrystals.<sup>111</sup> This formation of oxidation species at the

surface of the InP can create charge carrier traps and could prevent a pristine core/shell interface, both of which would reduce the quantum yields of the InP. Therefore, in InP nanocrystals, reducing oxygen exposure to the nanocrystals, especially during the synthesis process, is critically important for increasing quantum efficiencies and decreasing nonradiative recombination.

Thus, based on the several studies and findings on CdSe and InP, it is important to carefully consider chain length, ligand packing density, and electronegativity when choosing coordinating solvents and ligands. Utilizing ligands such as oleic acid, TOPO, and trioctylphosphine (TOP) has shown to improve quantum efficiencies in CdSe,<sup>16,106</sup> while using oxygen-free coordinating solvents like oleylamine are ideal for InP.<sup>36,111</sup>

### 1.3 DISSERTATION OVERVIEW

The research in this dissertation focuses on the development and optimization of luminescent semiconductor nanocrystals. Collectively, the studies included efforts toward making nanocrystals more clinically or commercially viable, including decreasing nanocrystal toxicity, developing scalable and high-throughput nanocrystal synthesis methods, and studying techniques for improving the photoluminescent properties of nanostructures.

Chapter 2 describes an investigation carried out on a model system of luminescent nanocrystals for biological imaging and targeting. By adjusting the surface functionalization of CdSe/CdS nanocrystals, we investigate the impact that the surface chemistry of these quantum dots has on nanocrystal stability, toxicity, and uptake through *in vitro*, *ex vivo*, and *in vivo* studies utilizing biologically relevant fluids and mouse models. Importantly, this chapter demonstrates the significant impact that the specific study model and surface chemistry have on the resultant

quantum dot behavior, which will help to inform and guide future research on QD imaging probes in neurological applications.

Chapter 3 highlights the sonochemical synthesis of CdSe quantum dots and magic sized clusters. This system allows for the on-demand growth of nanostructures whose properties can easily be tuned through active sonication time and system type, specifically through single-phase or emulsion-based synthesis. These syntheses are also performed in atmospheric conditions with common equipment, making this system a potentially scalable and sustainable option for commercial nanocrystal synthesis.

Chapter 4 presents a highly reproducible synthesis of monodisperse ZnS nanocrystals. This one-pot solvothermal synthesis employs a highly reactive sulfur precursor that results in improved reproducibility and narrower size distributions, while also utilizes coordinating solvents that facilitate efficient nanocrystal purification in order to decrease processing steps and improve purified nanocrystal yield. The size of the nanocrystals can also be tuned via the reaction temperature, where increased temperatures result in increased nanocrystal diameters.

Chapter 5 focuses on the development of InP shelling techniques in order to investigate strain-engineered InP spherical quantum wells, an architecture that has been demonstrated to enhance the quantum efficiencies, reduce blinking, and generate narrow photoluminescence bandwidths in other material systems. Developing and improving the photoluminescence properties of InP is of particular interest since InP is a significantly safer material than what is currently being utilized for visible spectrum emitters in commercial products. A selection of indium and phosphorus precursors were explored, and our results indicate that aminophosphines, a low-cost family of precursors that are safe to use under ambient conditions, are a good option for the epitaxial growth of InP shells onto zinc chalcogenide nanocrystal substrates. In addition, we can utilize the spherical

quantum well model to highlight the importance of symmetry, band alignment, and lattice match in these systems for making higher quantum efficiency emitters.

Finally, Chapter 6 will highlight the conclusions from these studies and their contributions to the field, as well as future projects that can continue and expand upon this work.

## Chapter 2. SURFACE FUNCTIONALIZATION OF FLUORESCENT NANOCRYSTALS FOR BIOLOGICAL IMAGING

The work presented in this chapter is result of a collaborative project between the Holmberg Lab and the Nance Lab (UW Chemical Engineering). I, with the assistance of Nicole Thompson and Reyn Aoki, led the synthesis, surface functionalization, and characterization of the CdSe quantum dots. Dr. Mengying Zhang and I worked together closely to study the cadmium dissolution and photoluminescent stability of the CdSe quantum dots. Dr. Mengying Zhang, Kate Hildahl, Binh Dang, Olesya Mironchuk, Nina Chen, and Dr. Elizabeth Nance led the remaining studies on nanocrystal toxicity, stability, and cellular uptake.

This chapter is adapted and reproduced in part from “Zhang, Mengying; Bishop, Brittany P.; Thompson, Nicole L.; Hildahl, Kate; Dang, Binh; Mironchuk, Olesya; Chen, Nina; Aoki, Reyn; Holmberg, Vincent C.;\* Nance, Elizabeth,\* Quantum Dot Cellular Uptake and Toxicity in the Developing Brain: Implications for Use as Imaging Probes. *Nanoscale Advances* (2019), **1**, 3424-3442. <https://doi.org/10.1039/C9NA00334G>” with permission from the Royal Society of Chemistry.

### 2.1 INTRODUCTION

Fluorescent imaging has become an important tool for use in biological studies and clinical practice.<sup>14–16,20,113–118</sup> This technique is particularly important for viral and molecular tracking<sup>113</sup>, cellular imaging,<sup>114</sup> and in vivo imaging and tracking of diseases inside the body.<sup>15,115</sup>

Traditionally, biological imaging has been conducted using a variety of fluorescent proteins and dyes, which can emit in a wide-range of wavelengths and are able to target different tissues and cells.<sup>115</sup> While these dyes can be versatile, these proteins can often exhibit low quantum yields and exhibit photobleaching when exposed to the excitation wavelengths required to excite them,<sup>115,118</sup> making them difficult to use in time-dependent techniques, such as viral and molecular tracking.

A recent approach to improved biological imaging is through fluorescent semiconductor nanomaterials, such as cadmium selenide (CdSe) quantum dots (QDs), which have been optimized to have high quantum yields,<sup>16</sup> can be tuned to emit various wavelengths of light for multicolor imaging,<sup>14,20</sup> can be functionalized for cell and disease targeting,<sup>20</sup> and are more stable than proteins, reducing the effects of photobleaching—or “blinking.”<sup>16–19</sup> The use of these semiconductor nanocrystals in biological studies have since been critical in making more robust and versatile biological imaging techniques and improving the study of several diseases.<sup>14,15,20,119</sup>

In particular, CdSe nanocrystals (NCs), with a high-quality cadmium sulfide (CdS) shell, are incredibly bright, with quantum yields approaching 95% in organic media and up to 70% in aqueous media. In 2013, Chen, *et al.* developed a method for generating this CdS shell via a slow-drip method, followed by a high-temperature annealing period, resulting in a low defect interface and increasing the quantum yields significantly.<sup>119</sup> Since then, the Peng lab has also showed that minimizing surface species and defects on these CdSe/CdS NCs through a combination of surface treatment and choice of ligand can reduce blinking and dramatically improve the quantum yields of the nanocrystals.<sup>17–19</sup>

To improve the application of semiconductor nanocrystals in biological studies, these materials must be optimized for biological compatibility. Specifically, it is important for the

photoluminescence (PL) emission wavelength of the semiconductor material to be tuned near or within the near-infrared (NIR) tissue transparency window,<sup>117</sup> from ~700 to 1300 nanometers (nm), in order to maximize visibility of the fluorescent light through biological samples. Since CdSe/CdS NCs can be tuned to emit up to 650-700 nm, on the edge of the NIR window, they are useful for shall-depth biological imaging. To utilize these CdSe/CdS nanocrystals in biological studies, the nanocrystals must also be compatible in biological samples, which can be done through functionalization of the nanocrystal surface. By changing the surface chemistry, the CdSe/CdS can be dispersed into aqueous media and target different types of cells or parts of the body.

One area of particular interest is the use of QDs for functionalized drug delivery and targeted imaging biomarkers in the brain. However, there has not been a comprehensive assessment of QD behavior in the brain, which could hinder the use of QDs for targeted drug delivery or neurological imaging. A significant concern is the toxicity of QDs, which can result from the leaching of inorganic ions from the QD crystal,<sup>120</sup> or the loss of QD stability and subsequent nanocrystal aggregation.<sup>121-123</sup> Furthermore, different QD surface functionalities and terminal end groups can have different cell- or tissue-targeting effects, resulting in diverse cell cytotoxicity,<sup>124</sup> varying degrees of injury,<sup>125</sup> and distinctions during *in vivo* biodistribution.<sup>126</sup> Despite significant interest in QD engineering, little is known about QDs in physiological environments, which has limited the use of QDs in biological applications.<sup>127</sup> Therefore, a systematic evaluation of QDs focused on both nanoparticle engineering and physiological variance in the tissue environment is essential.

Herein, we present the synthesis of CdSe QDs for use in biological studies conducted by Dr. Elizabeth Nance and her students at the University of Washington. Upon growth of a CdS shell onto the CdSe core, monodisperse NCs were formed with an overall increase in quantum efficiency. To effectively disperse these materials in aqueous solution, a ligand exchange and

surface functionalization was conducted on the CdSe/CdS NCs. The NCs were customized to have one of three surface functionalities—3-mercaptopropionic acid (MPA), poly(ethylene glycol) (PEG)-5000k-methoxy (PEG-OMe), and (PEG)-5000k-hydroxyl (PEG-OH)—to allow for further study of the surface chemistry in neurophysiologically important environments, including investigations into photoluminescent stability and ion leaching. Dr. Mengying Zhang, Kate Hildahl, Binh Dang, Olesya Mironchuk, Nina Chen, and Dr. Elizabeth Nance then studied the impact that the surface chemistry had on the quantum dot stability, cellular uptake, and toxicity in relevant brain environments, including *in vitro*, in cultured brain slices (*ex vivo*), and *in vivo*.

## 2.2 SYNTHESIS AND SURFACE FUNCTIONALIZATION OF CADMIUM SELENIDE QUANTUM DOTS FOR BIOLOGICAL IMAGING

### 2.2.1 *Materials*

Cadmium oxide (CdO,  $\geq 99.99\%$ ), selenium ( $\geq 99.99\%$ ), trioctylphosphine oxide (TOPO, 90%), trioctylphosphine (TOP, 97%), hexadecylamine (HDA, 90%), oleic acid (OLA, 90%), 1-octadecene (ODE, 90%), 1-octanethiol ( $\geq 98\%$ ) and 3-mercaptopropionic acid (MPA,  $\geq 99\%$ ) were purchased from Sigma-Aldrich. PEG5000k-methoxy (PEG-OMe, PLS-604), and PEG5000k-hydroxyl (PEG-OH, PBL-8083) were purchased from Creative PEGWorks. Hexanes ( $\geq 98.5\%$ ), toluene ( $\geq 99.5\%$ ), acetone ( $\geq 99.5\%$ ), methanol ( $\geq 99.8\%$ ) and citric acid ( $\geq 99.5\%$ ) were purchased from Fischer Scientific. All reagents were used as received, without further purification.

### 2.2.2 *Synthesis of Cadmium Selenide Quantum Dots*

CdSe nanocrystal cores were synthesized via a modified version of the protocol developed by De Nolf *et al.*<sup>128</sup> In a typical synthesis, 150 mg cadmium oxide (CdO), 12 g 1-octadecene (ODE), and 1 g oleic acid (OLA) were added to a 100 mL 3-neck flask on a Schlenk line, heated to 110 °C under nitrogen, and degassed for 30 min while stirring. The mixture was then heated to 280 °C under nitrogen and stirred at 600 rpm until clear and colorless. After lowering the temperature to 100 °C, 2 g of hexadecylamine (HDA) and 2 g of trioctylphosphine oxide (TOPO) were quickly added and the mixture was degassed for an additional hour. The flask was then heated to 280 °C under nitrogen, after which a solution of TOP:Se (190 mg of Se dissolved in 4 mL of trioctylphosphine) was rapidly injected. Aliquots were taken as the nanocrystals grew, and UV-vis absorption spectroscopy was used to monitor nanocrystal diameter by tracking the position of the  $1S_{3/2}S_e$  excitonic absorption feature.<sup>129</sup> Once the desired nanocrystal diameter was achieved, the heating mantle was removed, and the mixture was allowed to cool. When the temperature of the flask reached 100 °C, 10 mL of toluene was injected in order to facilitate nanocrystal purification. Once cooled to room temperature, the nanocrystal cores were purified by adding antisolvent (ethanol) to the reaction mixture until the point of opalescence, followed by rapid centrifugation, and dispersion of the resulting nanocrystal precipitate in clean toluene – a process which was repeated three times.

### 2.2.3 *Growth of Cadmium Sulfide Shells onto Cadmium Selenide Cores*

Protective CdS shells were grown onto the CdSe nanocrystal cores using a modified version of the protocol developed by Chen *et al.*<sup>16</sup> Prior to shell growth, cadmium oleate was prepared using previously established procedures.<sup>24</sup> Briefly, 129 mg CdO, 950  $\mu$ L OLA, and 10 mL ODE

were heated to 110 °C and degassed for 45 minutes using standard Schlenk line methods. The mixture was then heated to 280 °C under nitrogen and stirred at 700 rpm until clear and colorless. The resulting cadmium oleate complex was then cooled to 100 °C and degassed for an additional hour prior to being cooled to room temperature and transferred to a nitrogen-filled glove box for storage. Core-shell CdSe/CdS QDs were then prepared by adding 200 nmol of CdSe nanocrystal cores to a mixture of 2.5 g ODE and 2 g HDA in a 100 mL flask attached to a Schlenk line. The mixture was heated to 60 °C under nitrogen and degassed for 1 h while stirring at 850 rpm, followed by heating under nitrogen to 120 °C and degassing for an additional 20 min. A syringe pump was then loaded with two separate syringes: one containing cadmium oleate dissolved in ODE, and one containing 1-octanethiol dissolved in ODE. For the 3.4 nm-diameter CdSe cores used in this study, 8.7 mL of cadmium oleate complex mixed with an additional 0.8 mL of ODE were loaded into one syringe, and 300  $\mu$ L of 1-octanethiol mixed with 9.2 mL of ODE were loaded into the other syringe. To facilitate shell growth, the dispersion of nanocrystal cores was heated under nitrogen to 290 °C at a rate of  $\sim 14$  °C  $\text{min}^{-1}$ , and once the solution temperature reached 200 °C, the syringes containing the cadmium and sulfur precursors were slowly injected at a rate of 2.3 mL  $\text{h}^{-1}$  using the syringe pump. After completion of the injection, the dispersion was held at 290 °C for an additional 30 min. 2 mL of OLA were then rapidly injected, and the dispersion was cooled to 200 °C and left to anneal at that temperature for 1 h. After cooling to room temperature, the core-shell QD dispersion was purified several times by the addition of ethanol, followed by centrifugation and dispersion of the precipitated QDs into clean toluene.

#### 2.2.4 Surface Functionalization of Cadmium Selenide/Cadmium Sulfide Quantum Dots

Core-shell CdSe/CdS QDs were functionalized via ligand exchange procedures modified from Zhang *et al.*<sup>130</sup> using three different target surface chemistries, including 3-mercaptopropionic acid (MPA), PEG5000k-methoxy (PEG-OMe), and PEG5000k-hydroxyl (PEG-OH). In a typical synthesis, QD surface functionalization and transfer to aqueous media was achieved by dissolving either 70  $\mu$ L MPA, 120 mg PEG-OMe, or 120 mg PEG-OH into a mixture of 300  $\mu$ L deionized water and 1 mL methanol. The ligand solution was then adjusted to a pH of  $\sim$ 12 by the gradual addition of 40% NaOH.  $\sim$ 15 nmols of core-shell CdSe/CdS QDs dispersed in 500  $\mu$ L chloroform (for MPA functionalization) or hexanes (for PEG-OMe and PEG-OH functionalization) were added to the 1.3 mL ligand solution along with a stir bar. The solution was then stirred at 1000 rpm for 30 min, followed by the addition of 1 mL deionized water. The solution was then left to stir for another 20 min. The organic and aqueous phases were then separated, and the functionalized QDs (now dispersed in the aqueous phase) were collected. MPA-functionalized QDs (QD-MPA) were purified via the addition of acetone, followed by centrifugation, dispersion of the precipitated QDs into deionized water, and filtration through a 0.2  $\mu$ m nylon filter. For PEG-OMe and PEG-OH functionalized QDs (QD-PEG-OMe and QD-PEG-OH), the dispersions were filtered through a 0.2  $\mu$ m nylon filter, neutralized with citric acid, and placed under vacuum using a rotary evaporator to remove excess hexanes and methanol. The optimized syntheses outlined in the preceding sections were carried out numerous times to produce the large quantities of functionalized QDs necessary for the *in vitro*, *ex vivo*, and *in vivo* studies.

### 2.2.5 *Quantum Dot Characterization*

QD absorption characteristics were determined by collecting ultraviolet-visible (UV-vis) extinction spectra with an Agilent Cary 60 UV-vis spectrophotometer. Care was taken such that all absorbance values recorded were below 1.0. Nanocrystal morphology was evaluated via transmission electron microscopy (TEM) using a FEI Tecnai G2 F20 Supertwin TEM operating at an accelerating voltage of 200 kV. ImageJ software was used to determine nanocrystal size distributions. Photoluminescence characteristics were determined for each sample of functionalized CdSe/CdS QDs using a PerkinElmer LS-55 fluorescence spectrometer. Absolute photoluminescence quantum yield measurements were carried out using a Hamamatsu C9920-12 integrating sphere and verified using a rhodamine 640 perchlorate reference dye (Exciton, Inc.). QD particle concentrations were determined by measuring the position and intensity of the  $1S_{3/2}1S_e$  excitonic absorption feature.<sup>24</sup> FTIR spectra for MPA, PEG-OMe, and PEG-OH-functionalized CdSe/CdS QDs were obtained using a Bruker Alpha IR spectrometer equipped with a platinum attenuated total reflectance (ATR) accessory and a diamond crystal sampling module. Prior to FTIR analysis, the QD-PEG-OMe and QD-PEG-OH samples were placed under vacuum in a rotary evaporator until completely dry, and then were re-dispersed into chloroform. The MPA-functionalized QDs were purified via the addition of acetone, followed by centrifugation and dispersion of the precipitated QDs into methanol. Spectra were recorded under a nitrogen atmosphere after forming thin films of material on the diamond ATR crystal. QD thin films were formed by drop-casting the chloroform or methanol particle dispersions directly onto the surface of the ATR crystal and allowing the solvents to evaporate completely.

### 2.3 CHARACTERIZATION AND SURFACE FUNCTIONALIZATION OF CADMIUM SELENIDE/CADMIUM SULFIDE QUANTUM DOTS

Due to the effects of quantum confinement, CdSe NCs and their absorbance properties change based on the NC diameter. During the synthesis process, the NCs increase in diameter over time, and the PL and ultraviolet-visible (UV-Vis) absorbance red-shift with the increase in size. In 2003, Yu, *et al.* correlated the wavelength of the first excitonic peak, the lowest energy—or highest wavelength—peak, and the diameter of the NCs, as seen in Equation 2.1.<sup>129</sup>

$$D = (1.6122 * 10^{-9})\lambda^4 - (2.6575 * 10^{-6})\lambda^3 + (1.6242 * 10^{-3})\lambda^2 - (0.4277)\lambda + (41.57) \quad (2.1)$$

where D = nanocrystal diameter and  $\lambda$  = wavelength of first excitonic absorption peak<sup>129</sup>

To monitor the growth of the NCs, aliquot samples were taken over time and using Equation 2.1, the diameter of the NCs were calculated. Scaled absorption of the CdSe NCs at various time points throughout the synthesis can be seen in Figure 2.1. To synthesize CdSe compatible for

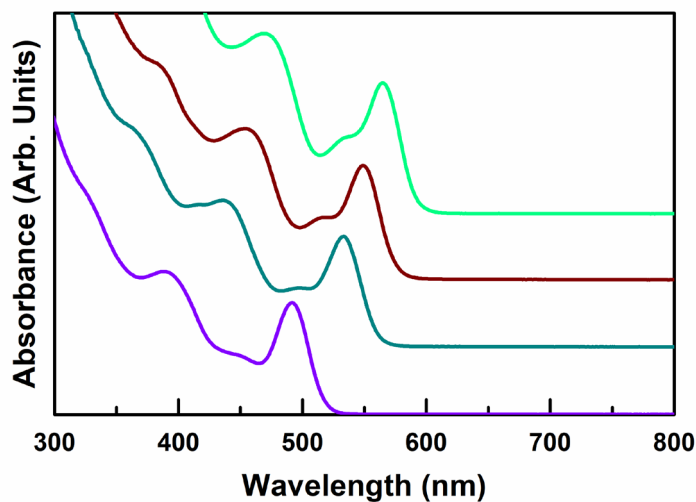


Figure 2.1. Absorbance spectra for CdSe quantum dots as they grow in diameter over time. The purple spectrum indicates the smallest nanocrystals, while the light green spectrum indicates the largest.

biological imaging, the NCs grown had to be small enough for use in the body, but large enough for PL emission to be seen through biological samples. Specifically, nanocrystals with a hydrodynamic size below  $\sim 20$  nm have reported to be suitable for neuron and glial labeling and

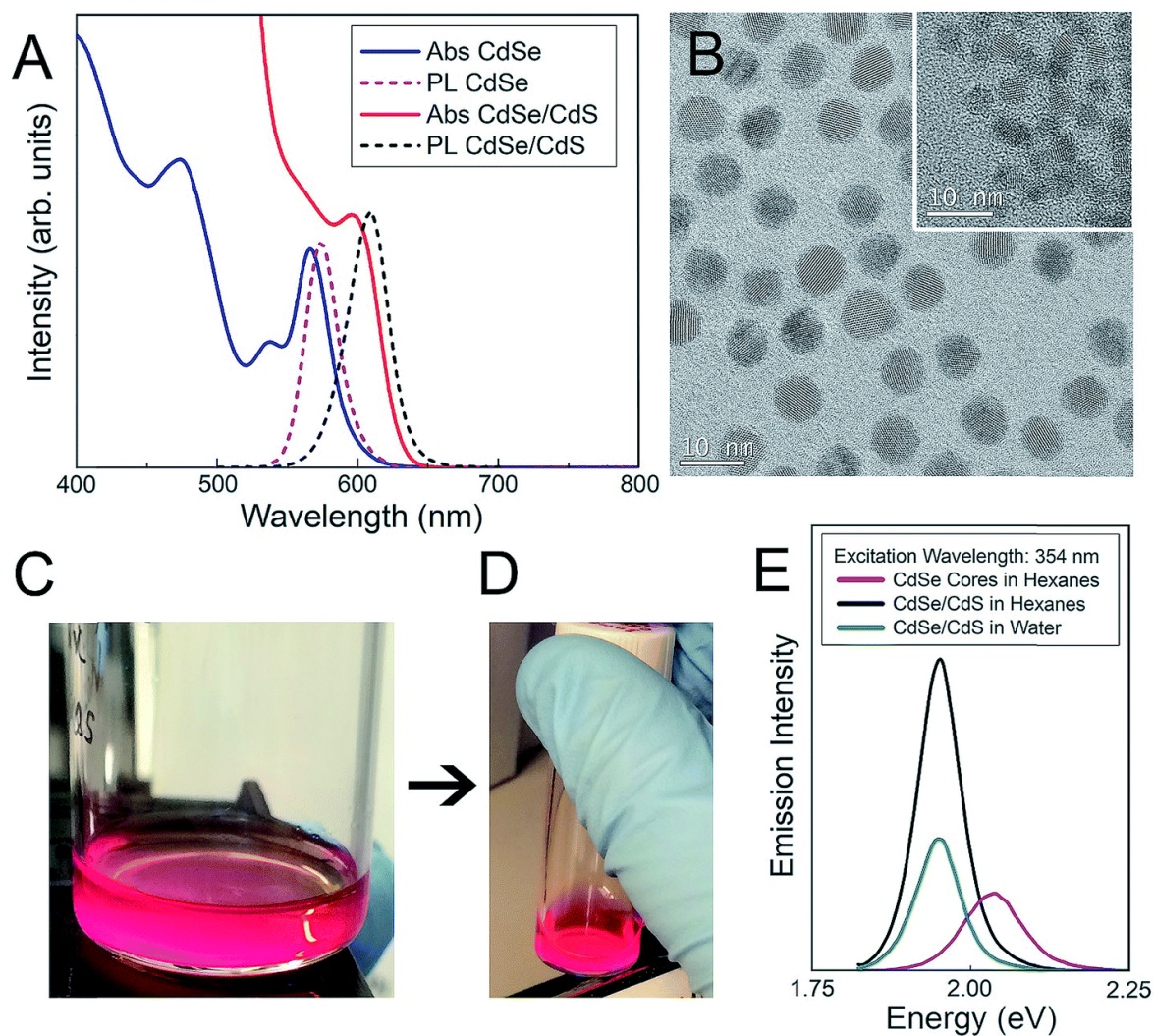


Figure 2.2. Surface functionalization and characterization of CdSe–CdS core–shell QDs. (A) Absorbance and photoluminescence of CdSe nanocrystal cores (blue and pink) and final core–shell CdSe/CdS QDs (red and black) with 60% quantum yield. (B) TEM images of final  $6.7 \pm 0.5$  nm diameter core–shell QDs and initial  $3.4 \pm 0.4$  nm-diameter nanocrystal cores (inset). (C, D) Images of QD dispersions under UV excitation (C) before and (D) after surface functionalization and transfer to aqueous media. (E) Relative emission intensity of initial nanocrystal cores (pink), and final core–shell QDs before (black) and after (green) surface functionalization and transfer to aqueous media.

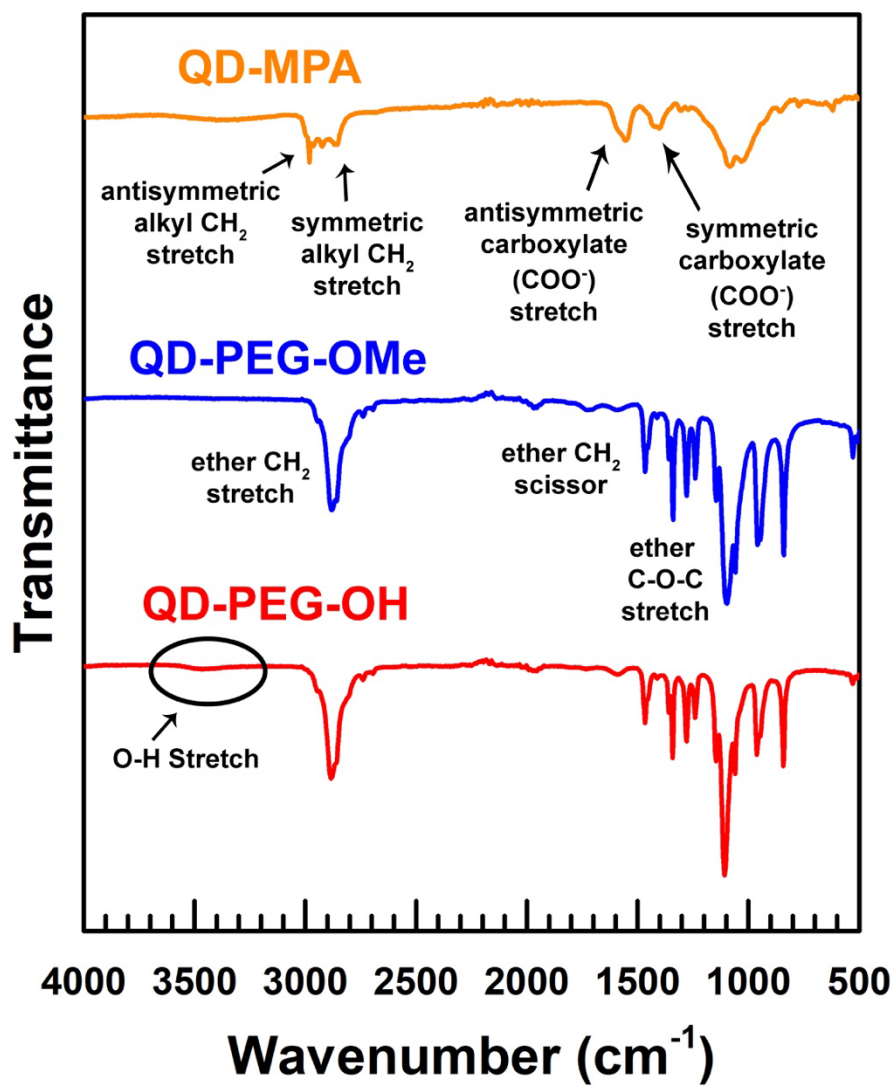


Figure 2.3. ATR-FTIR spectra of QD-MPA (orange), QD-PEG-OMe (blue), and QD-PEG-OH (red). The FTIR spectra of the PEGylated QDs show the distinct features of the polyethylene glycol polymer ligand. The peak at 1100 cm<sup>-1</sup> is characteristic of an ether C-O-C band, while the peaks at 2870 and 1465 cm<sup>-1</sup> correspond to CH<sub>2</sub> stretching and scissoring vibrations, respectively. The remaining peaks indicate the presence of a long-chain polyether. The peaks at 1340, 1280, and 1235 cm<sup>-1</sup> are indicative of CH<sub>2</sub> wagging, symmetric twisting, and antisymmetric twisting, respectively. The peak at 960 cm<sup>-1</sup> corresponds to a combination of coupled symmetric CH<sub>2</sub> rocking, C-C stretching, and C-O stretching, while the peak at 840 cm<sup>-1</sup> corresponds to coupled CH<sub>2</sub> rocking and C-O stretching. The QD-PEG-OH samples show an additional broad O-H stretching band extending from 3300 to 3560 cm<sup>-1</sup>, which is indicative of the additional terminal O-H functional group attached to the PEG. The 3-mercaptopropionic acid-functionalized QDs exhibited characteristic antisymmetric and symmetric alkyl CH<sub>2</sub> stretching bands at 2920 and 2860 cm<sup>-1</sup>, respectively, along with clear antisymmetric and symmetric carboxylate (COO<sup>-</sup>) stretching bands at 1560 and 1410 cm<sup>-1</sup>, respectively. These observations, in combination with the absence of a strong carboxylic acid C=O stretch at 1710 cm<sup>-1</sup>, indicate complete deprotonation of the carboxylic acid groups on the MPA ligands.

tracking.<sup>131,132</sup> Therefore, care was taken to keep the overall diameter of the inorganic nanocrystal below 8 nm, such that the overall hydrodynamic diameter of the functionalized QDs would be below ~20 nm (accounting for a ~6 nm-thick ligand corona).

Both CdSe nanocrystal cores and core-shell CdSe/CdS QDs have a roughly spherical morphology (Figure 2.2), with CdSe nanocrystal cores exhibiting diameters of  $3.4 \pm 0.4$  nm and final core-shell CdSe/CdS QDs exhibiting diameters of  $6.7 \pm 0.5$  nm (Figure 2.2B) excluding the outer ligand corona. The spectral profiles of the QDs (Figure 2.2) remained largely unperturbed, irrespective of which surface ligation was selected. Additional physicochemical evidence of successful surface functionalization via attenuated total reflectance Fourier transform infrared (ATR-FTIR) spectroscopy can be found in Figure 2.3. Both PEGylated QD samples exhibit all of the expected characteristic FTIR peaks,<sup>133–135</sup> with the QD-MPA samples exhibiting clear carboxylate ( $\text{COO}^-$ ) stretches at  $1560$  and  $1410$   $\text{cm}^{-1}$ ,<sup>136,137</sup> indicating full deprotonation of the MPA ligands.

## 2.4 NANOCRYSTAL STABILITY, TOXICITY, AND CELLULAR UPTAKE

### 2.4.1 *Quantum Dot Photoluminescence Stability*

QD-MPA, QD-PEG-OH and QD-PEG-OMe particles were diluted by artificial cerebrospinal fluid (aCSF) to form  $0.1$   $\mu\text{M}$  suspensions and incubated at  $37$  °C for up to 24 h. The aCSF was adjusted to pH 7.4–7.6 before adding the QDs. Photoluminescence spectra of QD suspensions were measured at 0 h, 1 h, 4 h and 24 h using a SpectraMax M5 Microplate Reader (Molecular Devices) with a 450 nm excitation wavelength, and the photoluminescence intensity was then plotted as a function of time.

### 2.4.2 Quantum Dot Dissolution Stability

QD-MPA, QD-PEG-OH and QD-PEG-OMe particles were diluted by aCSF to form 0.1  $\mu\text{M}$  suspensions and incubated at 37 °C for up to 24 h. The aCSF was adjusted to pH 7.4–7.6 before adding the QDs. At 0 h and 24 h, 1 mL of QD suspension was transferred to an Amicon Ultra-2 Centrifugal Filter Unit (50 kDa) and centrifuged at  $3000 \times g$  for 10 min in order to filter out the QDs. The fluid that passed through the filter was then collected for inductively coupled plasma mass spectroscopy (ICP-MS) analysis using a NexION 2000 ICP Mass Spectrometer (PerkinElmer) to measure the quantity of  $\text{Cd}^{2+}$  ions released into the suspension.

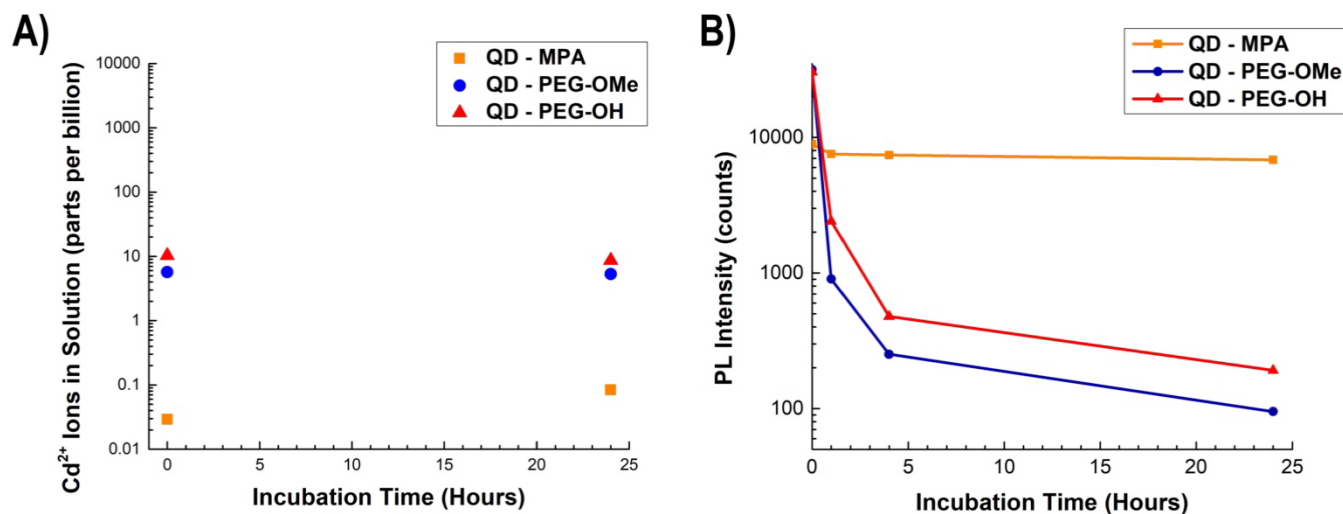


Figure 2.4. (A) Cadmium ion release of 0.1  $\mu\text{M}$  CdSe/CdS QDs with different surface functionalities in aCSF at 37°C after 0 h and 24 h incubation. The level of free  $\text{Cd}^{2+}$  ions in all groups tested was less than 10 parts per billion (ppb). Note that the initial 0-h baseline levels of  $\text{Cd}^{2+}$  are due to a small subset of CdSe particles that pass through the 50-kD filter and are digested to  $\text{Cd}^{2+}$  during ICP-MS sample preparation. When a lower molecular weight cutoff filter (3 kD) was used on identical PEGylated samples, a baseline  $\text{Cd}^{2+}$  ion level of 1 ppb was achieved. The concentration of free  $\text{Cd}^{2+}$  ions remained virtually unchanged (less than 1 ppb change in concentration) for all samples over the 24-hour measurement period. (B) Photoluminescence intensity of QDs incubated in aCSF under physiological conditions as a function of time.

### 2.4.3 *Cadmium Dissolution and Photoluminescence Stability of Quantum Dots in Neurophysiologically Relevant Fluids*

Importantly, in aCSF we see no dissolution of QDs into appreciable amounts of Cd ions. Using ICP-MS analysis, we measured Cd-ion concentrations following incubation for 0 and 24 h in aCSF. Cd-ion concentrations were stable for all QDs across the experimental time frame, and remained less than 10 parts per billion (ppb) (Figure 2.4A). We also incubated 0.1  $\mu$ M QDs in aCSF at 37 °C for 24 h, and measured the luminescence intensity of the QD suspensions at 0 h, 1 h, 4 h, and 24 h of incubation (Figure 2.4B). The photoluminescence (PL) of the QD-MPA particles remained stable over 24 h, while the PL intensity of the PEGylated QDs decreased over time. This likely occurs because the well-dispersed PEGylated QDs are completely exposed to the aCSF environment, while the non-PEGylated QDs (QD-MPA) aggregate quickly (Figure 2.5A), resulting in a lower initial PL intensity, but a less rapid decrease in PL intensity since the QD-MPA particles contained within the aggregate are protected from aCSF exposure. Independent of the change in PL, all confocal imaging studies (Figure 2.5D and E) have clear QD detection at low laser power with high signal to noise in the *in vitro* cell culture, *ex vivo* brain slices, and *in vivo* tissue sections.

### 2.4.4 *Nanocrystal Stability, Toxicity, and Cellular Uptake*

The following studies on nanocrystal stability, toxicity, and cellular uptake were conducted by Dr. Mengying Zhang, Kate Hildahl, Binh Dang, Olesya Mironchuk, Nina Chen, and Dr. Elizabeth Nance. While several studies took place to study QD-MPA, QD-PEG-OH, and QD-PEG-OMe, Figure 2.5 provides a few examples of the different *in vitro*, *ex vivo*, and *in vivo* studies that were performed.

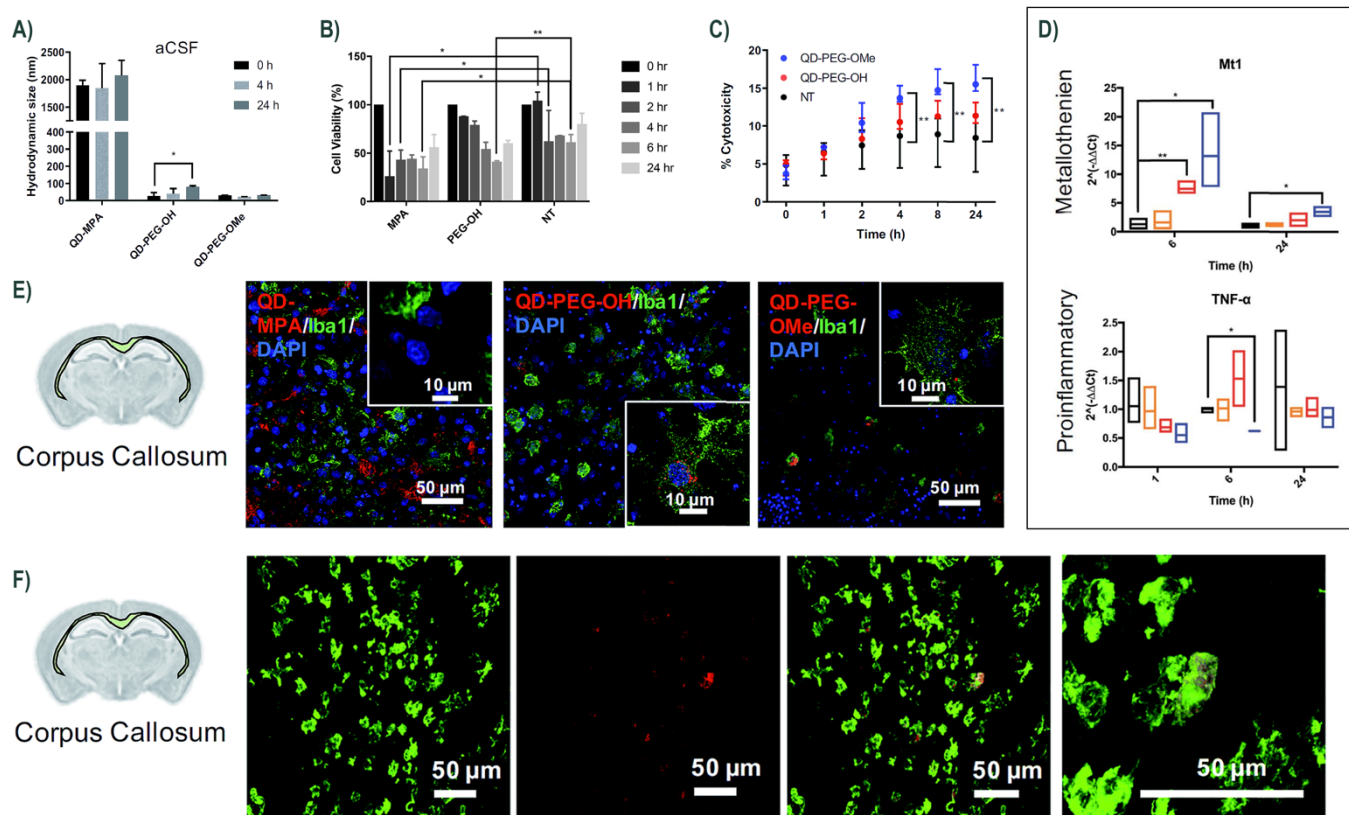


Figure 2.5. (A) QD hydrodynamic diameter at 37 °C in aCSF at 0, 4, 24 h ( $n = 3$  measurements per particle type). (B) Toxicity of QDs on in vitro BV-2 cells. Treatment of QD-MPA and QD-PEG-OH at 0.01  $\mu\text{M}$  concentration on in vitro BV-2 cells for 1, 2, 4, 6, and 24 h, with reported % cell viability. For each condition,  $n = 3$  wells were evaluated with 10,000 cells per well when plated. (C) Dose-dependent toxicity of QD-PEG-OH and QD-PEG-OME in ex vivo OWH slices. Treatment of QD-PEG-OH (red) and QD-PEG-OME (blue) at 1  $\mu\text{M}$  concentrations in P14 rat organotypic brain slices for 24 h. QD toxicity was determined by LDH assay at 0, 1, 2, 4, 8, and 24 h as follows. For each QD concentration,  $n = 3$  slices per QD per concentration condition were evaluated; for NT group (black),  $n = 5$  slices. (D) Time-dependent mRNA profiles of QD-induced proinflammatory and metallothionein markers in OWH slices. Fold-changes in mRNA expression were measured at 1 h, 6 h, and 24 h of QD-MPA (orange), QD-PEG-OH (red), and QD-PEG-OME (blue) exposure at 0.1 mM concentration in OWH slices. The fold-changes were measured for metallothionein isoform Mt1 and proinflammatory cytokine TNF- $\alpha$ , and compared to NT slices (black). For 1 h, 6 h, and 24 h time points,  $n = 3$  groups and  $n = 3$ –6 slices per group were evaluated for each experimental sample (except for the QD-PEG-OME 6 h proinflammatory sample, where  $n = 2$  groups with  $n = 6$  slices in total were evaluated). All data are reported as median values with 95% confidence intervals. (E) Iba1+ microglia and lysosome uptake of QDs in ex vivo OWH slices. Representative 40 $\times$  magnification images of QD-MPA, QD-PEG-OH, and QD-PEG-OME distribution and Iba1+ cellular uptake in the corpus callosum in P14 Sprague-Dawley (SD) rat OWH slices (300  $\mu\text{m}$  thickness). QDs (red, all images) were found internalized into Iba1+ microglia (green, all images). Representative high-magnification images of QD-MPA, QD-PEG-OH, and QD-PEG-OME localization inside Iba1+ cells are shown as insets. Cell nuclei were stained with DAPI and display blue luminescence. (F) QD cellular uptake in P7 rats, 4 h post-administration. Representative images of QD-PEG-OH (red, all images) colocalization with Iba1+ microglia cells (green, all images) in the corpus callosum regions in P7 mglur5 WT, 4 h after i.p. administration. 40 $\times$  magnification images with 4-fold zoom (160 $\times$ ) are presented in the rightmost column to show QD-PEG-OH internalization in cells. Data provided courtesy of Dr. Mengying Zhang, Kate Hildahl, Binh Dang, Olesya Mironchuk, Nina Chen, and Dr. Elizabeth Nance.

To study the stability of the QDs under neurophysiologically relevant conditions, the hydrodynamic diameter of the core–shell CdSe/CdS QDs with different surface functionalities was monitored in aCSF at 0 h, 4 h, and 24 h at 37 °C, using dynamic light scattering (DLS) to evaluate any long-term tendency toward aggregation in brain-related fluids at physiological temperatures. QD-MPA particles tended to aggregate immediately (hydrodynamic diameter > 1500 nm), while QD-PEG-OMe particles were relatively stable in aCSF over the entire 24-hour period and QD-PEG-OH showed a statistically increased hydrodynamic diameter at 24 h but remained below 100 nm in total hydrodynamic size (Figure 2.5A).

*In vitro* QD toxicity studies demonstrated the importance of surface functionality on cellular vitality of BV-2 microglia cells. When applied directly to microglia, 0.01  $\mu$ M QD-MPA induced significant cell death starting at 1 h, as compared to a non-treated (NT) group treated only with 1 $\times$  phosphate-buffered saline (PBS). The viability of QD-MPA-treated cells was observed to drop below 50% before some recovery at 24 h. QD-PEG-OH, however, did not show any statistically significant decrease in cell viability, as compared with NT, except at 6 h (Figure 2.5B).

To study the amount of QD-induced toxicity in organotypic whole hemisphere (OWH) slices, whole-slice cytotoxicity caused by the QDs was evaluated by measuring cell death after 24 h of QD exposure, as a function of QD surface functionality. To note, QD-MPA was not included in the OWH slice toxicity assessment due to the observed rapid aggregation in biological fluids and subsequent hindered penetration and cellular uptake in OWH slices. Cytotoxicity at 0.01 and 0.1  $\mu$ M showed no significant differences between QD-PEG-OMe, QD-PEG-OH, or the NT samples. However, at 1  $\mu$ M, QD-induced cytotoxicity was around 15% for QD-PEG-OMe and slightly above 10% for QD-PEG-OH. The cytotoxicity of 1  $\mu$ M QD-PEG-OMe was significantly higher than the NT group, starting at 4 h post-treatment, and remained statistically higher at 8 h and 24 h

(Figure 2.5C). The relatively low toxicity of QD-PEG-OH and QD-PEG-OMe at low concentration is likely imparted due to the PEG coating, which has been previously shown to effectively decrease cytotoxicity and maintain tissue viability.<sup>138</sup>

To investigate QD-induced inflammation, mRNA profiles for metal detoxification and oxidative stress. At 0.1  $\mu\text{M}$  QD concentrations, the pegylated QDs induced significant increase of the M1t expression (Figure 2.5D), indicating a cellular response to activate metal detoxification for  $\text{Cd}^{2+}$  exposure. However, QD exposure resulted in almost no statistically significant inflammatory response, as seen via the TNF- $\alpha$  expression (Figure 2.5D), or other oxidative stress responses, indicating that PEGylated QDs are not inducing inflammation to brain cells under 24-hr time frames.

The cellular uptake of QDs in OWH slices was evaluated as a function of surface functionality. Independent of surface chemistry, all QDs were found localized primarily in microglia in the neonatal rat brain, particularly in the corpus collosum (Figure 2.5E) and hippocampus regions. Confocal images acquired at 60 $\times$  magnification and 4-fold zoom enabled a closer look at QD internalization in microglia at the single-cell level. Although several QD-MPA aggregates were still observed to uptake in the microglia, the QD-PEG-OH and QD-PEG-OMe uptake was much more distinctive and diffuse in the microglial cytosol (Figure 2.5E inset). An additional study also showed that while QD-MPA aggregated in *ex vivo* brain slices and showed decreased cellular uptake, QD-MPA penetrated nicely during *in vitro* studies due to direct access to the cells, emphasizing the importance of the model utilized during biological studies.

A metabotropic glutamate receptor 5 (mglur5) neuroinflammatory rat model was used to evaluate QD uptake *in vivo*. QD-PEG signals were detected in the brain, at both 4 h and 24 h time points, after intraperitoneal (i.p.) injection in postnatal day (P) 7 wild-type (WT) rat pups (Figure

2.5F). However, the QD signal was minimal, due to the majority of the sub-20 nm QD-PEG being cleared rapidly.<sup>139</sup> Although the total quantity of QDs in the brain was low, colonized QDs were identified in microglia in various regions. QD-PEG-OH particles were found colocalized with Iba1+ microglia in the cortex, corpus callosum (Figure 2.5F), hippocampus, and periventricular region (PVR), with the majority of accumulation in the corpus callosum region at 4 h post-injection (Figure 2.5F).

Additional studies demonstrated the impact of brain region, QD concentration, cell type, pH, and type of neurophysiological-relevant fluid on the QD stability, toxicity, and cellular uptake. These studies revealed that each factor plays a significant role in the QD behavior during *in vitro*, *ex vivo*, and *in vivo* studies.

## 2.5 CONCLUSIONS

The implementation of engineered nanoparticles as biomarkers is a challenging task, requiring a comprehensive understanding of both nanoparticle engineering and the disease environment in which the nanoparticle will be applied. To develop QD-based biomarkers for application to the brain, it is necessary to better understand QD behavior in the brain environment. Here, we synthesized and functionalized CdSe/CdS QDs for use in biological studies. We comprehensively assessed the interaction of functionalized, core-shell CdSe/CdS QDs with the brain microenvironment, including QD colloidal stability, toxicity, and cellular uptake *in vitro*, *ex vivo*, and *in vivo*. Importantly, stability, toxicity, and cellular uptake of QDs were dependent on one another, and dependent on the model used to evaluate the effect. We found that surface chemistry strongly influenced QD behavior in the brain. PEG-coatings improved QD stability in complex neurophysiological-relevant fluids, induced low cytotoxicity in brain slices, and led to stable,

diffuse cellular uptake. QDs were preferentially taken up into microglia, especially in the corpus callosum, which was further confirmed *in vivo*. Non-PEGylated QDs, however, destabilized rapidly when exposed to brain-relevant fluids, which likely led to the increased photoluminescence stability, but prevented penetration into brain tissue. We also found that administration of functionalized QDs can result in dose-dependent toxicity in brain slices. Lastly, our results clearly demonstrate the importance of considering the specific model system that is used to evaluate QD behavior.

## 2.6 AUTHOR CONTRIBUTIONS AND ACKNOWLEDGEMENTS

### 2.6.1 *Author Contributions*

MZ and EN designed the stability, toxicity, uptake, and real-time imaging studies. BPB, NLT, and VCH designed and synthesized the QD emitter platforms and performed the structural and photophysical characterization experiments. BPB and RA performed and optimized the QD functionalization experiments, and we thank David Ollodart and Gary Boon for assisting with these efforts. MZ and BPB performed the cadmium dissolution and photoluminescent stability studies, and we thank Dr Cole DeForest for use of his SpectraMax M5 Microplate Reader. BPB performed the FTIR analysis and we thank Dr Alexandra Velian for use of her FTIR spectrometer. MZ performed the pH dependence study for QD stability. We thank Soohyung Lee for assisting BPB and MZ with ICP-MS measurements and analysis. MZ and KH performed the OWH slice toxicity and mRNA studies. OM and MZ performed all *in vitro* characterization studies for DLS, QD stability, and QD aggregation kinetics. NC and MZ performed the *in vitro* BV-2 culture studies. MZ and BD performed the OWH slice studies to evaluate cell-specific QD uptake. MZ and EN performed the *in vivo* studies in the *mglur5* model and KH managed the *mglur5* colony,

including breeding and genotyping for this study. MZ performed all statistical analysis. EN and VCH directed the research. MZ, BPB, VCH, and EN wrote and revised the manuscript.

### 2.6.2 *Acknowledgements*

This material is based in part upon work supported by the University of Washington Interdisciplinary Center for Exposures, Diseases, Genomics and Environment of the National Institutes of Health under award number: P30ES007033, and funding from the Burroughs Wellcome Fund Career Award at Scientific Interfaces. Part of this work was conducted at the Photonics Research Center and the Research Training Testbed facility at the University of Washington, which are supported in part by funds from the Clean Energy Institute and the Washington Research Foundation, and at the Molecular Analysis Facility, a National Nanotechnology Coordinated Infrastructure site at the University of Washington which is supported in part by the National Science Foundation (grant ECC-1542101), the University of Washington, the Molecular Engineering & Sciences Institute, and the Clean Energy Institute.

### Chapter 3. SONOCHEMICAL SYNTHESIS OF FLUORESCENT SEMICONDUCTOR QUANTUM DOTS AND MAGIC-SIZE CLUSTERS

The work presented in this chapter is result of a collaborative project between the Holmberg Lab and the Pozzo Lab (UW Chemical Engineering). Dr. Ryan Kastilani conducted the majority of the initial sonochemistry experiments, characterization, and analysis, including temperature profiles, absorbance and photoluminescence spectra, quantum yields, X-ray diffraction, precursor conversion, and TEM after 180 minutes of sonication. I assisted in designing the sonochemistry experiments, synthesized all CdSe precursors, provided guidance to Dr. Kastilani with respect to the cleaning and characterization and analysis of the quantum dots and magic-size clusters, synthesized and characterized the CdSe magic-size clusters in the emulsion system via 20 minute periodic on-off cycles, and carried out TEM characterization of the magic-size clusters after 60 minutes of sonication.

This chapter is adapted and reprinted in part with permission from “Kastilani, Ryan; Bishop, Brittany P.; Holmberg, Vincent C.; Pozzo, Lilo D.\*, On-Demand Sonochemical Synthesis of Ultrasmall and Magic-Size CdSe Quantum Dots in Single-Phase and Emulsion Systems. *Langmuir* (2019), **35**(50), 16583-16592. <https://doi.org/10.1021/acs.langmuir.9b02891>”. © Copyright 2019 American Chemical Society.

### 3.1 INTRODUCTION

In recent decades, semiconductor quantum dots (QDs) have been of great interest due to their tunable and unique properties. In addition to tuning photoluminescent emission by the size and shape of the nanocrystal, semiconductor QDs, such as cadmium selenide (CdSe) have been optimized to have high quantum yields, narrow bandwidths, and high stability,<sup>16,26,140</sup> making them advantageous for a variety of applications, including biolabeling and imaging, light-emitting diodes (LEDs), solar cells, photodetectors, field-effect transistors (FETs), and memory elements.<sup>12,141,142</sup> One subset of semiconductor QDs is magic-size clusters (MSCs), which are nanostructures typically less than 2 nm that have a discrete size and number of atoms.<sup>143,144</sup> Their small size and physical structure sets them between molecules and nanocrystals, resulting in sharp absorbance features, unique optical properties, and entirely surface-state luminescence, making them beneficial to a wide range of applications. For example, their surface-state emission results in wide-band luminescence, making them useful for white-light LEDs, and their small size makes them advantageous for biological applications due to their rapid clearance through the renal system.<sup>60</sup> In addition, they have proved useful as precursors for larger nanostructures, including quantum dots and nanorods.<sup>51,53,60,61</sup>

Traditionally, these quantum dots and magic-size clusters are synthesized with high temperatures, expensive equipment like a Schlenk line, and the hot-injection method, which make these syntheses difficult to scale and can result in batch-to-batch inconsistencies.<sup>46,47</sup> While one-pot solvothermal syntheses are scalable, nucleation and growth of the nanocrystals can be difficult to separate, leading to several nucleation events and polydisperse nanocrystals.<sup>50</sup>

A relatively new and less frequently utilized nanocrystal synthesis technique is through sonochemistry, which is a method of generating nanocrystals via ultrasound, or sonic energy.

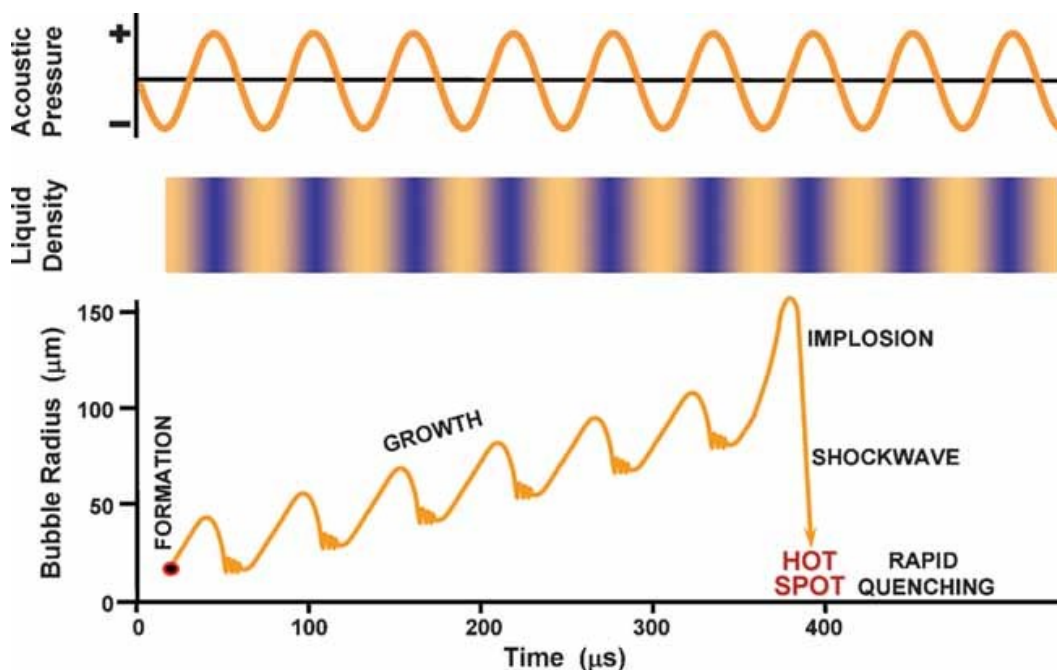


Figure 3.1. Schematic representation of transient acoustic cavitation.<sup>146</sup>

When ultrasound is applied to a liquid, in this case nanocrystal precursors, transient vapor bubbles, or cavities, form during the negative pressure period of the applied sound waves.<sup>145</sup> These bubbles primarily form at interfaces within the system, which act as nucleation sites. As the sound waves alternate between positive and negative pressure, the bubbles oscillate in size and grow, continually gaining potential energy, as seen in Figure 3.1.<sup>146</sup> As the bubbles continue to grow, they can overgrow and become unstable, resulting in an implosion that releases all of the accumulated energy in a highly localized space, or a hot spot.<sup>147</sup> While direct measurement of the conditions generated during bubble collapse is difficult to measure, chemical reactions induced through sonochemistry have been studied to estimate the localized conditions post-cavitation. These hot spots are believed to reach up to 5000 K and 1000 bar in the center of the cavitation event, and up to 2000 K in the surrounding liquid.<sup>147,148</sup>

These extreme conditions have been shown to decompose chemical precursors,<sup>149,150</sup> facilitating the growth of colloidal nanostructures, including metal oxide nanoparticles,<sup>151</sup> metal nanoparticles,<sup>150,152</sup> metal nanobelts,<sup>153</sup> metal nanoclusters,<sup>154</sup> semiconductor nanoparticles and nanowires,<sup>155</sup> two-dimensional nanosheets,<sup>156</sup> and doped metal oxides.<sup>157</sup> With the application of ultrasound, these sonochemical syntheses are more easily reproducible and require relatively simple equipment in comparison to traditional nanocrystal syntheses. In addition, they do not require external heating sources for the nucleation and growth of nanostructures. While sonochemical synthesis is an advantageous method for cheap and reproducible nanocrystal synthesis, there are few controlled and systematic studies, and the effects of sonication are often convoluted with other effects, including a possible rise of the bulk solvent temperature, which results during continuous sonication without active cooling.

In this work, the sonochemical synthesis of ultrasmall and magic-sized CdSe QDs is reported in single-phase and emulsion-based systems, while actively maintaining the solvent temperature

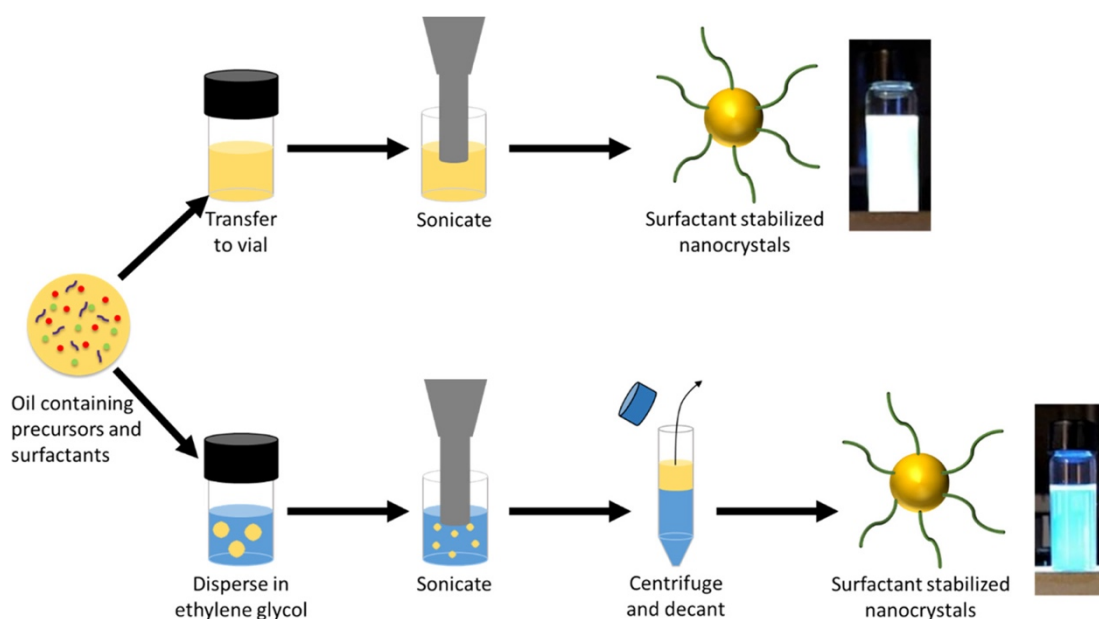


Figure 3.2. Schematic of the sonochemical nanoparticle synthesis procedure, along with photos of the final products under UV excitation.

to minimize effects related to bulk temperature increases. We hypothesize that sonochemical synthesis in emulsion systems offers an efficient, accelerated, and controllable pathway toward the on-demand synthesis of complex nanomaterials. A schematic of the synthesis process is shown in Figure 3.2.

## 3.2 MATERIALS AND METHODS

### 3.2.1 *Materials*

1-Octadecene (90%), oleic acid (90%), oleylamine (70%), cadmium oxide ( $\geq 99.99\%$ ), selenium ( $\geq 99.99\%$ ), trioctylphosphine (97%) (TOP), and dodecane ( $\geq 99\%$ ) were purchased from Millipore-Sigma (St. Louis, MO). Hexanes (mixed isomers, 99.9%) and ethylene glycol were purchased from Fisher Scientific (Hampton, NH). All chemicals were used as received.

### 3.2.2 *Precursor Preparation*

The cadmium precursor, 84 mM cadmium oleate, is prepared in the following way. To a round bottom flask, 0.256 g of cadmium oxide, 20 mL of octadecene, and 2.6 mL of oleic acid were added. Using a Schlenk line, the flask is degassed by applying vacuum while stirring at 800 rpm using a magnetic stir bar. Under the nitrogen atmosphere, the flask is heated to 270 °C and is held at this temperature for 30 min or until the mixture becomes clear and colorless; the temperature is then held for 30 additional minutes. At this time, the temperature is lowered to 150 °C, and 1.3 mL of oleylamine is added. The temperature is then lowered to 100 °C, and the flask is degassed for 30 min. Finally, the resulting product is cooled to room temperature. The selenium precursor, 1 M

TOP:Se, is prepared by mixing Se powder and TOP overnight in a glovebox until all of the Se is dissolved and the solution is clear and colorless.

### 3.2.3 *Sonochemical Quantum Dot and Magic-Size Cluster Synthesis*

The cadmium precursor is first mixed with the selenium precursor at a 1:4 molar ratio. A schematic of the synthesis process is depicted in Figure 3.2. In the emulsion system, 2.245 mL of the cadmium precursor is mixed with 0.755 mL of the selenium precursor in a 20 mL glass scintillation vial. The vial is hand-shaken to mix the two precursor solutions, before adding 7 mL of ethylene glycol. The capped vial is again shaken by hand vigorously to create a coarse emulsion. The vial is then placed in a cooling bath containing water at 20 °C. Sonication is then initiated using a Branson 450 Digital Sonifier (400 W max power, 20 kHz), equipped with a 3/8 in. titanium horn directly immersed 0.5 cm into the solution. Sonication is performed continuously at a 20% power setting on the control panel, which has been calibrated to be equivalent to a power dissipation of 12.6 W. Sonication is then temporarily stopped to collect sample aliquots at each relevant time stamp, and an equivalent volume of ethylene glycol is added into the scintillation vial such that the volume is always kept at 10 mL. The volume of aliquot that is withdrawn is such that there is approximately 250  $\mu\text{L}$  of oil phase (octadecene) in each aliquot. The water in the cooling bath is also exchanged with fresh cold water, and the sonication is continued. The temperature of the vials is also monitored with a thermocouple to separate the effect of sonication/cavitation from that of a possible bulk temperature increase.

Each sample aliquot is then centrifuged and decanted to separate the dispersed oil phase containing the quantum dots from the continuous ethylene glycol phase in the emulsions. These samples are referred to as “unpurified” because of the presence of excess unreacted precursors and

organic components. The “as-synthesized” samples are diluted about 100-fold in octadecene for UV–visible (vis) spectroscopy as a function of sonication time. For X-ray diffraction (XRD), the as-synthesized samples are purified by simply precipitating with the addition of excess ethanol. The powder is then separated and deposited onto a silicon wafer for analysis. Alternatively, the as-synthesized samples are diluted 10-fold in dodecane, and purification is performed by liquid–liquid extraction using an equivalent volume of methanol (250  $\mu$ L) that is changed three times. After each addition of methanol, the samples are vortexed and centrifuged. Care is taken to replace the dodecane lost during the extraction process to prevent the particles from precipitating since precipitates are not redispersible. After cleaning, particles are also diluted into hexanes 10-fold for UV–vis spectroscopy, 1000-fold for photoluminescence (PL) spectroscopy, and 100-fold for transmission electron microscopy (TEM).

In the single-phase system, the sonication procedure is very similar. The only difference is that the 10 mL reaction volume is entirely composed of the precursor mixture. No ethylene glycol is used and no emulsification is necessary. Also, for these samples, no makeup solvent is added upon removal of sample aliquots as a function of time. The as-synthesized samples are diluted about 10-fold in octadecene for UV–vis spectroscopy. Purification of these samples is also performed by liquid–liquid extraction using an ethanol wash of equivalent volume (250  $\mu$ L) three times, after which, the particles spontaneously adhere to the walls of the plastic centrifuge tubes. For XRD sample preparation, the purified samples are redispersed into toluene and drop-cast onto a silicon wafer. Samples are also redispersed into 250  $\mu$ L of dodecane and then diluted into hexanes 10-fold for UV–vis spectroscopy, 1000-fold for PL spectroscopy, and 100-fold for TEM.

### 3.2.4 *UV–Visible (UV–Vis) Absorbance and Photoluminescence (PL) Spectroscopy.*

Both UV–vis and PL spectroscopy are performed using quartz cuvettes with a 1 cm pathlength. UV–vis spectroscopy is performed using a Thermo Scientific Evolution 300 (Waltham, MA) spectrophotometer operating over a 300–700 nm wavelength range. PL spectra are obtained using a Molecular Devices SpectraMax M5 (San Jose, CA) fluorescence spectrophotometer. PL quantum yield (PLQY) is measured using an integrating sphere, Hamamatsu C9920, using an excitation wavelength of 360 nm. For PL measurements, the concentration was low enough such that the absorbance at and above 360 nm is below 0.1 to minimize inner-filter effects.

### 3.2.5 *Transmission Electron Microscopy (TEM)*

Bright-field TEM is performed using FEI Tecnai G2 F20 Super-Twin (Hillsboro, OR) operating at 200 kV. Samples are deposited over a copper TEM grid with 300-mesh carbon from Electron Microscopy Sciences (Hatfield, PA) by drop casting 3  $\mu$ L of the sample and letting it dry.

## 3.3 RESULTS AND DISCUSSION

While CdSe QDs have previously been synthesized via sonochemistry,<sup>158</sup> these studies did not control the temperature of the system and the solutions reached up to 200 °C, which is nearing temperatures of typical hot-injection and solvothermal CdSe syntheses.<sup>16,159</sup> This rise in temperature makes it difficult to determine whether the nanocrystals were synthesized entirely due to the cavitation events in solution or a combination of high temperature and ultrasound. To decouple the effects of temperature and sonochemistry, CdSe QDs and MSCs were sonicated with

a water bath to maintain low temperatures. After sonicating both the single-phase and emulsion-based systems, temperatures did not exceed 65 °C (Figure 3.3), which is significantly lower than temperatures utilized for typical CdSe syntheses. To verify that this temperature does not induce QD generation, the CdSe precursors were then heated to 60 °C on a hot plate. Even after 3 hours of heating, there was no color change and no indication of CdSe QDs via absorbance spectra, indicating that this temperature does not induce the nucleation and growth of CdSe.

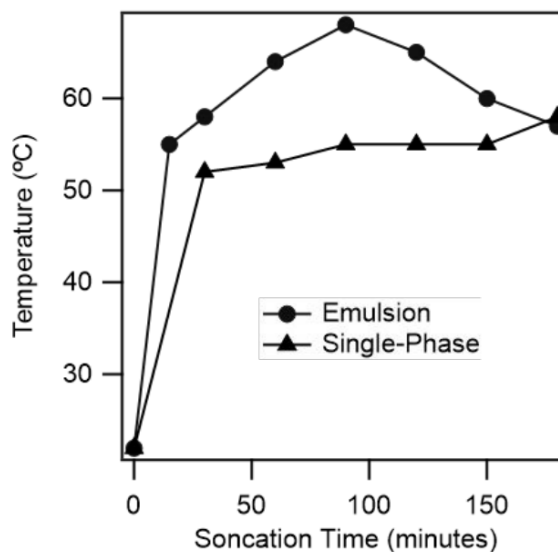


Figure 3.3. Temperature of the mixture tracked with sonication time.

To compare the single-phase and emulsion-based systems, both were sonicated and tracked over 3 hours. Aliquots were taken at several time points throughout the synthesis, and the cooling

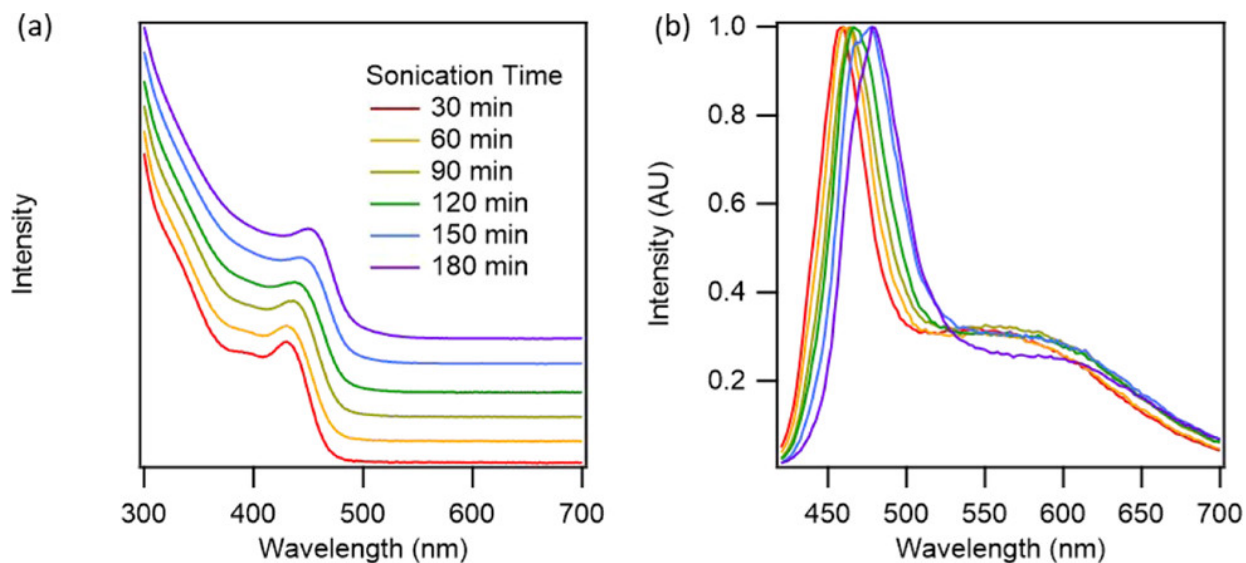


Figure 3.4. (a) Absorbance and (b) PL spectra ( $\lambda_{exc} = 360$  nm) of CdSe QDs synthesized via sonication in the single-phase solvent system.

bath was replenished to maintain low temperature synthesis conditions. In this single-phase system, the absorbance spectra matched with ultrasmall CdSe QDs (Figure 3.4a) and the size of the nanocrystals were determined by tracking the  $1S_{3/2}1S_e$  excitonic absorption feature. Over time, these ultra-small CdSe QDs grow slowly over time, as indicated by the red-shift in the first absorption peak and band-edge photoluminescence peak (Figure 3.4b). Using the position of the  $1S_{3/2}1S_e$  peak to calculate the size of the nanocrystals,<sup>129</sup> the CdSe QDs had a diameter of  $\sim 1.75$  nm and grew to  $\sim 1.9$  nm after 180 min. In addition to absorbance, the nanocrystals exhibited both band-edge emission and a wide-band surface-state emission, resulting in white-light emitting nanocrystals (Figure 3.2) with 8% quantum yields (QY). This defect emission can arise from several factors, including the high surface area of the ultrasmall nanocrystals and the ligands present on the surface of the QDs.<sup>160–165</sup>

In contrast, the results in the emulsion-based system are drastically different. Instead of generating ultrasmall QDs, like in the single-phase system, the emulsion-based system produced

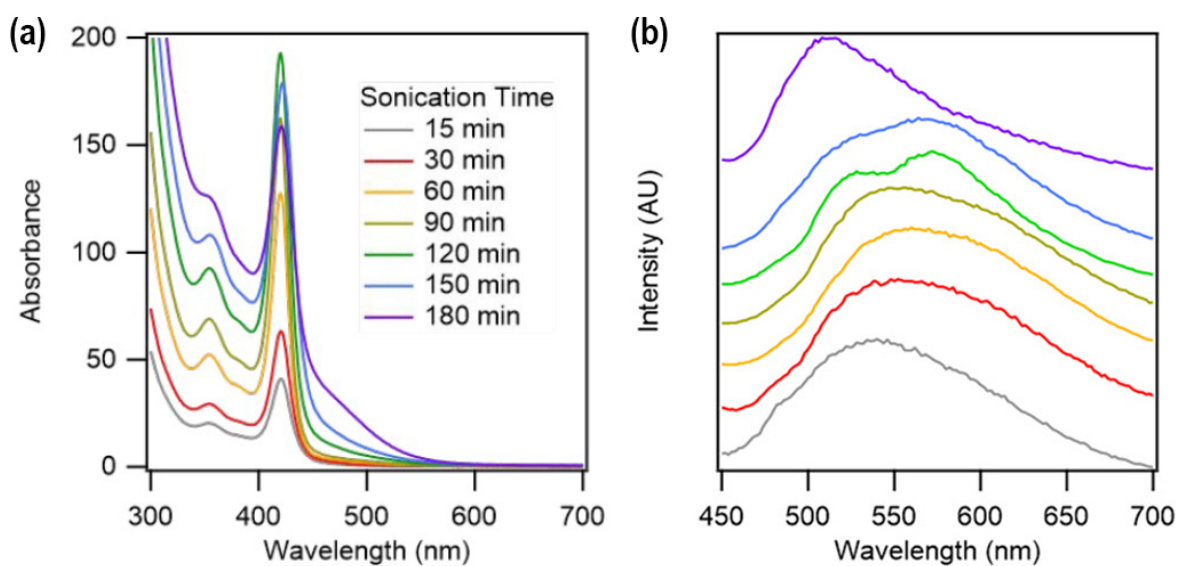


Figure 3.5. (a) Absorbance and (b) PL spectra ( $\lambda_{exc} = 420$  nm) of CdSe particles synthesized using sonication in the emulsion-based systems as a function of sonication time.

magic-sized clusters (MSCs), which are ultrasmall QDs with a discrete number of atoms.<sup>60,143</sup> As the emulsion-based system is sonicated, there is no shift in first excitation peak in the absorbance spectra. Instead, a sharp absorbance feature is observed at 420 nm that increases in intensity over time (Figure 3.5). In addition, these samples do not exhibit a band-edge emission and only exhibit a broad-band “white-light” surface-state emission. The combination of the sharp excitonic feature and lack of band-edge emission is strongly characteristic of MSCs.<sup>55,60,166–168</sup> In particular, the absorption feature at 420 nm corresponds well to  $(\text{CdSe})_{33}$  and  $(\text{CdSe})_{34}$  MSCs, which have similar size and spectroscopic signatures,<sup>59,168–170</sup> making them difficult to distinguish and separate from one another for independent analysis. Interestingly, after 120 min, the intensity of 420 nm extinction peak began to decline and a tail in the UV-spectra forms at higher wavelengths. In addition, after 120 minutes, a peak begins to form that resembles band-edge luminescence, which blue-shifts over time. The combination of the higher-wavelength absorption tail and the emergence of blue-shifted photoluminescence peak suggests the formation of larger QDs after extensive

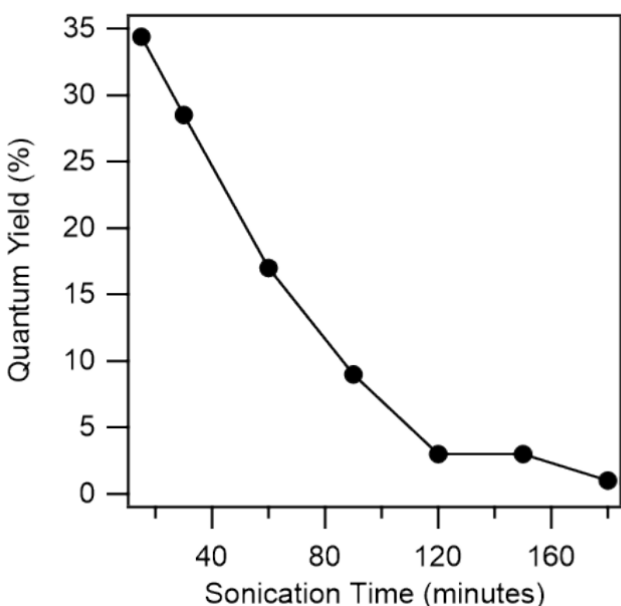


Figure 3.6. Quantum yield of samples synthesized in the emulsion system as a function of sonication time.

sonication. More so, the decrease in the 420 nm peak indicates that the MSCs are acting as precursors for the larger QDs. Incredibly, after 15 minutes, the MSCs have a PL quantum yield of 34%, which is remarkably higher than previously reported PLQY of CdSe MSCs.<sup>11,45,60,63,167,171</sup> However, as the emulsion-based system is sonicated for longer periods of time, the quantum

yield significantly drops to  $\sim 5\%$  (Figure 3.6), which may be explained by the formation of larger CdSe QDs. While significant additional studies would be necessary to pinpoint the reason for the drop in PLQY, CdSe QDs typically have PLQYs ranging from 1 to 30%, including the CdSe QDs synthesized via our single-phase system, and can increase up to 100% upon carefully engineering CdS shell growth.<sup>16,87</sup> Similarly, CdSe MSCs have reported PLQYs ranging from 0.15 to 22%.<sup>11,60,168,172</sup> In comparison to typical CdSe QD syntheses, this system is performed entirely under atmospheric conditions, can be readily scaled, and turns on and off rapidly, making this process advantageous for large-scale commercial synthesis and allowing us to isolate small MSCs with high quantum efficiencies as needed.

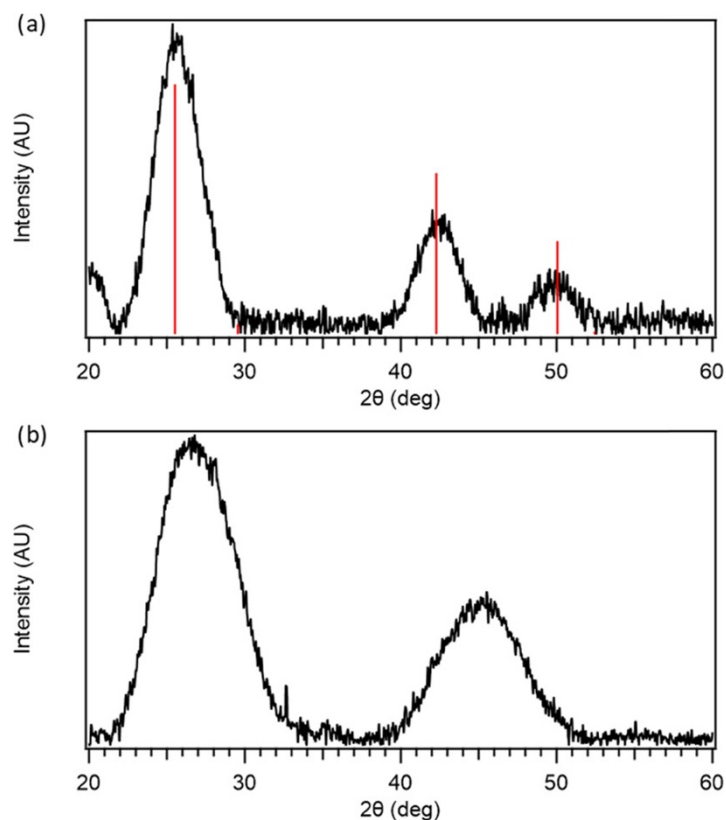


Figure 3.7. XRD spectra of CdSe particles synthesized via sonication in (a) single-phase and (b) emulsion-based systems. Red lines represent the expected peak positions for the bulk zincblende CdSe structure.

After 180 minutes of sonication, XRD (Figure 3.7) and TEM (Figure 3.8) was taken of both the purified QDs and MSCs. Due to the ultrasmall size of the CdSe samples, the XRD of the CdSe QDs synthesized via both single-phase and emulsion demonstrate significant peak broadening. While the XRD profile of the CdSe QDs synthesized via single phase matches that of zinc blende CdSe (PDF 04-003-6493, Figure 3.7a),

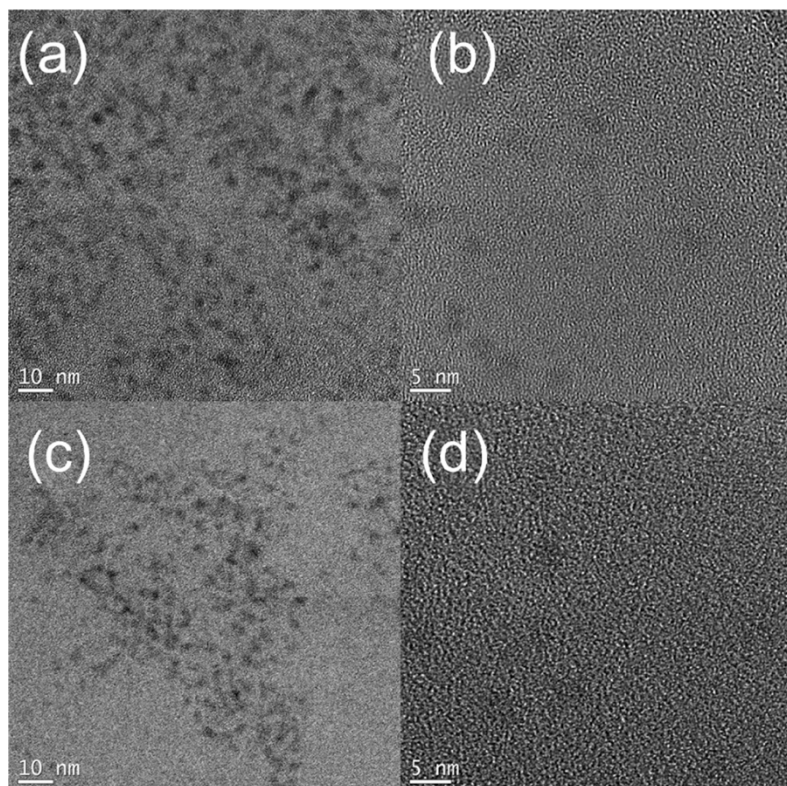


Figure 3.8. TEM of CdSe nanoparticles formed after 180 min of sonication in single phase at (a) low and (b) high magnifications. (c) MSCs formed after 60 min in emulsion-based systems. (d) CdSe nanoparticles formed after 180 min in emulsion-based systems.

the peak broadening makes it difficult to differentiate between cubic zincblende and hexagonal wurtzite CdSe.<sup>60,173,174</sup> XRD of the MSCs (Figure 3.7b) are even broader due their even smaller size. These broad peaks at 27 and 45° correspond very closely to previous XRD characterization of CdSe MSCs.<sup>175,176</sup>

Figure 3.8 shows TEM images of the QDs produced via 180 min of sonication in the single-phase system, along with 60 and 180 min of sonication for

the emulsion-based system. The contrast in the TEM images is very limited due to the small size of the QDs; nonetheless, the QDs observed from the endpoint of the 3 h emulsion-based synthesis are larger than would be expected for MSCs, which supports the data discussed above that suggested the formation of larger QDs after extensive sonication. The particles after 180 min of sonication are also larger in size than what was determined from TEM after 60 min of sonication, further supporting the idea that MSCs are converted into regular-sized QDs after prolonged sonication in emulsions. Given the vanishingly low contrast associated with ultras-small QDs, it was

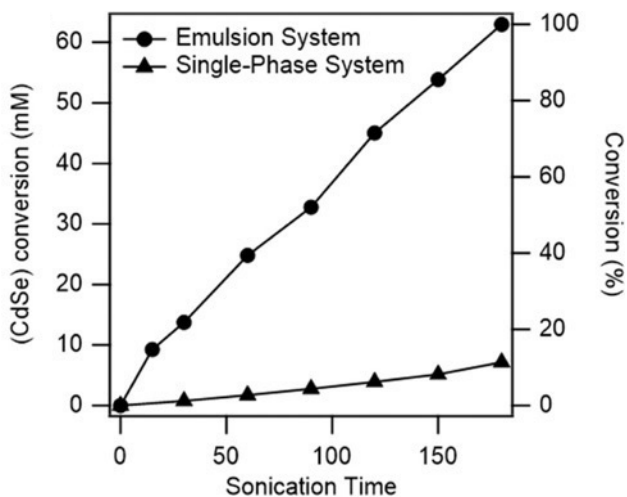


Figure 3.9. Conversion of Cd and Se precursors in (CdSe) with sonication.

not possible to obtain high-resolution images of the MSCs using TEM, which is also consistent with the previous literature.<sup>51,168,170</sup>

In addition to optical and physical characteristics, the rate of conversion from precursors to QDs is remarkably higher in the emulsion-phase system (Figure 3.9), which was calculated using the absolute absorbance spectra of the CdSe QDs and

MSCs. After 3 hours of sonication, complete conversion of precursors was observed in the single-phase system, while only 11% conversion was observed in the single-phase system. Using a linear fit, the rates of conversion in the emulsion system and in the single-phase system were found to be 3.8 and 0.48 g/(L h), respectively, where the conversion rate of the former is comparable to that of a typical hot-injection synthesis of CdSe QDs.<sup>177,178</sup> For example, an optimized hot-injection synthesis of CdSe QDs yields about 3.7 g/L and it takes approximately 1 h, including the initial heating of the reaction mixture.<sup>179</sup> Thus, sonication in the emulsion system provides a competitive conversion rate for the synthesis of CdSe.

We hypothesize that this increased conversion rate results from the increased interfaces between the precursor droplets and ethylene glycol in the emulsion-phase system. On the other hand, the only interfaces that occur in a single-phase system are at the vial walls and surface of the sonication horn. Since interfaces act as nucleation sites for bubble formation, there would theoretically be a higher number of cavitation events in an emulsion with the large number of

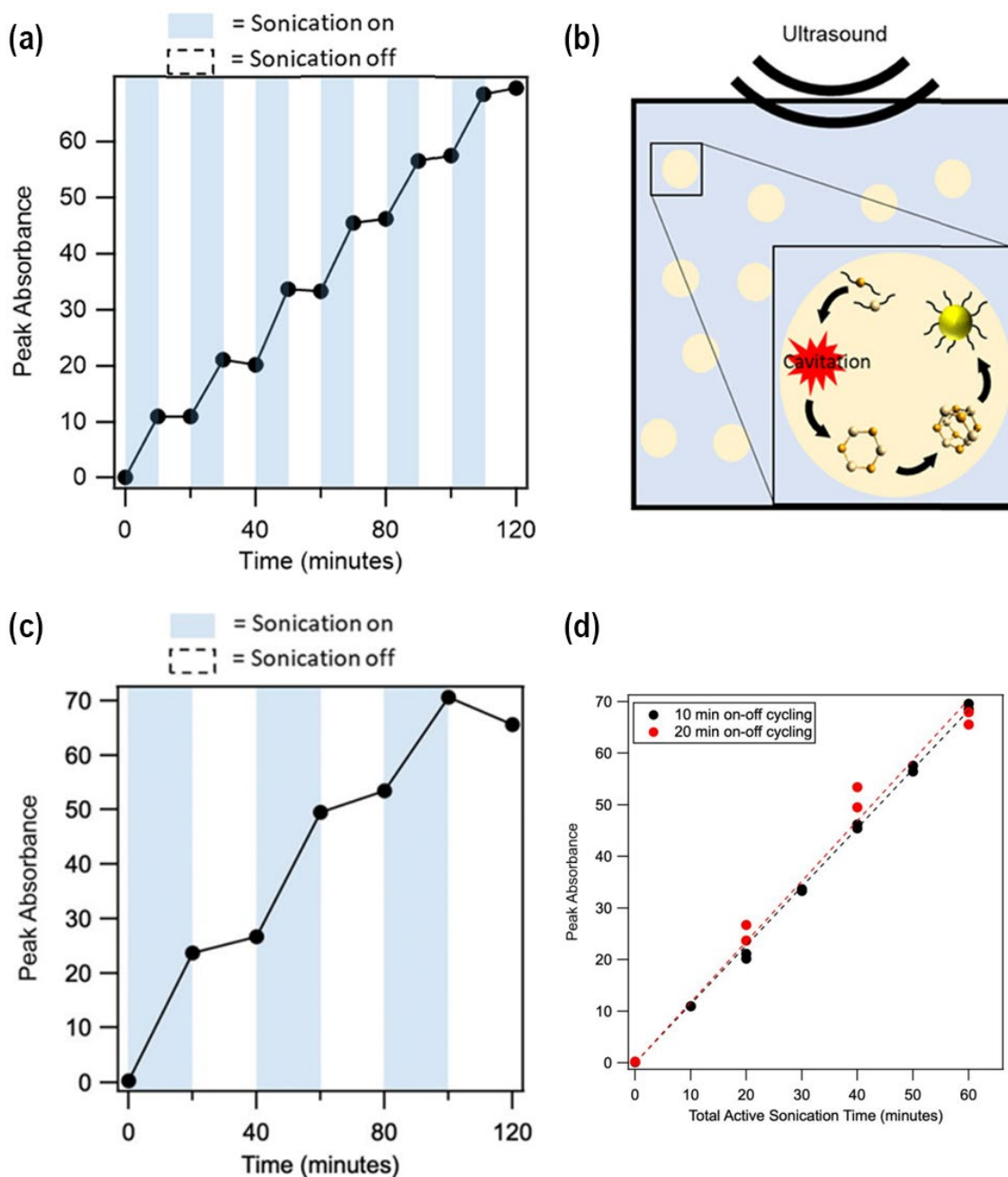


Figure 3.10. Quantitative absorbance at 420 nm of CdSe MSCs synthesized in the emulsion system with periodic (a) 10 min on-off cycles and (c) 20 min on-off cycles. Blue shades indicate the time period during which sonication is active. (b) Schematic of the sonochemical QD synthesis mechanism, where cavitation provides the energy required for precursors to react, form clusters, and grow into QDs. (d) Quantitative absorbance at 420 nm of CdSe MSCs synthesized in the emulsion system with periodic 10-minute and 20-minute on-off cycles normalized by the total active sonication time.

liquid-liquid interfaces.<sup>180</sup> Furthermore, in an emulsion-system, cavitation events would occur directly on the boundary of the oil droplets, which would dissipate energy and generate the high temperatures needed for precursor decomposition and QD formation. Hence, sonication of the emulsion system results in more frequent and numerous cavitation events that are more efficiently distributed near the precursors, quickly driving nucleation and growth of the QDs (Figure 3.10b). This increase in cavitation events also explains the larger increase in temperature of the emulsion-based system compared to the single-phase system (Figure 3.3).

In addition, when using sonochemical synthesis methods, temporal control over when the reaction starts and stops is remarkable. To demonstrate this, an experiment where the sonication system was systematically turned “on” and “off” every 10 min was also performed with the emulsion-based synthesis (Figure 3.10a). Once again, the absorbance at 420 nm was tracked as a function of elapsed time. The data clearly shows that the absorbance increases only when the sonication is turned on, which results in a step-like growth curve. When this experiment was repeated with 20 min cycles (Figure 3.10c), the absorbance increased in a similar stepwise manner. Once the absorption data was normalized for the total active sonication time, it was found that the morphology and concentration of the MSCs did not change based on the time interval that was chosen (Figure 3.10d), further supporting that the reactions stop once sonication is removed, with MSC production purely dependent on total active sonication time.

There are several important outcomes from this experiment, which suggest that precise temporal control of the reaction can further elevate QD synthesis methods. First, this conclusively demonstrates that conversion of precursors to QDs is a direct result of ultrasound and not due to a rise in the temperature of the sample, which is a side effect of power dissipation during sonication. Although allowing the temperature to rise may increase QD production rates, such a precise level

of temporal control may not be possible, and it may also interfere with the selective formation of MSCs observed in the emulsion system. Second, the choice of using trioctylphosphine selenide (TOP:Se) as the chalcogen precursor, as opposed to more reactive secondary phosphine precursors, such as diphenylphosphine selenide, is necessary to carefully control the sonochemical reactions. To note, there are several separate mechanisms for the formation of CdSe monomers.<sup>181</sup> One mechanism requires the decomposition of a tertiary phosphine–chalcogenide to form highly reactive H<sub>2</sub>Se, while another mechanism does not involve precursor decomposition and instead is a direct reaction of secondary phosphine– chalcogenides and metal carboxylates. Since secondary phosphines are much more reactive than tertiary phosphines,<sup>182,183</sup> it has been shown that CdSe MSCs can be synthesized at temperatures as low as 45 °C using diphenylphosphine selenide.<sup>167</sup> However, in this application, the low reactivity of TOP:Se prevents unwanted reactions from progressing uncontrollably at low temperatures. The extreme conditions that are locally exhibited by cavitation are more than sufficient to decompose TOP:Se and drive the conversion of CdSe QDs and MSCs. These design choices open the door toward the efficient, on-demand synthesis of QDs, where the reaction can be started and stopped simply by turning the ultrasound on and off. Moreover, secondary phosphines are typically extremely pyrophoric; using TOP:Se allows for the synthesis of QDs without the safety risks associated with such highly reactive precursors.

### 3.4 CONCLUSIONS

Sonochemical synthesis of CdSe QDs was performed in a single-phase and an emulsion-based system, while keeping the bulk sample temperatures low (<70 °C). Conversion of precursors into QDs is much faster in emulsion systems because the liquid–liquid interfaces serve as heterogeneous nucleation sites for bubbles, which leads to more frequent and more effective

cavitation events to drive the reactions. In emulsion systems, MSCs,  $(\text{CdSe})_{33}$ , and  $(\text{CdSe})_{34}$  were synthesized, although prolonged sonication beyond 120 min does also lead to the formation of regular QDs. Controlled, on-demand synthesis of CdSe QDs is also demonstrated by simply turning the ultrasound on and off at any arbitrary rate. The rate of QD production in the emulsion system was found to be 3.8 g/(L h) with complete conversion of precursors, which is much faster than that in the single-phase system [0.48 g/(L h)] and is comparable to that of the typical hot-injection QD synthesis, and can likely be further optimized. Letting the temperature rise higher may speed up QD production but likely at the cost of a loss in temporal reaction control. Finally, although this work focuses on CdSe QDs, there are no theoretical limitations that would prevent the synthesis of other types of QDs. Future work will involve a more detailed characterization of these CdSe QDs, along with other types of semiconductor materials.

### 3.5 ACKNOWLEDGEMENTS

Acknowledgment is made to the National Science Foundation (NSF) through the UW Molecular Engineering Materials Center, a Materials Research Science and Engineering Center (DMR-1719797) for support of this research. L.D.P. also acknowledges the Donors of the American Chemical Society Petroleum Research Fund. We also acknowledge Prof. Brandi Cossairt from the Department of Chemistry at the University of Washington for her expert input into this project. Part of this work was conducted at the Molecular Analysis Facility, a National Nanotechnology Coordinated Infrastructure site at the University of Washington, which is supported in part by the National Science Foundation (grant ECC-1542101), the University of Washington, the Molecular Engineering & Sciences Institute, the Clean Energy Institute, and the National Institutes of Health.

## Chapter 4. HIGHLY REPEATABLE ONE-POT SYNTHESIS OF MONODISPERSE ZINC SULFIDE NANOCRYSTALS WITH BROADBAND NEAR-UV AND VISIBLE EMISSION

For this study, Dr. Caitlyn Wolf and Dr. Lilo Pozzo (UW Chemical Engineering) conducted and analyzed SAXS, as well as modeled the data for obtaining size distributions of the nanocrystals.

Reproduced with permission from Royal Society of Chemistry, submitted for publication.

### 4.1 INTRODUCTION

Over the last 30 years, zinc sulfide (ZnS) nanomaterials have been recognized for their wide-bandgap, low toxicity, and versatile applications. In addition, zinc and sulfur are cheap and widely abundant materials, making them appealing for large-scale production and commercial use. Because of these advantageous characteristics, ZnS nanocrystals have become an attractive material for imaging, energy conversion, and sensing applications, including electro- and photocatalysis,<sup>184,185</sup> optical imaging agents,<sup>119,186</sup> photo- and electronic sensing,<sup>187</sup> and LEDs.<sup>188,189</sup>

In particular, ZnS has been widely investigated as a photocatalyst and photodetector material due its rapid generation of electron-hole pairs,<sup>190–192</sup> high photocatalytic production of H<sub>2</sub>,<sup>191–193</sup> and effectiveness at CO<sub>2</sub> reduction.<sup>194,195</sup> One of the hallmark features of ZnS that contributes to its potential as a photoactive material is the presence of strong broadband near-UV and visible photoluminescence,<sup>196,197</sup> which has been attributed to a combination of surface defects and vacancies.<sup>187,196–198</sup> The presence of these defect sites in photo-responsive devices are important

for decreasing the rate of electron-hole recombination, facilitating separation of charge, and enabling electron transfer for enhanced photocatalytic activity.<sup>185,190,196</sup>

While defects are beneficial for creating photoactive ZnS, a defect concentration that is too high can decrease the efficiency of photocatalysis or photocurrent responses due to charge carrier trapping.<sup>187,190</sup> However, a recent study showed that the clustering of multiple 5-nm-diameter, defect-rich ZnS nanoparticles facilitated electronic wavefunction overlap, reduced carrier trapping, and improved charge carrier transport between the clustered particles, resulting in UV sensors with enhanced photocurrent.<sup>187</sup> Based on these studies, generating high-defect-concentration ZnS nanocrystals with controlled clustering is desirable for the generation of efficient photodevices.

In addition to the important physical and electronic properties of ZnS, creating a one-pot ZnS nanocrystal synthesis with easily processed chemical compounds would significantly simplify the chemical separation and purification process, which is advantageous for more efficient, larger-scale production. Over the last 20 years, many ZnS quantum dot syntheses have utilized a combination of the hot injection method and high-melting-point coordinating ligands, such as trioctylphosphine oxide, stearic acid, and hexadecylamine, which are all solid at room temperature.<sup>44,199–201</sup> While the presence of these compounds assists in nanocrystal nucleation, growth, and stability, their high melting point and white color make the purification of white ZnS nanocrystals difficult and inefficient. Transitioning to ligands with melting points below room temperature would prevent solidification of any unreacted chemicals and streamline the separation process. Furthermore, in comparison to the hot-injection method, one-pot solvothermal syntheses do not rely on a rapid injection of compounds, resulting in more consistent nanocrystal nucleation and size. As the precursors and ligands are heated simultaneously, once a temperature is reached

where all precursors have decomposed, burst nucleation and nanocrystal growth proceeds. However, it is critically important to control the kinetics in these syntheses carefully since it is often difficult to separate the nucleation and growth steps, potentially resulting in multiple nucleation events and undesirable polydisperse samples.<sup>49,50</sup> Therefore, when designing the system, it is essential to utilize precursors that are stable at low temperatures, but rapidly decompose upon heating to a certain threshold, thereby generating a single nucleation event. Diphenylphosphine (DPP) is a reactive chalcogen coordinating compound that is stable at room temperature under inert conditions, but rapidly reacts upon heating. This has been demonstrated previously in the zinc selenide (ZnSe) material system, where DPP:selenide has been used to induce rapid nucleation upon heating and generate monodisperse ZnSe nanocrystals.<sup>202</sup>

In this study, the solvothermal synthesis of small, monodisperse ZnS nanocrystals is reported. To facilitate efficient purification and processing, unsaturated fatty acids and amines with low melting points (oleic acid and oleylamine) were utilized as the coordinating ligands. In addition, the synthesis utilizes diphenylphosphine:sulfur (DPP:S) as the highly reactive sulfur source, which facilitates rapid, consistent, and monodisperse nanocrystal growth. The diameter of these ZnS nanocrystals can also be systematically increased by increasing the reaction temperature, allowing for careful tuning of nanocrystal size and band gap. These ZnS nanocrystals also exhibit clustering and broad near-UV and visible photoluminescence, which makes them promising for photocatalytic and photosensing applications.

The improved ZnS nanocrystal synthesis presented here was compared to conventional ZnS nanocrystal synthesis protocols that utilize less reactive sulfur precursors and saturated fatty compounds. This comparison demonstrates the importance of utilizing unsaturated coordinating solvents and reactive sulfur precursors for improving ZnS nanocrystal yield and monodispersity,

respectively. To further confirm the impact of these changes, two control experiments were conducted, where the unsaturated coordinating solvents were replaced with saturated ligands to compare the nanocrystal yield, and where the DPP:S was replaced with less reactive sulfur powder to compare the polydispersity of the resulting product. These experiments clearly demonstrate that utilizing DPP:S as the sulfur precursor increases the monodispersity of the ZnS nanocrystals, while using unsaturated coordinating solvents increases the overall nanocrystal yield after cleaning and purification.

## 4.2 MATERIALS AND METHODS FOR ZNS

### 4.2.1 *Chemicals*

Zinc acetate (99.99%), oleic acid (OLA, 90%), 1-octadecene (ODE, 90%), oleylamine (OAm, 70%), diphenylphosphine (DPP, 98%), sulfur powder (99.99%), zinc stearate (technical grade), octadecylamine (99.8%), toluene (99.8%, anhydrous), ethanol ( $\geq 99.5\%$ , anhydrous), methanol ( $\geq 99.5\%$ , anhydrous), and chloroform ( $\geq 99\%$ ) were purchased from Sigma-Aldrich. Hexanes ( $\geq 98.5\%$ ), methanol ( $\geq 99\%$ ) and acetone (99.5%) were purchased from Fisher Scientific. Preparation of 0.15 M diphenylphosphine:sulfur (DPP:S) was carried out by stirring 1.5 mmol of DPP and 1.5 mmol of sulfur powder in 10 mL of anhydrous toluene overnight inside of a nitrogen-filled glove box.

### 4.2.2 *ZnS Nanocrystal Syntheses with Unsaturated Fatty Compounds*

Cubic-phase ZnS nanocrystals were synthesized by modifying zinc selenide nanocrystal syntheses from Saeboe *et al.*<sup>203</sup> and Yu *et al.*<sup>202</sup> Prior to synthesis, 0.2 M zinc oleate was prepared

according to previously established procedures.<sup>204</sup> Briefly, 1.1 g of zinc acetate, 3.8 mL of OLA, and 21 mL of ODE were degassed three times at room temperature while stirring at 800 RPM using standard Schlenk line methods. The mixture was then heated to 200°C under N<sub>2</sub> until clear and colorless, then held at 200°C for an additional 30 minutes. The temperature was then decreased to 150°C and 4 mL of degassed OAm was injected. The zinc oleate solution was then cooled to 100°C and degassed for 30 minutes before being cooled to room temperature and transferred to a nitrogen-filled glove box for storage.

For the growth of monodisperse ZnS nanocrystals, 6 mL of 0.2 M zinc oleate and 4 mL of degassed ODE were degassed at room temperature at 600 RPM using standard Schlenk line procedures. The mixture was then heated to 100°C and further degassed for 1 hour. Next, the solution was cooled to 80°C and 2 mL of 0.15 M DPP:S in toluene were added, followed by 45 minutes of degassing to remove the toluene. The mixture was then heated to 210°C and held at that temperature for 10 minutes. The heating mantle was then removed, and the flask was cooled to room temperature before being transferred to the glove box. The nanocrystals were precipitated by the addition of anhydrous ethanol/methanol and centrifugation, and were redispersed in clean anhydrous toluene, which was repeated 3-4 times. The control experiments carried out with elemental sulfur were performed by omitting the DPP:S and instead, adding 0.3 mmol (0.0096 g) of sulfur powder to the reaction flask during setup. The experiments with excess oleic acid were carried out using nearly identical procedures, except that 2 mL of oleic acid were injected after 5 minutes at the specified synthesis temperature.

#### 4.2.3 *ZnS Nanocrystal Synthesis with Saturated Fatty Compounds and DPP:S*

Control experiments carried out with saturated fatty compounds were performed by utilizing the same reaction conditions as above, but replacing the initial precursors and ligands with 1.2 mmol (0.756 g) of zinc stearate, 2.5 mmol (0.682 g) of octadecylamine, and 8.4 mL of ODE, while keeping the amount of DPP:S the same. These nanocrystals were precipitated by the addition of ethanol/methanol and centrifugation, and were redispersed in clean hexanes, which was repeated 3-4 times. The nanocrystals were then precipitated by the addition of ethanol/methanol and dispersed in toluene.

#### 4.2.4 *ZnS Nanocrystal Synthesis with Saturated Fatty Compounds and Sulfur Powder*

Cubic-phase ZnS nanocrystals were synthesized via a modified version of the solvothermal protocol from Srivastava *et al.*<sup>201</sup> Typically, 0.063 g of zinc stearate, 0.016 g of sulfur powder, 0.8 g of octadecylamine, and 10 mL of ODE were degassed at room temperature for 15 minutes in a 250 mL round-bottom flask attached to a Schlenk line. The mixture was heated to 270°C under N<sub>2</sub> while stirring at 1000 RPM and held under those conditions for 5 minutes. In a separate flask, 0.632 g of zinc stearate, 0.284 g of stearic acid, and 4 mL of ODE were mixed at room temperature, and then slowly added to the hot flask containing the zinc stearate, sulfur powder, and octadecylamine. The mixture was subsequently cooled to 250°C and held at that temperature for 30 minutes, followed by cooling to room temperature. The particles were precipitated via the addition of acetone and centrifugation, followed by dispersion of the particles into chloroform, which was repeated three times. The particles were then precipitated via the addition of methanol and centrifugation, followed by dispersion of the particles into chloroform, which was repeated an additional two times. The final particle dispersion was dispersed into hexanes and centrifuged

several times to remove unreacted precursor. For additional experiments requiring size-selective precipitation, size-selection was carried out through the addition of methanol, followed by centrifugation and redispersion into hexanes.

#### 4.2.5 *Characterization*

Transmission electron microscopy (TEM) images were collected using an FEI Tecnai G2 F20 Supertwin transmission electron microscope operating with an accelerating voltage of 200 kV. ImageJ software was used to determine nanocrystal size distributions. Ultraviolet-visible extinction measurements were collected using an Agilent Technologies Cary 60 UV-vis spectrometer, with a 1-cm pathlength quartz cuvette. Photoluminescence spectroscopy, quantum yield measurements, and photoluminescent lifetimes were collected using an Edinburgh-FLS1000 spectrometer equipped with a PMT-900 detector, with a 1-cm path length quartz cuvette. Absolute quantum yield measurements were performed using an integrating sphere and photoluminescence lifetimes were collected with a 405 nm pulsed diode laser attached to the Edinburgh-FLS1000 spectrometer. X-ray diffraction (XRD) measurements were carried out with a Bruker D8 powder X-ray diffractometer with a Cu anode X-ray source and a Pilatus 100k large-area 2D detector.

Small-angle X-ray scattering (SAXS) data was collected using an Anton-Paar (Graz, Austria) SAXSess X-ray scattering instrument at the University of Washington. The instrument was operated in line-collimated transmission mode with a Cu-K $\alpha$  source (wavelength of 1.54 Å). ZnS particles were dispersed in toluene and loaded into Charles Supper (Natick, MA, USA) quartz capillaries (outer diameter 1.0 mm, wall thickness 0.01 mm) sealed with two-part epoxy. An Anton Paar TCS 300 sample stage maintained the sample temperature at approximately 20°C, an Anton-Paar 1D diode array detector was used to collect the scattering signal, and Anton-Paar SAXSQuant

software was used to clean and reduce the data, including solvent subtraction and scaling to absolute intensity.

The SasView<sup>205</sup> and sasmodels<sup>206</sup> packages for Python 3 were used to fit the scattering data and account for smearing that results from the line-collimation configuration. To extract the radius of the ZnS cores,  $r_{core}$ , we utilized the fractal core-shell model.<sup>205,207,208</sup> The organic materials located at the surface of the particle have minimal contrast with the solvent (toluene), and so the scattering length density of the ‘shell’ and solvent,  $\rho_{shell}$  and  $\rho_{solvent}$ , respectively, were set equal to one another. Therefore, the resulting model differs slightly from previously reported models,<sup>205,209</sup> and is summarized by the following equations:

$$I(Q) = scale * P(Q)S(Q) + background \quad (4.1)$$

$$P(Q) = \frac{\phi}{V_{core+shell}} \left[ 3V_{core}(\rho_{core} - \rho_{shell}) \frac{\sin(Qr_{core}) - Qr_{core} \cos(Qr_{core})}{(Qr_{core})^3} \right]^2 \quad (4.2)$$

$$S(Q) = 1 + \frac{D_f \Gamma(D_f - 1)}{\left[1 + \frac{1}{(Q\zeta)^2}\right]^{\frac{D_f - 1}{2}}} \frac{\sin[(D_f - 1) \tan^{-1}(Q\zeta)]}{(Qr_{core+shell})^{D_f}} \quad (4.3)$$

where  $Q$  is the scattering vector,  $I(Q)$  is the scattering intensity,  $scale$  is a scaling factor,  $\phi$  is volume fraction of the scattering particles,  $V_{core}$  is volume of the core,  $V_{core+shell}$  is volume of the core and shell,  $\rho_{core}$  is the scattering length density (SLD) of the core,  $r_{core+shell}$  is radius of the ‘core-shell’ particle,  $D_f$  is the fractal dimension, and  $\zeta$  is the correlation length. Polydispersity was added to the  $r_{core}$  term with a Gaussian distribution and PD of 0.2. The standard deviation of the Gaussian distribution,  $\sigma$ , is related to PD by:<sup>205,210</sup>

$$PD = \frac{\sigma}{r_{core}} \quad (4.4)$$

### 4.3 RESULTS AND DISCUSSION

To synthesize reproducible and monodisperse ZnS nanocrystals, highly reactive DPP:S was utilized as the sulfur source, while unsaturated coordinating solvents were employed to maximize the nanocrystal yield after cleaning and purification (Figure 4.1c). This synthesis was compared to a previously established protocol from Srivastava, *et al.*,<sup>201</sup> which utilizes a less reactive sulfur precursor and saturated ligands (Figure 4.1f). The comparison between the two protocols emphasizes the large improvements that DPP:S and unsaturated coordinating solvents impart to the monodispersity and yield of the ZnS nanocrystals, respectively. The critical impact of these two parameters is further confirmed via control experiments carried out with sulfur powder and saturated ligands, which will be discussed later in this section.

While the two syntheses utilize different reaction conditions (Figure 4.1c and f), the overall concentration of precursors is very similar for both experiments. For ZnS nanocrystals synthesized with unsaturated coordinating solvents and DPP:S (ZnS-Unsaturated-DPP:S), 1.2 mmol of zinc oleate, 2.5 mmol of oleylamine, 0.3 mmol of DPP:S, and 8.4 mL of ODE were utilized. For ZnS nanocrystals synthesized with saturated ligands and sulfur powder (ZnS-Saturated-S), 0.1 mmol of zinc stearate, 3 mmol of octadecylamine, 0.5 mmol of sulfur powder, and 10 mL of ODE were initially heated, followed by the slow addition of 1 mmol of zinc stearate, 1 mmol of stearic acid, and 4 mL of ODE.<sup>201</sup> The difference between these sets of precursors and ligands had a significant impact on the efficiency of purification and overall nanocrystal yield. The easier separation of unsaturated compounds resulted in a product yield of 68% for ZnS-Unsaturated-DPP:S after purification, while the presence of solidified coordinating ligands led to a longer and more difficult nanocrystal purification process and overall yield of 11% for ZnS-Saturated-S (Appendix A).

While solvent-enabled improvements to the nanocrystal purification process impacted yield, the difference in precursor reactivity greatly impacted the optical and physical properties of the

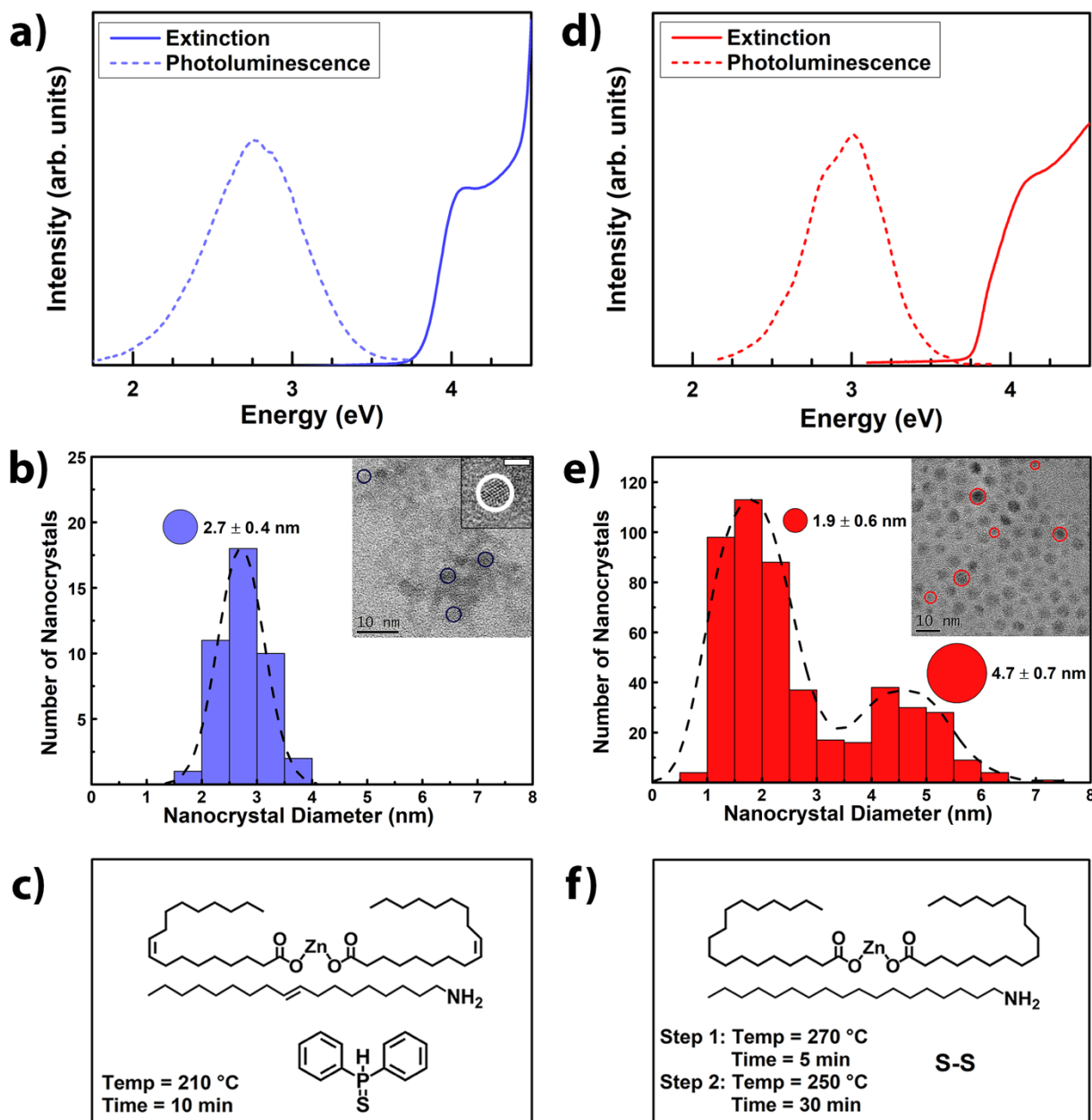


Figure 4.1. a) Extinction, photoluminescence, b) diameter distribution, and c) precursors and solvothermal synthesis conditions of ZnS nanocrystals produced using DPP:S and unsaturated fatty compounds. Inset shows TEM images of the resulting ZnS nanocrystals at low and high resolution. The high-resolution scale bar = 2 nm. d) Extinction, photoluminescence, e) diameter distribution, and f) precursors and solvothermal synthesis conditions of ZnS nanocrystals produced using sulfur powder and saturated fatty compounds. Inset shows TEM images of the resulting ZnS nanocrystals.

final nanocrystals. ZnS-Unsaturated-DPP:S nanocrystals were found to have a sharp and well-defined  $1S_{3/2}1S_e$  excitonic extinction peak at 4.1 eV, indicating the presence of small, highly monodisperse nanocrystals (Figure 4.1a). TEM confirms the monodispersity of the ZnS-Unsaturated-DPP:S nanocrystals, which have an average diameter of  $2.7 \pm 0.4$  nm (Figure 4.1b). TEM also indicates grouping of the ZnS-Unsaturated-DPP:S nanoparticles into 30-40 nm aggregate clusters, which likely arises from a low surface coverage of short-chain ligands, as seen in other nanocrystal systems where the degree of clustering can be tuned by the concentration of ligands added post-synthesis.<sup>187,211</sup> The ZnS-Unsaturated-DPP:S nanocrystals also exhibit broadband visible-frequency luminescence, which is attributed to nanocrystal surface defects and vacancies.<sup>187,196–198</sup> Specifically, photoluminescence features centered around 2.7 – 2.9 eV (430 – 460 nm) have been previously ascribed to surface states, including surface vacancies and dangling bonds,<sup>185,198,212–214</sup> which are often attributed to a low surface coverage of ligands in many semiconductor nanocrystal systems.<sup>1,215,216</sup> This assignment is supported by monitoring changes to the photoluminescence spectra upon ligand addition, which shows a decrease in quantum yield with the addition of 2 mL oleic acid after 5 minutes of growth at 210°C (Appendix A). Due to the high reactivity of DPP:S, the ZnS-Unsaturated-DPP:S nanocrystals nucleate and grow rapidly, followed by a period of slow growth. As similarly observed with lead sulfide nanocrystals, highly reactive sulfur precursors generate small nanocrystals that can fully consume the reactants and finish growing after only 1-2 minutes.<sup>217</sup> Similarly, after rapid nucleation and growth, the ZnS-Unsaturated-DPP:S nanocrystals continue to grow very slowly over time, which is indicated by the small redshift in the  $1S_{3/2}1S_e$  excitonic extinction peak over 15 minutes (Figure 4.2a). The observation of only a minimal shift in peak position indicates that most of the precursors have been consumed and that the nanocrystals are near their final diameter. Furthermore, the ZnS-

Unsaturated-DPP:S nanocrystal synthesis is robustly consistent and reproducible, shown by the uniform extinction spectra collected across multiple syntheses (Figure 4.2). In comparison, ZnS-Saturated-S particles have a less well-defined  $1S_{3/2}1S_e$  excitonic extinction peak and several additional peaks in the photoluminescence spectra, suggesting the presence of nanocrystals with higher polydispersity (Figure 4.1d). TEM imaging verifies the high level of polydispersity, indicating a bimodal distribution of nanocrystals with  $1.9 \pm 0.6$  nm and  $4.7 \pm 0.7$  nm (Figure 4.1e),

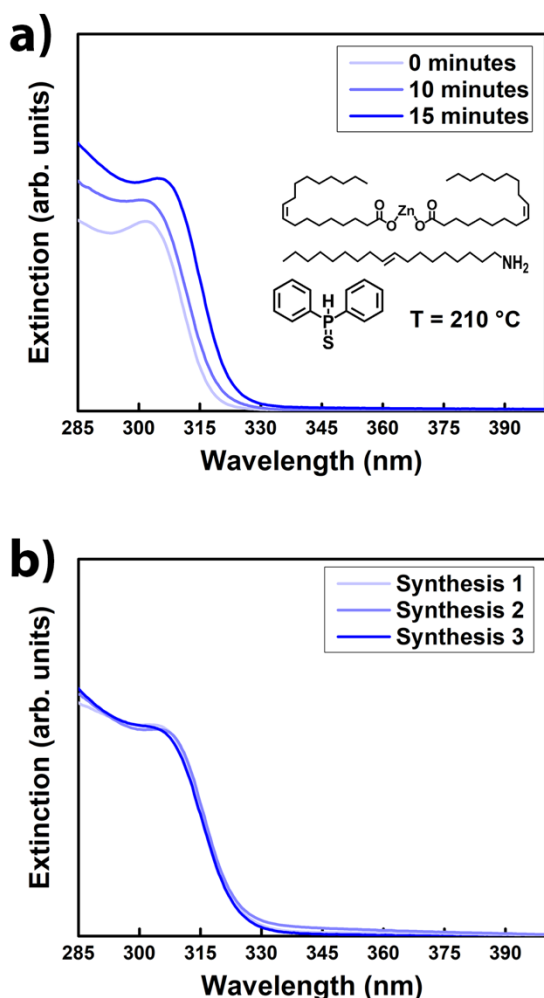


Figure 4.2. Extinction spectra of ZnS nanocrystals synthesized with DPP:S and unsaturated fatty compounds (a) at different time points during a single synthesis and (b) across multiple syntheses.

which may arise from the decreased reactivity of the sulfur precursor, resulting in multiple bursts of nucleation and growth.<sup>218</sup> Based on TEM analysis, the ZnS-Saturated-S nanocrystals exhibit less clustering, which is likely due to a higher ligand surface coverage.<sup>187,211,219</sup>

To further understand the roles that the precursors and ligands have in the nucleation and chemical yield of the ZnS nanocrystals, two control experiments were conducted. In the first control experiment (ZnS-Saturated-DPP:S), the reaction was once again carried out using the reactive DPP:S precursor at  $210^\circ\text{C}$ , but this time using saturated zinc stearate and octadecylamine instead of zinc oleate and oleylamine (Figure 4.3c). This

control experiment was conducted to verify that the use of saturated ligands mainly decreases the purified nanocrystal yield, and that the ligands do not have a large impact on the final size distribution. As expected, the size of the nanocrystals remained the same, at  $2.7 \pm 0.5$  nm (Figure 4.3 and b), and the presence of saturated fatty compounds made the separation process significantly more difficult, resulting in a yield of only 2% (Appendix A). Since stearic acid, octadecylamine, and the ZnS nanocrystals are all the same color (white) and are soluble/insoluble in similar solvents, it is very challenging to separate these compounds, resulting in a low yield of purified ZnS nanocrystals. In the second control experiment (ZnS-Unsaturated-S), an equivalent amount

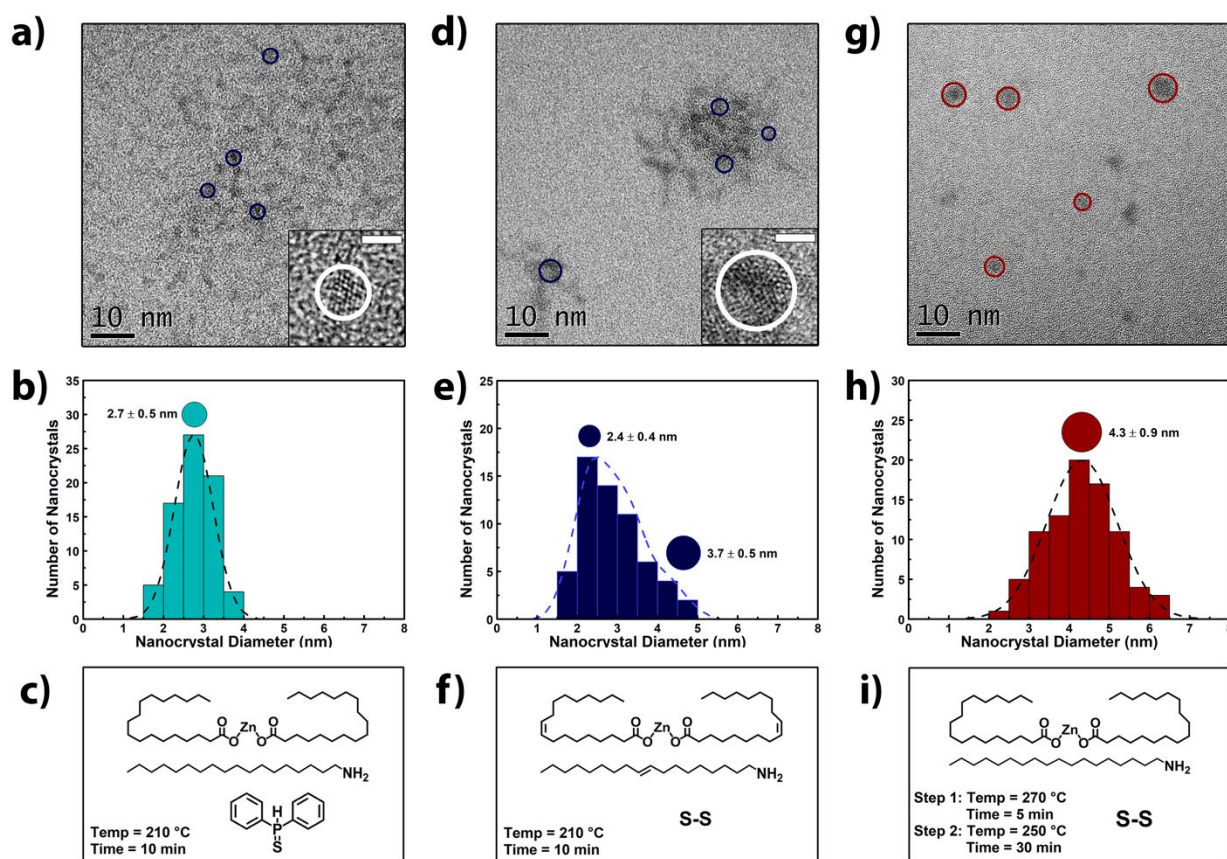


Figure 4.3. a) TEM at low and high resolution, b) diameter distribution, and c) precursors and conditions of ZnS nanocrystals synthesized with DPP:S and saturated fatty compounds. d) TEM at low and high resolution, e) diameter distribution, and f) precursors and conditions of ZnS nanocrystals synthesized with sulfur powder and unsaturated fatty compounds. g) TEM, h) diameter distribution, and i) precursors and conditions of size-selected ZnS nanocrystals synthesized with sulfur powder and saturated fatty compounds. High resolution scale bar = 2 nm.

of sulfur powder replaced the DPP:S, while keeping the zinc oleate and oleylamine amounts constant (Figure 4.3f). This control experiment was conducted to confirm that the low reactivity of sulfur powder results in multiple nucleation events and nanocrystal polydispersity without lowering the nanocrystal yield. In this case, the chemical yield was about the same, at 70% (Appendix A), but the nanocrystals were significantly more polydisperse (Figure 4.3d and e), confirming that the low reactivity of the sulfur powder results in more polydisperse nanocrystals but does not reduce the chemical yield. Notably, both of these control experiments also exhibited nanocrystal clustering, as observed during TEM analysis.

To further compare the ZnS syntheses, a size-selective precipitation was carried out on the polydisperse ZnS-Saturated-S product, where the majority of the 1.9-nm-diameter nanocrystals were removed, as well as some of the largest nanocrystals. The resultant size-selected ZnS-Saturated-S nanocrystals had an average diameter of  $4.2 \pm 0.7$  nm, which was confirmed by both TEM (Figure 4.3g and h) and SAXS (Figure 4.6b and d). After removal of the smallest nanocrystals, the  $1S_{3/2}1S_e$  excitonic extinction peak was found to be better defined (Figure 4.4a)

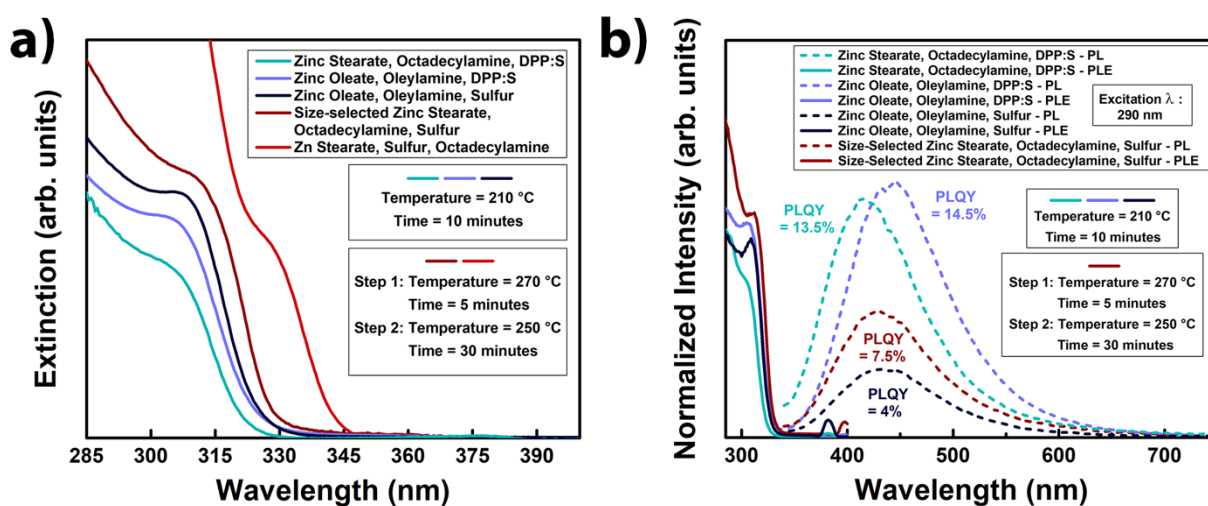


Figure 4.4. a) Extinction spectra, b) PL, and PLE spectra of ZnS nanocrystals synthesized via different solvothermal synthesis protocols.

and the photoluminescence peak at 3.1 eV (400 nm) was observed to disappear (Figure 4.4b, Appendix A), confirming that the poorly defined extinction features and multiple photoluminescence peaks from the original ZnS-Saturated-S nanocrystal product were due to polydispersity. ZnS-Saturated-DPP:S exhibited a similar  $1S_{3/2}1S_e$  excitonic extinction peak to the ZnS-Unsaturated-DPP:S nanocrystals, confirming that both nanocrystal products synthesized using reactive DPP:S precursor have the same average size (Figure 4.4a). ZnS-Unsaturated-S exhibited a  $1S_{3/2}1S_e$  excitonic extinction peak that is slightly red-shifted, resulting from the larger nanocrystals present in solution (Figure 4.4a). All four samples exhibited similar broadband near-UV and visible photoluminescence, indicating large defect densities in the samples (Figure 4.4b). The photoluminescence quantum yield of the ZnS-Unsaturated-DPP:S particles was found to be double that of the ZnS-Saturated-S particles when excited at 290 nm, at 14.5% and 7.5%,

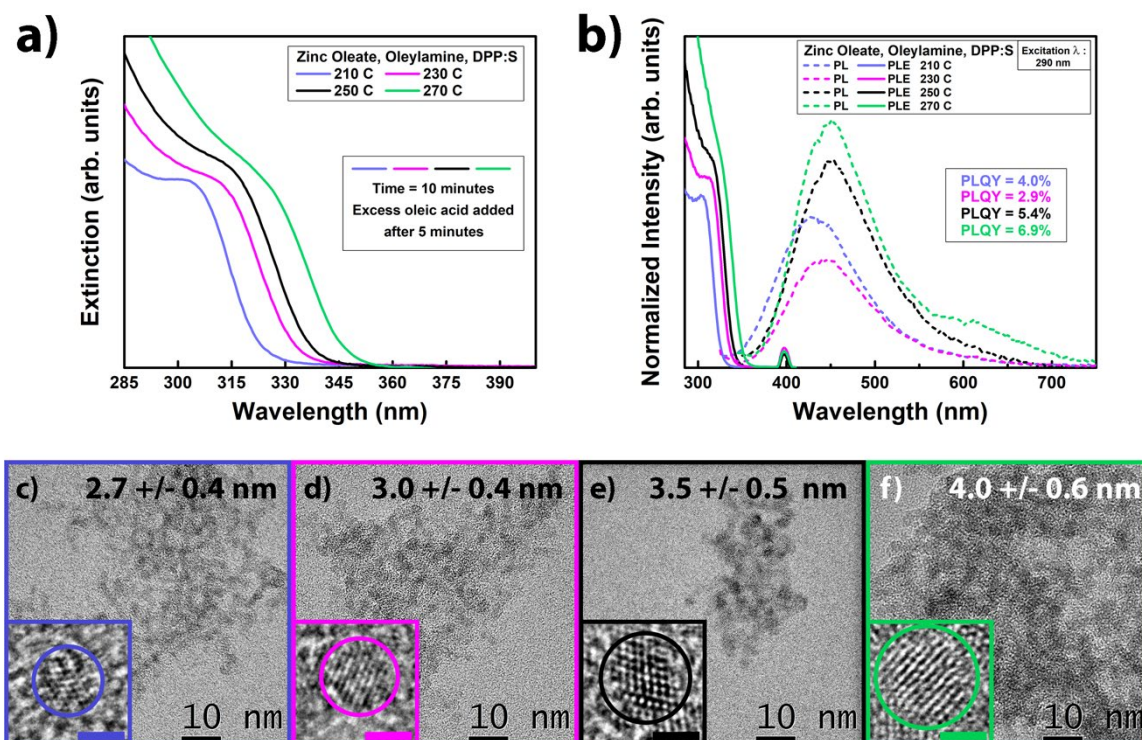


Figure 4.5. a) Extinction, b) PL, and PLE spectra of ZnS-Unsaturated-DPP:S nanocrystals synthesized at different reaction temperatures with excess oleic acid added after 5 minutes. TEM of ZnS nanocrystals synthesized at c) 210°C, d) 230°C, e) 250°C, and f) 270°C. Inset scale bar = 1.5 nm.

respectively. The quantum yields of the ZnS-Saturated-DPP:S and ZnS-Unsaturated-S particles were found to be 13.5% and 4%, respectively. The increased visible luminescence in ZnS-Unsaturated-DPP:S and ZnS-Saturated-DPP:S is most likely due to their smaller nanocrystal diameter and decreased surface passivation, resulting in a greater density of surface defects and vacancies.<sup>220–224</sup>

Furthermore, the size of the ZnS-Unsaturated-DPP:S nanocrystals can be systematically tuned by adjusting the reaction temperature of the synthesis, with excess oleic acid added after 5 minutes. By increasing the temperature in 20°C increments, it was found that the diameter of the nanocrystals could be adjusted by 0.3–0.5 nm per increment, resulting in nanocrystals with diameters of  $2.7 \pm 0.4$  nm,  $3.0 \pm 0.4$  nm,  $3.5 \pm 0.5$  nm, and  $4.0 \pm 0.6$  nm at 210, 230, 250, and 270°C, respectively (Figure 4.5c-f). Because the exciton Bohr radius of ZnS is very small, at 2.5 nm,<sup>225</sup> these sub-nanometer increases in diameter allow for significant red-shifting of the  $1S_{3/2}1S_e$  excitonic peak (Figure 4.5a). While all four samples exhibit broadband near-UV and visible photoluminescence (Figure 4.5b), the quantum yields, ranging from 2.9 to 6.9%, are lower than the ZnS-Unsaturated-DPP:S products without excess oleic acid, further indicating that the broadband photoluminescence is dependent on ligand coverage and unbound surface sites.

SAXS measurements were also carried out in order to confirm the size distributions and clustering characteristics of the ZnS-Unsaturated-DPP:S nanocrystals synthesized at 210°C (Figure 4.6a and b). In SAXS, the scattering wave vector ( $Q$ ) is inversely proportional to the size of the nanocrystals, where features at high  $Q$  values indicate smaller length scales and low  $Q$  values indicate larger ones. The SAXS profile of ZnS-Unsaturated-DPP:S displays a Guinier hump around  $0.13 \text{ \AA}^{-1}$ , while the Guinier hump of the size-selected ZnS-Saturated-S is around  $0.08 \text{ \AA}^{-1}$ , indicating smaller and larger nanocrystals, respectively. Interestingly, a second hump in the SAXS

profile for ZnS-Unsaturated-DPP:S emerges around  $0.02 \text{ \AA}^{-1}$ , indicating the presence of a structure with a larger length scale, while ZnS-Saturated-S does not exhibit this feature. In a previous study on clustered gold nanocrystals, a similar SAXS profile was observed, where a feature at high  $Q$  indicated the size of the individual nanocrystals, while a second feature at low  $Q$  indicated clustering of the gold nanocrystals.<sup>211</sup> The size of the nanocrystal clusters and intensity of the feature at lower  $Q$  was directly dependent on the concentration of ligands present, where a smaller amount of ligands resulted in larger clusters and a more pronounced SAXS feature at low  $Q$ . Accounting for clustering, these profiles were modeled as described in Equations 4.1 - 4.4 to

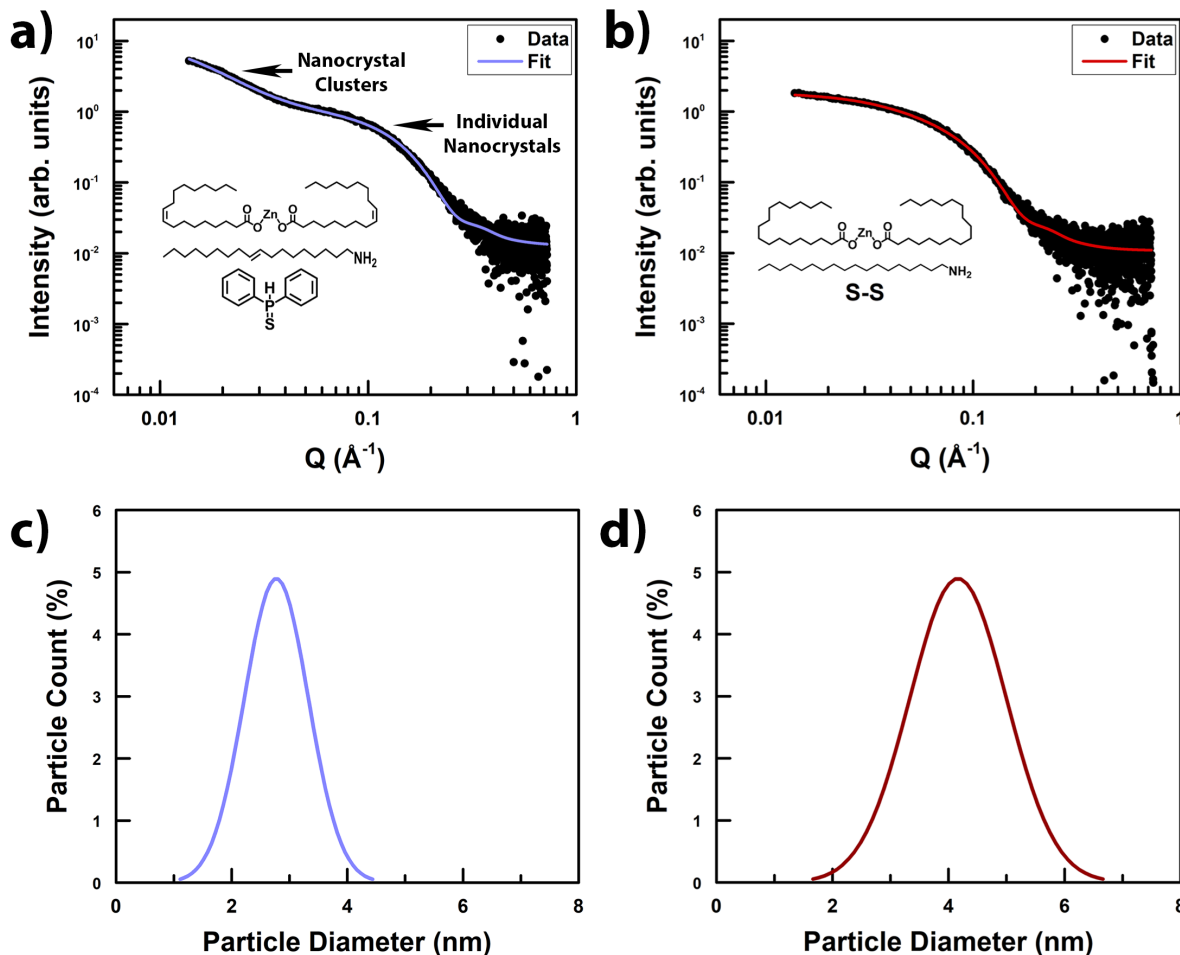


Figure 4.6. SAXS profiles and modeled size distributions for (a and c) ZnS nanocrystals synthesized with DPP:S and unsaturated fatty compounds and (b and d) size-selected ZnS nanocrystals synthesized with sulfur powder and saturated fatty compounds.

estimate the size distributions of both samples (Figure 4.6c and d), which were found to be in agreement with the distributions measured via TEM. Given that ZnS-Unsaturated-DPP:S and ZnS-Saturated-S have ligands with the same length and functional groups, this study suggests that the clustering of the ZnS-Unsaturated-DPP:S nanocrystals arises from a lower concentration of ligands on the surface.

#### 4.4 CONCLUSIONS

In summary, by utilizing low-melting-point solvents and a highly reactive sulfur precursor, monodisperse  $2.7 \pm 0.4$  nm ZnS nanocrystals were synthesized with minimal purification steps. By transitioning to lower melting point solvents and coordinating ligands, it is easier to separate the desired nanocrystals from unreacted precursors and solvents, shortening cleaning steps and resulting in a higher yield. The diameter of the ZnS nanocrystals is also dependent on the reaction temperature, allowing for careful tuning of the band gap and absorption onset. Furthermore, utilizing a one-pot system should enable a more scalable synthesis of ZnS nanocrystals, which is ideal for commercial implementation and larger-scale production. This nanocrystal synthesis is also highly repeatable due to the high reactivity of the DPP:S precursor, resulting in rapid nanocrystal nucleation and growth. Lastly, the small-diameter ZnS nanocrystals produced through this method exhibit nanocrystal clustering and broadband defect-based luminescence in the visible and UV, making them a promising material for photocatalytic and photodetection applications.

## 4.5 AUTHOR CONTRIBUTIONS AND ACKNOWLEDGEMENTS

### 4.5.1 *Author Contributions*

BPB and VCH designed the nanocrystal syntheses. BPB synthesized the nanocrystals and performed structural and optical characterization experiments, and we thank Benjamin Rinn and Kenny Andre for assisting with these efforts. We thank Christian Erickson for assisting BPB with measuring photoluminescence quantum yields. BPB performed TEM characterization for the ZnS-Saturated-S nanocrystals before size selection and the ZnS nanocrystals synthesized with excess oleic acid and different reaction temperatures, and we thank Ellen Lavoie and Soohyung Lee for assisting BPB in TEM characterization of the remaining ZnS nanocrystals. BPB performed all statistical analysis on the structural and optical characterization. CW and BPB performed the SAXS measurements. CW and LDP performed all modeling and characterization of SAXS measurements. LDP and VCH directed the research. BPB, CW, LDP, and VCH wrote and revised the manuscript.

### 4.5.2 *Acknowledgements*

This research was partially supported by the U.S. National Science Foundation through the UW Molecular Engineering Materials Center (MEM-C), a Materials Research Science and Engineering Center (DMR-1719797). Part of this work was conducted at the Molecular Analysis Facility, a National Nanotechnology Coordinated Infrastructure (NNCI) site at the University of Washington, which is supported in part by funds from the National Science Foundation (awards NNCI-2025489, NNCI-1542101), the Molecular Engineering & Sciences Institute, and the Clean Energy Institute. Funding for SAXS measurements and analysis (Wolf, Pozzo) was provided by

the Department of Energy Office of Basic Energy Sciences under award number DE-SC0019911. Wolf and Pozzo also acknowledge the National Science Foundation's Division of Material Research (DMR) for funding the small-angle X-ray scattering instrument that was used in this work (DMR 0817622).

## Chapter 5. IMPACT OF PRECURSORS AND SURFACE CHEMISTRY ON INDIUM PHOSPHIDE SHELL GROWTH IN STRAIN-ENGINEERED INDIUM PHOSPHIDE SPHERICAL QUANTUM WELLS

Reproduced with permission from Royal Society of Chemistry, submitted for publication.

### 5.1 INTRODUCTION

The study of indium phosphide (InP) quantum dots (QDs) has become an important area of research for generating non-toxic optoelectronic devices and fluorescent markers.<sup>13,25,36,226–228</sup> Compared to the more extensively developed cadmium selenide (CdSe) systems, InP QDs are a significantly safer alternative<sup>229</sup> with similar tunable emission across the visible spectrum.<sup>227,230</sup> In efforts to make InP QDs a commercially viable option, different precursors and nanocrystal morphologies have been studied in order to optimize photoluminescent and optical characteristics, while utilizing low-cost precursors that have low reactivity under ambient conditions.<sup>230–232</sup>

One strategy that has been investigated to improve the photoluminescent properties of InP is the use of strain engineering. In a traditional core/shell nanostructure, an emissive core is covered with a wider band-gap protective shell with type I band alignment (*e.g.*, InP/ZnS or InP/ZnSe). While this outer shell is necessary to confine the exciton to the emissive core, thereby mitigating the impact of surface-defect-related recombination, lattice mismatch between these two materials can result in epitaxial strain and interfacial defects between the core and shell, resulting in interfacial charge carrier trapping and decreased quantum yields.<sup>74,81</sup> Strain engineering is a potential strategy that can be used to alleviate this lattice mismatch, reducing defects at the

interface and improving overall quantum efficiencies.<sup>74,81,233–236</sup> Strain engineering methods that have been utilized in InP QDs include large-shell InP/ZnSe/ZnS and InP/ZnSe QDs,<sup>233,234</sup> alloying of the emissive core and protective shell,<sup>74,81</sup> and the implementation of gradient shells.<sup>236</sup> While these structures have been shown to suppress blinking<sup>234</sup> and improve photoluminescence (PL) quantum yields,<sup>81,236</sup> they have also resulted in broadened emission,<sup>81</sup> which has also been observed in other strain-engineered systems.<sup>79,237</sup>

Another approach to strain engineering in high-quantum-yield emissive materials is through the implementation of a layered heterostructure known as a quantum well, where a narrow band-gap emitter is layered between two or more wider band-gap substrates that impose a symmetric strain profile that alleviates strain at the interface and improves overall device performance. In these systems, if the emitting material is very thin—below a certain critical thickness value—and is equally and oppositely strained by the epitaxial substrate on each side, the lattice structure of the quantum well will remain coherent with the substrates, reducing strain at the interfaces between the materials and enhancing the photoluminescent characteristics of the heterostructure.<sup>86–89</sup> While initially implemented in planar devices, researchers have worked to port this strain engineering strategy to colloidal systems, applying the concept of the traditional quantum well and its strain engineering strategies to a colloidal semiconductor nanocrystal in a structure known as a spherical quantum well (SQW). In these systems, which were first explored in the mid-90s with HgS,<sup>89</sup> the emissive material is sandwiched between a wide bandgap core and wide bandgap outer shell in an effort to reduce interfacial strain between each layer and improve the overall photoluminescent properties of the nanocrystal heterostructure.<sup>87,89</sup> In 2016, Jeong, *et al.* developed a set of CdSe SQWs comprised of a small CdS core substrate coated with a thin epitaxial CdSe emissive shell, surrounded by a much larger CdS shell.<sup>87</sup> When the thickness of the

CdSe emissive layer was small enough, it became coherently strained and the lattice mismatch between the CdS and CdSe was reduced, thereby alleviating interfacial strain and suppressing the formation of interfacial defects. The combination of a thin CdSe shell, a large enough CdS shell, and a well-confined type-I band alignment between the two materials facilitated minimization of strain such that the quantum yields of the SQW structures approached 100% while maintaining narrow emission linewidths.<sup>87</sup> Similar nanostructures have also been studied for InP, where researchers investigated the growth of ZnSe/InP/ZnS nanostructures utilizing tris(trimethylsilyl)phosphine (TMS<sub>3</sub>P) as the phosphorus precursor.<sup>203,238</sup> Given that symmetry with equal and opposite strain was critical to the improved photoluminescence in quantum wells, further investigations into InP SQW structures, both with and without symmetry, would provide further insight into the impact that substrate choice has on the photoluminescent characteristics of these systems.

In addition to nanostructure morphology, the choice of phosphorus precursor has been a significant area of interest for InP nanostructure syntheses. Phosphorus precursors that have been investigated include TMS<sub>3</sub>P,<sup>25,203,238</sup> elemental phosphine (P<sub>4</sub>),<sup>239</sup> triarylsilylphosphines,<sup>240</sup> and aminophosphines,<sup>36,230,231</sup> among others. In particular, both TMS<sub>3</sub>P and aminophosphines have been of great interest due to their ability to generate InP QDs with high chemical and quantum yields.<sup>25,36,226,241</sup> While both of these precursors generate high-quality InP QDs, aminophosphines are especially attractive due to their lower cost and low reactivity under ambient conditions. To better understand the advantages of aminophosphines, researchers have been interested in investigating the role that these precursors play in the synthesis of InP QDs. In 2016, Tessier *et. al.* and Buffard *et. al.* studied the reaction mechanism of InP formation in aminophosphine-based syntheses, demonstrating that primary amines, indium halides, and aminophosphines all play a

critical role in the chemical reactions necessary for the nucleation of InP QDs.<sup>230,231</sup> Simulations of the InP reaction mechanism from Laufersky *et. al.* further verified the roles that these three chemicals play in InP QD synthesis.<sup>232</sup> While these investigations have been fundamental in understanding the nucleation and growth of InP QDs, little research has been done into the impact that these precursors have on the growth of InP shells onto other substrates. By utilizing the spherical quantum well structure as a platform, further information about the importance of precursors and primary amines on the growth of InP shells can be elucidated.

Herein, we investigate the synthesis of ZnSe/InP/ZnS, ZnS/InP/ZnS, and ZnSe/InP/ZnSe nanostructures. In order to evaluate the role of precursor choice on InP shell growth, attempts were made at SQW construction using TMS<sub>3</sub>P and tris(diethylamino) phosphine (TDAP) as phosphorus precursors, as well as indium oleate (InOl<sub>3</sub>) and indium chloride (InCl<sub>3</sub>) as indium precursors. In addition, we explore the critical role that surface chemistry plays on epitaxial growth from ZnS core substrates and its impact on InP shell growth when using aminophosphines and indium chloride. Our experimental evidence suggests that during InP shell growth with aminophosphines, the presence of a primary amine and indium halide is necessary for successful and uniform epitaxial shell growth.

## 5.2 MATERIALS AND METHODS

### 5.2.1 Chemicals

Tris(trimethylsilyl)phosphine (TMS<sub>3</sub>P, 95%), tris(diethylamino)phosphine (TDAP, 97%), 1-octadecene (ODE, 90%), and oleylamine (OAm, 70%) were purchased from Sigma-Aldrich. Hexanes ( $\geq 98.5\%$ ), methanol ( $\geq 99\%$ ) and toluene ( $\geq 99\%$ ) were purchased from Fisher Scientific. Prior to the syntheses, zinc oleate (ZnOl<sub>2</sub>), indium oleate (InOl<sub>3</sub>), indium chloride-oleylamine

(InCl<sub>3</sub>-OAm), (sulfur-oleylamine) OAm-S, and (selenium-oleylamine) OAm-Se precursors were synthesized (Appendix B).

### 5.2.2 *InP Syntheses with TMS<sub>3</sub>P and Indium Oleate*

Syntheses utilizing TMS<sub>3</sub>P were conducted via a modified version of the procedure from Saeboe *et. al.*,<sup>203</sup> where a 50-mL round-bottom flask was filled with 9 mL of ODE and 1 mL of OAm. For experiments utilizing zinc chalcogenide core substrates, either ~160 nmol of ZnS nanocrystals or ~350 nmol of ZnSe nanocrystals in toluene (Appendix B) were added to the flask. For control experiments, no cores were added. Using standard Schlenk line procedures, the flask was degassed for 15 minutes and then heated to 120°C under N<sub>2</sub> while stirring at 500 RPM. The mixture was then degassed for an additional 30 - 45 minutes to remove the toluene. The solution was then heated to 150°C and 0.1 mL of 0.2 M indium oleate was slowly added, dropwise, to the flask and allowed to react for 15 minutes. Next, 0.1 M TMS<sub>3</sub>P in ODE was added dropwise slowly over 10 minutes. The flask was then heated to 178°C and held at that temperature for 20 minutes. 0.45 mL Then, 0.2 M zinc oleate was slowly added, dropwise, followed by heating to 220°C and holding at that temperature for 20 minutes. Finally, 0.9 mL of 0.1 M OAm-S was slowly added, dropwise, and left to anneal for 1 hour. The flasks were then cooled to room temperature. The nanocrystals were precipitated by the addition of ethanol and centrifugation and were redispersed in toluene – a process which was repeated 3-4 times.

### 5.2.3 *InP Syntheses with TDAP and Indium Oleate*

In a 50 mL 3-neck flask, ~350 nmol of ZnSe nanocrystals in toluene, 4.5 mL of ODE, and 500  $\mu$ L of OAm were degassed using standard Schlenk line procedures. Under  $N_2$ , the flask was heated to 120°C and degassed for 45 minutes while stirring at 500 RPM to remove the toluene. The mixture was then heated to 220°C under  $N_2$  and 0.2 mL of 0.2 M zinc oleate was added, dropwise, and left to react for 15 minutes. Then, 0.4 mL of 0.1 M OAm-Se was then added, dropwise, and left to react for 20 minutes. Finally, 0.3 mL of 0.2 M zinc oleate was added and left for an additional 15 minutes. For the InP injections, 100  $\mu$ L of 0.2 M TDAP in ODE were added, dropwise, and left to react for 20 minutes. Then, 100  $\mu$ L of 0.2 M indium oleate were added, dropwise, and left to react for 15 minutes. This was repeated 3 times for a total of 3 TDAP and 3 indium oleate injections. An additional 100  $\mu$ L of 0.2 M TDAP were then added, dropwise, and left to react for 20 minutes. For experiments where the amount of InP was increased, 200  $\mu$ L injections of TDAP and indium oleate were utilized, and a total of 9 injections were used instead of 7. Here, 0.4 mL of 0.2 M zinc oleate were slowly added, dropwise, and held for 20 minutes, and then 0.8 mL of 0.1 M OAm-S were slowly added, dropwise, and left to react for 20 minutes. Next, 0.5 mL of 0.2 M zinc oleate were slowly added, dropwise, and held for 20 minutes, and then 1 mL of 0.1 M OAm-S was slowly added, dropwise, and left to react for 20 minutes. The flasks were then cooled to room temperature. The nanocrystals were precipitated by the addition of ethanol and centrifugation and were redispersed in toluene – a process which was repeated 3-4 times.

### 5.2.4 *InP Syntheses with TDAP and Indium Chloride*

For the synthesis of InP spherical quantum wells, a 50 mL round-bottom flask was filled with 4.5 mL of ODE and 0.5 mL of OAm. For experiments utilizing zinc chalcogenide cores, either

~160 nmol of ZnS nanocrystals or ~350 nmol of ZnSe nanocrystals in toluene (Appendix B) were added to the flask. For control experiments, no cores were added. Under N<sub>2</sub>, the flask was heated to 120°C and degassed for 45 minutes while stirring at 500 RPM to remove the toluene. The mixture was then heated to 220°C under N<sub>2</sub>. For reactions utilizing zinc chalcogenide cores, 0.2 mL of 0.2 M zinc oleate were added, dropwise, and left to react for 15 minutes. For ZnS nanocrystal cores, 0.4 mL of 0.1 M OAm-S were then added, dropwise, and left to react for 20 minutes. For ZnSe cores, 0.4 mL of 0.1 M OAm-Se were added, dropwise, and left to react for 20 minutes. For control reactions, the zinc oleate and chalcogenide injections were omitted. For the InP precursor injections, 400 uL of 0.1 M InCl<sub>3</sub>-OAm in ODE were added, dropwise, and left to react for 15 minutes. 600 uL of 0.2 M TDAP in ODE was then added, dropwise, and left to react for 15 minutes. For ZnSe cores subjected to increased InP shell growth, this process was repeated 3 times for a total of 3 TDAP and 3 InCl<sub>3</sub>-OAm injections. Next, 0.4 mL of 0.2 M zinc oleate were slowly added, dropwise, and held for 20 minutes, and then 0.8 mL of 0.1 M OAm-S were slowly added, dropwise, and left to react for 20 minutes. Finally, 0.5 mL of 0.2 M zinc oleate were slowly added, dropwise, and held for 20 minutes, and then 1 mL of 0.1 M OAm-S was slowly added, dropwise, and left to react for 20 minutes. The flasks were then cooled to room temperature. The nanocrystals were precipitated by the addition of ethanol and centrifugation and were redispersed in toluene – a process which was repeated 3-4 times.

### 5.2.5 *Characterization*

Transmission electron microscopy (TEM) images were collected using an FEI Tecnai G2 F20 Supertwin transmission electron microscope operating with an accelerating voltage of 200 kV. ImageJ software was used to determine nanocrystal size distributions. Ultraviolet-visible

spectroscopy measurements were taken using an Agilent Technologies Cary 60 UV-vis spectrometer, with a 1-cm pathlength quartz cuvette. Photoluminescence spectroscopy, quantum yield measurements, and photoluminescence lifetimes were taken using an Edinburgh-FLS1000 spectrometer equipped with a PMT-900 detector, with a 1-cm path length quartz cuvette. Absolute quantum yield measurements were carried out using an integrating sphere, and photoluminescence lifetimes were taken with a 405 nm pulsed diode laser attached to the Edinburgh-FLS1000 spectrometer. X-ray diffraction (XRD) measurements were performed with a Bruker D8 powder X-ray diffractometer with a Cu anode X-ray source and a Pilatus 100k large-area 2D detector. FTIR spectra of the ZnS nanocrystals was obtained using a Bruker Alpha IR spectrometer equipped with a platinum attenuated total reflectance (ATR) accessory and a diamond crystal sampling module. Under a nitrogen atmosphere, the toluene nanoparticle dispersions were drop-cast onto the surface of the ATR crystal, and the solvents were allowed to evaporate completely before recording the spectra.

### 5.3 RESULTS AND DISCUSSION

To create an optimal SQW structure, the wide bandgap core and wide bandgap outer shell materials must have low lattice mismatch and a well-confined type-I band alignment with the emissive InP shell. To investigate ZnS and ZnSe as nanocrystal core substrates and outer shell materials, lattice mismatch and band alignment with InP were assessed for both zinc chalcogenide materials. Unstrained bulk InP has a lattice mismatch of 8.3% and 3.5% with ZnS and ZnSe, respectively.<sup>242</sup> It is known that the interfacial strain within a quantum well heterostructure can be minimized when the thickness of the emitting layer is below a certain critical thickness value, or maximum allowable thickness, which is directly influenced by the lattice mismatch between the

thin emissive layer and the surrounding wider band-gap materials.<sup>86,87,243,244</sup> When the thickness of the emissive quantum well layer is below this critical thickness value, a coherent strain profile across the heterostructure is possible, thereby minimizing strain-induced interfacial defects and improving overall quantum efficiencies. This maximum allowable thickness of the emissive layer can be estimated using the equation below, developed for planar quantum well devices:<sup>86,87,243</sup>

$$h_c = \frac{|B|(1-\nu\cos^2\alpha)}{2\pi\varepsilon(1+\nu)\cos\lambda} \left( \ln \frac{|h_c|}{|B|} + 1 \right) \quad (5.1)$$

where  $\varepsilon$  = lattice mismatch,  $\nu$  = Poisson's ratio,  $h_c$  = critical thickness, and

$$\cos^2\alpha = \frac{a^2 + b^2}{a^2 + b^2 + c^2} \quad (5.2)$$

$$\cos\lambda = \frac{a}{\sqrt{a^2 + c^2}} \quad (5.3)$$

$$|B| = \frac{a}{2}\sqrt{2} \text{ (FCC)} \quad (5.4)$$

where a, b, and c are the lattice parameters of the thin film material. Poisson's ratio ( $\nu$ ) was estimated to fall between 0.25 and 0.4 for the materials under investigation, based on values found in literature.<sup>245,246</sup>

Since InP has a much greater lattice mismatch with ZnS than ZnSe, the maximum allowable thickness for a coherently strained InP thin film sandwiched between ZnS layers is only  $1.5 \pm 0.4$  nm, whereas the maximum allowable thickness of the emissive layer is  $5.5 \pm 1.0$  nm when ZnSe is utilized as the surrounding material (Figure 5.1a and b). Given that these values are for a thin film without curvature, the maximum allowable thickness of InP on a curved ZnS substrate would likely be even smaller, indicating that it may be difficult to grow thick layers of epitaxial InP onto the surface of ZnS. Looking at the bulk band alignment between zinc chalcogenides and indium pnictides, InP is well confined by both ZnS and ZnSe, with both conduction and valence bands having an offset larger than 0.6 eV.<sup>247</sup> However, studies have shown that small InP/ZnSe

nanocrystals do not exhibit quantum efficiencies as high as small InP/ZnS nanocrystals due to poor exciton confinement by the ZnSe shell.<sup>236,248</sup> This difference in band alignment should also affect the photoluminescent characteristics of InP SQWs with thin emissive layers, decreasing the quantum efficiencies of ZnSe/InP/ZnSe compared to ZnS/InP/ZnS. In addition, the thin film and substrate must have crystallographic registry to facilitate epitaxial growth and minimize defects at

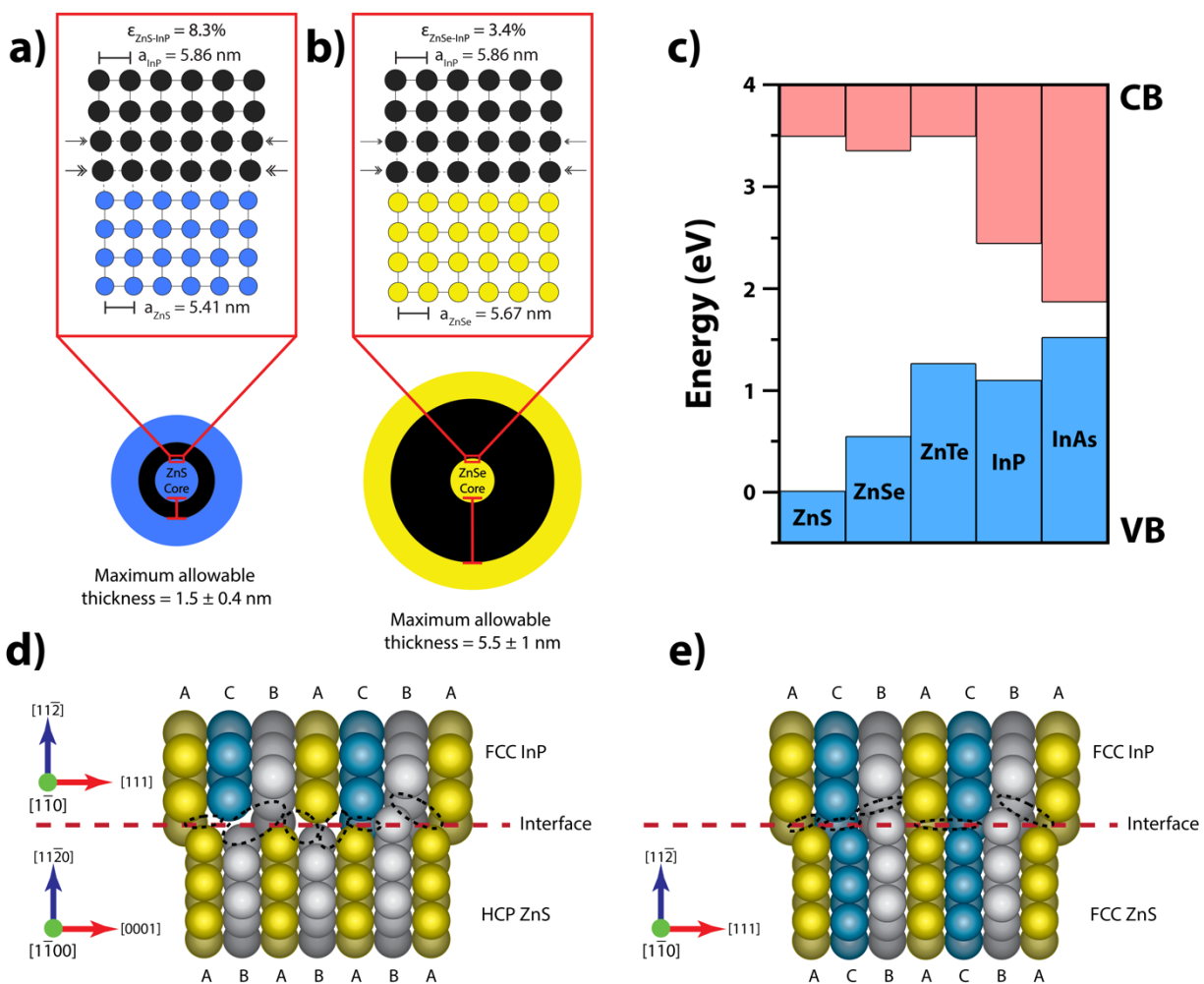


Figure 5.1. Schematic of the maximum possible InP shell thickness for coherently strained InP SQWs grown onto a) ZnS cores and b) ZnSe cores, based on the critical thickness values calculated from Equations 5.1 – 5.4. The zoomed-in sections demonstrate the lattice mismatch between InP and the zinc chalcogenide. c) Band alignment of zinc chalcogenides and indium pnictogens in relation to the ZnS valence band. Interface between d) a hexagonal (HCP) ZnS and cubic (FCC) InP crystal structures and e) two cubic (FCC) ZnS/InP crystal structures. Black dashed lines highlight defects at the interface.

the interface.<sup>249</sup> If the two materials have significantly different crystal structures (*e.g.*, hexagonal ZnS and cubic InP), high levels of strain and defects will be present at the interface. As seen in Figure 5.1d, when cubic InP is interfaced with hexagonal ZnS, large concentrations of interfacial defects are expected, as indicated by the vacancies shown between the atoms in the figure. On the other hand, if the two materials have similar crystal structures, interfacial strain can be minimized, and the density and size of the vacancies will decrease (Figure 5.1e). Thus, when choosing the thin film emissive layer and surrounding wide bandgap materials, choosing two materials that have the same crystal structure is ideal. Since InP, ZnS, and ZnSe are most stable in a zinc blende crystal structure,<sup>250–253</sup> these materials should have well-matched crystallographic registry for epitaxial growth. Synthesizing ZnSe/InP/ZnS, ZnS/InP/ZnS, and ZnSe/InP/ZnSe nanostructures provides a template to study the impact that lattice mismatch and band alignment have on the structural and photoluminescent properties of InP SQWs.

Several phosphorus and indium precursor combinations were tested to investigate the impact of precursor choice on the growth of InP shells onto ZnS and ZnSe nanocrystal core substrates (Figure 5.2). While previous studies have used TMS<sub>3</sub>P in attempts to synthesize ZnSe/InP/ZnS,<sup>203,238</sup> our data shows that the high reactivity of this precursor also results in the simultaneous nucleation of indium phosphide nanocrystals as a byproduct. Our first attempts to grow ZnSe/InP/ZnS, ZnS/InP/ZnS, utilized TMS<sub>3</sub>P and InO<sub>3</sub> as the InP precursors. However, it was found that all of these samples exhibited PL spectra, photoluminescence excitation (PLE) spectra (Figure 5.2a), and extinction spectra (Appendix B) that were nearly identical to the spectra obtained from control reactions carried out in the absence of zinc chalcogenide substrates, indicating that the predominant luminescent structures in these reactions likely correspond to conventional InP/ZnS core-shell QD byproducts. In addition, the matched optical properties to the

InP/ZnS control indicates nucleation of InP in solution, as opposed to epitaxial growth on the wide bandgap core substrates, with the photoluminescence originating from InP/ZnS nanocrystals in all cases. Epitaxial growth of InP shells was also attempted by increasing the number of injections and decreasing the concentration of TMS<sub>3</sub>P by 10-fold, but InP/ZnS QDs were nucleated under these conditions as well. While it was apparent that TMS<sub>3</sub>P was too reactive to prevent the nucleation of isolated InP QDs, it is unclear by the optical properties alone as to whether ZnS/InP/ZnS and ZnSe/InP/ZnS were also grown.

As an alternative strategy, the use of aminophosphines as the phosphorus precursor was also investigated, with TDAP paired with either InO<sub>3</sub> or InCl<sub>3</sub> both tested as InP precursor pairings.

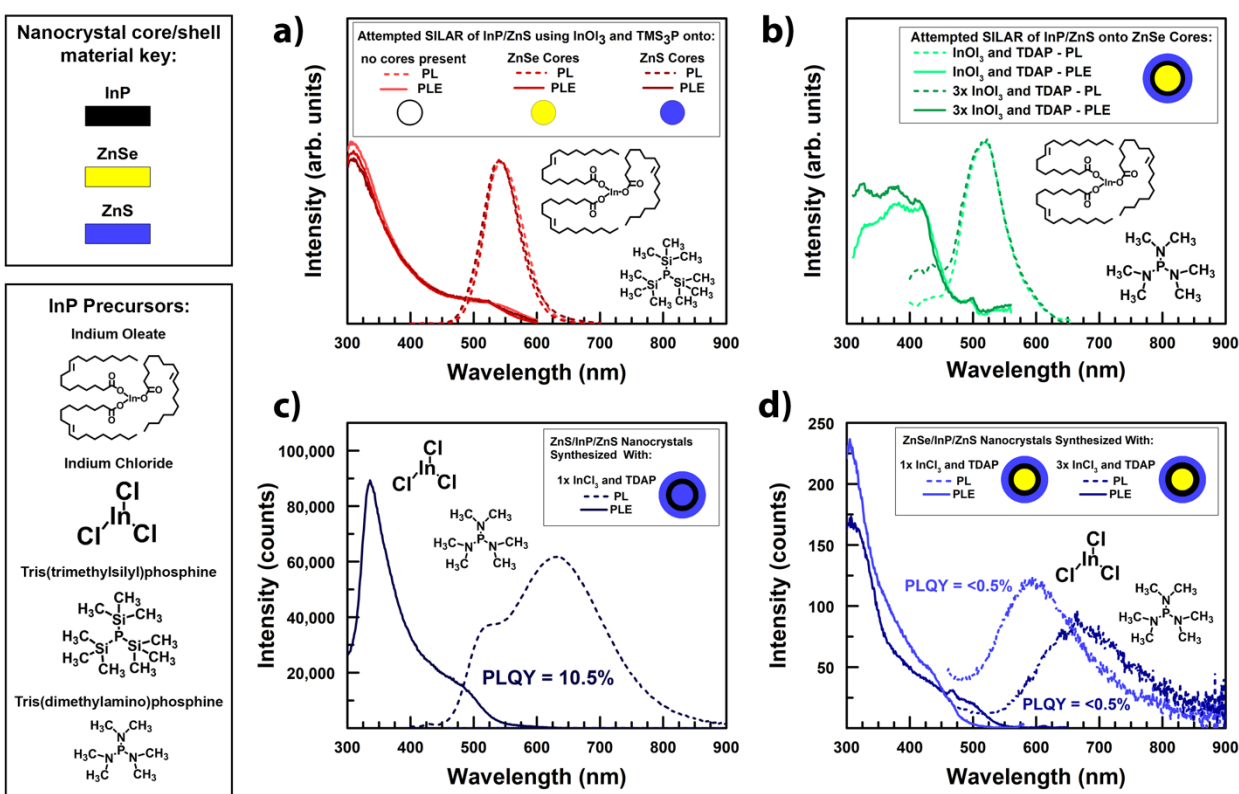


Figure 5.2. PL and PLE spectra of products obtained after attempted SILAR growth of InP/ZnS using a) InO<sub>3</sub> and TMS<sub>3</sub>P and b) InO<sub>3</sub> and TDAP as InP precursors. PL and PLE spectra of c) ZnS/InP/ZnS nanocrystals and d) ZnSe/InP/ZnS nanocrystals using InCl<sub>3</sub> and TDAP as InP precursors. The legends in panels c and d illustrate the structures that were formed in each synthesis. Quantum yield measurements were collected using an excitation wavelength of 390 nm.

For the case of TDAP and  $\text{InO}_3$ , only ZnSe/InP/ZnS nanostructures were investigated, using two different quantities of InP precursors. With the utilization of these precursors, the PL and PLE spectra also remained largely unchanged even when tripling the amount of TDAP and  $\text{InO}_3$  (Figure 5.2b). In addition, the extinction spectra did not change with the increase in precursor quantity and had a similar absorption edge and first excitonic peak as the initial ZnSe nanocrystal cores (Appendix B), indicating very little growth of InP onto the ZnSe cores. In contrast, nanostructures grown with TDAP and  $\text{InCl}_3$  exhibited very different results, where ZnS/InP/ZnS and ZnSe/InP/ZnS nanostructures with different InP shell thicknesses exhibited very distinct photoluminescence and extinction spectra (Figure 5.2c and d, Appendix B), suggesting the successful growth of InP SQWs. In addition, the extinction, PL, and PLE spectra of InP/ZnS QD control syntheses were found to be markedly different from the distinct photoluminescence data obtained from the SQW structures, indicating minimal levels of InP QD byproducts or undesired nucleation of ZnS nanocrystals (Appendix B). These results suggest that the presence of an aminophosphine and indium chloride is necessary for the successful growth of epitaxial InP shells while having low enough reactivity to inhibit the isolated nucleation of InP QDs.

In order to compare the impact of structural symmetry, lattice match, and band alignment on the photoluminescent properties of the InP SQWs successfully synthesized using TDAP and  $\text{InCl}_3$ , ZnS and ZnSe nanocrystal cores with similar size distributions and average diameters of  $\sim 3$  nm were utilized as SQW growth substrates (Appendix B). The resulting photoluminescence spectra of the ZnS/InP/ZnS SQWs were found to have two distinct peaks at 525 nm and 620 nm, likely corresponding to band-edge luminescence and defect-based emission (Figure 5.2c). The observed defect-based luminescence most likely arises from the large lattice mismatch between InP and ZnS and the expected resultant interfacial defects. Despite the presence of these defects, the

ZnS/InP/ZnS SQWs still had a photoluminescence quantum yield (PLQY) of 10.5%. When attempts were made to increase the thickness of the InP layer by adding 3 times the amount of InP precursors, no significant changes were seen in the PL, PLE, or extinction spectra (Appendix B), suggesting that the strain within the ZnS/InP system is too large to facilitate the growth of anything beyond a thin InP shell onto the ZnS particle substrates. The PLE spectrum also exhibits a distinct

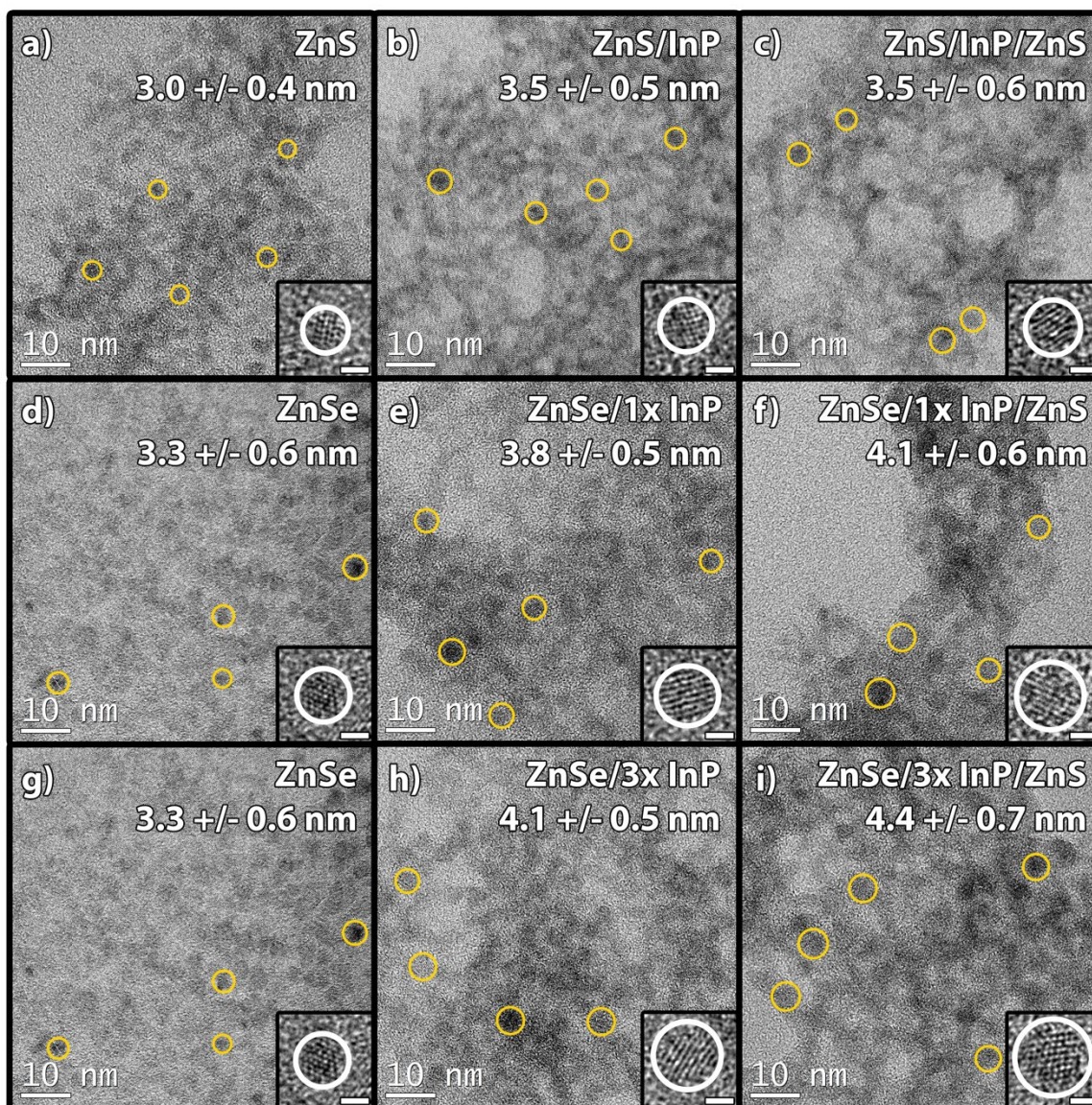


Figure 5.3. TEM of InP SQWs synthesized with TDAP and InCl<sub>3</sub>: a) ZnS, b) ZnS/InP, c) ZnS/InP/ZnS, d) ZnSe, e) ZnSe/1XInP, f) ZnSe/1XInP/ZnS, g) ZnSe, h) ZnSe/3XInP, and i) ZnSe/3XInP/ZnS. Insets show high-resolution images of individual nanocrystals (inset scale bar = 1.5 nm).

dip from 300 to 325 nm, which corresponds to the absorbance on-set of small ZnS nanocrystals.<sup>187</sup> The absence of this feature in the intermediate data collected on the ZnS/InP nanocrystals prior to outer shell growth (Appendix B) and the wavelength at which this onset appears suggests the nucleation of ZnS particles during outer shell growth in this system. TEM characterization of the ZnS/InP/ZnS product can be seen in Figure 5.3a-c. TEM analysis carried out on aliquots of the structures collected throughout the synthesis process shows the steady growth of the spherical quantum well, with  $3.0 \pm 0.4$  nm ZnS nanocrystals cores and  $3.5 \pm 0.5$  nm ZnS/InP structures with 0.25 nm thick InP shells (Figure 5.3a and b). The TEM images also show a final nanostructure size of  $3.5 \pm 0.6$  nm, which is likely a combination of larger ZnS/InP/ZnS SQWs and smaller ZnS nanocrystal byproducts. In contrast, ZnSe/InP/ZnS SQWs were successfully grown with two different InP layer thicknesses, with 1X and 3X the amount of InP precursors added during synthesis. However, these SQWs exhibited quantum efficiencies of less than 0.5%. TEM analysis of the structures shows that ZnSe/1XInP/ZnS resulted in a 0.25-nm-thick InP shell and a 0.15-nm-thick ZnS outer shell, similar to the very thin outer layers observed in the ZnS/InP/ZnS SQWs (Figure 5.3e and f). Upon tripling the amount of InP precursors, ZnSe/3XInP/ZnS resulted in a 0.4-nm-thick InP Shell and a 0.15-nm-thick ZnS outer shell (Figure 5.3h and i). Given the similar size of the ZnS/InP/ZnS and ZnSe/1XInP/ZnS SQWs, the difference in quantum yield implies that the symmetry of the ZnS/InP/ZnS SQWs resulted in a significantly higher quantum efficiency compared to the asymmetric ZnSe/InP/ZnS SQWs. Despite an increase in lattice mismatch between the ZnS and InP, the symmetric architecture most likely resulted in a symmetric strain profile within the nanostructure and improved the overall quantum efficiencies. Growing a larger outer shell should further decrease strain at the interfaces, increasing the PLQY and further reducing the intensity of the defect-based luminescence. To further study the impact of symmetry

and band alignment, ZnSe/InP/ZnSe SQWs were also grown (Appendix B); however, these nanostructures did not exhibit any detectable photoluminescence. This is most likely due to the poor band alignment between the thin InP layer and the outer ZnSe shell, resulting in reduced confinement and a low quantum yield, which has also been observed in small green-emitting InP/ZnSe nanocrystals.<sup>236</sup>

To analyze the structural properties of the nanostructures, XRD characterization of the ZnSe/InP/ZnS, ZnS/InP/ZnS, and InP/ZnS samples synthesized with TMS<sub>3</sub>P/InOl<sub>3</sub> and TDAP/InCl<sub>3</sub> was performed (Figure 5.4, Appendix B). Each of the InP SQWs synthesized with TDAP and InCl<sub>3</sub> exhibited slight shifts in peak position and lattice parameter that would be expected upon shell growth. After InP shell growth, the (220) reflection of the zinc chalcogenide nanocrystal substrate shifts to a slightly lower angle, toward the expected (220) peak position of InP. After ZnS outer shell growth, the (220) reflection shifts back to a higher angle, toward the expected (220) peak position of ZnS (Figure 5.4a). These same shifts in peak position can be seen in the (111) and (311) XRD peaks as well (Appendix B). This shifting is typical in InP/ZnS and InP/ZnSe structures after shell growth,<sup>226,239,248</sup> corresponding to slight changes in lattice parameter that are the result of interfacial strain, and are also observed in the CdS/CdSe/CdS SQWs developed by Jeong *et. al*,<sup>87</sup> further confirming that InP and ZnS shells have successfully been grown onto the wide-band-gap zinc chalcogenide nanocrystal substrates. In contrast, the XRD profiles of the InP nanostructures synthesized with TMS<sub>3</sub>P and InOl<sub>3</sub> look very different. In particular, the XRD profile of the attempted ZnS/InP/ZnS structures exhibit peaks corresponding to both ZnS and InP/ZnS QDs. This is particularly evident for the (220) plane, where peaks at 44.6° and 47.6° can be seen (Figure 5.4b). The 44.6° peak directly matches with the (220) feature of the InP/ZnS control, while the 47.6° reflection matches the (220) feature of the ZnS cores,

suggesting the presence of both InP/ZnS and ZnS nanostructures, without any indication of ZnS/InP/ZnS SQWs. Secondary peaks and broad shoulders can also be seen for the (111) and (311) planes (Appendix B). For the attempted growth of ZnSe/InP/ZnS, the (220) peak is wider,

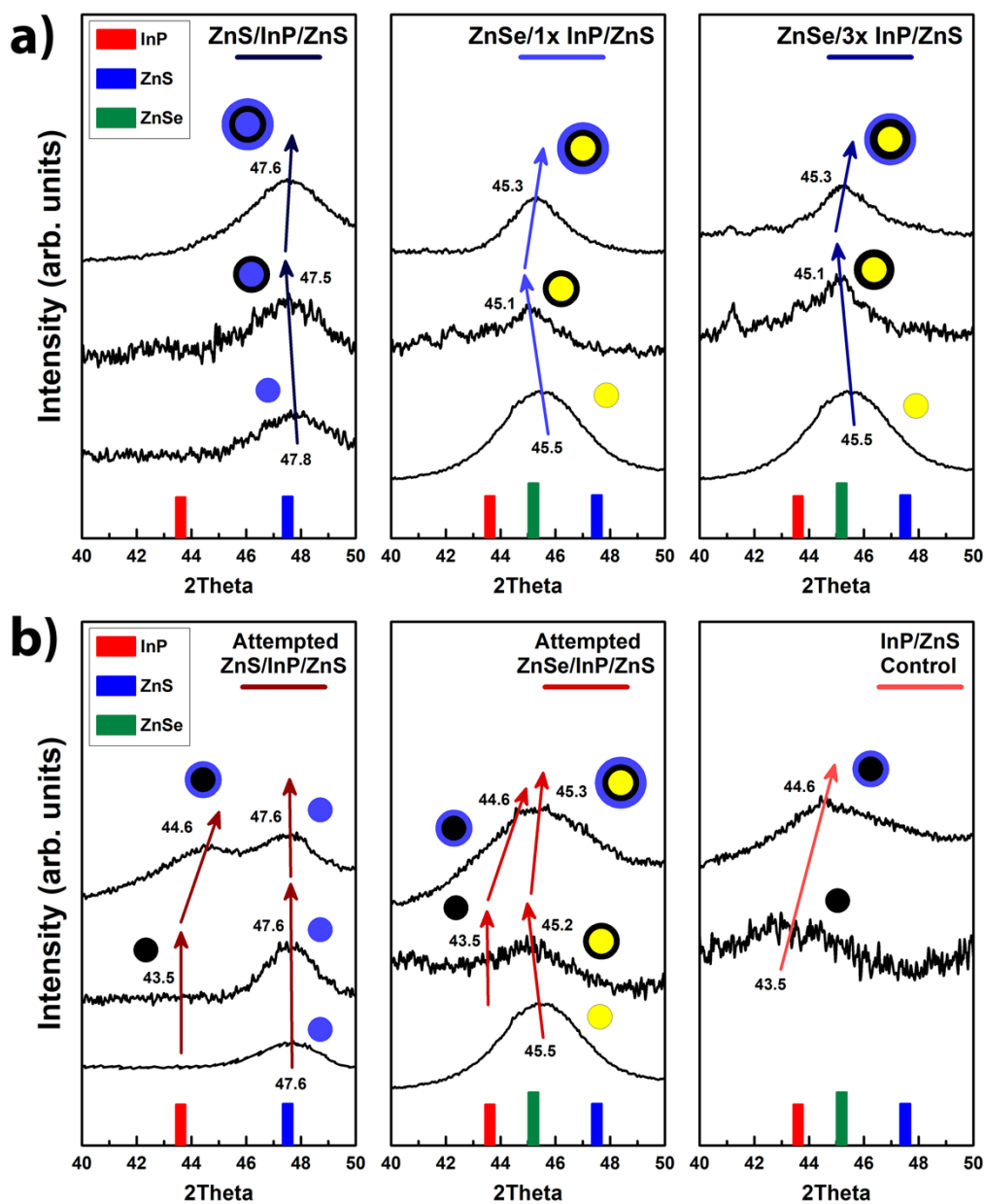


Figure 5.4. a) Shifting of the (220) XRD peak of InP SQWs synthesized with TDAP and  $\text{InCl}_3$ . b) Shifting of the (220) XRD peak of attempted InP SQWs synthesized with  $\text{TMS}_3\text{P}$  and  $\text{InOCl}_3$ . Diagrams show the structures at each step in the synthesis process, from cores to shelled nanostructures.

appearing to correspond to two peaks overlapping with one another. In particular, the ZnSe/InP/ZnS and InP/ZnS peaks happen to overlap significantly, at  $44.6^\circ$  and  $45.3^\circ$ , respectively, making it difficult to distinguish between the two. Peak overlaps are also present for the (111) and (311) planes, but broad shoulders from InP can still be seen for these peaks as well (Appendix B). Unlike the samples with ZnS cores, the shifting of XRD peaks in this sample indicates that both InP/ZnS and ZnSe/InP/ZnS are present. The combination of this XRD analysis with the identical photoluminescence and extinction spectra obtained for samples synthesized with  $\text{TMS}_3\text{P}$  strongly supports that InP nanocrystals have indeed been nucleated in each of these syntheses.

While these precursor investigations confirmed that TDAP and  $\text{InCl}_3$  together were necessary to grow InP SQWs, additional analysis is needed to investigate the importance of primary amines on successful InP shell growth. In all cases discussed thus far, the wide band-gap nanocrystal substrates were dispersed in oleylamine, but the significance that the surface chemistry of the underlying zinc chalcogenide nanocrystal substrate has on the growth of InP shells is unclear. To further understand the importance of primary amines on the InP shell growth process, a ligand exchange was carried out on an aliquot of the ZnS nanocrystal substrates in order to study the impact that surface chemistry has on the growth of InP shells. Growth of InP SQWs was then attempted on ZnS cores with two different sets of surface chemistries, oleic-acid-capped ZnS and oleylamine-capped ZnS (Figure 5.5a and b), which was confirmed via attenuated total reflectance Fourier-transform infrared (ATR-FTIR) spectroscopy (Figure 5.5e and f). Since oleylamine and oleic have identical alkene chains, both FTIR spectra exhibit peaks corresponding to symmetric methyl CH bending at  $1377\text{ cm}^{-1}$  and  $1406\text{ cm}^{-1}$ , antisymmetric methyl CH bending at  $1457\text{ cm}^{-1}$ , methylene CH bending at  $1466\text{ cm}^{-1}$ , and symmetric and antisymmetric alkyl  $\text{CH}_2$  stretching at  $2860\text{ cm}^{-1}$  and  $2920\text{ cm}^{-1}$ , respectively.<sup>133,136,254,255</sup> Additional small fingerprints from the aliphatic

carbon chain can be seen from 1100-500  $\text{cm}^{-1}$ , including methylene rocking, C-H in- and out-of-plane bending, and C-C stretching.<sup>136,256</sup> The FTIR spectrum of the oleylamine-functionalized ZnS nanocrystals exhibits an amine NH stretching band from 3350 to 3100  $\text{cm}^{-1}$  and a peak corresponding to aliphatic amine CN stretching at 1080  $\text{cm}^{-1}$ . In addition, the ZnS-Oleylamine spectrum shows a peak from secondary amine NH bending at 1569  $\text{cm}^{-1}$ , instead of a primary

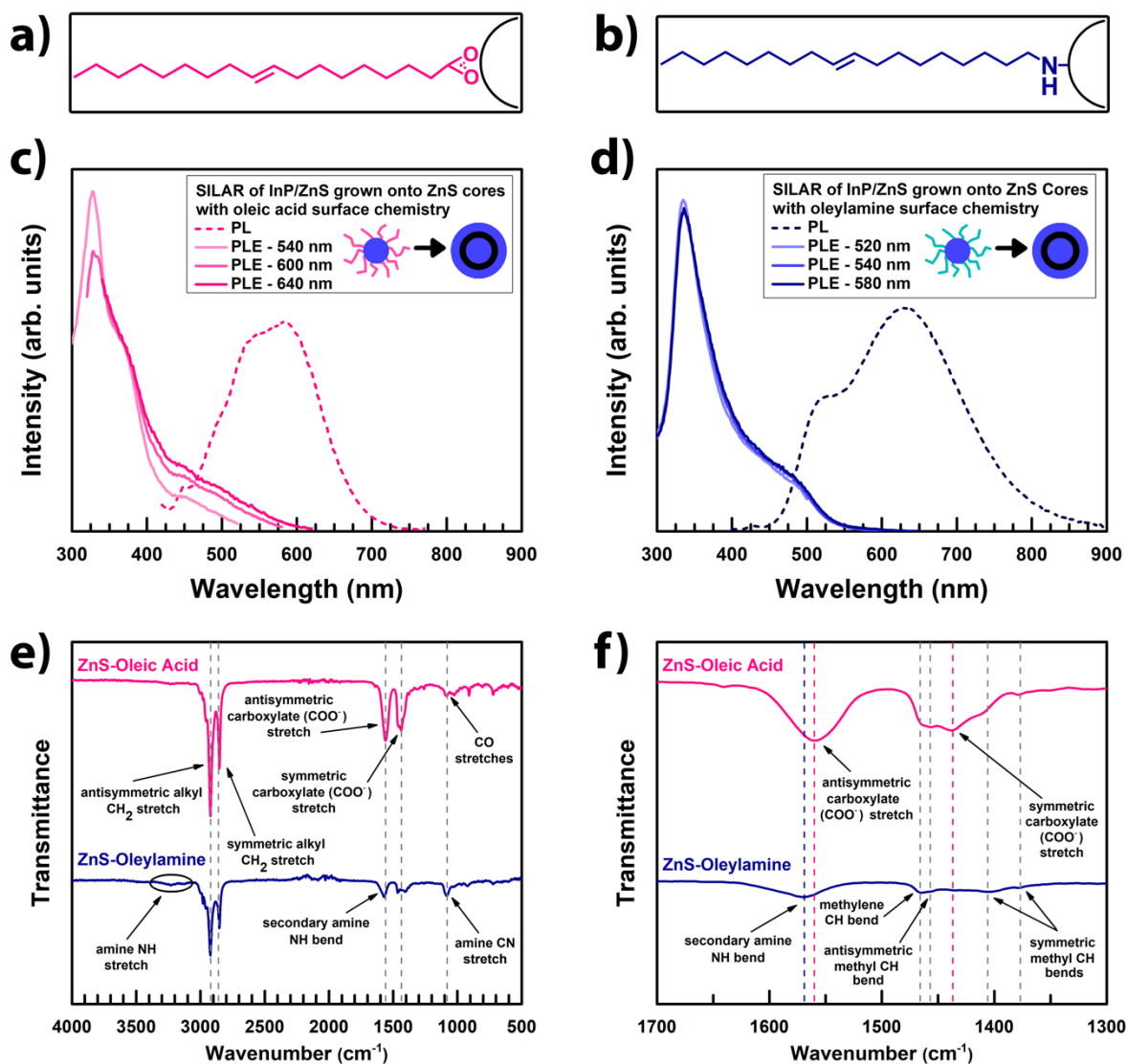


Figure 5.5. Schematic of a ZnS nanocrystal with a) oleic acid and b) oleylamine surface functionalization. PL and normalized PLE spectra of ZnS/InP/ZnS synthesized using ZnS cores with c) oleic acid and b) oleylamine surface functionalization. e and f) ATR-FTIR of ZnS nanocrystals before (oleic acid, pink) and after (oleylamine, blue) ligand exchange.

amine NH bend at 1650-1590  $\text{cm}^{-1}$ , indicating full deprotonation of the oleylamine ligands.<sup>136,256</sup> Similarly, the FTIR spectrum of oleic acid-functionalized ZnS nanocrystals does not display a carboxylic acid peak at 1700-1725  $\text{cm}^{-1}$ , but instead exhibits symmetric and antisymmetric carboxylate ( $\text{COO}^-$ ) stretches at 1437  $\text{cm}^{-1}$  and 1560  $\text{cm}^{-1}$ , respectively, indicating full deprotonation of the oleic acid ligands.<sup>136,254</sup> Additional small peaks from C-O stretches can be seen from 1000 to 1100  $\text{cm}^{-1}$ .

When the ZnS cores had an oleic acid surface termination, after attempted InP and ZnS shell growth, the resultant PL spectra were observed to have several peaks and the normalized PLE spectra collected at several different emission wavelengths did not align (Figure 5.5c). These features are typical of multi-population or heterogenous systems,<sup>257-259</sup> indicating that the oleic-acid-terminated ZnS nanocrystal substrates resulted in multiple populations or non-uniform growth of the InP. In stark contrast, when ZnS nanocrystals with oleylamine ligands were used, the photoluminescent characteristics of the resultant materials were significantly more uniform (Figure 5.5d). The PL spectra exhibited two distinct peaks relating to band-edge luminescence and defect-based emission, and the normalized PLE spectra collected at several different emission wavelengths were nearly identical, indicating that the entire PL spectrum can be attributed to a single nanocrystal population. Therefore, it is clear that the presence of oleylamine on the surface of the ZnS nanocrystal substrate is critical to the successful homogenous epitaxial growth of InP shells – an observation that is likely to be very important for future studies into these material systems.

## 5.4 CONCLUSIONS

In summary, we have investigated the impact that precursors, surface chemistry, and wide-band gap substrate choice have on the structural and photoluminescent properties of InP SQWs. Our studies indicate that  $\text{TMS}_3\text{P}$  is too reactive for the successful growth of InP shells without concurrently nucleating InP nanocrystal byproducts, while the combination of TDAP and  $\text{InO}_3$  is not reactive enough for sufficient growth of InP. Similar to the nucleation of InP nanocrystals with aminophosphines, utilizing indium halide and a primary amine was found to be necessary for the InP shelling process. Furthermore, oleylamine surface chemistry was found to be necessary for the successful growth of uniform InP shells onto wide-band-gap ZnS nanocrystal substrates. Despite the large lattice mismatch between ZnS and InP, ZnS/InP/ZnS SQWs exhibited higher quantum efficiencies than ZnSe/InP/ZnS and ZnSe/InP/ZnSe, indicating that both structurally symmetric strain profiles and well-confined type-I band-alignment are necessary to minimize strain and improve the photoluminescence properties in these spherical quantum-well systems. With further development, InP SQWs are promising candidates as low-toxicity and high quantum yield emitters. While this work focuses on the impacts of precursors, strain, wide-bandgap substrate choice, and substrate surface chemistry, future work will involve the synthesis and characterization of InP SQWs with larger shells in order to optimize and improve these nanostructures. Moreover, the insight gained through these studies provides valuable information for creating successful SQW architectures with different types of quantum-well emitters and wide-band substrates, such as InAs for near-infrared applications or zinc chalcogenides for applications in the near-UV.

## 5.5 AUTHOR CONTRIBUTIONS AND ACKNOWLEDGEMENTS

### 5.5.1 *Author Contributions*

BPB and VCH designed the nanocrystal syntheses. BPB synthesized the nanocrystals and performed structural and optical characterization experiments, and we thank Benjamin Rinn and Kenny Andre for assisting with these efforts. We also thank Beth Mundy and Prof. Brandi Cossairt from the Department of Chemistry at the University of Washington for their expert input into this project. We thank Christian Erickson for assisting BPB with measuring photoluminescence quantum yields. We thank Samantha Young for assisting BPB with XRD measurements and analysis. BPB performed the FTIR analysis, and we thank Dr. Alexandra Velian for use of her FTIR spectrometer. We thank Soohyung Lee for assisting BPB in TEM characterization of the nanostructures. BPB performed all statistical analysis and structural and optical characterization. VCH directed the research. BPB and VCH wrote and revised the manuscript.

### 5.5.2 *Acknowledgements*

This research was partially supported by the U.S. National Science Foundation through the UW Molecular Engineering Materials Center (MEM-C), a Materials Research Science and Engineering Center (DMR-1719797). Part of this work was conducted at the Molecular Analysis Facility, a National Nanotechnology Coordinated Infrastructure (NNCI) site at the University of Washington, which is supported in part by funds from the National Science Foundation (awards NNCI-2025489, NNCI-1542101), the Molecular Engineering & Sciences Institute, and the Clean Energy Institute.

## Chapter 6. CONCLUSIONS AND FUTURE DIRECTIONS

### 6.1 CONCLUSIONS

In summary, several advances have been made in making nanocrystals more viable for clinical and commercial studies. Each study has investigated and developed processes that will enhance research studies, make nanocrystals less toxic, or enable a more streamlined synthesis process for scalable and repeatable nanocrystal syntheses.

#### 6.1.1 *Surface Functionalization of Fluorescent Nanocrystals for Biological Imaging*

Cadmium selenide/cadmium sulfide quantum dots were utilized to study the impact of surface chemistry on the stability, toxicity, and cellular uptake in biologically relevant fluids, *ex vivo* brain slices, and *in vivo* mouse models. This study demonstrated the importance that the testing model had on the outcome and differences between three different surface chemistries (QD-PEG-OH, QD-PEG-OMe, and QD-MPA). Overall, the quantum dots functionalized with mercaptopropionic acid (MPA) demonstrated higher photoluminescence stability, but higher levels of aggregation, increased toxicity, and decreased cellular uptake in the brain. In comparison, the quantum dots conjugated with polyethylene glycol (PEG) were significantly more stable, less toxic to cells, and exhibited higher cell uptake. While QD-PEG-OH demonstrated some nanocrystal aggregation, it still resulted in high cellular uptake and the lowest cytotoxicity. This study also demonstrated that the fluids and concentrations used in models, as well as the type of model, can greatly impact the behavior of the quantum dots. These results provide increased information to researchers on how to develop their models for quantum dot studies, as well as demonstrates the positives and negatives that surface chemistry can have in a biological system.

### 6.1.2 *Sonochemical Synthesis of Fluorescent Semiconductor Quantum Dots and Magic-size Clusters*

Sonochemistry was used to synthesize cadmium selenide quantum dots and magic-sized clusters. Notably, the synthesis was conducted entirely in ambient conditions with standard equipment, specifically ultrasound, which is drastically more scalable and accessible than typical hot-injection or solvothermal syntheses. Through a single-phase system, where just quantum dot precursors were sonicated, quantum dots were grown that slowly increased in size with longer sonication times. In contrast, when an emulsion-based system was used, where the quantum dot precursors were mixed with ethylene glycol to create an emulsion, magic-sized clusters were generated where the concentrations of MSCs increased with longer sonication times. After long periods of sonication, the concentration of these MSCs dropped and larger QDs began to grow, suggesting that MSCs acted as precursors to the larger CdSe QDs. These MSCs exhibited quite high quantum yields compared to previous studies, at ~35%. In addition, the sonochemistry was shown to be entirely dependent on active sonication time. When the sonication was turned on, the concentration of MSCs increased, and when the sonication was turned off, the concentration of MSCs remained the same. This sonochemistry system greatly streamlines the synthesis of nanocrystals and MSCs, provides a cheap and scalable platform for generating nanocrystals, and allows researchers to pinpoint exact nanocrystal sizes by turning off sonication at the exact size or concentration needed.

### 6.1.3 *Highly Repeatable One-Pot Synthesis of Monodisperse Zinc Sulfide Nanocrystals with Broadband Near-UV and Visible Emission*

Monodisperse zinc sulfide nanocrystals were generated through a highly repeatable one-pot solvothermal synthesis. A highly reactive sulfur precursor was used to enable rapid nucleation of nanocrystals and subsequent growth of monodisperse nanocrystals, which was consistent over several nanocrystal syntheses. Controls with sulfur powder demonstrated that polydispersity was dependent on the precursor reactivity in the system. Using unsaturated fatty compounds, oleic acid and oleylamine, as ligands made the nanocrystal purification process faster and produced a high yield compared to syntheses with saturated fatty compounds, stearic acid and octadecylamine. All nanocrystals generated also exhibited broadband near-UV and visible surface state emission, which indicates a high number of surface defects. The diameter of the ZnS nanocrystals could also be adjusted via the reaction temperature, allowing for controllable tuning of the nanocrystal bandgap. In addition, the nanocrystals demonstrate clustering of the small nanocrystals into 30-40 nm clusters. Since previous studies have shown that high defect and clustered ZnS nanocrystals are beneficial for catalysis and photocurrent generation, this protocol allows for high yield synthesis of ZnS nanocrystals with advantageous attributes for charge-transfer applications and minimized processing steps for purification.

### 6.1.4 *Impact of Precursors and Surface Chemistry on Indium Phosphide Shell Growth in Strain-Engineered Indium Phosphide Spherical Quantum Wells*

The spherical quantum well has been utilized to study the impact of precursors and surface chemistry on the growth of InP shells onto zinc chalcogenides. This material system is desired for their low toxicity, especially in comparison to currently used nanocrystal systems that emit in the

visible spectrum. Moreover, these structures are advantageous for minimizing strain at the interfaces of shelled nanocrystal heterostructures, increasing quantum yields and maintaining narrow bandwidths. The study indicated that the use of highly reactive tris(trimethylsilyl) phosphine results in the nucleation of InP nanocrystals, while using less reactive tris(diethylamino)phosphine prevented this undesired nucleation. Furthermore, tris(diethylamino)phosphine, indium chloride, and oleylamine were all necessary for indium phosphide shell growth into zinc sulfide and zinc selenide nanocrystals. Interestingly, in zinc sulfide nanocrystals, having oleylamine present was not sufficient for consistent growth. Rather, an oleylamine surface chemistry was necessary for the uniform epitaxial growth of the InP onto the ZnS cores. This study also demonstrated the importance of band alignment and symmetry in these spherical quantum well systems. The impact of symmetry was revealed by comparing ZnSe/InP/ZnS and ZnS/InP/ZnS nanostructures. Despite having a higher lattice mismatch between InP and ZnS, ZnS/InP/ZnS exhibited higher quantum efficiencies, showing that symmetry is necessary for relaxation of strain within the spherical quantum wells. In addition, ZnSe/InP/ZnSe did not exhibit any detectable emission, indicating that the bands alignment between InP and ZnSe is not effective at localizing excitons to the InP shell, resulting in decreased quantum yields. Understanding these aspects of the system provides important information for designing and generating uniform InP spherical quantum wells with increased band-edge emission in the future.

## 6.2 FUTURE DIRECTIONS

### 6.2.1 *Sonochemical Synthesis of Doped Quantum Dots and Magic-Size Clusters*

As an extension of the sonochemical synthesis of cadmium selenide quantum dots, this system will be used in attempt to dope CdSe QDs and MSCs. The extreme temperatures and pressures in

a highly localized location allows for rapid precursor degradation and nanocrystal growth. We hypothesize that these conditions will facilitate the incorporation of dopants into the nanocrystals, and more so, that the extreme conditions could incorporate dopants that haven't previously been incorporated into CdSe before. Furthermore, this system could be extended to additional material systems outside of CdSe.

Recently, the Pozzo Lab (Chemical Engineering) and the Peek Lab (Human Centered Design & Engineering) at the University of Washington developed a high-throughput automated system for sonicating up to 120 samples in succession. This platform will allow for extensive exploration into the sonochemical synthesis of quantum dots and magic-sized clusters. Utilizing this automated system will allow for the testing of a large range of variables, including sonication power, sonication time, concentrations of precursors and dopants, and types of nanocrystals and dopants.

### 6.2.2 *Optimization and Further Investigation into the Indium Phosphide Spherical Quantum Well*

To understand and optimize the InP spherical quantum well system, the impact of shell thicknesses should be studied in more depth. The thickness of the InP and outer zinc chalcogenide shells in ZnS/InP/ZnS, ZnSe/InP/ZnSe, and ZnSe/InP/ZnS structures should be investigated to understand its impact on the InP photoluminescent quantum yields, linewidths, and blinking. We hypothesize that increasing the outer zinc chalcogenide shell should enhance the band-edge emission of the InP, while decreasing interfacial and surface-state defect emission. Based on previous spherical quantum wells, this should also maintain narrow bandwidths and decrease blinking in these systems.

Besides the architectures themselves, the precursors and solvents used for making these nanostructures should also be studied. Since InP is extremely sensitive to water and oxygen, even under ambient and low-temperature conditions, care must be taken to prevent the presence of oxygen.<sup>108–112,260</sup> In 2010, Cros-Gagneux, *et al.* demonstrated that using carboxylates during the synthesis of InP NCs can result in ketonization of the carboxylic acids, leading to the formation of water and oxidation at the surface of the nanocrystals and subsequent charge carrier traps.<sup>111</sup> Since the current synthesis for InP SQWs uses several precursors containing carboxylic acids, the presence of these materials could result in the formation of oxidative species and prevent the formation of a high-quality SQW interface. The presence of oxidative species could also disrupt the strain-relaxation in the SQWs, resulting in lower quantum efficiencies. If problems arise with achieving higher quantum yields in these InP SQWs, alternative precursors and solvents that do not have carboxylic acids or other oxygen-containing species will need to be tested.

### 6.2.3 *Extension of the Spherical Quantum Well into New Material Systems*

In addition to optimizing the indium phosphide spherical quantum well, this system can also be explored for other material sets. For example, alloyed InZnP/ZnMgSe/ZnS nanocrystals have been studied and have shown promise for generating tunable visible spectra emission with relatively narrow photoluminescence bandwidths.<sup>82</sup> Extending this nanostructure further and generating InZnP/ZnMgSe/InZnP could utilize two different strain-engineering techniques, alloying and the spherical quantum well, to reduce interfacial defect emission, increase quantum efficiencies, and maintain narrow emission bandwidths. Furthermore, this system could be extended to materials that emit in the near infrared. One promising material for this application is InAs, which Bruns, *et al.* showed could be tuned throughout the NIR window with quantum yields

up to 30% when capped with CdSe and ZnSe shells.<sup>116</sup> While InAs is more toxic than InP, InAs has a much higher tunability throughout the NIR window than InP. For InAs SQWs, InAs and ZnTe have good band alignment,<sup>247</sup> as well as nearly identical lattice parameters, making these materials advantageous for a future NIR SQW.

## APPENDIX A. CHAPTER 4 SUPPLEMENTAL INFORMATION

### A1. Additional Characterization of ZnS Nanocrystals

#### A1.1. Calculating Percent Reaction Yield of ZnS Nanocrystals

The theoretical yield of ZnS nanocrystals was based on the synthesis protocols and the limiting reagent in the system:

$$m_t = M_{LR} * MW_{ZnS}$$

Where  $M_{LR}$  is the moles of the limiting reagent,  $MW_{ZnS}$  is the molecular weight of bulk ZnS, and  $m_t$  is the theoretical yield in grams. The yields from the two different syntheses were calculated using Beer's Law:

$$A = \epsilon l C$$

Where  $A$  is the absorbance,  $\epsilon$  is the extinction coefficient of ZnS in  $M^{-1} cm^{-1}$ ,  $l$  is the optical pathlength in cm, and  $C$  is the concentration of ZnS nanocrystals in the dispersion in mol/L. The optical pathlength  $l$  was 1 cm, and  $\epsilon$  was assumed to be  $3.3 \times 10^5 M^{-1} cm^{-1}$  at an absorption wavelength of 305 nm based on previous data of 2.9 nm ZnS nanocrystals.<sup>261</sup> The concentration was then adjusted based on the dilution of the ZnS nanocrystals used for absorbance measurements, and the concentrated nanocrystal concentration ( $C_{NC}$ ) was calculated:

$$C_{NC} = \frac{C * V_{Dilution}}{V_{NC}}$$

Where  $V_{Dilution}$  is the total volume of the diluted nanocrystals and  $V_{NC}$  is volume of concentrated nanocrystals added.

Once the concentration of nanocrystals was calculated, the total milligrams of ZnS nanocrystals were calculated:

$$m_{NC} = \left(\frac{4}{3}\right) \pi r^3 * C_{NC} * N_A * \rho * V_T$$

Where  $r$  is the nanocrystal radius,  $N_A$  is Avogadro's number,  $\rho$  is the bulk density of ZnS, and  $V_T$  is the total volume of nanocrystal dispersion collected after synthesis. For the bimodal distribution in ZnS-Saturated-S, the concentration of nanocrystals was assumed to be a 3:1 ratio of 1.9-nm:4.7-nm diameter particles.

**Table A1:** Summary of the theoretical and calculated yields of the ZnS syntheses with varying synthesis protocols

ZnS Synthesis	Limiting Reagent	M <sub>LR</sub> (mmols)	m <sub>t</sub> (mg)	Absorbance at 305 nm	Dilution Level	C <sub>NC</sub> (mM)	V <sub>T</sub> (mL)	m <sub>NC</sub> (mg)	Total Yield (%)
ZnS-Sat., Sulfur – 270/250 C	Sulfur	0.5	48.7	0.327	70x	0.069	2	5.56	11
ZnS-Sat, DPP:S – 210 C	Sulfur	0.3	29.2	0.0795	30x	0.007	2	0.379	2
ZnS-Unsat., Sulfur – 210 C	Sulfur	0.3	29.2	0.4018	300x	0.366	2	18.6	70
ZnS-Unsat. DPP:S – 210 C	Sulfur	0.3	29.2	0.213	300x	0.194	4	19.7	68

### A1.2. X-Ray Diffraction (XRD) of ZnS Nanocrystals

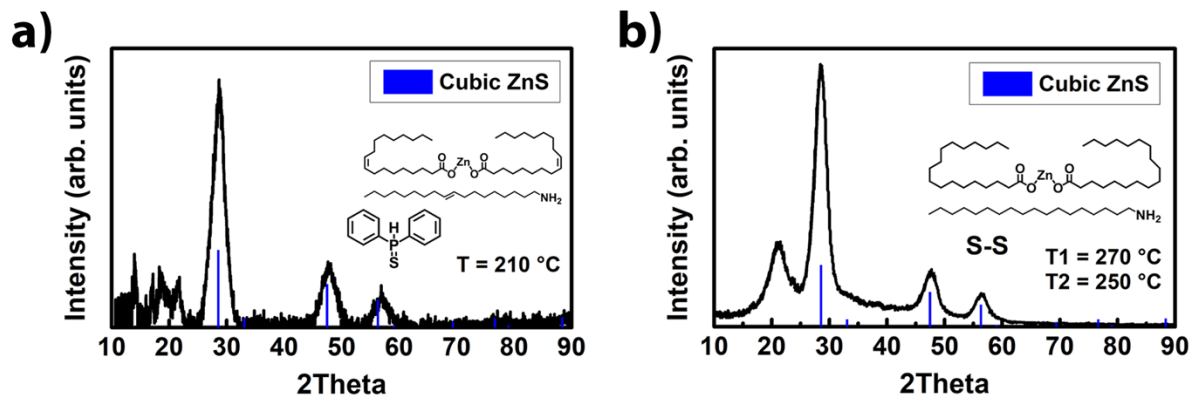


Figure A1. a) XRD of ZnS nanocrystals synthesized with DPP:S and unsaturated fatty compounds. b) XRD of ZnS nanocrystals synthesized with sulfur powder and saturated fatty compounds. ZnS XRD reference pattern: PDF 00-005-0566.

### A1.3. Photoluminescence Before and After Size-Selection of ZnS-Saturated-Sulfur

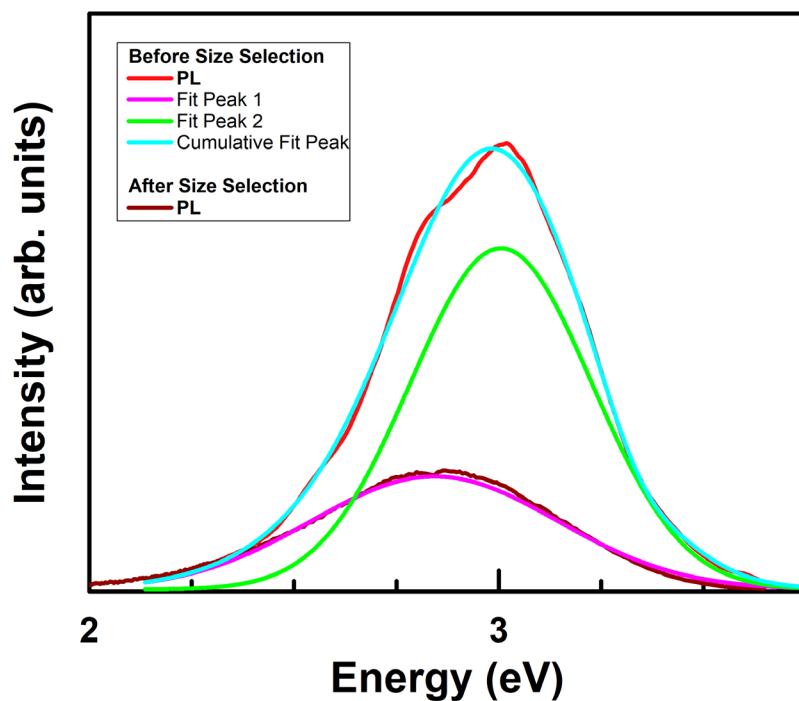


Figure A2. Photoluminescence peak fit of ZnS nanocrystals synthesized with sulfur powder and saturated fatty compounds before size selection, with comparison to the photoluminescence after size selection.

#### A1.4. Photoluminescence Lifetime of ZnS Nanocrystals

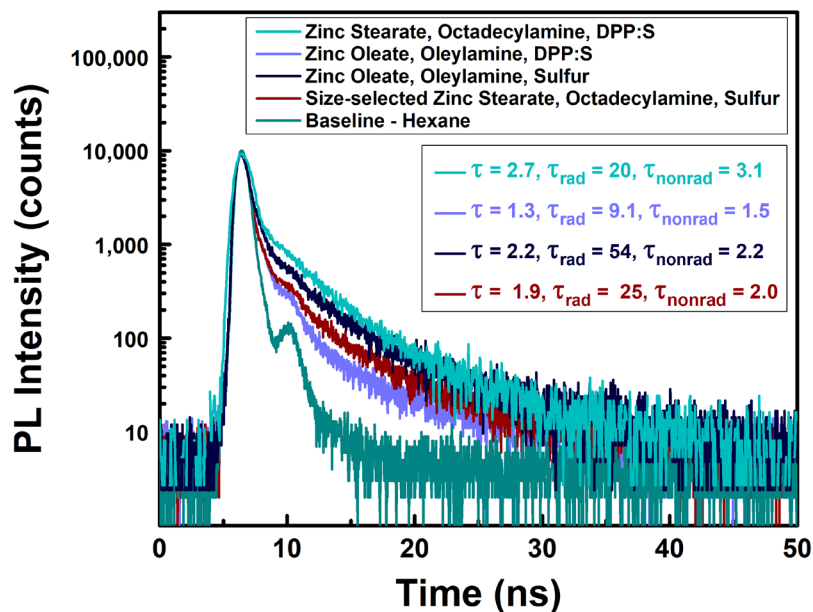


Figure A3. Photoluminescence lifetimes of ZnS nanocrystals synthesized under different synthesis conditions. The small hump in the photoluminescence lifetime data at 10 ns is from the instrumental response function (IRF), which can be seen more sharply in the hexane solvent baseline (dark green) that was used to disperse the nanocrystals.

#### A1.5. Extinction and Photoluminescence Characteristics of ZnS-Unsaturated-DPP:S Nanocrystals with and without Excess Oleic Acid

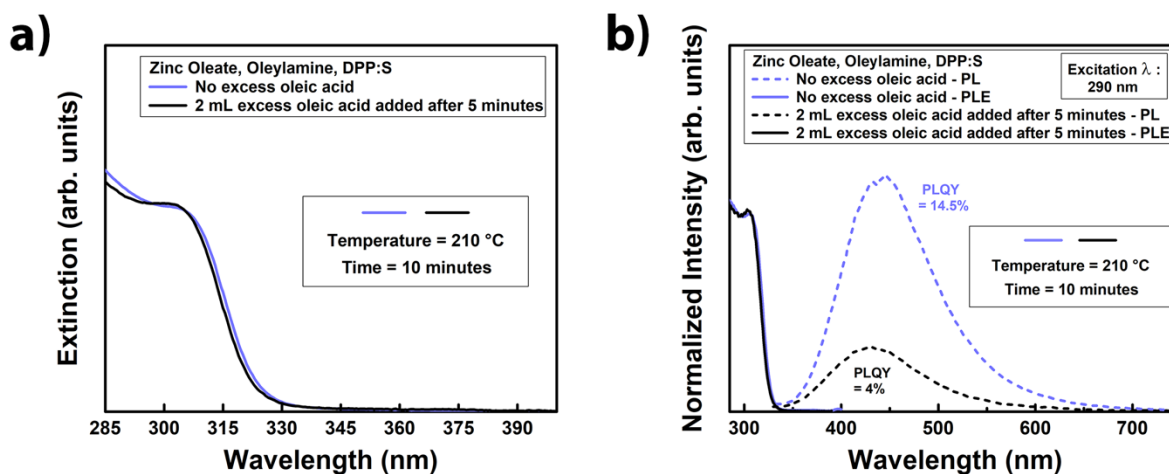


Figure A4. a) Absorbance, b) PL, and PLE spectra of ZnS-Unsaturated-DPP:S nanocrystals with and without the addition of excess oleic acid during the synthesis.

## APPENDIX B. CHAPTER 5 SUPPLEMENTAL INFORMATION

### **B1. Materials and Methods**

#### **B1.1. Chemicals**

Zinc acetate (99.99%), indium acetate (99.99%), indium chloride (99.999%), oleic acid (OLA, 90%), 1-octadecene (ODE, 90%), oleylamine (OAm, 70%), diphenylphosphine (DPP, 98%), sulfur powder (99.99%), selenium powder (99.99%), selenium pellets ( $\geq 99.999\%$ ), zinc stearate (technical grade), octadecylamine (99.8%), toluene (99.8%, anhydrous), ethanol ( $\geq 99.5\%$ , anhydrous), methanol ( $\geq 99.5\%$ , anhydrous), and chloroform ( $\geq 99\%$ ) were purchased from Sigma-Aldrich. Hexanes ( $\geq 98.5\%$ ), methanol ( $\geq 99\%$ ), and acetone (99.5%) were purchased from Fisher Scientific. Preparation of 0.15 M diphenylphosphine:sulfur (DPP:S) precursor was carried out by stirring 1.5 mmol of DPP and 1.5 mmol of sulfur powder in 10 mL of anhydrous toluene overnight inside of a nitrogen-filled glove box. Preparation of 0.15 M diphenylphosphine:selenium (DPP:Se) precursor was carried out by stirring 1.5 mmol of DPP and 1.5 mmol of selenium powder in 10 mL of anhydrous toluene overnight inside of a nitrogen-filled glove box.

#### **B1.2. Zinc Oleate**

Preparation of 0.2 M zinc oleate was carried out according to previously established procedures.<sup>204</sup> Briefly, 1.1 g of zinc acetate, 3.8 mL of OLA, and 21 mL of ODE were degassed three times at room temperature while stirring at 800 RPM using standard Schlenk line methods. The mixture was then heated to 200°C under N<sub>2</sub> until clear and colorless, then held at that temperature for an additional 30 minutes. The solution was then cooled to 150°C and 4 mL of

degassed OAm were injected. The zinc oleate was then cooled to 100°C and degassed for 30 minutes before being cooled to room temperature and transferred to a nitrogen-filled glove box for storage.

### **B1.3. Indium Oleate**

Preparation of 0.2 M indium oleate was carried out according to the procedure of Saeboe, *et al.*<sup>203</sup> by combining 4 mmol of indium acetate, 5 mL of OLA, and 15 mL of ODE in a 50 mL 3-neck round-bottom flask on a Schlenk line. The flask was heated to 120°C under N<sub>2</sub> and degassed until the solution was clear and colorless (~30-45 minutes). The mixture was then heated to 160°C and held at that temperature for 20 minutes. The flask was then cooled to 120°C and degassed for 1 hour before being cooled to room temperature and transferred to a nitrogen-filled glove box for storage.

### **B1.4. Indium Chloride**

Preparation of 0.1 M InCl<sub>3</sub>-OAm was carried out by heating indium chloride and oleylamine on a hot plate at 200°C in a nitrogen-filled glove box. The mixture was stirred at 200°C at 1000 RPM overnight until the indium chloride was completely dissolved.

### **B1.5. Se:Oleylamine Complex**

To synthesize 0.1 M oleylamine:Se complex for ZnSe SILAR reactions, 1 mmol of Se powder and 10 mL of OAm were added to a 25 mL 3-neck round-bottom flask. Using a Schlenk line, the mixture was heated to 120°C under N<sub>2</sub> and degassed 3 times. The mixture was then

heated to 22 °C for ~2 hours until the Se was completely dissolved. The complex was then cooled to room temperature and transferred to a nitrogen-filled glovebox for future use.

### **B1.6. S:Oleylamine Complex**

To synthesize 0.1 M oleylamine:S complex for ZnS SILAR reactions, 2 mmol of S powder, 10 mL of OAm, and 10 mL of ODE were added to a 20 mL glass vial and sealed with parafilm. The vial was sonicated for ~2 hours until the sulfur powder was completely dissolved. The complex was then transferred to a nitrogen-filled glovebox for future use.

### **B1.7. ZnS Nanocrystal Cores Used with TMS<sub>3</sub>P Experiments**

Cubic-phase ZnS nanocrystals were synthesized via a modified version of the solvothermal method from Srivastava, *et al.*<sup>201</sup> Briefly, 3.15 g of zinc stearate, 0.5 g of sulfur powder, 4g of octadecylamine, and 100 mL of ODE were degassed at room temperature for 15 minutes in a 250 mL round-bottom flask attached to a Schlenk line. The mixture was raised to 270°C under N<sub>2</sub> while stirring at 1000 RPM and held under those conditions for 5 minutes. The mixture was subsequently cooled to 250°C, held at that temperature for 30 minutes, then cooled to room temperature. The particles were precipitated via the addition of acetone and centrifugation, followed by dispersion into chloroform, which was repeated three times. The particles were then precipitated via the addition of methanol and centrifugation, followed by dispersion into chloroform, which was repeated an additional two times. The final particles were dispersed into hexanes and centrifuged several times to remove any remaining precursor.

### **B1.8. ZnS and ZnSe Nanocrystal Cores**

Cubic-phase ZnS and ZnSe nanocrystals were synthesized by modifying zinc selenide nanocrystal synthesis protocols from Saeboe, *et al.*<sup>203</sup> and Yu, *et al.*<sup>202</sup> For the growth of ZnS nanocrystals, 6 mL of 0.2 M zinc oleate and 4 mL of degassed ODE were degassed at room temperature at 600 RPM using standard Schlenk line procedures. The mixture was then heated to 100°C and further degassed for 1 hour. Next, the solution was cooled to 80°C and 2 mL of 0.15 M DPP:S in toluene were added, followed by 45 minutes of degassing to remove the toluene. The mixture was then heated to 210°C and held at that temperature for 10 minutes. The heating mantle was then removed, and the flask was cooled to room temperature before being transferred to a nitrogen-filled glove box. The nanocrystals were precipitated by the addition of anhydrous ethanol/methanol and centrifugation, and were redispersed in clean anhydrous toluene, which was repeated 3-4 times. For the ligand exchange to oleylamine, 2 mL of clean ZnS nanocrystals in toluene and 4 mL of oleylamine were stirred at 1000 RPM in the glovebox overnight. The nanocrystals were precipitated by the addition of anhydrous ethanol/methanol and centrifugation, and were redispersed in clean anhydrous toluene, which was repeated 2-3 times.

For the growth of ZnSe nanocrystals, 6 mL of 0.2 M zinc oleate and 4 mL of degassed ODE were degassed at room temperature at 600 RPM using standard Schlenk line procedures. The mixture was then heated to 100°C and degassed for 1 hour. Next, the solution was cooled to 80°C and 2 mL of 0.15 M DPP:Se in toluene were added, followed by 45 minutes of degassing to remove the toluene. The mixture was then heated to 220°C and held at that temperature for 15 minutes. The heating mantle was then removed, and the flask was cooled to room temperature before being transferred to a nitrogen-filled glove box. The nanocrystals were precipitated by the

addition of anhydrous ethanol/methanol and centrifugation, and were redispersed in clean anhydrous toluene, which was repeated 3-4 times.

## **B2. Additional Characterization of Nanocrystal Cores and InP SQWs**

### **B2.1. Characterization of Zinc Chalcogenide Nanocrystal Cores**

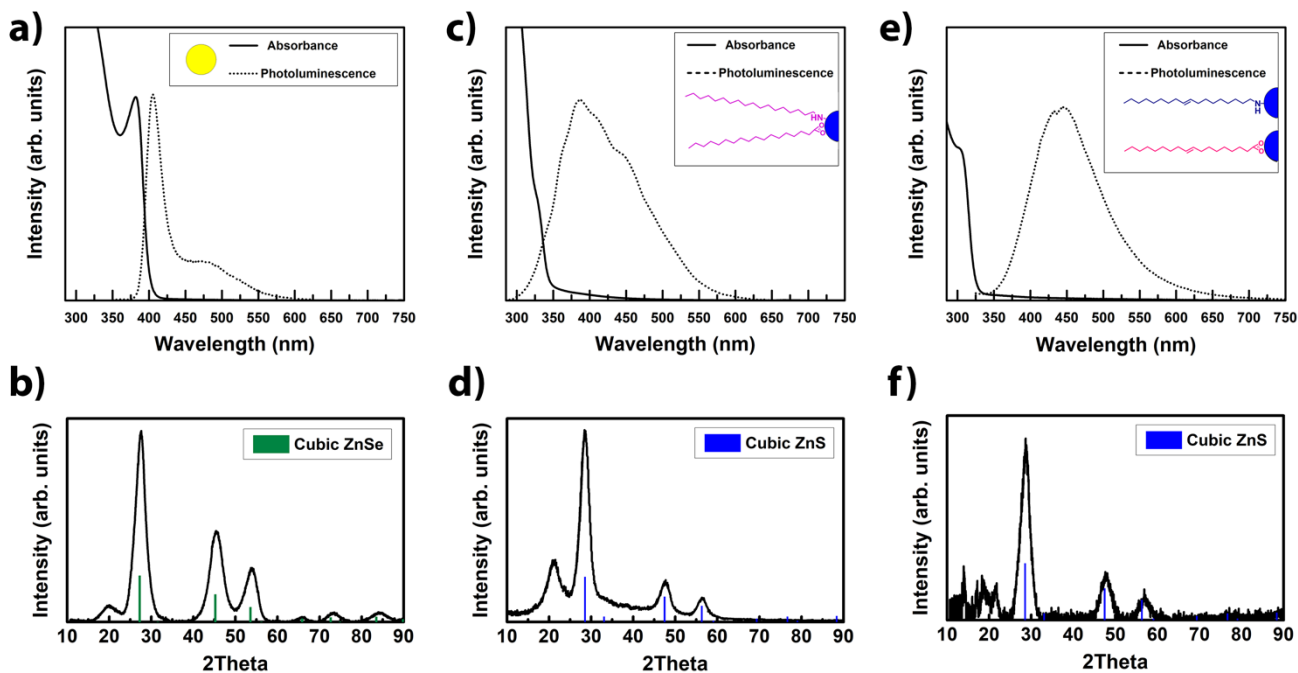


Figure B1. a) Extinction, PL, and b) XRD spectra of ZnSe nanocrystal cores. c) Extinction, PL, and d) XRD spectra of ZnS nanocrystal cores used in TMS<sub>3</sub>P experiments. e) Extinction, PL, and f) XRD spectra of ZnS nanocrystal cores used in TDAP experiments. ZnS XRD reference pattern: PDF 00-005-0566. ZnSe XRD reference pattern: PDF 00-037-1463.

## B2.2. Extinction Characterization of InP Structures Synthesized with Different Precursors

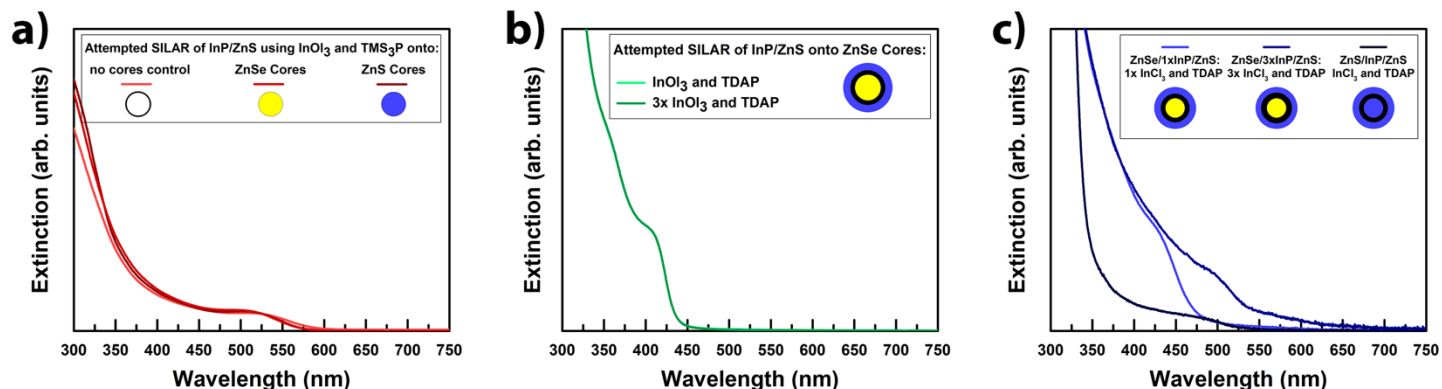


Figure B2. a) Extinction spectra of products resulting from attempted SILAR growth of InP/ZnS using a)  $\text{InO}_3$  and  $\text{TMS}_3\text{P}$ , b)  $\text{InO}_3$  and TDAP, and c)  $\text{InCl}_3$  and TDAP as InP precursors.

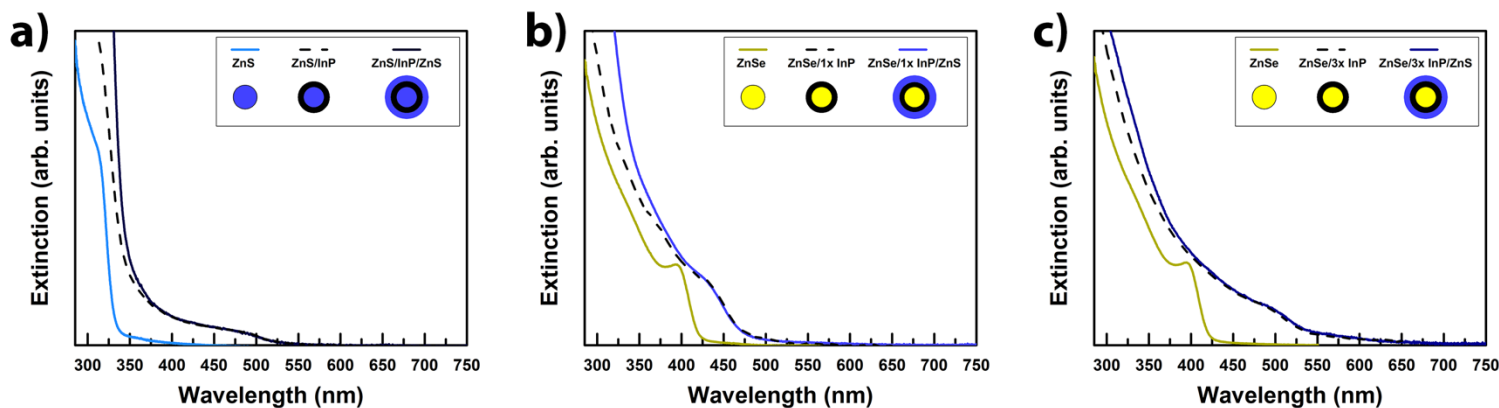


Figure B3. Extinction spectra of InP SQWs synthesized with TDAP and  $\text{InCl}_3$ : a) ZnS, ZnS/InP, and ZnS/InP/ZnS, b) ZnSe, ZnSe/1XInP, and ZnSe/1XInP/ZnS, and c) ZnSe, ZnSe/3XInP, and ZnSe/3XInP/ZnS.

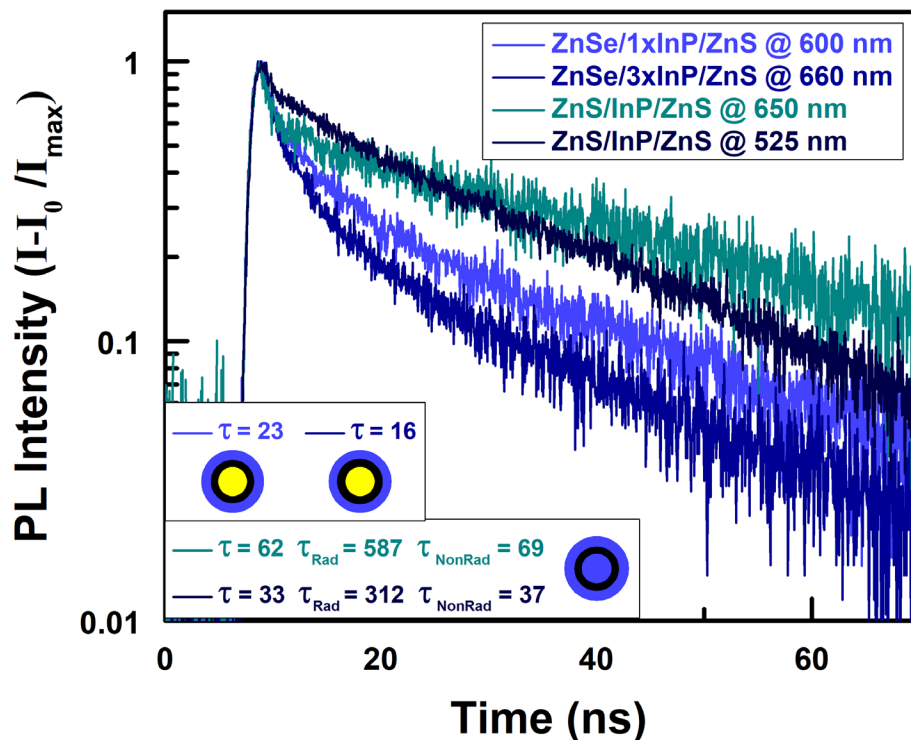


Figure B4. Photoluminescence lifetimes of ZnSe/InP/ZnS and ZnS/InP/ZnS nanostructures synthesized with  $\text{InCl}_3$  and TDAP.

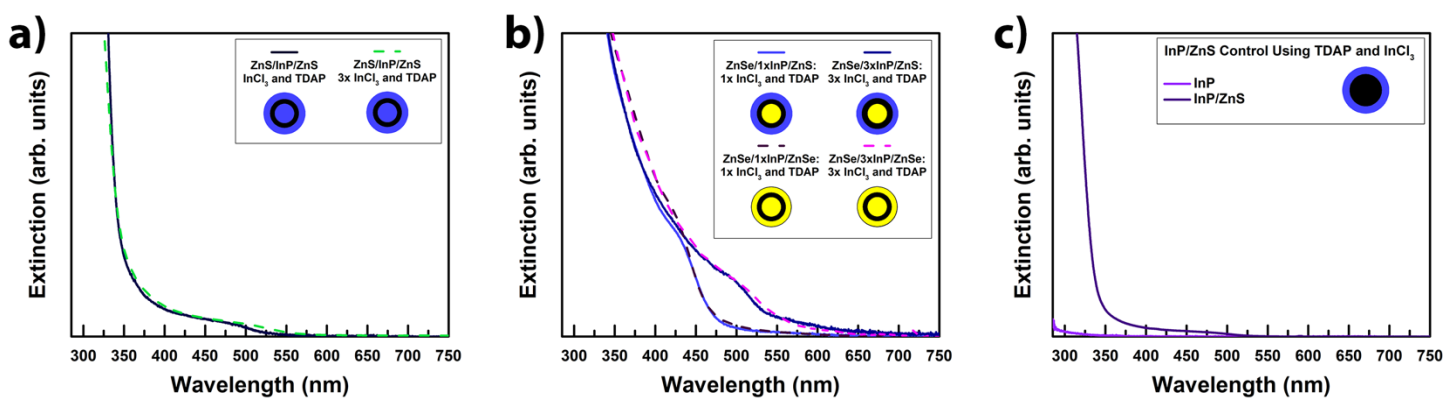


Figure B5. a) Extinction spectra of ZnS/InP/ZnS SQWs grown with 1X and 3X  $\text{InCl}_3$  and TDAP. b) Extinction spectra of ZnSe/1XInP/ZnS, ZnSe/3XInP/ZnS, ZnSe/1XInP/ZnSe, and ZnSe/3XInP/ZnSe. c) Extinction spectra of control syntheses of InP and InP/ZnS nanocrystals carried out with TDAP and  $\text{InCl}_3$ .

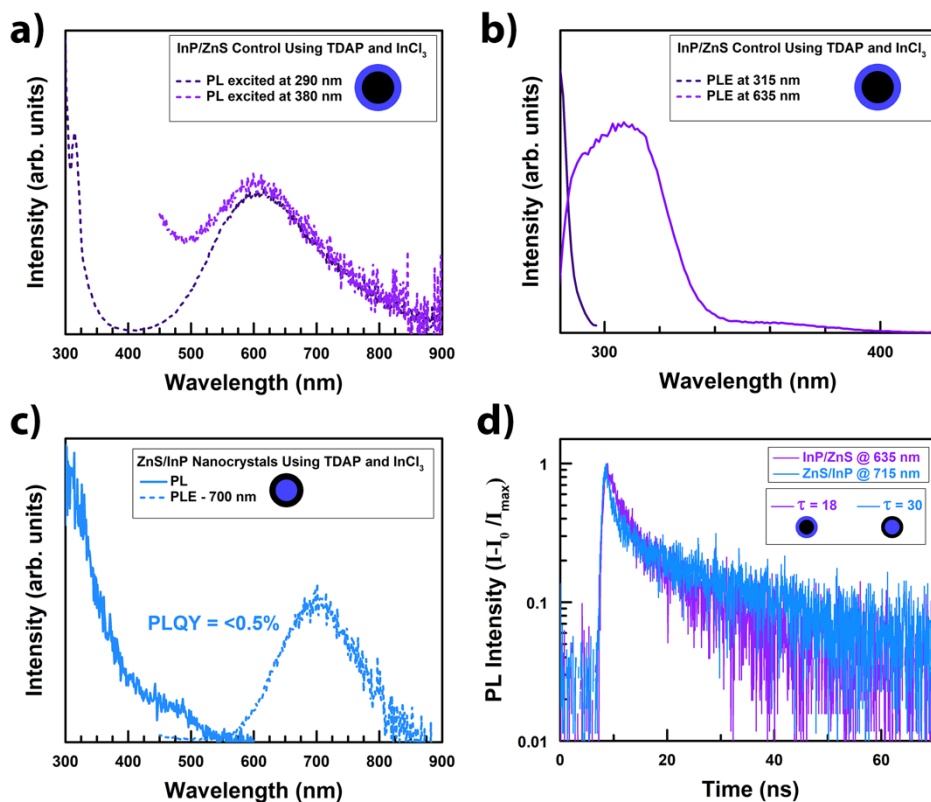


Figure B6. a) PL and b) PLE spectra of InP/ZnS nanocrystals synthesized with TDAP and  $\text{InCl}_3$ . c) PL and PLE spectra of ZnS/InP nanocrystals synthesized with TDAP and  $\text{InCl}_3$ . d) Photoluminescence lifetimes of the InP/ZnS and ZnS/InP nanocrystals.

### B2.3. Extinction Spectra of ZnS/InP/ZnS Nanocrystals with Synthesized with Different Core Surface Chemistries

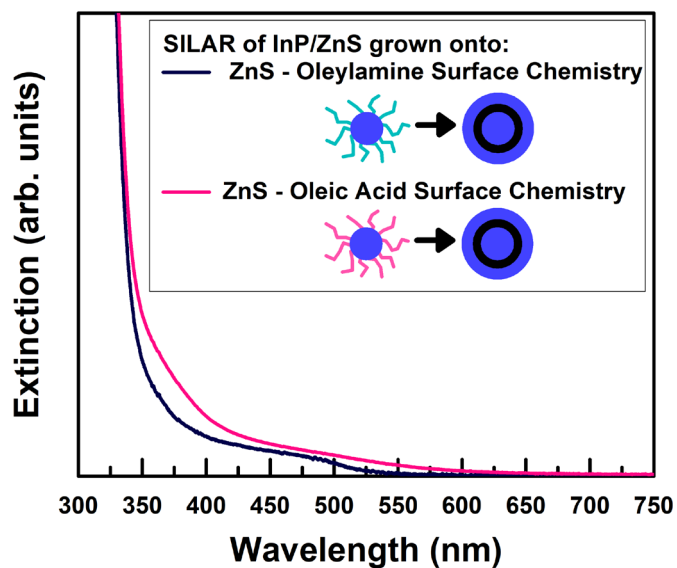


Figure B7. a) Extinction spectra of ZnS/InP/ZnS nanocrystals synthesized using ZnS cores with oleylamine (blue) and oleic acid (pink) surface functionalization.

### B2.4. XRD Characterization of Neat Oleylamine

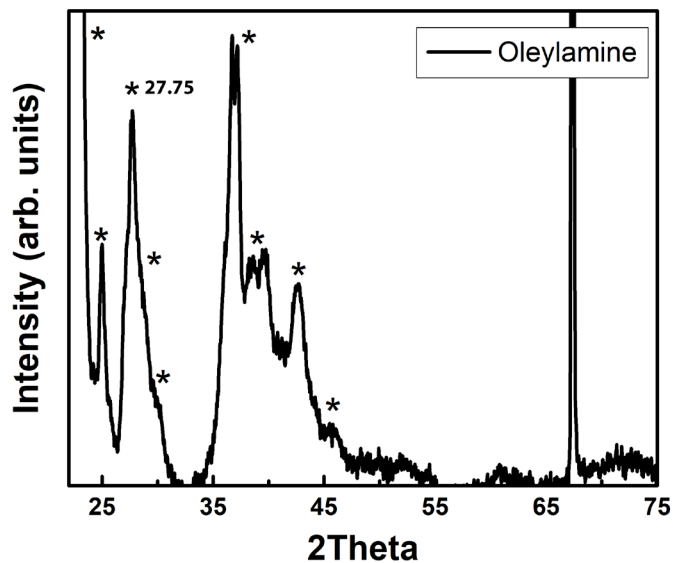


Figure B8. XRD pattern of crystallized oleylamine.

## B2.5. XRD Characterization of InP Structures Synthesized with Different Precursors

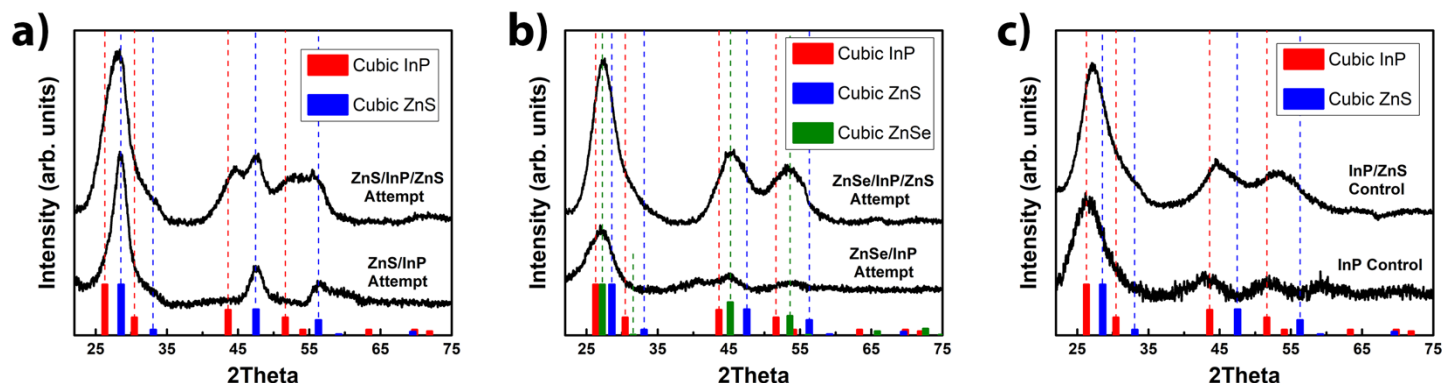


Figure B9. a) XRD of products resulting from attempted growth of ZnS/InP and ZnS/InP/ZnS nanocrystals, b) attempted growth of ZnSe/InP and ZnSe/InP/ZnS nanocrystals, and c) control syntheses of InP and InP/ZnS nanocrystals carried out using  $\text{TMS}_3\text{P}$  and  $\text{InOCl}_3$ . ZnS XRD reference pattern: PDF 00-005-0566. ZnSe XRD reference pattern: PDF 00-037-1463. InP XRD reference pattern: PDF 00-032-0452.

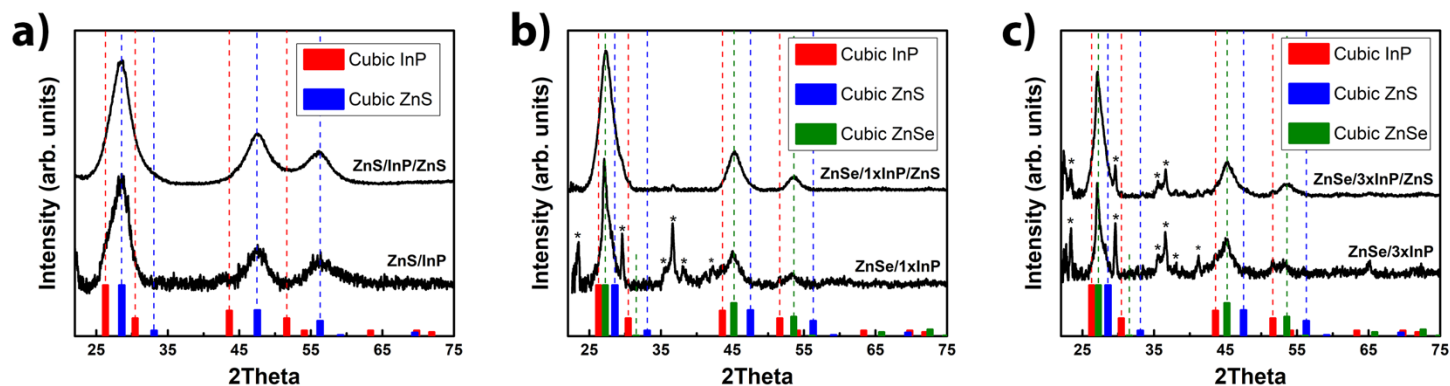


Figure B10. a) XRD of ZnS/InP and ZnS/InP/ZnS, b) ZnSe/1XInP and ZnSe/1XInP/ZnS, and c) ZnSe/3XInP and ZnSe/3XInP/ZnS nanocrystals synthesized using TDAP and  $\text{InCl}_3$ . Asterisks in b) and c) indicate reflections associated with the presence of excess oleylamine. ZnS XRD reference pattern: PDF 00-005-0566. ZnSe XRD reference pattern: PDF 00-037-1463. InP XRD reference pattern: PDF 00-032-0452.

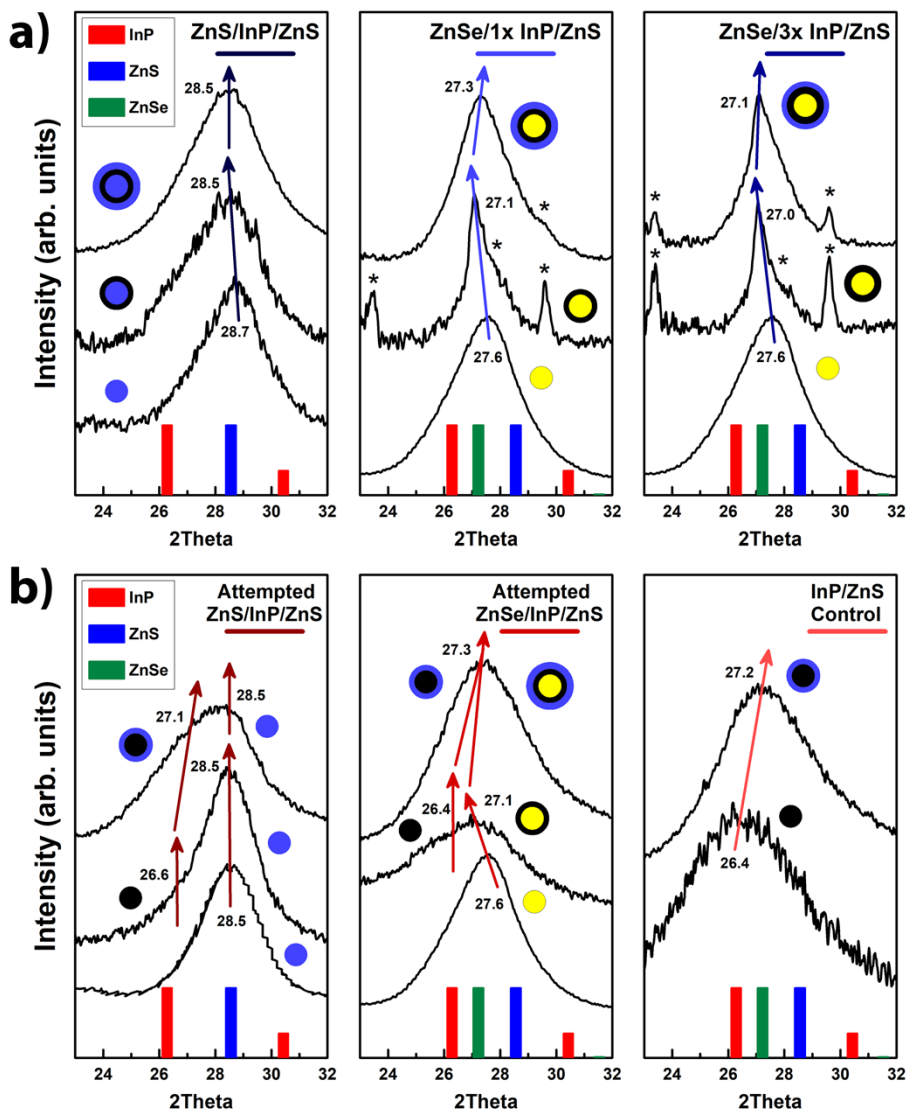


Figure B11. a) Shifting of the (111) XRD peak of InP SQWs synthesized with TDAP and  $\text{InCl}_3$ . b) Shifting of the (111) XRD peak of products resulting from attempted InP SQW syntheses with  $\text{TMS}_3\text{P}$  and  $\text{InOl}_3$  and the corresponding InP QD control synthesis. Diagrams show the target structures and byproducts present at each step in the synthesis process, from initial nanocrystal cores to shelled nanostructures. Asterisks in a) indicate reflections associated with the presence of excess oleylamine.

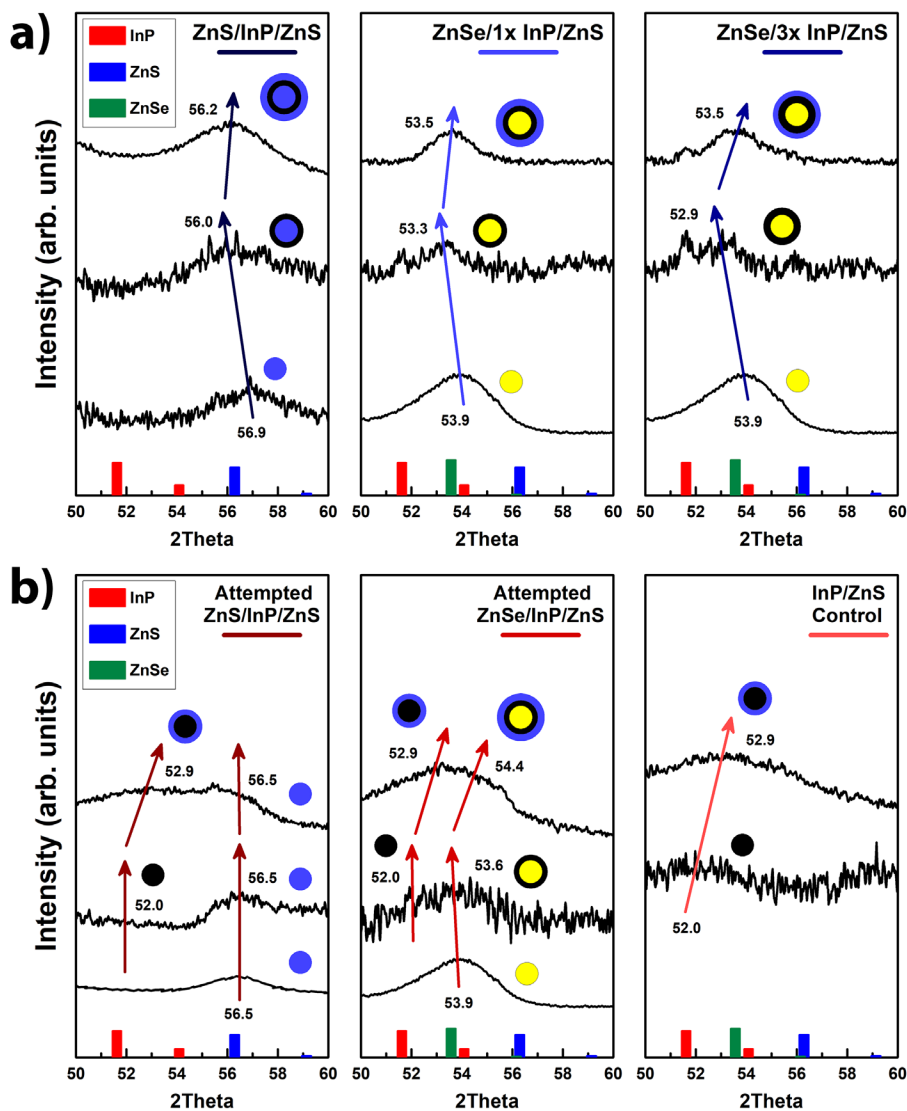


Figure B12. a) Shifting of the (311) XRD peak of InP SQWs synthesized with TDAP and InCl<sub>3</sub>. b) Shifting of the (311) XRD peak of products associated with attempted InP SQW syntheses with TMS<sub>3</sub>P and InO<sub>3</sub> and the corresponding InP QD control synthesis. Diagrams show the target structures and byproducts present at each step in the synthesis process, from initial nanocrystal cores to shelled nanostructures.

## **APPENDIX C. SILVER SULFIDE AS A SPHERICAL AND ANNULAR QUANTUM WELL**

### **C1. Materials and Methods**

#### **C1.1 Chemicals for Spherical and Annular Ag<sub>2</sub>S Quantum Wells**

Zinc Stearate (technical grade), zinc acetate (99.99%), zirconium (IV) chloride ( $\geq 99.5\%$ ), sulfur (99.99%), selenium powder (99.99%), zinc nitrate hexahydrate ( $\geq 99\%$ ), hexadecylamine (HDA, 90%), octadecylamine ( $\geq 99\%$ ), 1-octadecene (ODE, 90%), chloroform ( $\geq 99\%$ ), oleylamine (OAm, 70%), oleic acid (OLA, 90%), trioctylphosphine (TOP, 97%), silver nitrate (99.99%), and 1-octanethiol ( $\geq 98.5\%$ ) were purchased from Sigma-Aldrich. Hexanes ( $\geq 98.5\%$ ), methanol ( $\geq 99\%$ ), and acetone (99.5%) were purchased from Fisher Scientific. Ethanol (100%) was purchased from Decon Labs. Trioctylphosphine silver (TOP:Ag) was synthesized by stirring silver nitrate in TOP overnight. Trioctylphosphine selenide (TOP:Se) was synthesized by stirring selenium powder in TOP overnight.

#### **C1.2. Characterization and Modeling Techniques for Spherical and Annular Ag<sub>2</sub>S Quantum Wells**

Transmission electron microscopy (TEM) images and Energy-dispersive X-ray Spectroscopy (EDX) was taken using an FEI Technai G2 F20 Supertwin transmission electron microscope operating with an accelerating voltage of 200 kV. Ultraviolet-visible spectroscopy measurements were taken using an Agilent Technologies Carey 60-UV-vis spectrometer, with a 1 cm path length quartz cuvette. Photoluminescence spectroscopy measurements were taken using a PerkinElmer LS 55 Fluorescence spectrometer, with a 1 cm path length quartz cuvette. X-Ray Diffraction

(XRD) was taken with a Bruker D8 powder X-ray diffractometer and a Pilatus 100k large-area 2D detector.

### C1.3. Constants Used for Theoretical Critical Thickness Modeling

Table C1. Lattice Parameters of Zinc Chalcogenides and Silver Sulfide

Material	Lattice Parameters
ZnS	<b>Cubic: a = 0.541 nm</b> <b>Hexagonal:</b> <b>a = 0.381 nm</b> <b>c = 0.6234 nm</b>
ZnSe	<b>Cubic: a = 0.567 nm</b> <b>Hexagonal:</b> <b>a = 0.398 nm</b> <b>c = 0.653 nm</b>
Ag <sub>2</sub> S	<b>Monoclinic:</b> <b>a = 0.432 nm</b> <b>b = 0.691 nm</b> <b>c = 0.787 nm</b>

Since a range of values were found online for Poisson's Ratio ( $\nu$ ), a low value of 0.27 and a high value for 0.43 was used for all materials, providing a range of critical thicknesses for each material. Lattice mismatch was determined by the percentage difference in lattice parameters for the various materials. The same critical thickness equation from Chapter 5 was used.

### C1.4. Synthesis of Cubic Zinc Sulfide Nanocrystals

Cubic zinc sulfide (ZnS) nanocrystals were synthesized via a modified solvothermal method from Srivastava, *et al.*<sup>201</sup> Typically, 3.15 g zinc stearate, 0.5 g sulfur powder, 4g octadecylamine, and 100 mL ODE were degassed at room temperature for 15 minutes. The mixture was raised to 270 °C under N<sub>2</sub> while stirring at 1000 RPM and held here for 5 minutes. The mixture was subsequently lowered to 250 °C and held here for 30 minutes, then lowered to room temperature.

The particles were precipitated via the addition of acetone and centrifugation, followed by dispersion of the particles into chloroform, which was repeated three times. The particles were then precipitated via the addition of methanol and centrifugation, followed by dispersion of the particles into chloroform, which was repeated an additional two times. The final particle dispersion was dispersed into hexanes and centrifuged to remove additional precursor.

### **C1.5. Growth of Silver Sulfide onto Cubic Zinc Sulfide Cores**

An attempted growth of silver sulfide ( $\text{Ag}_2\text{S}$ ) onto cubic ZnS cores was conducted via a slow-drip method. Typically, 7 mL ZnS dispersed in hexanes was used, where 50  $\mu\text{L}$  of nanocrystals dispersed in a total of 3.5 mL hexanes had an optical density of 0.47 at 250 nm. The ZnS in hexanes, 3 mL ODE, and 1 mL OLA were degassed at room temperature for 30 minutes while stirring at 500 RPM, followed by 15 minutes of degassing at 120  $^\circ\text{C}$ . Two syringe pumps were prepared, one with 3 mL of 0.166 M TOP:Ag and the other with 52  $\mu\text{L}$  1-octanethiol in 3 mL ODE. The dispersion was heated to 160  $^\circ\text{C}$  under  $\text{N}_2$ , and the syringe pump began dripping silver and sulfur precursors into solution at 1.5 mL/hour. After being lowered to room temperature, 10 mL of chloroform was injected into the dispersion. The nanocrystals were precipitated by the addition of 1:1 methanol/acetone and centrifugation, and were redispersed in clean chloroform, which was repeated several times.

### **C1.6. Synthesis of Hexagonal Zinc Selenide**

Hexagonal zinc selenide ( $\text{ZnSe}$ ) was synthesized using a protocol from Jana, *et al.*<sup>262</sup> Here, 0.041 g zinc acetate, 0.0117 g zirconium chloride, 16 mL TOP, and 12 mL OLA were degassed at room temperature 3 times, then heated to 120  $^\circ\text{C}$  under  $\text{N}_2$  and degassed an additional 3 times at 800 RPM. The mixture was heated to 180  $^\circ\text{C}$  and stirred for 30 minutes until all precursors were

dissolved. The mixture was then heated to 240 °C and 26 mL of 1 M TOP:Se was quickly injected and left to react for 25 minutes. The heating mantle was then removed and 20 mL of hexanes was injected at 100 °C before being lowered to room temperature. The materials were precipitated via centrifugation, and were redispersed in clean hexanes, which was repeated several times.

### **C1.7. Synthesis of Hexagonal Zinc Selenide Nanowires**

Hexagonal ZnSe nanowires were synthesized using a protocol from Li, *et al.*<sup>263</sup> Prior to synthesis, an OAm selenium complex (OAm:Se) was synthesized by degassing 78.9 mg selenium powder and 10 mL OAm at room temperature 3 times, followed by heating to 120 °C under N<sub>2</sub> and degassing another 3 times. The mixture was heated to 220 °C and left to stir at 800 RPM for 2-3 hours until all selenium powder was dissolved, and the solution was a dark amber. The solution was transferred to the glove box for storage. For nanowire growth, 59.5 mg zinc nitrate hexahydrate and 8 mL OAm were degassed at room temperature for 1 hour at 800 RPM. The mixture was heated to 75 °C under N<sub>2</sub> and degassed for 30 minutes, followed by heating to 100 °C and degassed for an additional 30 minutes. The mixture was heated to 160 °C and 2 mL of OAm:Se was injected rapidly into solution. The dispersion was lowered to 120 °C and degassed for 10 minutes, before being raised to 250 °C and held here for 20 minutes. The heating mantle was then removed, and the dispersion was quenched via a water bath at 200 °C. The nanowires were precipitated by the addition of ethanol and centrifugation, and were redispersed in clean chloroform. The nanowires were then precipitated by the addition of methanol and centrifugation, and were redispersed in clean chloroform, which was repeated several times.

### C1.8. Growth of Zinc Sulfide Shells onto Zinc Selenide Nanowires

ZnS shells were grown onto ZnSe cores via Li, *et al.*'s method.<sup>263</sup> Before synthesis, 0.2 M zinc oleate was synthesized according to Kress, *et al.*<sup>204</sup> by degassing 1.1 g zinc acetate, 3.8 mL OLA, and 21 mL ODE three times at room temperature at 800 RPM. The mixture was heated to 200 °C under N<sub>2</sub> until clear and colorless, then left for an additional 30 minutes. The solution was then lowered to 150 °C and 3.95 mL of degassed OAm was injected. The zinc oleate was then lowered to 100 °C and degassed for 30 minutes before being lowered to room temperature and transferred to a glove box for storage. A 0.1 M sulfur injection was prepared by sonicating 33.3 mg sulfur in 10 mL ODE for 2 hours. For shell growth, 0.8 mL ZnSe dispersed in hexanes was used, where 50 uL of nanowires dispersed in a total of 2.05 mL hexanes had an optical density of 0.80 at 325 nm. The ZnSe nanowires in hexanes, 0.5 g HDA, and 7.6 mL ODE were heated to 65 °C under N<sub>2</sub> and degassed for 30 minutes at 500 RPM. The dispersion was then raised to 100 °C and degassed for an additional 30 minutes. The system was then cycled under vacuum 3 times before being heated to 200 °C under N<sub>2</sub> for the shell growth. A series of injections were then conducted for shell growth via a successive ionic layer adsorption and reaction (SILAR) method. The first injection was 0.3 mL of a 0.1 M sulfur in ODE, which was added dropwise, and held at 200 °C for 10-15 minutes. The second injection was 0.15 mL of 0.2 M zinc oleate, which was added dropwise, and held at 200 °C for 10 – 15 minutes. The proceeding injection volumes were calculated using a method from Li, *et al.*<sup>32</sup>, and a total of 5 sulfur and 5 zinc syringes were injected. Each injection was allowed to react for 10-15 minutes, and the temperature was raised by 10 °C after each set of sulfur and zinc injections. After being lowered to room temperature, 4 mL of chloroform was injected into solution. The nanowires were precipitated by the addition of ethanol and centrifugation, and were redispersed in clean chloroform, which was repeated several times. The nanowires were then

precipitated by the addition of methanol and centrifugation, and were redispersed in clean chloroform, which was repeated several times.

### **C1.9. Growth of Silver Sulfide onto Hexagonal Zinc Selenide/Zinc Sulfide Nanowires**

Growth of Ag<sub>2</sub>S onto ZnSe/ZnS core/shells was conducted via a slow-drip method. Typically, 1 mL of ZnSe/ZnS dispersed in hexanes was used, where 20 uL of nanowires dispersed in a total of 2.02 mL chloroform had an optical density of 1.3 at 300 nm. The ZnSe/ZnS in chloroform, 2 mL ODE, and 2 mL OAm were heated to 60 °C under N<sub>2</sub> and degassed for 15 minutes at 500 RPM, followed by heating to 120 °C and an additional hour of degassing. Two 3 mL syringes were then prepared, one with 42 uL 1-octanethiol in 3 mL ODE and another with 3 mL of 0.54 M TOP:Ag. The dispersion was heated to 160 °C under N<sub>2</sub>, and the syringe pump began dripping silver and sulfur precursor into solution at 1.5 mL/hour. The syringe was stopped after 40 minutes due to observable color change and nucleation of silver sulfide. After being lowered to room temperature, the heavy nanomaterials in the dispersion were precipitated via centrifugation to remove nucleated Ag<sub>2</sub>S. The ZnSe/ZnS/Ag<sub>2</sub>S nanowires in the supernatant were precipitated by the addition of 2:5:5 chloroform/ethanol/methanol and centrifugation and were redispersed in clean chloroform. The nanowires were then precipitated via the addition of methanol and centrifugation, and were redispersed in clean chloroform, which was repeated several times.

## **C2. Results and Discussion**

Ag<sub>2</sub>S was studied as a low-energy quantum well due to its ability to be tuned through the NIR and its low toxicity. Since ZnS and zinc selenide (ZnSe) both have good band alignment with Ag<sub>2</sub>S,<sup>247,264</sup> and zinc is nontoxic and earth-abundant, these materials were explored for the high-energy material in spherical and annular quantum well structures.

While  $\text{Ag}_2\text{S}$  is most commonly found in its monoclinic form,  $\text{ZnS}$  and  $\text{ZnSe}$  can be synthesized in either cubic or hexagonal (wurtzite) forms. Both crystal structures were investigated when calculating the critical thickness of monoclinic  $\text{Ag}_2\text{S}$  on  $\text{ZnS}$  and  $\text{ZnSe}$ .

Through comparison of these forms, I have calculated that the critical thickness of  $\text{Ag}_2\text{S}$  on cubic  $\text{ZnS}$  and  $\text{ZnSe}$  does not exist. Due to the large lattice mismatch between the crystal phases, the  $\text{Ag}_2\text{S}$  lattice structure will never remain coherent with a substrate of cubic  $\text{ZnS}$  or  $\text{ZnSe}$ , regardless of how thin the film is. Alternatively, I have calculated that the thickness of  $\text{Ag}_2\text{S}$  needs to be below  $3.8 \pm 0.6$  nm and  $8.9 \pm 1.6$  nm for growth onto hexagonal  $\text{ZnS}$  and  $\text{ZnSe}$ , respectively, both of which are reasonable values for growing a shell onto a nanocrystal core.

These initial calculations suggest that using  $\text{Ag}_2\text{S}$  and hexagonal  $\text{ZnSe}$  as the low and high-energy emitters, respectively, will have the greatest lattice match and therefore have the greatest chance of increasing the quantum yields in a SQW. However, the critical thickness model does not take into account the differences between the monoclinic and hexagonal crystal structures, and, therefore, differences in crystallographic registry could still prevent growth of  $\text{Ag}_2\text{S}$  onto specific facets.

Throughout the rest of this study, I have investigated the effect of  $\text{ZnS}$  and  $\text{ZnSe}$  crystal structure on the epitaxial growth of  $\text{Ag}_2\text{S}$  on route to the generation of NIR quantum well materials. As a control, I first synthesized cubic  $\text{ZnS}$  nanocrystals, and analyzed the growth of  $\text{Ag}_2\text{S}$  onto the surface. Upon failure to epitaxially grow a  $\text{Ag}_2\text{S}$  shell onto cubic  $\text{ZnS}$ , I have begun to study the growth of hexagonal  $\text{ZnSe}$  and subsequent growth of  $\text{Ag}_2\text{S}$  onto these structures. Specifically, I have transitioned to hexagonal  $\text{ZnSe}$  nanowires, which show preliminary evidence for successful epitaxial growth of  $\text{Ag}_2\text{S}$ .

### C2.1. Cubic Zinc Sulfide Nanocrystals and Silver Sulfide Growth

As an initial control, cubic ZnS was synthesized, and an attempt to grow Ag<sub>2</sub>S onto the surface was conducted to observe the ability for Ag<sub>2</sub>S to grow onto a strained substrate. Confirmation of the cubic ZnS crystal structure via X-ray diffraction (XRD) can be seen in Appendix C3. As seen

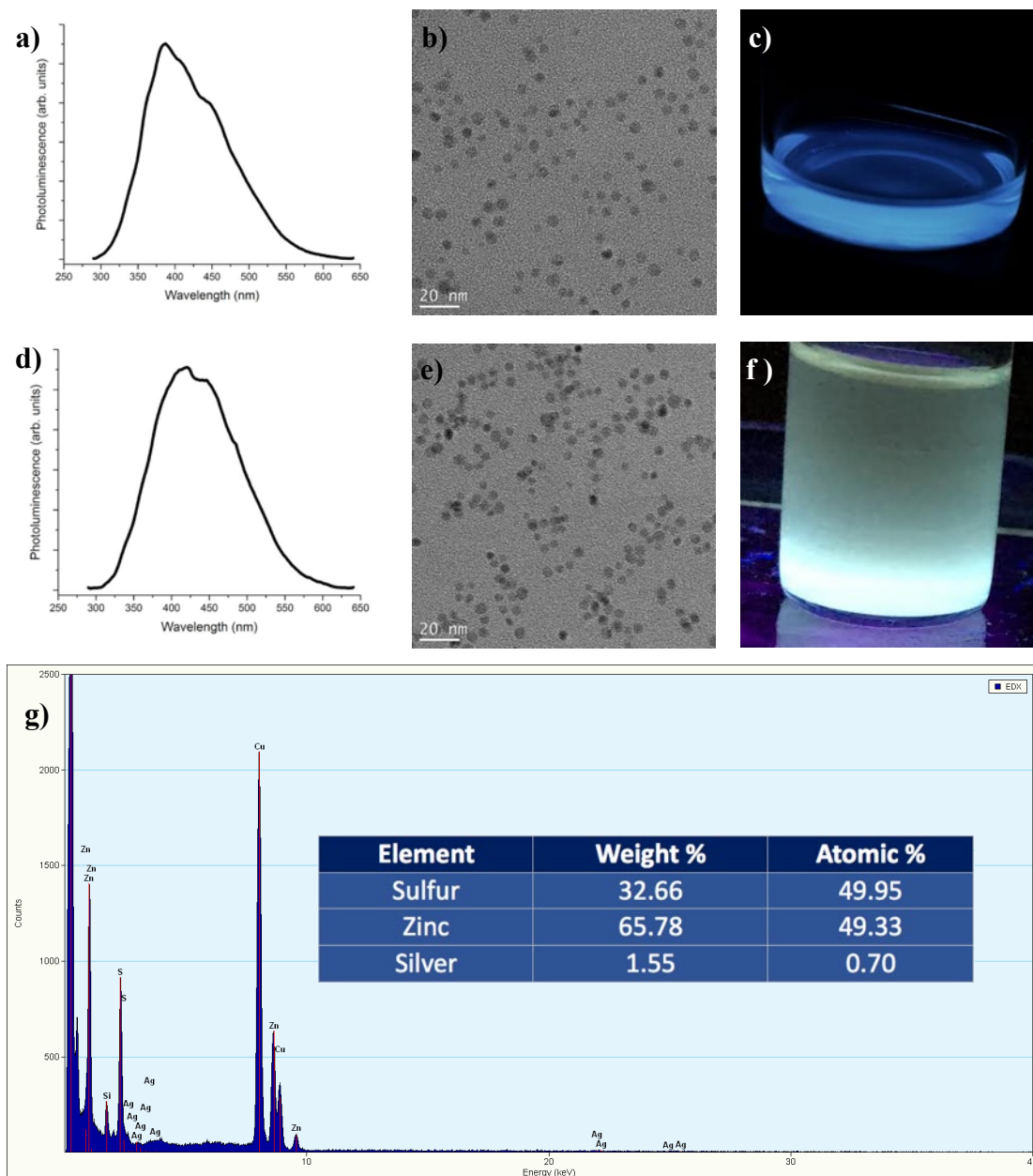


Figure C1. (a) PL spectra of ZnS NCs. (b) TEM of ZnS NCs. (c) ZnS emission under UV light. (d) PL spectra of ZnS NCs after Ag<sub>2</sub>S growth attempt. (e) TEM of ZnS NCs after Ag<sub>2</sub>S growth attempt. (f) ZnS emission under UV light after Ag<sub>2</sub>S growth attempt. (g) EDX of ZnS NCs after Ag<sub>2</sub>S growth attempt, with an inset of the compositional analysis.

by the TEM image in Figure C1b, the ZnS NCs are polydisperse, likely leading to the broad and multi-peaked emission spectrum in Figure C1a. Upon the addition of silver and sulfur precursors, the diameter of the nanocrystals did not observably change, as seen in Figure C1e, indicating an inability to grow a Ag<sub>2</sub>S shell onto cubic ZnS cores. While the size of the nanocrystals did not change, there was a broadening and red shift of the emission spectrum (Figure C1d). In addition, the emission under 365 nm UV light is visibly whiter in Figure C1f, compared to the blue emission of the initial ZnS nanocrystals in Figure C1c, suggesting the presence of silver in the ZnS nanocrystals. Upon further analysis via energy-dispersive X-ray spectroscopy (EDX), only 0.7 atomic percent of silver was present in the ZnS NCs (Figure C1g). This small atomic percent suggests that while silver is present, it is only able to form a sub-monolayer, likely due to the high strain between the cubic ZnS and monoclinic Ag<sub>2</sub>S, as calculated previously.

## C2.2. Hexagonal Zinc Selenide

While hexagonal ZnSe nanostructures are theoretically compatible for epitaxial Ag<sub>2</sub>S growth, the hexagonal phase of ZnSe is metastable, with a transformation temperature between cubic and hexagonal phase of 1425 °C.<sup>265</sup> Given this instability, there are limited reports of the synthesis of hexagonal ZnSe nanostructures. While Reiss, *et al.*<sup>266</sup> reports a few sources with hexagonal ZnSe nanocrystals, attempts at these syntheses proved unsuccessful and several protocols produced cubic nanocrystals instead. Eventually, the protocol from Jana, *et al.*<sup>262</sup> proved successful, as seen by the X-ray diffraction (XRD) in Figure C2a. While hexagonal ZnSe was achieved, TEM showed that these nanostructures were large and aggregated (Figure C2b). Aliquots taken at several time points (Appendix C3) showed large aggregations throughout the synthesis process, making these nanostructures unusable for growth of Ag<sub>2</sub>S.

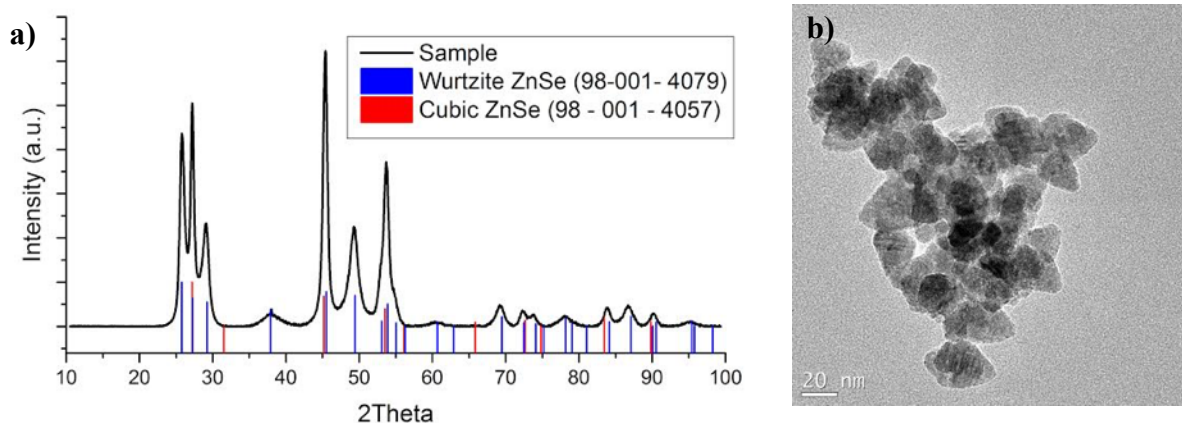


Figure C2. (a) XRD of Hexagonal ZnSe. (b) TEM of Hexagonal ZnSe.

### C2.3. Hexagonal Zinc Selenide Nanowires

As a model system for epitaxial  $\text{Ag}_2\text{S}$  growth, hexagonal ZnSe nanowires from Li, *et al.* were studied.<sup>263</sup> The nanowires had a very high aspect ratio, with diameters of  $\sim 3$  nm and lengths that were several hundred nanometers long (Figure C3b). XRD analysis (Figure C3a) demonstrated broad peaks, which were undistinguishable between hexagonal and cubic, possibly due to the narrow thickness of the nanowires. In addition, the nanowires did not efficiently emit light when excited by a 365 nm UV light, as seen in the inset in Figure C3b.

### C2.4. Hexagonal Zinc Selenide/Zinc Sulfide Nanowires and Silver Sulfide Growth

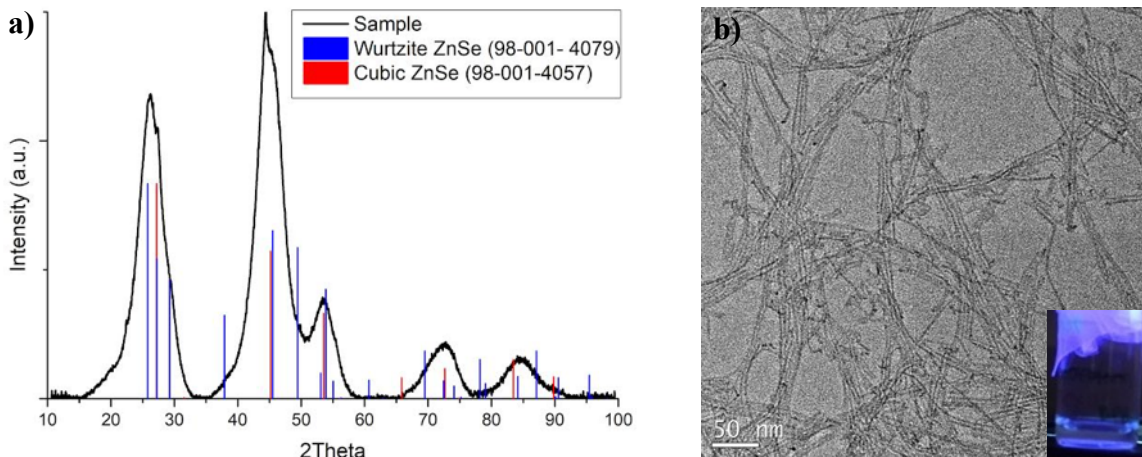


Figure C3. (a) XRD of ZnSe Nanowires. (b) TEM of ZnSe Nanowires with inset of emission under UV light.

Upon growth of a ZnS shell onto the ZnSe nanowires, XRD indicated a well-defined hexagonal crystal structure, matching with hexagonal ZnS (Figure C4). The larger peak at  $\sim 28.5$   $2\theta$  is indicative of the (002) direction of the ZnSe nanowires and is significantly larger than the other peaks due to the anisotropy of the nanowires.

While the ZnSe/ZnS wires exhibit hexagonal crystal structure, too much precursor was used during the ZnS shell growth, resulting in uncontrolled nucleation and growth of ZnS on and around the wires, as well as an overall increase in nanowire thickness, as seen in the TEM images in Figure C5a. While the ZnSe/ZnS nanowires exhibit blue emission when excited by a 365 nm UV light (Figure C5d), the broad tail in the PL spectrum around 500 nm in Figure C5c indicates the presence of defects, which is supported by the uncontrolled crystalline growths off of the ZnSe/ZnS wires seen in Figure C6a. The emission peak at  $\sim 360$  nm in Figure C5c also suggests the separate nucleation of individual ZnS nanoparticles in addition to the off-wire growths. This low-wavelength emission decreases in the ZnSe/ZnS/Ag<sub>2</sub>S emission, likely due to the additional cleaning steps between Ag<sub>2</sub>S growth and characterization.

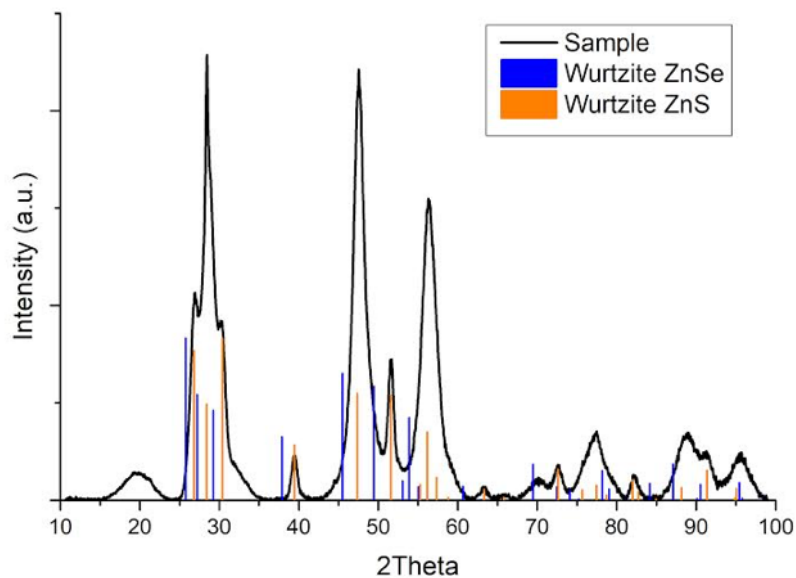


Figure C4. XRD of ZnSe/ZnS Nanowires.

Upon growth of  $\text{Ag}_2\text{S}$ , TEM images show that the nodules off of the ZnSe nanowires have grown significantly (Figure C5b and Figure C6b), suggesting that  $\text{Ag}_2\text{S}$  can successfully grow epitaxially off of the hexagonal ZnSe/ZnS nanowires. In addition, the broad peak at 500 nm in the PL spectra of the ZnSe/ZnS/ $\text{Ag}_2\text{S}$  wires has increased (Figure C5c) and the emission under UV light is visibly whiter, which is a similar feature as the previous ZnS nanocrystals upon the presence of silver. Collectively, all of these results suggest that  $\text{Ag}_2\text{S}$  has successfully grown epitaxially off of the ZnSe/ZnS nanowires.

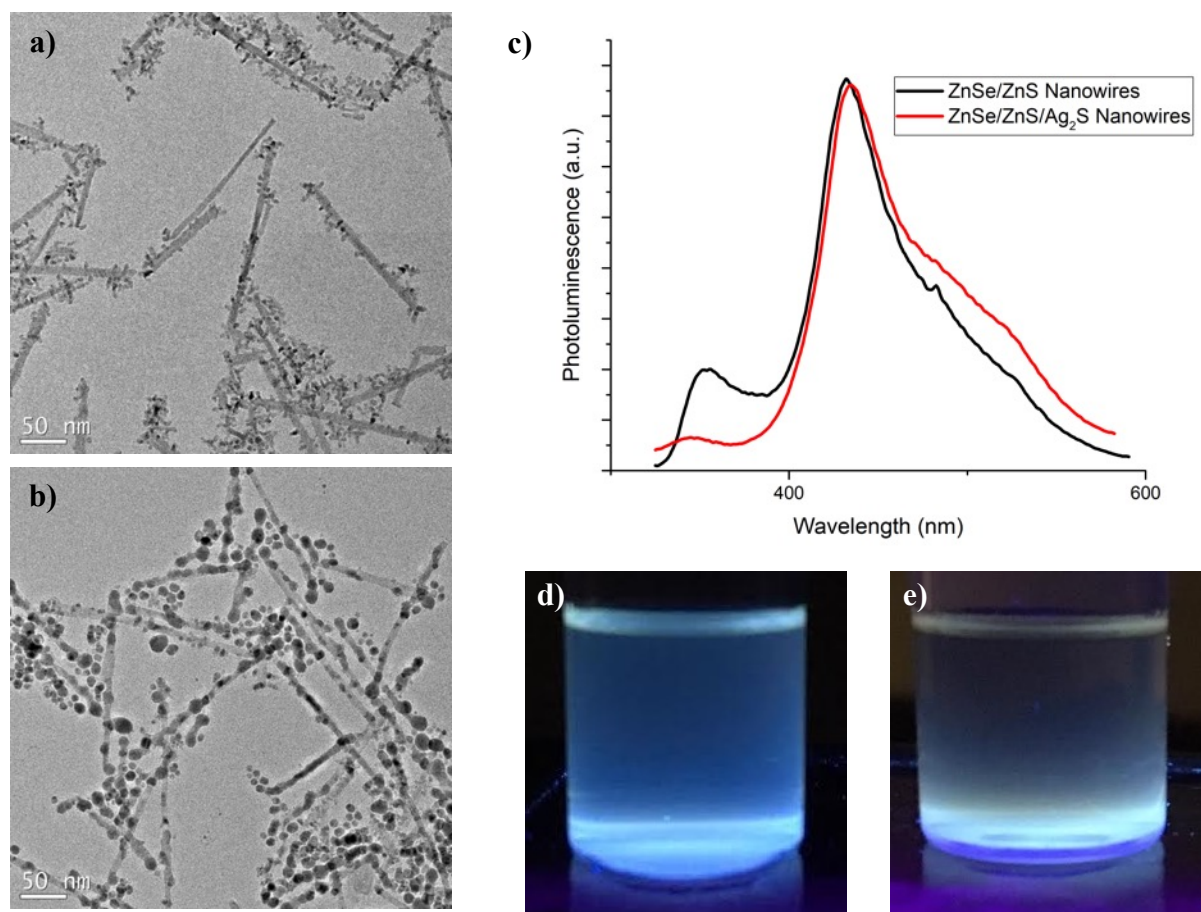


Figure C5. (a) TEM of ZnSe/ZnS Nanowires. (b) TEM of ZnSe/ZnS/ $\text{Ag}_2\text{S}$  Nanowires. (c) PL Spectra of ZnSe/ZnS and ZnSe/ZnS/ $\text{Ag}_2\text{S}$  Nanowires. (d) ZnSe/ZnS emission under UV light. (e) ZnSe/ZnS/ $\text{Ag}_2\text{S}$  emission under UV light.

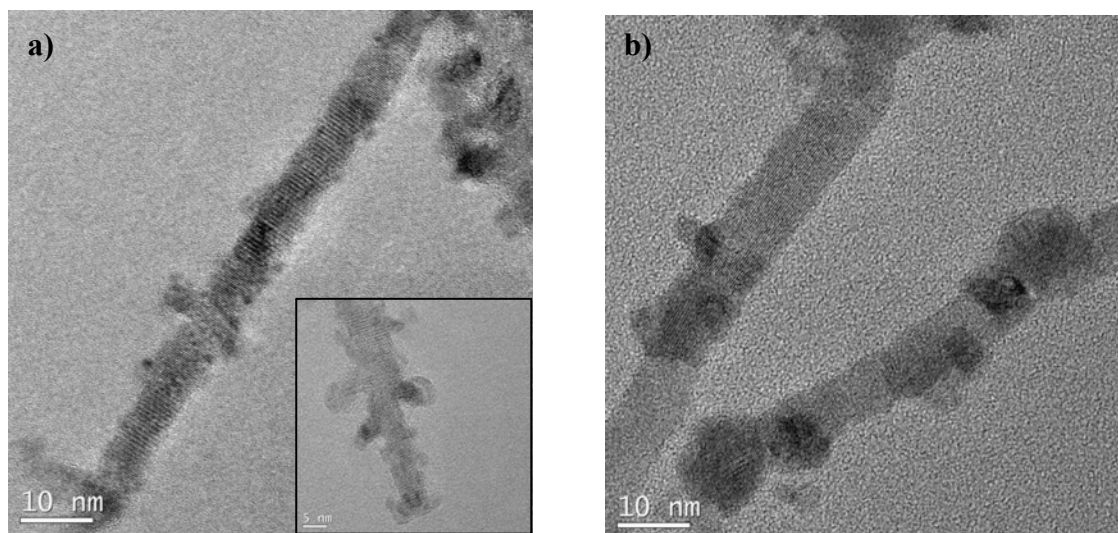


Figure C6. (a) High Resolution (HR)-TEM of ZnSe/ZnS Nanowires. (b) HR-TEM of ZnSe/ZnS/Ag<sub>2</sub>S Nanowires.

## C2.5. Conclusions

While the ZnSe/ZnS and ZnSe/ZnS/Ag<sub>2</sub>S nanowires show promise for use in a cylindrical quantum well, these systems still require further optimization. To prevent the uncontrolled growths and nucleation of ZnS and Ag<sub>2</sub>S onto the ZnSe nanowires, the concentration of the precursors must be decreased. In addition, transitioning from a slow-drip injection of the Ag<sub>2</sub>S precursors to a SILAR approach would likely further control the growth of the Ag<sub>2</sub>S shell and prevent uncontrolled growth and nucleation. SILAR injections have been shown to produce well-controlled and monodisperse shells onto nanocrystal cores for a variety of materials,<sup>71,267</sup> making this method an advantageous approach to the creation of a uniform and monodisperse NIR quantum well.

Although the Ag<sub>2</sub>S has been successfully grown onto the ZnSe/ZnS nanowires, it is still unclear which facets have crystallographic registry between the monoclinic Ag<sub>2</sub>S and hexagonal

zinc chalcogenides. For this reason, it must be verified that  $\text{Ag}_2\text{S}$  can grow in the annular direction of the nanowires, such that the annular quantum well can be achieved. In the case where  $\text{Ag}_2\text{S}$  cannot grow annularly, these nanowires cannot be used as an annular quantum well; however, the  $\text{ZnSe/ZnS}$  nanowires with  $\text{ZnS}$  growths could be investigated as a base for branched nanowire structures, which have shown potential for energy storage and conversion materials.<sup>268,269</sup>

### **C3. Additional Results and Characterization**

#### **C3.1. Characterization of Cubic ZnS Nanocrystals**

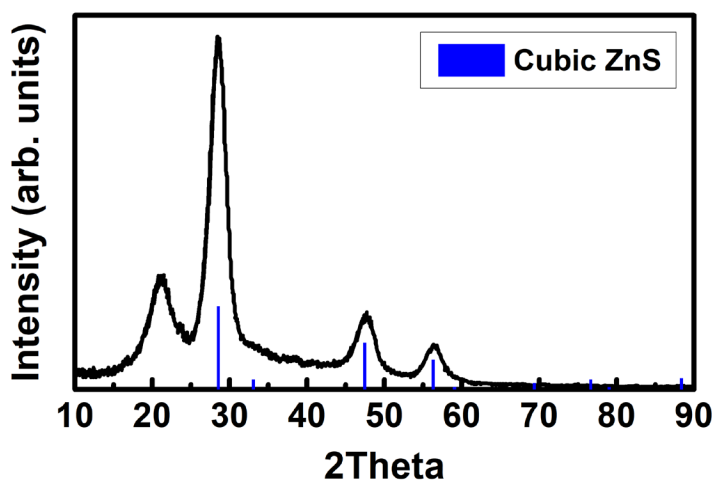


Figure C7. XRD Spectrum of ZnS nanocrystals, confirming a sphalerite, or cubic, crystal structure.

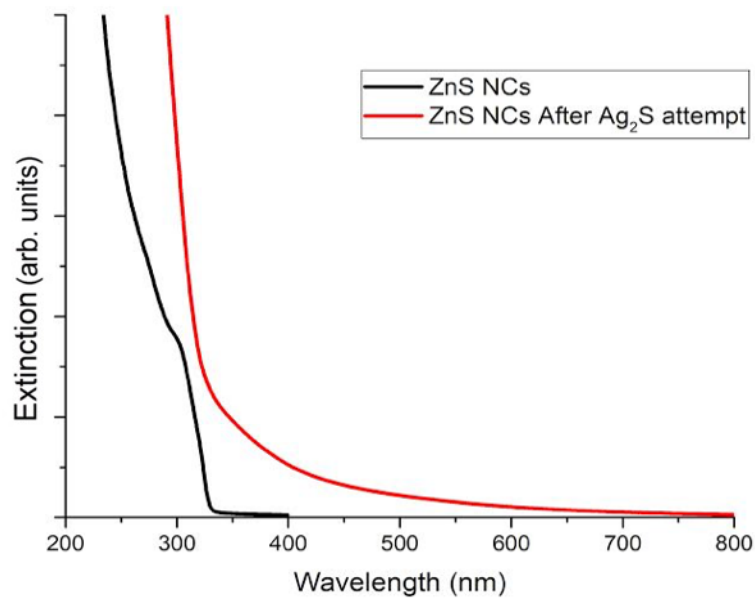


Figure C8. Extinction of ZnS Nanocrystals Before and After Ag<sub>2</sub>S Growth Attempt

### C3.2. Characterization of Hexagonal ZnSe

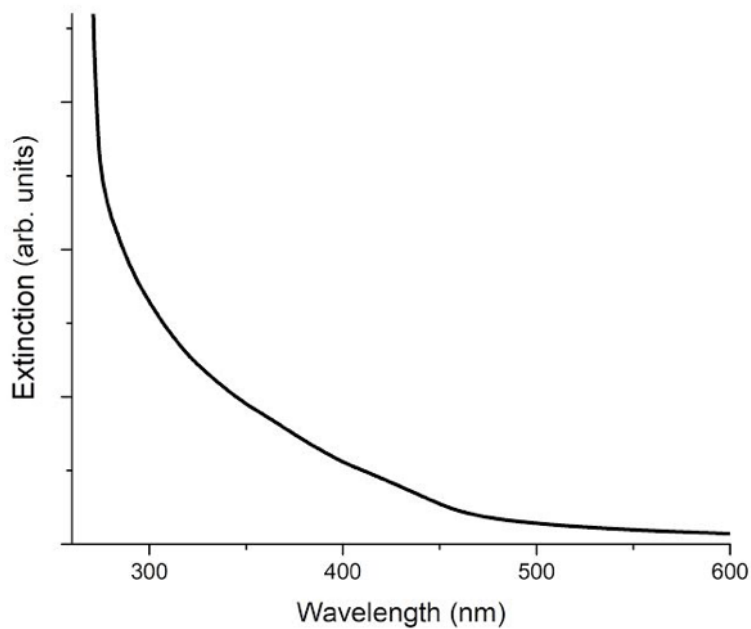


Figure C9. Extinction of Hexagonal ZnSe

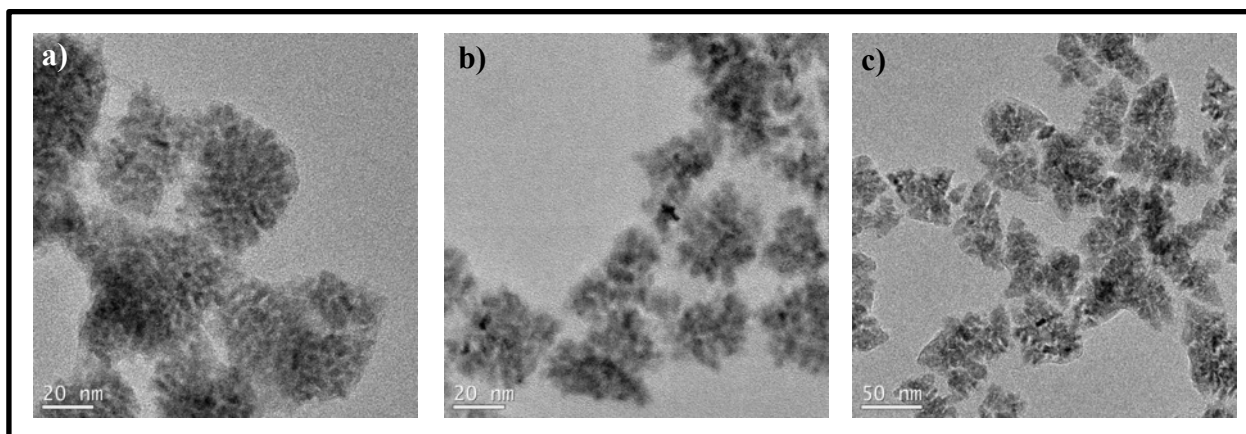


Figure C10. TEM images of hexagonal ZnSe aliquots (a) taken right after, (b) 4 minutes after, and (c) 25 minutes after an initial color change to yellow after the TOP:Se injection.

### C3.3. Characterization of ZnSe, ZnSe/ZnS, and ZnSe/ZnS/Ag<sub>2</sub>S Nanowires

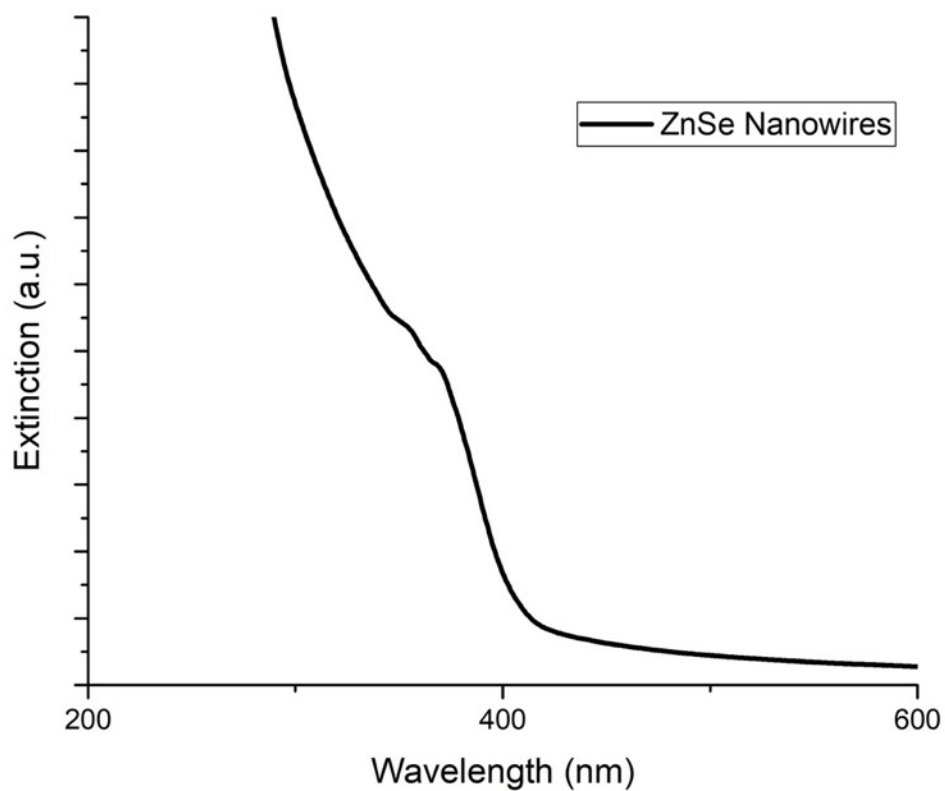


Figure C11. Extinction of ZnSe Nanowires

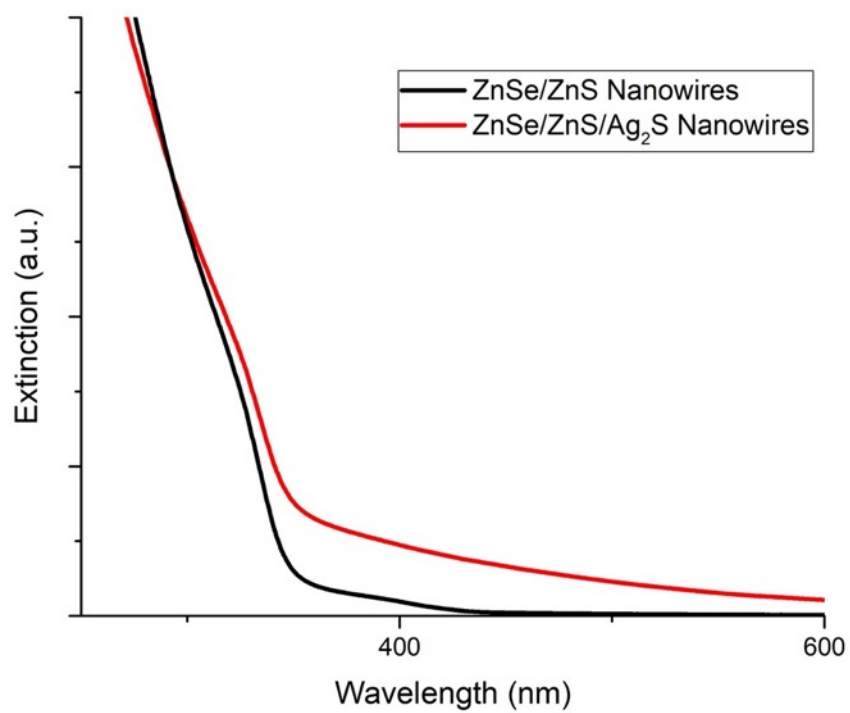


Figure C12. Extinction of ZnSe/ZnS and ZnSe/ZnS/Ag<sub>2</sub>S Nanowires

## **APPENDIX D. A DECADE WITH DYSS: LESSONS LEARNED AND LOOKING FORWARD**

Brittany P. Bishop and Cole A. DeForest. Reproduced with permission from Chemical Engineering Education, submitted for publication.

### **D1. Abstract**

Each summer over the past decade, the Chemical Engineering Department at the University of Washington has hosted the “Distinguished Young Scholars Seminar” (DYSS) series, bringing outstanding research trainees from top-tier programs around the country for day-long campus visits, each filled with student discussions, faculty meetings, mock interview questioning, and a research seminar. Here, we discuss the history and evolving structure of DYSS, highlighting prior successes and lessons learned, as well as opportunities for ongoing improvement.

### **D2. Background and Goals**

Ten years ago, graduate students in the Chemical Engineering Department at the University of Washington (UW) created the Distinguished Young Scholars Seminar (DYSS) series, held over the course of eight weeks each summer since 2011 to foster leadership and provide professional development opportunities to chemical engineers across the country. Though networking and communication is essential to long-term success in both academia and industry, these founding students recognized that the overwhelming majority of Chemical Engineering graduate programs in the United States – including those typically ranked in the top 50 – lacked formal department-level training in such skills.<sup>270,271</sup> Further, while many graduate students and postdoctoral researchers utilize seminars and colloquia to gain proficiency in authoring research abstracts and

delivering talks to a relatively broad audience, such conference presentations tend to be significantly shorter than what is expected during an interview or throughout employment. In hopes of better equipping up-and-coming chemical engineers for success on the job market and beyond through a uniquely valuable training experience, DYSS was born.

Since its inaugural offering, the DYSS program provides direct professional development to eight graduate and postdoc participants annually that have been competitively selected through a UW student-led evaluation panel and invited individually to Seattle for a day-long on-campus experience.

The three standing goals of DYSS have been to:

“1) simulate the day-long departmental visit associated with many interviews capped by a one-hour seminar talk given by rising stars in chemical engineering;

2) help our own graduate students at UW become aware of where they fit into the chemical engineering landscape; and

3) expose our own graduate students to the panel-style peer evaluation decision-making process that governs many funding decisions.”<sup>271</sup>

For the invited speakers, identified as emerging leaders in chemical engineering, DYSS provides an opportunity to cultivate skills necessary for future interview and career success, share their research orally with a chemical engineering audience with broad expertise, experience a mock interview firsthand, and receive informal feedback in a low-consequence environment that can help advance their next career stages. To accomplish the first goal and simulate the day-long departmental visit, each seminar speaker has individual meetings with our Chemical Engineering faculty to discuss their work and the job application process, engages in networking events with current graduate students and postdocs, and gains written and oral feedback on their seminar

presentation. Beyond opportunities for professional development, speakers are eligible to receive a \$500 cash prize awarded to the Best Speaker, as selected by our Chemical Engineering graduate students and postdocs. Overall, this process supports promising chemical engineers by providing a “practice run” with constructive feedback, which can strengthen upcoming applications and better prepare them for their future careers.

Within the UW Chemical Engineering Department, DYSS also provides our students and faculty a chance to learn about cutting-edge research through presentations from early-career professionals in topics beyond what they typically encounter. Furthermore, the program affords our departmental trainees a hands-on experience with an application evaluation process akin to that utilized by hiring and selection panels, as well as concrete examples of what successful student research presentations and applications look like. To achieve the second and third goals aimed within the department, DYSS is managed almost entirely by graduate students, with comparatively minor oversight provided by mentoring faculty. The primary management team consists of 3-4 graduate student teaching assistants (TAs), who work diligently to provide a seamless, guided visit for the seminar speakers. These TAs help advertise and solicit nominations for the program, collect applications and facilitate their evaluations, create and oversee each speaker’s travel and visit schedule, run and attend coffee and happy hours, and escort the speakers between meetings and around campus. Supporting these TAs each year is a team of 15-20 graduate students and postdocs volunteers that help evaluate applications as part of a National Science Foundation (NSF) grant review-style panel. All departmental graduate students and postdocs are invited to attend the seminar and provide written feedback, as well as to score each presentation to help decide which DYSS participant receives the “Best Speaker Award”. This translates to an educational experience

to current graduate students and postdocs, as well as promotes additional networking with up-and-coming chemical engineers from across the country.

In the subsequent sections of this article, we will take a deeper dive into the history and evolving structure of DYSS, highlighting prior successes and lessons learned over the past decade, as well as opportunities for future improvement.

### **D3. A Strong Start**

Over the past 10 years, 79 participants have been selected out of a total of 725 applicants. The selected DYSS speakers hail from 46 institutions spanning 17 of the 50 states, as well as Toronto, Canada. Of these prior participants, roughly 9% have been underrepresented minorities and 32% have been women, as seen in Figure D1. Through on-going efforts to select speakers that represent the entirety of our diverse field, the percentage of woman participants has increased from 0% in

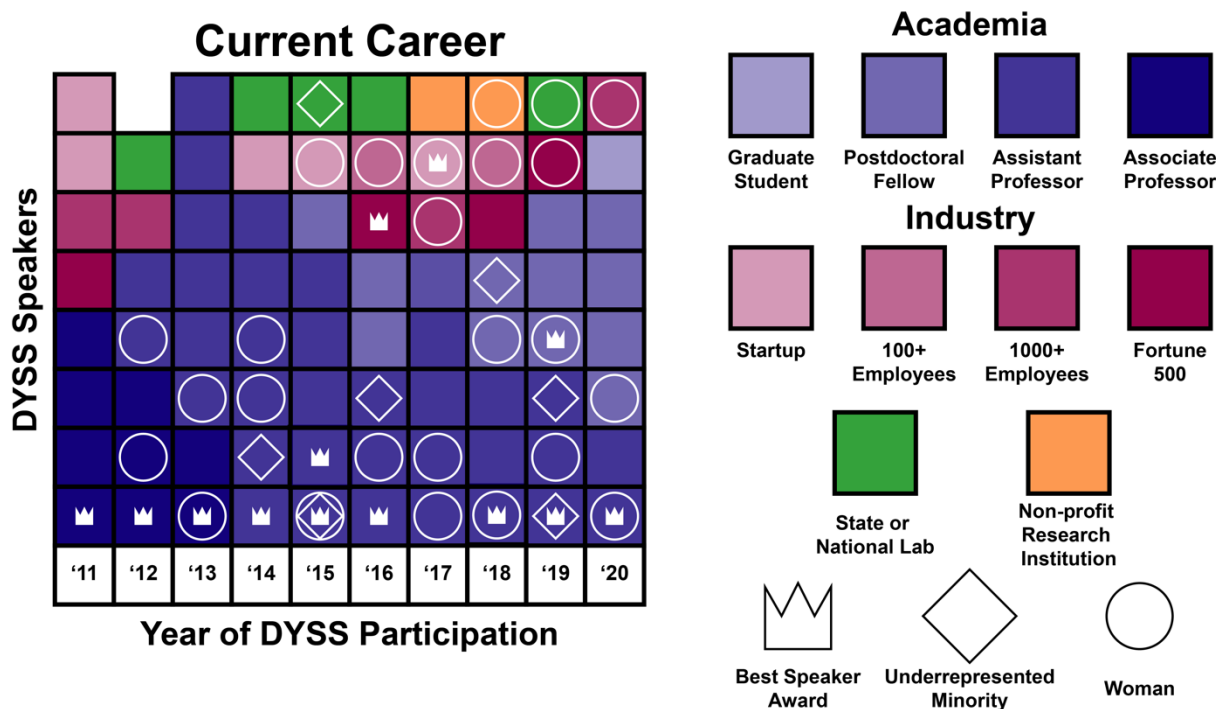


Figure D1. Current career stage of past DYSS presenters organized by the year they participated (data from June 2021).

2011 to an approximate level of 50% held steadily over the past 4 years. While the number of underrepresented minority speakers have also increased over the years, efforts to expand the program's overall diversity remain at the forefront of discussion.

In all cases, DYSS alumni have maintained an excellent professional trajectory (Figure D1). Approximately 75% of the 79 past DYSS seminar speakers have remained in academia. Half of the participants from DYSS's inaugural year have been promoted to the level of Associate Professor, and most other participants who remained in academia have begun their independent research careers as Assistant Professors (primarily in Chemical Engineering). Of the remaining participants, 18% have gone to industry, 6% work at state or national labs, and 2 people have taken positions at non-profit research institutions. Many of the past participants have continued to gain notoriety as leaders in Chemical Engineering, receiving major science and engineering honors including the NSF Presidential Early Career Award for Scientists and Engineers (PECASE), the NSF Faculty Early Career Development (CAREER) Award, Young Investigator Awards from the American Institute of Chemical Engineers (AIChE) and the American Chemical Society (ACS), and recognition as Forbes "30 under 30" honorees.

Based on surveys of past participants, DYSS seminar speakers have universally found participation in the series to be positive and that the skills honed would aid in their job search process. In addition, many participants had not previously prepared or delivered an hour-long research presentation, so this program afforded new and valuable experience. Major benefits and positive feedback of the program according to the speakers include:

- 1) "Presenting the seminar and interacting with various graduate students was an important reminder of the breadth of research pursued by chemical engineers. This is something I had forgotten after several years of specialized work. The seminar impressed in me the

need to present information for a much broader audience than typically encountered at meetings and conferences.” – 2011 Seminar Speaker

- 2) “My entire experience was nothing but positive, so I only have positive feedback to give. The opportunity to experience a “test run” of the day-long visits required for most faculty interviews was extremely insightful, and I learned tremendous amounts through the candid discussions I had with professors about (i) what they look for in candidates while on the UW search committee and (ii) their own experiences while applying as candidates themselves. It was also a real pleasure to interact and learn about all the exciting research going on through the graduate students in your department. It was my first visit to the Seattle, but this experience alone was enough to guarantee that I'll be applying to UW when I do put in my faculty applications in the coming time.” – 2015 Seminar Speaker
- 3) “It's a great platform for people who are applying for faculty positions. It gives us a chance to have a mock presentation and department visit experience. The best thing was getting honest feedback from the graduate students as well as the faculty members. One on one meetings with the faculty members were extremely helpful. It's amazing to see how the UW chemical engineering department is putting [in] so much [effort] and trying so hard to help people who are looking for jobs in academia.” – 2017 Seminar Speaker
- 4) “I anticipate that the DYSS experience will be incredibly helpful for my job search process. The faculty search process is a black box, and DYSS shined some much-needed light on the process, clarifying both details of the application itself and the goals of a hiring department. Going through the experience of interviewing and the associated rigors of meeting with professors and students working in very different backgrounds was invaluable. In particular, practicing my research pitch and honing it for individuals with

different backgrounds was a useful skill to gain in the setting of an interview. Similarly, comments that I received from faculty and students were constructive, and I've already found myself adding their suggestions into both everyday presentations and into the faculty applications.” – 2019 Seminar Speaker

Though we have been exceedingly happy with the program’s outcomes to date, we continue to learn each and every year on how to improve the DYSS experience. Based on feedback from our DYSS speakers, the greatest areas that needed focus include:

- 1) More diverse and targeted advertisement of the DYSS program
- 2) Early communication on the speakers’ schedule for advanced preparation
- 3) Significant time with professors for advice and feedback on faculty applications
- 4) Sufficient discussion and networking time with department graduate students and postdocs
- 5) Expanded feedback on their research presentations from both faculty and graduate students

Catalyzed by these suggestions, we have worked diligently over the last 10 years to modify the DYSS application, the evaluation methods utilized in selecting participants and awarding speaker prizes, and the overall program structure to improve the series and maximize the success of the program’s three major goals.

#### **D4. Application Solicitation and Review**

A major component of DYSS is the initial application solicitation and review conducted by the UW Chemical Engineering graduate student volunteers. Over the years, we have purposely expanded application solicitation to reach a broader community and more diverse groups of scientists, bringing application numbers each from the several tens to over 100. In DYSS’

inaugural offering, advertising was done exclusively at the department level, emailing department Chairs at top-tier Chemical Engineering programs directly. As the years have progressed, we have expanded our advertising efforts to include past DYSS applicants and previously selected participants, presenters of the AIChE “Meet the Faculty” poster session, as well as over 200 student organizations – including many diversity-focused groups in science, technology, engineering, and mathematics (STEM) – from the top 40 Chemical Engineering graduate programs. More recently, social media platforms including Twitter have proven useful in furthering awareness and extending engagement (Figure D2). Collectively, the expansion of advertising, along with word of mouth, has become a critical tool for increased application numbers and promotion of DYSS.



Figure D2. Twitter advertisement for DYSS in April 2020.

The application itself consists of several components, including a one-page research abstract, a three-page curriculum vitae, and an applicant-blind letter of support (most typically from a direct research advisor). In 2019, a 300-word “Statement of Interest” was added to the application

materials to help reviewers gauge the personal goals and backgrounds of each of the DYSS applicants.

All applications are reviewed by current Chemical Engineering graduate student and postdoc volunteers at the UW, and all participants are selected following full committee discussion. Prior to providing panelists the application materials for review, all reviewers are required to participate in a two-hour anti-bias training session that includes videos, case-studies about common biases in academia, and group discussions about how to combat biases in the DYSS evaluation process. This training has covered many aspects of cognitive bias, including cultural, implicit, explicit, and confirmation bias, factors that often plague professional evaluation panels.<sup>272-274</sup> Furthermore, the required training brings into the limelight focused discussions on diversity, equity, and inclusion (DEI). Almost exclusively, these trainings have been run by Dr. Joyce Yen from the University of Washington ADVANCE Center for Institutional Change, self-described as a “campus and national resource for effective practices in academic leadership development, cultural and policy change, and the advancement of women faculty in STEM”.<sup>275,276</sup> In years in which scheduling conflicts have prevented Dr. Yen from facilitating discussion, the DYSS TAs have managed their own training using publicly available materials from other universities including: the University of California-Los Angeles’ “Implicit Bias Video Series”, The University of Arizona’s tips for “Avoiding Gender Bias in Reference Writing,” and “Consciously Combating Unconscious Bias” by Dr. Maggie Kuo.<sup>277-279</sup> Despite an increase in anti-bias trainings across the country, there is still conflicting opinions and limited evidence on the effectiveness of these programs.<sup>280-282</sup> In particular, a 2016 study assessing 40 years of diversity training showed that diversity and implicit bias training only have short term impact,<sup>283</sup> while a report from the Equality and Human Rights Commission indicated that unconscious bias training

can reduce implicit bias but is unlikely to eliminate it.<sup>282</sup> Other studies also indicate that consciously trying to avoid implicit biases can make people project their biases by overcompensating or overthinking the very biases they are trying to correct.<sup>284,285</sup> However, complementary to anti-bias training, evidence has shown that specific rubrics with well-defined evaluation criterion reduces racial bias in teachers when grading student's assignments.<sup>286</sup> Consistent with these reports, we have observed that anti-bias training shortly before the review process and well-defined evaluation rubrics sets important guidelines for reviewers in order to remain as impartial as possible when reviewing and discussing applications.

Over the years, the actual application review process has evolved based on feedback from the graduate student and postdoc reviewers within our department and morphed to capture different evaluation metrics. Early stages of the rubric were based on similar guidelines used for the selection of NSF Graduate Research Fellowship Program and consisted of very clear guidelines for review; specific points for what is included in the abstract, CV, and letter of recommendation items were established to assist the students in review.<sup>271</sup> The rubric also included sections based around "Communication", "Scholarship," and "Achievement." At these early stages, the rubric focused primarily on past research and academic achievements. Tied scoring between top-tier candidates were then broken weighting diversity representation (both in speaker identity and research areas), TA and speaking awards, and research productivity taking into consideration their school and supervisor.

As the years continued, prior experience and recognition of excellence in presenting, teaching, writing, entrepreneurship, and outreach were added as evaluation metrics to the rubric. From 2015 to 2018, a new approach was taken, with fewer rubric items and more general questions for each document in the application package (Figure D3). An additional section of the rubric was also added to include hard-to-quantify factors, such as excellence in mentoring, dedication to service, and interesting side projects. While this allowed the application to be viewed through a broader lens, many student reviewers felt as though the rubric needed to have clearer criteria to reduce subjectivity and potential bias. To help provide more clear guidelines in 2019, the rubric reverted back to a similar format as the earlier years of DYSS, but with

Category	Explanation	Sums
<b>Communication</b>		
Abstract: 1 – 5 pts	Reflection of how well the abstract reads from sentence to sentence, and also how well structured it is as an entity.	
CV: 1 – 3 pts	Items that indicate communication prowess (awards, presentations, etc.)	
L.o.R.: 1 – 2 pts	Indicates communication or presentation prowess	
<b>Scholarship</b>		
Abstract: 1 – 2 pts	Is it remotely interesting research?	
CV: 1 – 5 pts	1 <sup>st</sup> author papers and patents only (Requires knowledge of field publication rate, paper length, time in academia, journal impact*)	
L.o.R.: 1 – 3 pts	Is applicant a source of ideas and inspiration for their work, or something to that effect	
<b>Other</b>		
All Parts: 1 – 5 pts total	Hard to quantify factors: mentoring, service, 2 <sup>nd</sup> author papers, interesting side projects, wizardry	
		/25
Please score each application using the following rubric as a guideline. Do NOT give fractional scores. This is an imperfect process in every facet, but this will aide us in selecting qualified and interesting young scholars for the seminar series.		
* Impact factor of journals is far from perfect as an evaluation metric, but it is the best one we have.		

Figure D3. DYSS application rubric for 2015-2018.

Category	Application Item	Excellent (5)	Good (3)	Fair (1)	Score (1-5)
<p><b>Communication</b></p> <p>One of the most important skills for any successful researcher is the ability to communicate. Rate the application based on how well it shows the applicant is able to communicate. Look for presentations, talks, teaching experiences in the CV and the quality of the submitted abstract. Does the letter of recommendation mention anything special about the applicants presentation skills? Try to rate the applicant in this section based on how good of a presentation you would expect them to give if they were invited.</p>	<u>CV (4x)</u>	<ul style="list-style-type: none"> <li>- Has many presentations at different national conferences</li> <li>- Has invited talks</li> <li>- Has teaching awards</li> </ul>	<ul style="list-style-type: none"> <li>- Has presented at national conferences</li> <li>- Has teaching experience</li> </ul>	<ul style="list-style-type: none"> <li>- Has presented at at least one conferences.</li> <li>- Mentions mentoring undergraduate researchers</li> </ul>	
	<u>Letter of Rec (2x)</u>	<ul style="list-style-type: none"> <li>- Recommender praises applicant for clarity in presentations, giving specific examples</li> <li>- Recommender praises applicant as a teacher, giving examples of applicants mentorship</li> </ul>	<ul style="list-style-type: none"> <li>-Recommender mentions applicant's presentation ability.</li> <li>-Recommender mentions applicant's teaching ability</li> </ul>	<ul style="list-style-type: none"> <li>- Recommender mentions applicant's presentation experiences</li> <li>- Recommender mentions student as a teacher or mentor in lab</li> </ul>	
	<u>Abstract (5x)</u>	<ul style="list-style-type: none"> <li>- Abstract is excellently written and leaves you wanting to know more</li> <li>- Abstract is clear and easy to follow even for someone not in the field</li> </ul>	<ul style="list-style-type: none"> <li>- Abstract is well written and contains no significant spelling or grammar errors</li> <li>- Abstract is easy to follow, but a nonexpert may need to read it more than once to understand it</li> </ul>	<ul style="list-style-type: none"> <li>- Abstract is well written but contains some errors</li> <li>- Abstract is difficult to understand for someone not in the field.</li> </ul>	
	<u>Statement of Interest (2x)</u>	<ul style="list-style-type: none"> <li>-Clearly expressed an interest in sharing their accomplishments</li> <li>-Has a clear demonstration of their future career goals and potential impact</li> </ul>	<ul style="list-style-type: none"> <li>-Articulates goals, but does not have a strong sense of direction</li> <li>-Shows a future path to where they want to go, but doesn't express how DYSS helps them get there</li> </ul>	<ul style="list-style-type: none"> <li>-Does not articulate strong goals or a sense of direction</li> <li>-Does not express any future goals or how DYSS helps them get there</li> </ul>	
<p><b>Scholarship</b></p> <p>Scholastic achievements are a measure of the impact the applicant has had so far in their career. Primarily this comes about through published papers. How many first author papers has the applicant written? Are they in high impact journals? Have they been cited? Is their research topic significant and of broad interest? Do they have any patents? Try to rate the applicant in this section based on the quality of their research while keeping in mind the field they are in and the point in their career they are at (postdoc in computation will have more publications than a graduate student in bio).</p>	<u>CV (5x)</u>	<ul style="list-style-type: none"> <li>- Has a papers published in a variety of high impact journals</li> <li>- Papers have been cited numerous times</li> </ul>	<ul style="list-style-type: none"> <li>- Has at least one paper published in a high impact journal</li> <li>- Has numerous papers in a variety of journals</li> <li>- Papers have been cited a few times</li> </ul>	<ul style="list-style-type: none"> <li>- Has few first author papers</li> <li>- Majority of papers are published in a single journal</li> </ul>	
	<u>Letter of Rec (3x)</u>	<ul style="list-style-type: none"> <li>- Recommender praises applicant as a researcher and highlights their ability to come up with novel ideas</li> </ul>	<ul style="list-style-type: none"> <li>- Recommender highlights the applicant's research talents in solving problems</li> </ul>	<ul style="list-style-type: none"> <li>- Recommender praises applicant's technical abilities</li> </ul>	
	<u>Abstract (3x)</u>	<ul style="list-style-type: none"> <li>- Abstract communicates the importance of the research which has been done</li> <li>- Abstract show cases its broad impacts on the scientific community</li> </ul>	<ul style="list-style-type: none"> <li>- Abstract cites appropriate literature to show its place in the bigger research picture</li> <li>- Abstract shows the impact it has had and mentions future research directions</li> </ul>	<ul style="list-style-type: none"> <li>- Abstract highlights the important conclusions from the work done</li> <li>- Abstract shows its impact within its own specialty</li> </ul>	
	<u>Statement of Interest (2x)</u>	<ul style="list-style-type: none"> <li>- Has a clear idea of what they hope to gain through the DYSS program</li> <li>- Shows interest in sharing their expertise and gaining the skills to become a strong leader in the field</li> </ul>	<ul style="list-style-type: none"> <li>- Has a clear desire to gain skills, but does not express how DYSS will help them achieve their goals</li> </ul>	<ul style="list-style-type: none"> <li>-Does not express how DYSS will benefit them or provide skills to help achieve a goal</li> </ul>	
<p><b>Achievement</b></p> <p>What impact has the applicant had so far? How have they been recognized for their success? Do they show a commitment to the broader scientific and chemical engineering community Look for awards, outreach, and service and recognition to the broader community. Try to rate the applicant in this section based on their success outside of publishing papers.</p>	<u>CV (3x)</u>	<ul style="list-style-type: none"> <li>- Has won awards for presenting, teaching, writing, entrepreneurship, etc.</li> <li>- Has outreach activities on CV not directly related to their research.</li> <li>- Shows leadership</li> </ul>	<ul style="list-style-type: none"> <li>- Has won some awards for presenting, teaching, writing, entrepreneurship, etc.</li> <li>- Has many outreach activities on CV.</li> <li>- Is actively involved in scientific societies or other science-related extracurriculars</li> </ul>	<ul style="list-style-type: none"> <li>- Has few outreach activities on CV not directly related to their research</li> <li>- Does not participate in any science-related extracurriculars</li> <li>- Has no awards in their field</li> </ul>	
	<u>Letter of Rec (3x)</u>	<ul style="list-style-type: none"> <li>- Recommender praises the applicant's work ethic and leadership abilities</li> <li>- Recommender highlights extracurricular activities of applicant</li> </ul>	<ul style="list-style-type: none"> <li>- Recommender praises the applicant's work ethic and self motivation</li> </ul>	<ul style="list-style-type: none"> <li>- Recommender praises the applicant's work ethic and ability to succeed</li> </ul>	
	<u>Abstract (3x)</u>	<ul style="list-style-type: none"> <li>- Abstract demonstrates clear knowledge of their field and/or a novel approach to a broader impact topic</li> <li>-Abstract presents clear and exciting results, with data or figures to back up their research</li> </ul>	<ul style="list-style-type: none"> <li>- Abstract demonstrates a moderate knowledge of their field and/or has a relatively low impact on their field</li> <li>-Abstract does not back up their claims with substantial evidence or data</li> </ul>	<ul style="list-style-type: none"> <li>-Abstract mentions no papers or citations or clear understanding of the literature/impact</li> </ul>	

Figure D4. DYSS application rubric from 2019, a modified version of rubrics from 2011-2014.

expanded criteria to include extracurriculars, outreach, and other leadership activities (Figure D4). In 2020, an additional evaluation criterion was added to assess areas considered to be unique and “outside of the box”. While these aspects are important, reviewers again felt as though the lack of clear guidelines and criteria for this section allowed for personal bias. Another critique of this rubric was that many review criteria were repetitive between the three overarching categories, over-weighting certain application materials over others. Overall, we have learned through graduate student feedback that the best rubrics provide clear criteria for reviewers to follow, with specific points designated for different qualifications. Implementing this criterion is necessary both to streamline the reviewing process and minimize bias as best as possible. Including a broad spectrum of criterion, such as mentoring, teaching, outreach, and other extracurricular activities, also creates a more unique and diverse set of speakers for the seminar series.

With ~100 applications typically submitted in each recent year, fair evaluation of all proposals presents a substantial lift. For the panel-style review process, a team of 15-20 graduate students and postdoc volunteers within the department to read and evaluate submitted applications is assembled with the help of student/faculty listserv mailings and directed contact (email and in person). During the first few years of DYSS, reviewers could be assigned either a “primary” or “secondary” role on any number of proposals. Each application had a primary reviewer in the research field that led the conversation, as well as two secondary reviewers. Before the review panel, each application was evaluated following the rubric by the three assigned reviewers and average scores were assigned to each DYSS applicant. The overall process of the NSF-style panel included discussing the top 5-10% of applicants based on the given scores and deciding the first 4 seminar speakers based on the feedback. Next, the remaining top 20% of applicants were discussed and voted on by the entire group of reviewers to choose the remaining 4 seminar speakers.

In hopes of capturing the breadth of research spanning the field of chemical engineering, after a few years applications were separated into 5-6 broader categories that reviewers were assigned to evaluate based on their research expertise. Example topical categories include Biomaterial Applications, Computational & Simulations within Energy, Protein Design, Electrochemistry and Batteries, and Nanomaterials Design. Categories are adjusted annually to reflect the trends in focus of submitted applications. The review panel for these years were similar, except that a top researcher from each category was chosen to be a DYSS participant by the reviewers who evaluated that section. With 8 speakers each year and 5-6 identified as the top performer in their category, the remaining 2-3 speakers were identified through full panel review and discussion. Though year-to-year consistency helps ensure a smooth operation overall, we have observed that the reviewing process needs to remain somewhat flexible to accommodate the variation in research breakdown of applicants and the number of graduate students/postdocs on the review panel. The main aspects of the process that has remained consistent and successful has been dividing applicants into separate categories for grading by several reviewers in that general field and group discussion of all top candidates.

#### **D5. Experience and Evaluation**

Upon completing the review process, the eight DYSS seminar speakers are invited to Seattle during UW's summer quarter for a tailored individual visit meant to mimic important aspects of academic and industrial job interviews. On Mondays between June and August, a selected speaker travels to the University of Washington for a day of professional development and networking. The overall day-long experience has remained relatively consistent over the past decade, with the visit consisting of meetings with faculty and research groups with a break for

lunch, followed by the hour-long seminar, an hour-long happy hour with snacks and drinks, and finally a dinner with faculty and graduate students. In 2018, a 30-minute coffee chat was introduced in the mid-morning to create more time for graduate students to interact and talk with the seminar speaker. An example of a typical schedule from 2019 can be seen in Figure D5. In 2020, we designated a block in each speaker's schedule to meet with a member of our faculty's search committee. Since these faculty members have the perspective of both an applicant and a reviewer, this time allows DYSS participants to hear constructive feedback and guidance about the faculty application and interview process, which should strengthen their application packages as they transition into their future careers. These schedules are arranged at the beginning of summer and sent out to the DYSS speakers as early as possible, no later than one week ahead of their visit.

9:00 AM		TA pick up at Hotel after breakfast on your own	
9:00 — 9:25	BNS 257	<b>Faculty or Graduate Student Meeting</b>	<i>TA escort to Foege</i>
9:30 — 9:50	Foege N330B	<b>Faculty or Graduate Student Meeting</b>	<i>TA escort to BNS</i>
10:00 — 10:25	BNS 363	<b>Faculty or Graduate Student Meeting</b>	<i>TA escort to Lobby</i>
10:30 — 10:55	Benson Lobby	Coffee Break & Chat with ChemE Graduate Students	<i>TA escort to BNS</i>
11:00 — 11:25	BNS 259	<b>Faculty or Graduate Student Meeting</b>	<i>TA escort to BNS 353</i>
11:30 — 11:55	BNS 353	<b>Faculty or Graduate Student Meeting</b>	<i>TA escort to Lobby</i>
12:00 — 1:30		Lunch at nearby restaurant	<i>TA escort to BNS B45</i>
1:30 — 1:55	BNS B45	<b>Faculty or Graduate Student Meeting</b>	<i>TA escort to Benjamin Hall</i>
2:15 — 2:40	Benjamin Hall	<b>Faculty or Graduate Student Meeting</b>	<i>TA escort to BNS 219</i>
3:00 — 3:25	BNS 219	<b>Faculty or Graduate Student Meeting</b>	<i>TA escort to PAA 118 Lobby</i>
3:30 — 4:00	PAA 118 Lobby	Reception	
4:00 — 5:00	PAA 118	<b>Seminar</b>	
5:00 — 6:30	Benson Patio	Happy hour with graduate students	
6:00 PM		<b>Dinner</b> with graduate students	

Figure D5. Example DYSS schedule, shown from 2019.

To further incentivize UW trainee attendance of the seminar, a pre-seminar coffee hour and post-seminar happy hour were included in each weekly schedule. Additionally, a raffle was established, in which a completed speaker evaluation form was counted as an entry. The raffle

consists of a small prize (e.g., gift card to local coffee shop) for one attendee of each week, and larger 1st through 3rd place prizes (e.g., Amazon gift card) at the middle and end of the summer. A bonus raffle entry was given for people who attended all 8 seminars. The raffle approach helped boost attendance, as well as provided a useful conduit for UW students to share feedback with DYSS presenters on strengths and weaknesses of their research seminar.

For most of DYSS's history, evaluation of the seminars remained simple, where both the speaker and the content were ranked from 1-5 (low-to-high). In 2019, we introduced a scoring sheet that included 11 questions. Example questions evaluated the speaker's delivery, enthusiasm, organization, visualization, and presentation content. All questions were as "Good", "Very Good", or "Excellent," which corresponded to scores of 1, 3, and 5. The challenge with both of these scoring methods was that the scoring range was too small, such that speaker scores were often compressed to the point where it was difficult to statistically differentiate from one another. In addition, for the first nine years, all scoring remained anonymous, which makes it difficult to account for different average criticality of our student reviewers. In hopes of improving on this process, the scoring sheet was changed in 2020 in several ways (Figure D6). First, we reduced the evaluation to include just five criteria (i.e., communication/delivery, visual representation, research impact, depth of content, enthusiasm). In addition, the scoring range for each question was expanded to 1-8 with the corresponding associations: Does Not Meet Criteria (1), Could Use Improvement (2-3), Meets Expectations (4-5), Exceeds Expectations (6-7), and WOW! (8). Finally, we removed the anonymity of the scoring so that scores from a single reviewer could be normalized throughout the entirety of the summer following a Z-score. Specifically, the overall averages and standard deviations were determined for each reviewer, and a Z-score was subsequently calculated for each seminar that they attended, as seen in Equation D.1:

$$z_i = \frac{x_i - \bar{x}}{\sigma} \quad (\text{D.1})$$

where  $z_i$  and  $x_i$  are the reviewer's Z-score and overall average weekly score for a DYSS speaker, respectively, and  $\bar{x}$  and  $\sigma$  are the reviewer's score average and standard deviation across multiple seminars, respectively. All values shown are calculated for each reviewer that attended multiple seminars.

Are you a (circle one):										ChemE Graduate Student	Postdoc	Undergrad	Faculty	Other
Disclosure: All your scores will be Z-scored throughout the summer, so please use a full dynamic range of the scoring scale														
	Please circle a single number score for each category	Does Not Meet Criteria (1)	Could Use Improvement (2-3)	Meets Expectations (4-5)	Exceeds Expectations (6-7)	WOW! (8)								
1	The talk was communicated and delivered clearly, as well as understandable to a broad audience.	1	2	3	4	5	6	7	8					
2	How was the visual presentation of the speaker's work in terms of slides, data, and graphics?	1	2	3	4	5	6	7	8					
3	How impactful is their research?	1	2	3	4	5	6	7	8					
4	How was the depth of content?	1	2	3	4	5	6	7	8					
5	Was the speaker enthusiastic and did they maintain your interest?	1	2	3	4	5	6	7	8					
6	Not Scored: (for our data) Was the topic of this talk in your general field?				Yes	No								
Additional Comments:										Full Name: (Please print clearly)		Speaker Name: (Please print clearly)		

Figure D6. DYSS speaker scoring sheet from 2020.

Stemming from the expanded scoring range and examining average Z-scores for each seminar speaker, we were able to more easily differentiate relative scores between participants and to identify the "Best Speaker Award" recipient. This ultimate winner of DYSS, as determined by these normalized graduate student and postdoc Z-scores, receives a \$500 cash prize. The DYSS winner is also advertised on the website and on mailings to various departments as recognition of their excellence. In cases in which the winning score is statistically indistinguishable between several participants, this honor and prize is shared by several speakers (as occurred in 2016 and 2019). Creating a scoring system that successfully and succinctly evaluates all aspects of a

speaker's presentation and can be utilized to statistically differentiate speakers' scores has proven critical for accurate determination of the DYSS winner.

In addition to numerical scores, all DYSS scoring sheets have a section for additional written feedback that are anonymously forwarded to the speaker. Students, postdocs, and faculty have consistently filled out this section, which assists the speaker in improving their oral and visual communication skills. Additionally, DYSS speakers also spend time during the post-seminar happy hours talking with UW researchers who provide in-person suggestions on how to improve their seminars and future application packages. Based on DYSS speaker feedback, these comments and discussions have been incredibly useful for refining the speakers' presentations for future audiences.

#### **D6. The Digital Transition in the COVID era**

Due to COVID-19, and under threat of missing out on our milestone tenth year of DYSS, we made the decision to make the 2020 DYSS series virtual. All aspects of DYSS were conducted online and run through Zoom, including the anti-bias training, NSF-style panel, faculty meetings with the speakers, the seminar, and the happy hour. All meals were cancelled; we instead allotted a lunch break in the middle of the day.

While the virtual setting did not significantly change the anti-bias training, the introduction of Zoom for the review panel provided a large number of advantages. Based on previous critique, reviewers within the same topic wanted more time to discuss their top choices before engaging with the entire group. Zoom's Breakout Room platform proved very effective for accomplishing this, since we could easily split each topic's reviewers into rooms, while a head TA moved between groups to facilitate discussion and answer any questions. After 30 minutes, we reconvened and immediately had six speakers chosen, with one candidate per review category. To decide the last

two speakers, each topic group presented their second candidate, which were then discussed and voted on by the entire group.

The virtual format imposed the largest changes to the DYSS experience during the seminar speaker's visit. To best accommodate speakers spanning all US time zones while affording giving scheduling consistency, as well as to stave off "Zoom fatigue",<sup>287,288</sup> the DYSS day was shortened from its typical 9 am – 8 pm schedule to 9 am – 3:30 pm (all times given in PDT) through removal of the graduate student coffee hour and dinner. In addition, the seminar and accompanying happy hour were moved up from 4 – 6 pm to 1 – 3 pm to best accommodate speakers presenting from the east coast. The schedule consisted of meetings with faculty and research groups from 9:30 am – 12 pm, a lunch break with no meetings from 12 – 1 pm, the seminar from 1 – 2 pm, and a networking/happy hour from 2 – 3 pm. To keep this schedule running smoothly, only two Zoom rooms were utilized (i.e., one for the morning and one for the afternoon) that were both controlled by the DYSS TAs.

Within this schedule, the Zoom platform worked very well for the morning faculty meetings. In typical years, a TA has to escort the speaker across campus to meet with faculty in different buildings. In the Zoom environment, the time for in-person travel could be replaced with longer meetings with faculty and/or scheduled down time. In addition, a single Zoom room was utilized for the entire morning to facilitate smooth transitions between meetings. After introducing the seminar speaker and the faculty member, the TA would leave to allow for a private discussion between the two. After 25 minutes (i.e., 5 minutes before the next meeting), the TA would log back into the Zoom room to note the meeting's end and help transition to the next.

Though the 2020 DYSS took place near the start of the COVID-19 pandemic without much precedent, the seminar itself was run in a manner that is now standard for virtual meetings held

over Zoom. To prevent “Zoom bombing”, the seminar link was not shared publicly and was only disseminated amongst UW departments and the DYSS speakers.<sup>289</sup> Five minutes before the seminar, a TA would meet the speaker in the second Zoom room to help ensure correctly configured screen sharing capabilities for the presentation. At the beginning of the seminar, one of the TAs would introduce the speaker and read their biography, which typically included their education, research focus, awards, and broader impacts. Throughout the seminar, the TA would moderate the Q&A session at the end by calling on people who used the “raise hand” feature or by reading questions posted in the chat window. A raffle was also used to incentivize attendance, except all prizes were gift certificates that were purchased and could be used online (e.g., Amazon). Regardless of the raffle, the Zoom platform seemed to enhance overall seminar attendance, likely since Zoom presents a quick and accessible way to participate in seminar and can be viewed from any setting. The virtual platform also helped maintain high attendance throughout the Summer, though average attendee engagement (as indicated by questions and those remaining afterwards to discuss) appeared to decrease.

One of the biggest challenges of the 2020 DYSS was how to replicate a meaningful happy hour/networking session in the virtual setting. We found it difficult to motivate graduate students to participate without the usual incentive of food and beverage, which unfortunately often led to comparatively low attendance for these sessions. A future alternative is to schedule 20–30-minute meetings after the seminar between the DYSS speaker and graduate students from research groups in the speaker’s field. In addition, we expect it would be valuable to formally schedule a time block after the seminar for the speaker to meet with faculty and get feedback on their presentation. Creating a more set schedule after the seminar will allow the speaker to get more personal time with graduate students, as well as a time for constructive feedback on their research talks.

Another major challenge of running DYSS virtually lies in an inability to replicate the in-person experience of visiting the University of Washington. While there is really no way to perfectly replicate an in-person visit to Seattle purely online, we felt it essential that we still attempt to provide the speakers a way to learn about the culture of the city. Towards this, we created and mailed gift packages to presenter homes after their seminars that included UW-branded supplies and a cultural atlas focused on infographic visuals about Seattle and Washington State. Participants uniformly expressed thankfulness over these efforts, though all recognized that these were an imperfect substitute for a conventional visit.

Overall, a virtual seminar has both significant advantages and disadvantages to the DYSS experience. Moving forward, attempts to combine both in-person and virtual aspects to maximize the advantages of both formats could greatly elevate DYSS for both the speakers and the members of our department.

### **D7. Looking Forward**

As we plan for future years of DYSS, many aspects of the program will continue to morph to better meet our three goals, improve inclusivity of the program, and reduce bias from the review and evaluation processes. Areas of improvement will be primary focused on the application and rubrics.

For application solicitation, we plan to forward the call for DYSS submissions to more schools and student organizations extending beyond the top 40-ranked chemical engineering programs. In particular, we will send emails to more colleges and universities, included Historically Black Colleges and Universities (HBCUs), more diversity-focused student organizations, and science and engineering departments outside of chemical engineering. Based on NSF ADVANCE programs, this targeted outreach is important since diversifying candidate

pools typically results in more diverse hiring outcomes, which can be achieved through reformed recruitment practices and proactive pursuit of talented and diverse applicants.<sup>290</sup>

To better account for excellence stemming from a variety of areas and different backgrounds, the application rubric will also be redefined to include more unique areas of interest. To replace the general points section for unique and “out-of-the-box” experiences, the rubric will be broadened to include new measures of success, including patents, database development, software packages, open-source software, science communication, and tangible efforts to promote DEI. Furthermore, by removing ill-defined metrics (e.g., “other”, “out-of-the-box”) and instead assessing these unique experiences through specific rubric items, the application review process should be more objective and less biased.<sup>291,292</sup>

In addition to broadened rubric criteria, we have made plans to add a diversity statement to the application package. Alongside the critical goal of promoting DEI in the application and review process, this addition will provide applicants an opportunity to practice writing such a statement, which is now increasingly required as part of faculty application packages. Review criteria for this statement will be shaped by current evaluation standards and benchmarks of diversity statements at the university level.

Moving forward, the rubric will also be broken up into the individual application components, rather than by communication, scholarship, and achievement, in order to reduce repetition during application evaluation. The rubric will be divided by abstract, letter of recommendation, CV, statement of interest, and diversity statement, with aspects of communication, scholarship, achievement, and uniqueness woven into the evaluation criteria. Combining all of these changes to the application and review process should create a better-defined rubric, remove overemphasis

on certain criteria, and expand the definitions of success, which should reduce bias and improve diversity within the program.

Finally, changes will be made to the day-of visit in order to maximize feedback to the DYSS speakers, improve graduate student networking, and make the meetings and seminars more accessible through digital integration. As DYSS continues, improvements will regularly be applied throughout the entirety of the program. From application solicitation to the seminar visit, modifications will continue to be made to achieve a better professional development experience for all. We expect DYSS to remain a pillar experience of Chemical Engineering, both for our department and the field as a whole, for many years to come.

#### **D8. Acknowledgements**

The authors acknowledge the UW Department of Chemical Engineering for funding, Dr. Joyce Yen and the UW ADVANCE Center for Institutional Change for facilitating anti-bias trainings, the 120 UW Chemical Engineering graduate students and postdocs that have volunteered and participated in the panel evaluation process, and the 35 DYSS teaching assistants from the past 10 years for organizing and managing the seminar series.

#### **D9. Author Info**

**Brittany Bishop** holds a B.S.E. (Case Western Reserve University, 2015) and a Ph.D. (University of Washington, 2021) in Chemical Engineering. Her research interests include nanomaterial development for imaging and clean energy applications. In 2020, she was a Christine Mirzayan Science and Technology Policy Graduate Fellow with the Board on Chemical Sciences

and Technology at the National Academies of Sciences, Engineering, and Medicine. She served as the lead DYSS TA in 2019 and 2020.

**Cole DeForest** holds a B.S.E. (Princeton, 2006) and a Ph.D. (U. Colorado, 2011) in Chemical Engineering. He performed postdoctoral research at Caltech prior to joining UW Chemical Engineering as an Assistant Professor (2014). In 2020, he was promoted to Associate and appointed as the department's Associate Chair for Graduate Studies. His research interests include biomaterial development for tissue engineering and drug delivery. He has served as the primary faculty mentor for DYSS since 2015.

## BIBLIOGRAPHY

- (1) Rabouw, F. T.; de Mello Donega, C. Excited-State Dynamics in Colloidal Semiconductor Nanocrystals. *Top Curr Chem (Z)* **2016**, *374* (5), 58. <https://doi.org/10.1007/s41061-016-0060-0>.
- (2) Murray, C. B.; Norris, D. J.; Bawendi, M. G. Synthesis and Characterization of Nearly Monodisperse CdE (E = Sulfur, Selenium, Tellurium) Semiconductor Nanocrystallites. *J. Am. Chem. Soc.* **1993**, *115* (19), 8706–8715. <https://doi.org/10.1021/ja00072a025>.
- (3) Philippot, C.; Reiss, P. Chapter 3 - Synthesis of Inorganic Nanocrystals for Biological Fluorescence Imaging. In *Frontiers of Nanoscience*; de la Fuente, J. M., Grazu, V., Eds.; Nanobiotechnology; Elsevier, 2012; Vol. 4, pp 81–114. <https://doi.org/10.1016/B978-0-12-415769-9.00003-0>.
- (4) Zhang, M.; Yue, J.; Cui, R.; Ma, Z.; Wan, H.; Wang, F.; Zhu, S.; Zhou, Y.; Kuang, Y.; Zhong, Y.; Pang, D.-W.; Dai, H. Bright Quantum Dots Emitting at ~1,600 Nm in the NIR-IIb Window for Deep Tissue Fluorescence Imaging. *PNAS* **2018**, *115* (26), 6590–6595. <https://doi.org/10.1073/pnas.1806153115>.
- (5) McHugh, K. J.; Jing, L.; Severt, S. Y.; Cruz, M.; Sarmadi, M.; Jayawardena, H. S. N.; Perkinson, C. F.; Larusson, F.; Rose, S.; Tomasic, S.; Graf, T.; Tzeng, S. Y.; Sugarman, J. L.; Vlastic, D.; Peters, M.; Peterson, N.; Wood, L.; Tang, W.; Yeom, J.; Collins, J.; Welkhoff, P. A.; Karchin, A.; Tse, M.; Gao, M.; Bawendi, M. G.; Langer, R.; Jaklenec, A. Biocompatible Near-Infrared Quantum Dots Delivered to the Skin by Microneedle Patches Record Vaccination. *Science Translational Medicine* **2019**, *11* (523). <https://doi.org/10.1126/scitranslmed.aay7162>.
- (6) Tavakoli Dastjerdi, H.; Qi, P.; Fan, Z.; Tavakoli, M. M. Cost-Effective and Semi-Transparent PbS Quantum Dot Solar Cells Using Copper Electrodes. *ACS Appl. Mater. Interfaces* **2020**, *12* (1), 818–825. <https://doi.org/10.1021/acsami.9b18487>.
- (7) Ramade, J.; Qu, J.; Chu, A.; Gréboval, C.; Livache, C.; Goubet, N.; Martinez, B.; Vincent, G.; Lhuillier, E. Potential of Colloidal Quantum Dot Based Solar Cells for Near-Infrared Active Detection. *ACS Photonics* **2020**, *7* (1), 272–278. <https://doi.org/10.1021/acsp Photonics.9b01542>.
- (8) Tanabe, K.; Guimard, D.; Bordel, D.; Arakawa, Y. High-Efficiency InAs/GaAs Quantum Dot Solar Cells by Metalorganic Chemical Vapor Deposition. *Appl. Phys. Lett.* **2012**, *100* (19), 193905. <https://doi.org/10.1063/1.4714767>.
- (9) Graddage, N.; Ouyang, J.; Lu, J.; Chu, T.-Y.; Zhang, Y.; Li, Z.; Wu, X.; Malenfant, P. R. L.; Tao, Y. Near-Infrared-II Photodetectors Based on Silver Selenide Quantum Dots on Mesoporous TiO<sub>2</sub> Scaffolds. *ACS Appl. Nano Mater.* **2020**, *3* (12), 12209–12217. <https://doi.org/10.1021/acsanm.0c02686>.

- (10) Yin, X.; Zhang, C.; Guo, Y.; Yang, Y.; Xing, Y.; Que, W. PbS QD-Based Photodetectors: Future-Oriented near-Infrared Detection Technology. *J. Mater. Chem. C* **2021**, *9* (2), 417–438. <https://doi.org/10.1039/D0TC04612D>.
- (11) Sadeghi, S.; Khabbaz Abkenar, S.; Ow-Yang, C. W.; Nizamoglu, S. Efficient White LEDs Using Liquid-State Magic-Sized CdSe Quantum Dots. *Scientific Reports* **2019**, *9* (1), 10061. <https://doi.org/10.1038/s41598-019-46581-2>.
- (12) Shen, W.; Tang, H.; Yang, X.; Cao, Z.; Cheng, T.; Wang, X.; Tan, Z.; You, J.; Deng, Z. Synthesis of Highly Fluorescent InP/ZnS Small-Core/Thick-Shell Tetrahedral-Shaped Quantum Dots for Blue Light-Emitting Diodes. *J. Mater. Chem. C* **2017**, *5* (32), 8243–8249. <https://doi.org/10.1039/C7TC02927F>.
- (13) Liu, Z.; Lin, C.-H.; Hyun, B.-R.; Sher, C.-W.; Lv, Z.; Luo, B.; Jiang, F.; Wu, T.; Ho, C.-H.; Kuo, H.-C.; He, J.-H. Micro-Light-Emitting Diodes with Quantum Dots in Display Technology. *Light: Science & Applications* **2020**, *9* (1), 83. <https://doi.org/10.1038/s41377-020-0268-1>.
- (14) Kobayashi, H.; Hama, Y.; Koyama, Y.; Barrett, T.; Regino, C. A. S.; Urano, Y.; Choyke, P. L. Simultaneous Multicolor Imaging of Five Different Lymphatic Basins Using Quantum Dots. *Nano Lett* **2007**, *7* (6), 1711–1716. <https://doi.org/10.1021/nl0707003>.
- (15) Gao, X.; Cui, Y.; Levenson, R. M.; Chung, L. W. K.; Nie, S. In Vivo Cancer Targeting and Imaging with Semiconductor Quantum Dots. *Nat Biotechnol* **2004**, *22* (8), 969–976. <https://doi.org/10.1038/nbt994>.
- (16) Chen, O.; Zhao, J.; Chauhan, V. P.; Cui, J.; Wong, C.; Harris, D. K.; Wei, H.; Han, H.-S.; Fukumura, D.; Jain, R. K.; Bawendi, M. G. Compact High-Quality CdSe–CdS Core–Shell Nanocrystals with Narrow Emission Linewidths and Suppressed Blinking. *Nature Materials* **2013**, *12* (5), 445–451. <https://doi.org/10.1038/nmat3539>.
- (17) Qin, H.; Niu, Y.; Meng, R.; Lin, X.; Lai, R.; Fang, W.; Peng, X. Single-Dot Spectroscopy of Zinc-Blende CdSe/CdS Core/Shell Nanocrystals: Nonblinking and Correlation with Ensemble Measurements. *J. Am. Chem. Soc.* **2014**, *136* (1), 179–187. <https://doi.org/10.1021/ja4078528>.
- (18) Pu, C.; Peng, X. To Battle Surface Traps on CdSe/CdS Core/Shell Nanocrystals: Shell Isolation versus Surface Treatment. *J. Am. Chem. Soc.* **2016**, *138* (26), 8134–8142. <https://doi.org/10.1021/jacs.6b02909>.
- (19) Zhou, J.; Zhu, M.; Meng, R.; Qin, H.; Peng, X. Ideal CdSe/CdS Core/Shell Nanocrystals Enabled by Entropic Ligands and Their Core Size-, Shell Thickness-, and Ligand-Dependent Photoluminescence Properties. *J. Am. Chem. Soc.* **2017**, *139* (46), 16556–16567. <https://doi.org/10.1021/jacs.7b07434>.
- (20) Jaiswal, J. K.; Mattoussi, H.; Mauro, J. M.; Simon, S. M. Long-Term Multiple Color Imaging of Live Cells Using Quantum Dot Bioconjugates. *Nature Biotechnology* **2003**, *21* (1), 47–51. <https://doi.org/10.1038/nbt767>.

- (21) Goodwin, H.; Jellicoe, T. C.; Davis, N. J. L. K.; Böhm, M. L. Multiple Exciton Generation in Quantum Dot-Based Solar Cells. *Nanophotonics* **2018**, *7* (1), 111–126. <https://doi.org/10.1515/nanoph-2017-0034>.
- (22) You, Y.; Tong, X.; Wang, W.; Sun, J.; Yu, P.; Ji, H.; Niu, X.; Wang, Z. M. Eco-Friendly Colloidal Quantum Dot-Based Luminescent Solar Concentrators. *Advanced Science* **2019**, *6* (9), 1801967. <https://doi.org/10.1002/advs.201801967>.
- (23) Hegg, M. C.; Horning, M. P.; Baehr-Jones, T.; Hochberg, M.; Lin, L. Y. Nanogap Quantum Dot Photodetectors with High Sensitivity and Bandwidth. *Appl. Phys. Lett.* **2010**, *96* (10), 101118. <https://doi.org/10.1063/1.3356224>.
- (24) Monguzzi, A.; Braga, D.; Gandini, M.; Holmberg, V. C.; Kim, D. K.; Sahu, A.; Norris, D. J.; Meinardi, F. Broadband Up-Conversion at Subsolar Irradiance: Triplet–Triplet Annihilation Boosted by Fluorescent Semiconductor Nanocrystals. *Nano Lett.* **2014**, *14* (11), 6644–6650. <https://doi.org/10.1021/nl503322a>.
- (25) Won, Y.-H.; Cho, O.; Kim, T.; Chung, D.-Y.; Kim, T.; Chung, H.; Jang, H.; Lee, J.; Kim, D.; Jang, E. Highly Efficient and Stable InP/ZnSe/ZnS Quantum Dot Light-Emitting Diodes. *Nature* **2019**, *575* (7784), 634–638. <https://doi.org/10.1038/s41586-019-1771-5>.
- (26) Ramasamy, P.; Kim, N.; Kang, Y.-S.; Ramirez, O.; Lee, J.-S. Tunable, Bright, and Narrow-Band Luminescence from Colloidal Indium Phosphide Quantum Dots. *Chem. Mater.* **2017**, *29* (16), 6893–6899. <https://doi.org/10.1021/acs.chemmater.7b02204>.
- (27) Cotta, M. A. Quantum Dots and Their Applications: What Lies Ahead? *ACS Appl. Nano Mater.* **2020**, *3* (6), 4920–4924. <https://doi.org/10.1021/acsnm.0c01386>.
- (28) Q. Grim, J.; Manna, L.; Moreels, I. A Sustainable Future for Photonic Colloidal Nanocrystals. *Chemical Society Reviews* **2015**, *44* (16), 5897–5914. <https://doi.org/10.1039/C5CS00285K>.
- (29) Amiri, G.; Valipour, A.; Parivar, K.; Modaresi, M.; Noori, A.; Gharamaleki, H.; Taheri, J.; Kazemi, A. Comparison of Toxicity of CdSe: ZnS Quantum Dots on Male Reproductive System in Different Stages of Development in Mice. *Int J Fertil Steril* **2016**, *9* (4), 512–520.
- (30) Wang, L.; Nagesha, D. K.; Selvarasah, S.; Dokmeci, M. R.; Carrier, R. L. Toxicity of CdSe Nanoparticles in Caco-2 Cell Cultures. *J Nanobiotechnology* **2008**, *6*, 11. <https://doi.org/10.1186/1477-3155-6-11>.
- (31) Kim, J.-H.; Kim, H.-R.; Lee, B.-R.; Choi, E.-S.; In, S.-I.; Kim, E. Carcinogenic Activity of PbS Quantum Dots Screened Using Exosomal Biomarkers Secreted from HEK293 Cells. *Int J Nanomedicine* **2015**, *10*, 5513–5528. <https://doi.org/10.2147/IJN.S89593>.
- (32) Ginterseder, M.; Franke, D.; Perkinson, C. F.; Wang, L.; Hansen, E. C.; Bawendi, M. G. Scalable Synthesis of InAs Quantum Dots Mediated through Indium Redox Chemistry. *J. Am. Chem. Soc.* **2020**, *142* (9), 4088–4092. <https://doi.org/10.1021/jacs.9b12350>.

- (33) Franke, D.; Harris, D. K.; Chen, O.; Bruns, O. T.; Carr, J. A.; Wilson, M. W. B.; Bawendi, M. G. Continuous Injection Synthesis of Indium Arsenide Quantum Dots Emissive in the Short-Wavelength Infrared. *Nature Communications* **2016**, *7* (1), 12749. <https://doi.org/10.1038/ncomms12749>.
- (34) Ortega-Rodríguez, A.; Shen, Y.; Zabala Gutierrez, I.; Santos, H. D. A.; Torres Vera, V.; Ximendes, E.; Villaverde, G.; Lifante, J.; Gerke, C.; Fernández, N.; Calderón, O. G.; Melle, S.; Marques-Hueso, J.; Mendez-Gonzalez, D.; Laurenti, M.; Jones, C. M. S.; López-Romero, J. M.; Contreras-Cáceres, R.; Jaque, D.; Rubio-Retama, J. 10-Fold Quantum Yield Improvement of Ag<sub>2</sub>S Nanoparticles by Fine Compositional Tuning. *ACS Appl. Mater. Interfaces* **2020**, *12* (11), 12500–12509. <https://doi.org/10.1021/acsami.9b22827>.
- (35) Zhao, D.-H.; Yang, J.; Xia, R.-X.; Yao, M.-H.; Jin, R.-M.; Zhao, Y.-D.; Liu, B. High Quantum Yield Ag<sub>2</sub>S Quantum Dot@polypeptide-Engineered Hybrid Nanogels for Targeted Second near-Infrared Fluorescence/Photoacoustic Imaging and Photothermal Therapy. *Chem. Commun.* **2018**, *54* (5), 527–530. <https://doi.org/10.1039/C7CC09266K>.
- (36) Clarke, M. T.; Viscomi, F. N.; Chamberlain, T. W.; Hondow, N.; Adawi, A. M.; Sturge, J.; Erwin, S. C.; Bouillard, J.-S. G.; Tamang, S.; Stasiuk, G. J. Synthesis of Super Bright Indium Phosphide Colloidal Quantum Dots through Thermal Diffusion. *Communications Chemistry* **2019**, *2* (1), 1–7. <https://doi.org/10.1038/s42004-019-0138-z>.
- (37) Jo, J.-H.; Jo, D.-Y.; Lee, S.-H.; Yoon, S.-Y.; Lim, H.-B.; Lee, B.-J.; Do, Y. R.; Yang, H. InP-Based Quantum Dots Having an InP Core, Composition-Gradient ZnSeS Inner Shell, and ZnS Outer Shell with Sharp, Bright Emissivity, and Blue Absorptivity for Display Devices. *ACS Appl. Nano Mater.* **2020**, *3* (2), 1972–1980. <https://doi.org/10.1021/acsanm.0c00008>.
- (38) Liu, P.; Lou, Y.; Ding, S.; Zhang, W.; Wu, Z.; Yang, H.; Xu, B.; Wang, K.; Sun, X. W. Green InP/ZnSeS/ZnS Core Multi-Shelled Quantum Dots Synthesized with Aminophosphine for Effective Display Applications. *Advanced Functional Materials* **2021**, *31* (11), 2008453. <https://doi.org/10.1002/adfm.202008453>.
- (39) LaMer, V. K.; Dinegar, R. H. Theory, Production and Mechanism of Formation of Monodispersed Hydrosols. *J. Am. Chem. Soc.* **1950**, *72* (11), 4847–4854. <https://doi.org/10.1021/ja01167a001>.
- (40) Polte, J. Fundamental Growth Principles of Colloidal Metal Nanoparticles – a New Perspective. *CrystEngComm* **2015**, *17* (36), 6809–6830. <https://doi.org/10.1039/C5CE01014D>.
- (41) Murray, C. B.; Kagan, C. R.; Bawendi, M. G. Synthesis and Characterization of Monodisperse Nanocrystals and Close-Packed Nanocrystal Assemblies. *Annu. Rev. Mater. Sci.* **2000**, *30* (1), 545–610. <https://doi.org/10.1146/annurev.matsci.30.1.545>.
- (42) Heuer-Jungemann, A.; Feliu, N.; Bakaimi, I.; Hamaly, M.; Alkilany, A.; Chakraborty, I.; Masood, A.; Casula, M. F.; Kostopoulou, A.; Oh, E.; Susumu, K.; Stewart, M. H.; Medintz, I. L.; Stratakis, E.; Parak, W. J.; Kanaras, A. G. The Role of Ligands in the Chemical

- Synthesis and Applications of Inorganic Nanoparticles. *Chem. Rev.* **2019**, *119* (8), 4819–4880. <https://doi.org/10.1021/acs.chemrev.8b00733>.
- (43) Ningthoujam, R. S.; Gautam, A.; Padma, N. Oleylamine as a Reducing Agent in Syntheses of Magic-Size Clusters and Monodisperse Quantum Dots: Optical and Photoconductivity Studies. *Phys. Chem. Chem. Phys.* **2017**, *19* (3), 2294–2303. <https://doi.org/10.1039/C6CP07052C>.
- (44) Munro, A. M. Synthetic Approaches for Growing Zinc Sulfide and Zinc Selenide Colloidal Nanocrystals. *Journal of Vacuum Science & Technology A* **2020**, *38* (2), 020805. <https://doi.org/10.1116/1.5141992>.
- (45) Cossairt, B. M.; Juhas, P.; Billinge, S. J. L.; Owen, J. S. Tuning the Surface Structure and Optical Properties of CdSe Clusters Using Coordination Chemistry. *J. Phys. Chem. Lett.* **2011**, *2* (24), 3075–3080. <https://doi.org/10.1021/jz2013769>.
- (46) Rao, C. N. R.; Vivekchand, S. R. C.; Biswas, K.; Govindaraj, A. Synthesis of Inorganic Nanomaterials. *Dalton Trans.* **2007**, No. 34, 3728–3749. <https://doi.org/10.1039/B708342D>.
- (47) Park, J.; Joo, J.; Kwon, S. G.; Jang, Y.; Hyeon, T. Synthesis of Monodisperse Spherical Nanocrystals. *Angewandte Chemie International Edition* **2007**, *46* (25), 4630–4660. <https://doi.org/10.1002/anie.200603148>.
- (48) de Mello Donegá, C.; Liljeroth, P.; Vanmaekelbergh, D. Physicochemical Evaluation of the Hot-Injection Method, a Synthesis Route for Monodisperse Nanocrystals. *Small* **2005**, *1* (12), 1152–1162. <https://doi.org/10.1002/sml.200500239>.
- (49) Kwon, S. G.; Piao, Y.; Park, J.; Angappane, S.; Jo, Y.; Hwang, N.-M.; Park, J.-G.; Hyeon, T. Kinetics of Monodisperse Iron Oxide Nanocrystal Formation by “Heating-Up” Process. *J. Am. Chem. Soc.* **2007**, *129* (41), 12571–12584. <https://doi.org/10.1021/ja074633q>.
- (50) van Embden, J.; Chesman, A. S. R.; Jasieniak, J. J. The Heat-Up Synthesis of Colloidal Nanocrystals. *Chem. Mater.* **2015**, *27* (7), 2246–2285. <https://doi.org/10.1021/cm5028964>.
- (51) Gary, D. C.; Terban, M. W.; Billinge, S. J. L.; Cossairt, B. M. Two-Step Nucleation and Growth of InP Quantum Dots via Magic-Sized Cluster Intermediates. *Chem. Mater.* **2015**, *27* (4), 1432–1441. <https://doi.org/10.1021/acs.chemmater.5b00286>.
- (52) Liu, M.; Wang, K.; Wang, L.; Han, S.; Fan, H.; Rowell, N.; Ripmeester, J. A.; Renoud, R.; Bian, F.; Zeng, J.; Yu, K. Probing Intermediates of the Induction Period Prior to Nucleation and Growth of Semiconductor Quantum Dots. *Nature Communications* **2017**, *8* (1), 15467. <https://doi.org/10.1038/ncomms15467>.
- (53) Jiang, Z.-J.; Kelley, D. F. Role of Magic-Sized Clusters in the Synthesis of CdSe Nanorods. *ACS Nano* **2010**, *4* (3), 1561–1572. <https://doi.org/10.1021/nn100076f>.

- (54) Peng, Z. A.; Peng, X. Nearly Monodisperse and Shape-Controlled CdSe Nanocrystals via Alternative Routes: Nucleation and Growth. *J. Am. Chem. Soc.* **2002**, *124* (13), 3343–3353. <https://doi.org/10.1021/ja0173167>.
- (55) Kudera, S.; Zanella, M.; Giannini, C.; Rizzo, A.; Li, Y.; Gigli, G.; Cingolani, R.; Ciccarella, G.; Spahl, W.; Parak, W. J.; Manna, L. Sequential Growth of Magic-Size CdSe Nanocrystals. *Advanced Materials* **2007**, *19* (4), 548–552. <https://doi.org/10.1002/adma.200601015>.
- (56) Baek, W.; Bootharaju, M. S.; Walsh, K. M.; Lee, S.; Gamelin, D. R.; Hyeon, T. Highly Luminescent and Catalytically Active Suprastructures of Magic-Sized Semiconductor Nanoclusters. *Nature Materials* **2021**, *20* (5), 650–657. <https://doi.org/10.1038/s41563-020-00880-6>.
- (57) Zhang, J.; Rowland, C.; Liu, Y.; Xiong, H.; Kwon, S.; Shevchenko, E.; Schaller, R. D.; Prakapenka, V. B.; Tkachev, S.; Rajh, T. Evolution of Self-Assembled ZnTe Magic-Sized Nanoclusters. *J. Am. Chem. Soc.* **2015**, *137* (2), 742–749. <https://doi.org/10.1021/ja509782n>.
- (58) Xu, H.; Hou, Y.; Zhang, H. CdTe Magic-Sized Clusters and the Use as Building Blocks for Assembling Two-Dimensional Nanoplatelets. *J Nanopart Res* **2017**, *19* (6), 189. <https://doi.org/10.1007/s11051-017-3878-7>.
- (59) Wang, Y.; Zhang, Y.; Wang, F.; Giblin, D. E.; Hoy, J.; Rohrs, H. W.; Loomis, R. A.; Buhro, W. E. The Magic-Size Nanocluster (CdSe)<sub>34</sub> as a Low-Temperature Nucleant for Cadmium Selenide Nanocrystals; Room-Temperature Growth of Crystalline Quantum Platelets. *Chem. Mater.* **2014**, *26* (7), 2233–2243. <https://doi.org/10.1021/cm404068e>.
- (60) Harrell, S. M.; McBride, J. R.; Rosenthal, S. J. Synthesis of Ultrasmall and Magic-Sized CdSe Nanocrystals. *Chem. Mater.* **2013**, *25* (8), 1199–1210. <https://doi.org/10.1021/cm303318f>.
- (61) Kwon, Y.; Oh, J.; Lee, E.; Lee, S. H.; Agnes, A.; Bang, G.; Kim, J.; Kim, D.; Kim, S. Evolution from Unimolecular to Colloidal-Quantum-Dot-like Character in Chlorine or Zinc Incorporated InP Magic Size Clusters. *Nature Communications* **2020**, *11* (1), 3127. <https://doi.org/10.1038/s41467-020-16855-9>.
- (62) Wang, Z.; Li, Z.; Kornowski, A.; Ma, X.; Myalitsin, A.; Mews, A. Solution–Liquid–Solid Synthesis of Semiconductor Nanowires Using Clusters as Single-Source Precursors. *Small* **2011**, *7* (17), 2464–2468. <https://doi.org/10.1002/sml.201100343>.
- (63) Bowers, M. J.; McBride, J. R.; Rosenthal, S. J. White-Light Emission from Magic-Sized Cadmium Selenide Nanocrystals. *J. Am. Chem. Soc.* **2005**, *127* (44), 15378–15379. <https://doi.org/10.1021/ja055470d>.
- (64) Lawrence, K. N.; Dolai, S.; Lin, Y.-H.; Dass, A.; Sardar, R. Enhancing the Physicochemical and Photophysical Properties of Small (<2.0 Nm) CdSe Nanoclusters for Intracellular Imaging Applications. *RSC Adv.* **2014**, *4* (58), 30742–30753. <https://doi.org/10.1039/C4RA02549K>.

- (65) Kwon, Y.; Kim, S. Indium Phosphide Magic-Sized Clusters: Chemistry and Applications. *NPG Asia Materials* **2021**, *13* (1), 1–16. <https://doi.org/10.1038/s41427-021-00300-4>.
- (66) Smith, A. M.; Nie, S. Semiconductor Nanocrystals: Structure, Properties, and Band Gap Engineering. *Acc. Chem. Res.* **2010**, *43* (2), 190–200. <https://doi.org/10.1021/ar9001069>.
- (67) Ji, B.; Koley, S.; Slobodkin, I.; Remennik, S.; Banin, U. ZnSe/ZnS Core/Shell Quantum Dots with Superior Optical Properties through Thermodynamic Shell Growth. *Nano Lett.* **2020**, *20* (4), 2387–2395. <https://doi.org/10.1021/acs.nanolett.9b05020>.
- (68) Ghosh Chaudhuri, R.; Paria, S. Core/Shell Nanoparticles: Classes, Properties, Synthesis Mechanisms, Characterization, and Applications. *Chem. Rev.* **2012**, *112* (4), 2373–2433. <https://doi.org/10.1021/cr100449n>.
- (69) Kovtun, O.; Tomlinson, I. D.; Bailey, D. M.; Thal, L. B.; Ross, E. J.; Harris, L.; Frankland, M. P.; Ferguson, R. S.; Glaser, Z.; Greer, J.; Rosenthal, S. J. Single Quantum Dot Tracking Illuminates Neuroscience at the Nanoscale. *Chem Phys Lett* **2018**, *706*, 741–752. <https://doi.org/10.1016/j.cplett.2018.06.019>.
- (70) Efros, A. L.; Nesbitt, D. J. Origin and Control of Blinking in Quantum Dots. *Nature Nanotechnology* **2016**, *11* (8), 661–671. <https://doi.org/10.1038/nnano.2016.140>.
- (71) Li, J. J.; Wang, Y. A.; Guo, W.; Keay, J. C.; Mishima, T. D.; Johnson, M. B.; Peng, X. Large-Scale Synthesis of Nearly Monodisperse CdSe/CdS Core/Shell Nanocrystals Using Air-Stable Reagents via Successive Ion Layer Adsorption and Reaction. *J. Am. Chem. Soc.* **2003**, *125* (41), 12567–12575. <https://doi.org/10.1021/ja0363563>.
- (72) Hao, J.; Liu, H.; Miao, J.; Lu, R.; Zhou, Z.; Zhao, B.; Xie, B.; Cheng, J.; Wang, K.; Delville, M.-H. A Facile Route to Synthesize CdSe/ZnS Thick-Shell Quantum Dots with Precisely Controlled Green Emission Properties: Towards QDs Based LED Applications. *Sci Rep* **2019**, *9*. <https://doi.org/10.1038/s41598-019-48469-7>.
- (73) Greytak, A. B.; Allen, P. M.; Liu, W.; Zhao, J.; Young, E. R.; Popović, Z.; Walker, B. J.; Nocera, D. G.; Bawendi, M. G. Alternating Layer Addition Approach to CdSe/CdS Core/Shell Quantum Dots with near-Unity Quantum Yield and High on-Time Fractions. *Chem. Sci.* **2012**, *3* (6), 2028–2034. <https://doi.org/10.1039/C2SC00561A>.
- (74) Rafipoor, M.; Dupont, D.; Tornatzky, H.; Tessier, M. D.; Maultzsch, J.; Hens, Z.; Lange, H. Strain Engineering in InP/(Zn,Cd)Se Core/Shell Quantum Dots. *Chem. Mater.* **2018**, *30* (13), 4393–4400. <https://doi.org/10.1021/acs.chemmater.8b01789>.
- (75) Chen, X.; Lou, Y.; Samia, A. C.; Burda, C. Coherency Strain Effects on the Optical Response of Core/Shell Heteronanostructures. *Nano Lett.* **2003**, *3* (6), 799–803. <https://doi.org/10.1021/nl034243b>.
- (76) Bailey, R. E.; Nie, S. Alloyed Semiconductor Quantum Dots: Tuning the Optical Properties without Changing the Particle Size. *J. Am. Chem. Soc.* **2003**, *125* (23), 7100–7106. <https://doi.org/10.1021/ja035000o>.

- (77) Dey, S.; Chen, S.; Thota, S.; Shakil, M. R.; Suib, S. L.; Zhao, J. Effect of Gradient Alloying on Photoluminescence Blinking of Single CdS<sub>x</sub>Se<sub>1-x</sub> Nanocrystals. *J. Phys. Chem. C* **2016**, *120* (37), 20547–20554. <https://doi.org/10.1021/acs.jpcc.5b11651>.
- (78) Zhang, J.; Yang, Q.; Cao, H.; Ratcliffe, C. I.; Kingston, D.; Chen, Q. Y.; Ouyang, J.; Wu, X.; Leek, D. M.; Riehle, F. S.; Yu, K. Bright Gradient-Alloyed CdS<sub>x</sub>Se<sub>1-x</sub> Quantum Dots Exhibiting Cyan-Blue Emission. *Chem. Mater.* **2016**, *28* (2), 618–625. <https://doi.org/10.1021/acs.chemmater.5b04380>.
- (79) Cho, J.; Jung, Y. K.; Lee, J.-K.; Jung, H.-S. Highly Efficient Blue-Emitting CdSe-Derived Core/Shell Gradient Alloy Quantum Dots with Improved Photoluminescent Quantum Yield and Enhanced Photostability. *Langmuir* **2017**, *33* (15), 3711–3719. <https://doi.org/10.1021/acs.langmuir.6b04333>.
- (80) Lee, S. H.; Kim, Y.; Jang, H.; Min, J. H.; Oh, J.; Jang, E.; Kim, D. The Effects of Discrete and Gradient Mid-Shell Structures on the Photoluminescence of Single InP Quantum Dots. *Nanoscale* **2019**, *11* (48), 23251–23258. <https://doi.org/10.1039/C9NR06847C>.
- (81) Pietra, F.; De Trizio, L.; Hoekstra, A. W.; Renaud, N.; Prato, M.; Grozema, F. C.; Baesjou, P. J.; Koole, R.; Manna, L.; Houtepen, A. J. Tuning the Lattice Parameter of In<sub>x</sub>Zn<sub>1-x</sub>P for Highly Luminescent Lattice-Matched Core/Shell Quantum Dots. *ACS Nano* **2016**, *10* (4), 4754–4762. <https://doi.org/10.1021/acsnano.6b01266>.
- (82) Mulder, J. T.; Kirkwood, N.; De Trizio, L.; Li, C.; Bals, S.; Manna, L.; Houtepen, A. J. Developing Lattice Matched ZnMgSe Shells on InZnP Quantum Dots for Phosphor Applications. *ACS Appl. Nano Mater.* **2020**, *3* (4), 3859–3867. <https://doi.org/10.1021/acsanm.0c00583>.
- (83) Charles H. Henry, Bell Laboratories <https://www.aip.org/aip/awards/industrial-physics-prize/charles-h-henry-bell-laboratories> (accessed 2021 -07 -09).
- (84) Maruska, H. P.; Rhines, W. C. A Modern Perspective on the History of Semiconductor Nitride Blue Light Sources. *Solid-State Electronics* **2015**, *111*, 32–41. <https://doi.org/10.1016/j.sse.2015.04.010>.
- (85) Chen, L. Quantum Well Lasers and Their Applications. *Int. J. Hi. Spe. Ele. Syst.* **1996**, *07* (03), 373–381. <https://doi.org/10.1142/S0129156496000190>.
- (86) Matthews, J. W.; Blakeslee, A. E. Defects in Epitaxial Multilayers. I. Misfit Dislocations. *Journal of Crystal Growth* **1974**, *27*, 118–125. [https://doi.org/10.1016/0022-0248\(74\)90424-2](https://doi.org/10.1016/0022-0248(74)90424-2).
- (87) Jeong, B. G.; Park, Y.-S.; Chang, J. H.; Cho, I.; Kim, J. K.; Kim, H.; Char, K.; Cho, J.; Klimov, V. I.; Park, P.; Lee, D. C.; Bae, W. K. Colloidal Spherical Quantum Wells with Near-Unity Photoluminescence Quantum Yield and Suppressed Blinking. *ACS Nano* **2016**, *10* (10), 9297–9305. <https://doi.org/10.1021/acsnano.6b03704>.

- (88) Du, C.; Huang, X.; Jiang, C.; Pu, X.; Zhao, Z.; Jing, L.; Hu, W.; Wang, Z. L. Tuning Carrier Lifetime in InGaN/GaN LEDs via Strain Compensation for High-Speed Visible Light Communication. *Scientific Reports* **2016**, *6* (1), 37132. <https://doi.org/10.1038/srep37132>.
- (89) Mews, A.; Eychmueller, A.; Giersig, M.; Schooss, D.; Weller, H. Preparation, Characterization, and Photophysics of the Quantum Dot Quantum Well System Cadmium Sulfide/Mercury Sulfide/Cadmium Sulfide. *J. Phys. Chem.* **1994**, *98* (3), 934–941. <https://doi.org/10.1021/j100054a032>.
- (90) Mout, R.; Moyano, D. F.; Rana, S.; Rotello, V. M. Surface Functionalization of Nanoparticles for Nanomedicine. *Chem Soc Rev* **2012**, *41* (7), 2539–2544. <https://doi.org/10.1039/c2cs15294k>.
- (91) Sanità, G.; Carrese, B.; Lamberti, A. Nanoparticle Surface Functionalization: How to Improve Biocompatibility and Cellular Internalization. *Front. Mol. Biosci.* **2020**, *7*. <https://doi.org/10.3389/fmolb.2020.587012>.
- (92) Thiruppathi, R.; Mishra, S.; Ganapathy, M.; Padmanabhan, P.; Gulyás, B. Nanoparticle Functionalization and Its Potentials for Molecular Imaging. *Advanced Science* **2017**, *4* (3), 1600279. <https://doi.org/10.1002/advs.201600279>.
- (93) Zhang, M.; Bishop, B. P.; Thompson, N. L.; Hildahl, K.; Dang, B.; Mironchuk, O.; Chen, N.; Aoki, R.; Holmberg, V. C.; Nance, E. Quantum Dot Cellular Uptake and Toxicity in the Developing Brain: Implications for Use as Imaging Probes. *Nanoscale Adv.* **2019**, *1* (9), 3424–3442. <https://doi.org/10.1039/C9NA00334G>.
- (94) Hines, D. A.; Kamat, P. V. Recent Advances in Quantum Dot Surface Chemistry. *ACS Appl. Mater. Interfaces* **2014**, *6* (5), 3041–3057. <https://doi.org/10.1021/am405196u>.
- (95) Tang, J.; Birkedal, H.; McFarland, E. W.; Stucky, G. D. Self-Assembly of CdSe/CdS Quantum Dots by Hydrogen Bonding on Au Surfaces for Photoreception. *Chem. Commun.* **2003**, No. 18, 2278–2279. <https://doi.org/10.1039/B306888A>.
- (96) Yamauchi, M.; Masuo, S. Self-Assembly of Semiconductor Quantum Dots Using Organic Templates. *Chemistry – A European Journal* **2020**, *26* (32), 7176–7184. <https://doi.org/10.1002/chem.201905807>.
- (97) Beygi, H.; Sajjadi, S. A.; Babakhani, A.; Young, J. F.; van Veggel, F. C. J. M. Solution Phase Surface Functionalization of PbS Nanoparticles with Organic Ligands for Single-Step Deposition of p-Type Layer of Quantum Dot Solar Cells. *Applied Surface Science* **2018**, *459*, 562–571. <https://doi.org/10.1016/j.apsusc.2018.08.056>.
- (98) Nguyen, B. P.; Kim, T.; Park, C. R. Nanocomposite-Based Bulk Heterojunction Hybrid Solar Cells. *Journal of Nanomaterials* **2014**, *2014*, e243041. <https://doi.org/10.1155/2014/243041>.

- (99) Hines, D. A.; Kamat, P. V. Quantum Dot Surface Chemistry: Ligand Effects and Electron Transfer Reactions. *J. Phys. Chem. C* **2013**, *117* (27), 14418–14426. <https://doi.org/10.1021/jp404031s>.
- (100) Goswami, P. N.; Mandal, D.; Rath, A. K. The Role of Surface Ligands in Determining the Electronic Properties of Quantum Dot Solids and Their Impact on Photovoltaic Figure of Merits. *Nanoscale* **2018**, *10* (3), 1072–1080. <https://doi.org/10.1039/C7NR06116A>.
- (101) Suk, J. S.; Xu, Q.; Kim, N.; Hanes, J.; Ensign, L. M. PEGylation as a Strategy for Improving Nanoparticle-Based Drug and Gene Delivery. *Adv Drug Deliv Rev* **2016**, *99* (Pt A), 28–51. <https://doi.org/10.1016/j.addr.2015.09.012>.
- (102) Jokerst, J. V.; Lobovkina, T.; Zare, R. N.; Gambhir, S. S. Nanoparticle PEGylation for Imaging and Therapy. *Nanomedicine (Lond)* **2011**, *6* (4), 715–728. <https://doi.org/10.2217/nmm.11.19>.
- (103) Gao, J.; Zhang, J.; van de Lagemaat, J.; Johnson, J. C.; Beard, M. C. Charge Generation in PbS Quantum Dot Solar Cells Characterized by Temperature-Dependent Steady-State Photoluminescence. *ACS Nano* **2014**, *8* (12), 12814–12825. <https://doi.org/10.1021/nm506075s>.
- (104) Green, M. The Nature of Quantum Dot Capping Ligands. *J. Mater. Chem.* **2010**, *20* (28), 5797–5809. <https://doi.org/10.1039/C0JM00007H>.
- (105) Altintas, Y.; Talpur, M. Y.; Mutlugun, E. The Effect of Ligand Chain Length on the Optical Properties of Alloyed Core-Shell InPZnS/ZnS Quantum Dots. *Journal of Alloys and Compounds* **2017**, *711*, 335–341. <https://doi.org/10.1016/j.jallcom.2017.03.326>.
- (106) Guyot-Sionnest, P.; Shim, M.; Matranga, C.; Hines, M. Intraband Relaxation in CdSe Quantum Dots. *Phys. Rev. B* **1999**, *60* (4), R2181–R2184. <https://doi.org/10.1103/PhysRevB.60.R2181>.
- (107) Jasieniak, J.; Mulvaney, P. From Cd-Rich to Se-Rich – the Manipulation of CdSe Nanocrystal Surface Stoichiometry. *J. Am. Chem. Soc.* **2007**, *129* (10), 2841–2848. <https://doi.org/10.1021/ja066205a>.
- (108) Tamang, S.; Lincheneau, C.; Hermans, Y.; Jeong, S.; Reiss, P. Chemistry of InP Nanocrystal Syntheses. *Chem. Mater.* **2016**, *28* (8), 2491–2506. <https://doi.org/10.1021/acs.chemmater.5b05044>.
- (109) Virieux, H.; Le Troedec, M.; Cros-Gagneux, A.; Ojo, W.-S.; Delpech, F.; Nayral, C.; Martinez, H.; Chaudret, B. InP/ZnS Nanocrystals: Coupling NMR and XPS for Fine Surface and Interface Description. *J. Am. Chem. Soc.* **2012**, *134* (48), 19701–19708. <https://doi.org/10.1021/ja307124m>.
- (110) Baquero, E. A.; Virieux, H.; Swain, R. A.; Gillet, A.; Cros-Gagneux, A.; Coppel, Y.; Chaudret, B.; Nayral, C.; Delpech, F. Synthesis of Oxide-Free InP Quantum Dots: Surface

- Control and H<sub>2</sub>-Assisted Growth. *Chem. Mater.* **2017**, *29* (22), 9623–9627. <https://doi.org/10.1021/acs.chemmater.7b04069>.
- (111) Cros-Gagneux, A.; Delpech, F.; Nayral, C.; Cornejo, A.; Coppel, Y.; Chaudret, B. Surface Chemistry of InP Quantum Dots: A Comprehensive Study. *J. Am. Chem. Soc.* **2010**, *132* (51), 18147–18157. <https://doi.org/10.1021/ja104673y>.
- (112) Jasinski, J.; Leppert, V. J.; Lam, S.-T.; Gibson, G. A.; Nauka, K.; Yang, C. C.; Zhou, Z.-L. Rapid Oxidation of InP Nanoparticles in Air. *Solid State Communications* **2007**, *141* (11), 624–627. <https://doi.org/10.1016/j.ssc.2006.12.033>.
- (113) Brandenburg, B.; Zhuang, X. Virus Trafficking – Learning from Single-Virus Tracking. *Nature Reviews Microbiology* **2007**, *5* (3), 197–208. <https://doi.org/10.1038/nrmicro1615>.
- (114) Yu, J.; Choi, S.; Dickson, R. M. Shuttle-Based Fluorogenic Silver-Cluster Biolabels. *Angew Chem Int Ed Engl* **2009**, *48* (2), 318–320. <https://doi.org/10.1002/anie.200804137>.
- (115) Day, R. N.; Davidson, M. W. The Fluorescent Protein Palette: Tools for Cellular Imaging. *Chem. Soc. Rev.* **2009**, *38* (10), 2887–2921. <https://doi.org/10.1039/B901966A>.
- (116) Bruns, O. T.; Bischof, T. S.; Harris, D. K.; Franke, D.; Shi, Y.; Riedemann, L.; Bartelt, A.; Jaworski, F. B.; Carr, J. A.; Rowlands, C. J.; Wilson, M. W. B.; Chen, O.; Wei, H.; Hwang, G. W.; Montana, D. M.; Coropceanu, I.; Achorn, O. B.; Kloepper, J.; Heeren, J.; So, P. T. C.; Fukumura, D.; Jensen, K. F.; Jain, R. K.; Bawendi, M. G. Next-Generation in Vivo Optical Imaging with Short-Wave Infrared Quantum Dots. *Nat Biomed Eng* **2017**, *1*. <https://doi.org/10.1038/s41551-017-0056>.
- (117) Weissleder, R. A Clearer Vision for in Vivo Imaging. *Nature Biotechnology* **2001**, *19* (4), 316–317. <https://doi.org/10.1038/86684>.
- (118) Eggeling, C.; Widengren, J.; Rigler, R.; Seidel, C. A. M. Photobleaching of Fluorescent Dyes under Conditions Used for Single-Molecule Detection: Evidence of Two-Step Photolysis. *Anal. Chem.* **1998**, *70* (13), 2651–2659. <https://doi.org/10.1021/ac980027p>.
- (119) Chen, Z.; Wang, A.; Sun, W.; Wang, C.; Kong, L.; Li, F.; Tian, X.; Li, S.; Wu, J.; Tian, Y. Synthesis, Nonlinear Optical Properties and Cellular Imaging of Hybrid ZnS Nanoparticles Capped with Conjugated Terpyridine Derivatives. *J Mater Sci* **2018**, *53* (3), 1791–1800. <https://doi.org/10.1007/s10853-017-1621-5>.
- (120) Gobe, G.; Crane, D. Mitochondria, Reactive Oxygen Species and Cadmium Toxicity in the Kidney. *Toxicology Letters* **2010**, *198* (1), 49–55. <https://doi.org/10.1016/j.toxlet.2010.04.013>.
- (121) Cormode David P.; Skajaa Torjus; Fayad Zahi A.; Mulder Willem J.M. Nanotechnology in Medical Imaging. *Arteriosclerosis, Thrombosis, and Vascular Biology* **2009**, *29* (7), 992–1000. <https://doi.org/10.1161/ATVBAHA.108.165506>.

- (122) Chapman, S.; Dobrovolskaia, M.; Farahani, K.; Goodwin, A.; Joshi, A.; Lee, H.; Meade, T.; Pomper, M.; Ptak, K.; Rao, J.; Singh, R.; Sridhar, S.; Stern, S.; Wang, A.; Weaver, J. B.; Woloschak, G.; Yang, L. Nanoparticles for Cancer Imaging: The Good, the Bad, and the Promise. *Nano Today* **2013**, *8* (5), 454–460. <https://doi.org/10.1016/j.nantod.2013.06.001>.
- (123) Adisheshaiah, P. P.; Hall, J. B.; McNeil, S. E. Nanomaterial Standards for Efficacy and Toxicity Assessment. *WIREs Nanomedicine and Nanobiotechnology* **2010**, *2* (1), 99–112. <https://doi.org/10.1002/wnan.66>.
- (124) Hoshino, A.; Fujioka, K.; Oku, T.; Suga, M.; Sasaki, Y. F.; Ohta, T.; Yasuhara, M.; Suzuki, K.; Yamamoto, K. Physicochemical Properties and Cellular Toxicity of Nanocrystal Quantum Dots Depend on Their Surface Modification. *Nano Lett.* **2004**, *4* (11), 2163–2169. <https://doi.org/10.1021/nl048715d>.
- (125) Zhang, Y.; Pan, H.; Zhang, P.; Gao, N.; Lin, Y.; Luo, Z.; Li, P.; Wang, C.; Liu, L.; Pang, D.; Cai, L.; Ma, Y. Functionalized Quantum Dots Induce Proinflammatory Responses in Vitro: The Role of Terminal Functional Group-Associated Endocytic Pathways. *Nanoscale* **2013**, *5* (13), 5919–5929. <https://doi.org/10.1039/C3NR01653F>.
- (126) Tang, Y.; Han, S.; Liu, H.; Chen, X.; Huang, L.; Li, X.; Zhang, J. The Role of Surface Chemistry in Determining in Vivo Biodistribution and Toxicity of CdSe/ZnS Core–Shell Quantum Dots. *Biomaterials* **2013**, *34* (34), 8741–8755. <https://doi.org/10.1016/j.biomaterials.2013.07.087>.
- (127) Blanco, E.; Shen, H.; Ferrari, M. Principles of Nanoparticle Design for Overcoming Biological Barriers to Drug Delivery. *Nature Biotechnology* **2015**, *33* (9), 941–951. <https://doi.org/10.1038/nbt.3330>.
- (128) De Nolf, K.; Capek, R. K.; Abe, S.; Sluydts, M.; Jang, Y.; Martins, J. C.; Cottenier, S.; Lifshitz, E.; Hens, Z. Controlling the Size of Hot Injection Made Nanocrystals by Manipulating the Diffusion Coefficient of the Solute. *J. Am. Chem. Soc.* **2015**, *137* (7), 2495–2505. <https://doi.org/10.1021/ja509941g>.
- (129) Yu, W. W.; Qu, L.; Guo, W.; Peng, X. Experimental Determination of the Extinction Coefficient of CdTe, CdSe, and CdS Nanocrystals. *Chem. Mater.* **2003**, *15* (14), 2854–2860. <https://doi.org/10.1021/cm034081k>.
- (130) Zhang, H.; Cheng, K.; Hou, Y. M.; Fang, Z.; Pan, Z. X.; Wu, W. J.; Hua, J. L.; Zhong, X. H. Efficient CdSe Quantum Dot-Sensitized Solar Cells Prepared by a Postsynthesis Assembly Approach. *Chem. Commun.* **2012**, *48* (91), 11235–11237. <https://doi.org/10.1039/C2CC36526J>.
- (131) Pathak, S.; Cao, E.; Davidson, M. C.; Jin, S.; Silva, G. A. Quantum Dot Applications to Neuroscience: New Tools for Probing Neurons and Glia. *J. Neurosci.* **2006**, *26* (7), 1893–1895. <https://doi.org/10.1523/JNEUROSCI.3847-05.2006>.
- (132) Wu, X.; Liu, H.; Liu, J.; Haley, K. N.; Treadway, J. A.; Larson, J. P.; Ge, N.; Peale, F.; Bruchez, M. P. Immunofluorescent Labeling of Cancer Marker Her2 and Other Cellular

- Targets with Semiconductor Quantum Dots. *Nature Biotechnology* **2003**, *21* (1), 41–46. <https://doi.org/10.1038/nbt764>.
- (133) Holmberg, V. C.; Rasch, M. R.; Korgel, B. A. PEGylation of Carboxylic Acid-Functionalized Germanium Nanowires. *Langmuir* **2010**, *26* (17), 14241–14246. <https://doi.org/10.1021/la102124y>.
- (134) Matsuura, H.; Miyazawa, T. Intrachain Force Field and Normal Vibrations of Polyethylene Glycol. *BCSJ* **1968**, *41* (8), 1798–1808. <https://doi.org/10.1246/bcsj.41.1798>.
- (135) Matsuura, H.; Miyazawa, T. Frequency Distribution and Neutron Scattering of Polyethylene Glycol Chain. *J. Chem. Phys.* **1969**, *50* (2), 915–919. <https://doi.org/10.1063/1.1671143>.
- (136) Coates, J. Interpretation of Infrared Spectra, A Practical Approach. In *Encyclopedia of Analytical Chemistry*; Meyers, R. A., Ed.; John Wiley & Sons, Ltd: Chichester, UK, 2000; pp 10881–10882. <https://doi.org/10.1002/9780470027318.a5606>.
- (137) Oomens, J.; Steill, J. D. Free Carboxylate Stretching Modes. *J. Phys. Chem. A* **2008**, *112* (15), 3281–3283. <https://doi.org/10.1021/jp801806e>.
- (138) Jevprasesphant, R.; Penny, J.; Jalal, R.; Attwood, D.; McKeown, N. B.; D’Emanuele, A. The Influence of Surface Modification on the Cytotoxicity of PAMAM Dendrimers. *International Journal of Pharmaceutics* **2003**, *252* (1), 263–266. [https://doi.org/10.1016/S0378-5173\(02\)00623-3](https://doi.org/10.1016/S0378-5173(02)00623-3).
- (139) Hoshyar, N.; Gray, S.; Han, H.; Bao, G. The Effect of Nanoparticle Size on in Vivo Pharmacokinetics and Cellular Interaction. *Nanomedicine* **2016**, *11* (6), 673–692. <https://doi.org/10.2217/nnm.16.5>.
- (140) Wang, Z.; Dong, X.; Zhou, S.; Xie, Z.; Zalevsky, Z. Ultra-Narrow-Bandwidth Graphene Quantum Dots for Superresolved Spectral and Spatial Sensing. *NPG Asia Materials* **2021**, *13* (1), 1–13. <https://doi.org/10.1038/s41427-020-00269-6>.
- (141) Michalet, X.; Pinaud, F. F.; Bentolila, L. A.; Tsay, J. M.; Doose, S.; Li, J. J.; Sundaresan, G.; Wu, A. M.; Gambhir, S. S.; Weiss, S. Quantum Dots for Live Cells, in Vivo Imaging, and Diagnostics. *Science* **2005**, *307* (5709), 538–544. <https://doi.org/10.1126/science.1104274>.
- (142) Talapin, D. V.; Lee, J.-S.; Kovalenko, M. V.; Shevchenko, E. V. Prospects of Colloidal Nanocrystals for Electronic and Optoelectronic Applications. *Chem. Rev.* **2010**, *110* (1), 389–458. <https://doi.org/10.1021/cr900137k>.
- (143) Tan, L.; Misquitta, A. J.; Sapelkin, A.; Fang, L.; Wilson, R. M.; Keeble, D. S.; Zhang, B.; Zhu, T.; Riehle, F. S.; Han, S.; Yu, K.; Dove, M. T. X-Ray Total Scattering Study of Magic-Size Clusters and Quantum Dots of Cadmium Sulphide. *Nanoscale* **2019**, *11* (45), 21900–21908. <https://doi.org/10.1039/C9NR06355B>.

- (144) Ning, J.; Banin, U. Magic Size InP and InAs Clusters: Synthesis, Characterization and Shell Growth. *Chem. Commun.* **2017**, 53 (17), 2626–2629. <https://doi.org/10.1039/C6CC09778B>.
- (145) Thompson, L. H.; Doraiswamy, L. K. Sonochemistry: Science and Engineering. *Ind. Eng. Chem. Res.* **1999**, 38 (4), 1215–1249. <https://doi.org/10.1021/ie9804172>.
- (146) Suslick, K. S. Applications of Ultrasound to Materials Chemistry. *MRS Bulletin* **1995**, 20 (4), 29–34. <https://doi.org/10.1557/S088376940004464X>.
- (147) Jh, B.; Ks, S. Applications of Ultrasound to the Synthesis of Nanostructured Materials. *Adv Mater* **2010**, 22 (10), 1039–1059. <https://doi.org/10.1002/adma.200904093>.
- (148) Suslick, K. S. Sonochemistry. *Science* **1990**, 247 (4949), 1439–1445. <https://doi.org/10.1126/science.247.4949.1439>.
- (149) Suslick, K. S.; Choe, S.-B.; Cichowlas, A. A.; Grinstaff, M. W. Sonochemical Synthesis of Amorphous Iron. *Nature* **1991**, 353 (6343), 414–416. <https://doi.org/10.1038/353414a0>.
- (150) Suslick, K. S.; Fang, M.; Hyeon, T. Sonochemical Synthesis of Iron Colloids. *J. Am. Chem. Soc.* **1996**, 118 (47), 11960–11961. <https://doi.org/10.1021/ja961807n>.
- (151) Kumar, R. V.; Diamant, Y.; Gedanken, A. Sonochemical Synthesis and Characterization of Nanometer-Size Transition Metal Oxides from Metal Acetates. *Chem. Mater.* **2000**, 12 (8), 2301–2305. <https://doi.org/10.1021/cm000166z>.
- (152) Okitsu, K.; Mizukoshi, Y.; Bandow, H.; Maeda, Y.; Yamamoto, T.; Nagata, Y. Formation of Noble Metal Particles by Ultrasonic Irradiation. *Ultrasonics Sonochemistry* **1996**, 3 (3), S249–S251. [https://doi.org/10.1016/S1350-4177\(96\)00033-8](https://doi.org/10.1016/S1350-4177(96)00033-8).
- (153) Zhang, J.; Du, J.; Han, B.; Liu, Z.; Jiang, T.; Zhang, Z. Sonochemical Formation of Single-Crystalline Gold Nanobelts. *Angewandte Chemie International Edition* **2006**, 45 (7), 1116–1119. <https://doi.org/10.1002/anie.200503762>.
- (154) Xu, H.; Suslick, K. S. Sonochemical Synthesis of Highly Fluorescent Ag Nanoclusters. *ACS Nano* **2010**, 4 (6), 3209–3214. <https://doi.org/10.1021/nn100987k>.
- (155) Liu, L.; Peng, Q.; Li, Y. Preparation of Monodisperse Se Colloid Spheres and Se Nanowires Using Na<sub>2</sub>SeSO<sub>3</sub> as Precursor. *Nano Res.* **2008**, 1 (5), 403–411. <https://doi.org/10.1007/s12274-008-8040-5>.
- (156) Coleman, J. N.; Lotya, M.; O'Neill, A.; Bergin, S. D.; King, P. J.; Khan, U.; Young, K.; Gaucher, A.; De, S.; Smith, R. J.; Shvets, I. V.; Arora, S. K.; Stanton, G.; Kim, H.-Y.; Lee, K.; Kim, G. T.; Duesberg, G. S.; Hallam, T.; Boland, J. J.; Wang, J. J.; Donegan, J. F.; Grunlan, J. C.; Moriarty, G.; Shmeliov, A.; Nicholls, R. J.; Perkins, J. M.; Grievson, E. M.; Theuwissen, K.; McComb, D. W.; Nellist, P. D.; Nicolosi, V. Two-Dimensional Nanosheets Produced by Liquid Exfoliation of Layered Materials. *Science* **2011**, 331 (6017), 568–571. <https://doi.org/10.1126/science.1194975>.

- (157) Xiong, H.-M.; Shchukin, D. G.; Möhwald, H.; Xu, Y.; Xia, Y.-Y. Sonochemical Synthesis of Highly Luminescent Zinc Oxide Nanoparticles Doped with Magnesium(II). *Angew Chem Int Ed Engl* **2009**, *48* (15), 2727–2731. <https://doi.org/10.1002/anie.200805590>.
- (158) Murcia, M. J.; Shaw, D. L.; Woodruff, H.; Naumann, C. A.; Young, B. A.; Long, E. C. Facile Sonochemical Synthesis of Highly Luminescent ZnS–Shelled CdSe Quantum Dots. *Chem. Mater.* **2006**, *18* (9), 2219–2225. <https://doi.org/10.1021/cm0505547>.
- (159) Mekis, I.; Talapin, D. V.; Kornowski, A.; Haase, M.; Weller, H. One-Pot Synthesis of Highly Luminescent CdSe/CdS Core–Shell Nanocrystals via Organometallic and “Greener” Chemical Approaches. *J. Phys. Chem. B* **2003**, *107* (30), 7454–7462. <https://doi.org/10.1021/jp0278364>.
- (160) Majetich, S. A.; Carter, A. C. Surface Effects on the Optical Properties of Cadmium Selenide Quantum Dots. *J. Phys. Chem.* **1993**, *97* (34), 8727–8731. <https://doi.org/10.1021/j100136a013>.
- (161) Ning, Z.; Molnár, M.; Chen, Y.; Friberg, P.; Gan, L.; Ågren, H.; Fu, Y. Role of Surface Ligands in Optical Properties of Colloidal CdSe/CdS Quantum Dots. *Phys. Chem. Chem. Phys.* **2011**, *13* (13), 5848–5854. <https://doi.org/10.1039/C0CP02688C>.
- (162) Leatherdale, C. A.; Woo, W.-K.; Mikulec, F. V.; Bawendi, M. G. On the Absorption Cross Section of CdSe Nanocrystal Quantum Dots. *J. Phys. Chem. B* **2002**, *106* (31), 7619–7622. <https://doi.org/10.1021/jp025698c>.
- (163) Lazarenkova, O. L.; Balandin, A. A. Electron and Phonon Energy Spectra in a Three-Dimensional Regimented Quantum Dot Superlattice. *Phys. Rev. B* **2002**, *66* (24), 245319. <https://doi.org/10.1103/PhysRevB.66.245319>.
- (164) Jiang, C.-W.; Green, M. A. Silicon Quantum Dot Superlattices: Modeling of Energy Bands, Densities of States, and Mobilities for Silicon Tandem Solar Cell Applications. *Journal of Applied Physics* **2006**, *99* (11), 114902. <https://doi.org/10.1063/1.2203394>.
- (165) Schreuder, M. A.; McBride, J. R.; Dukes, A. D.; Sammons, J. A.; Rosenthal, S. J. Control of Surface State Emission via Phosphonic Acid Modulation in Ultrasmall CdSe Nanocrystals: The Role of Ligand Electronegativity. *J. Phys. Chem. C* **2009**, *113* (19), 8169–8176. <https://doi.org/10.1021/jp900300t>.
- (166) Landes, C. F.; Braun, M.; El-Sayed, M. A. On the Nanoparticle to Molecular Size Transition: Fluorescence Quenching Studies. *J. Phys. Chem. B* **2001**, *105* (43), 10554–10558. <https://doi.org/10.1021/jp0118726>.
- (167) Cossairt, B. M.; Owen, J. S. CdSe Clusters: At the Interface of Small Molecules and Quantum Dots. *Chem. Mater.* **2011**, *23* (12), 3114–3119. <https://doi.org/10.1021/cm2008686>.

- (168) Dukes, A. D.; McBride, J. R.; Rosenthal, S. J. Synthesis of Magic-Sized CdSe and CdTe Nanocrystals with Diisooctylphosphinic Acid. *Chem. Mater.* **2010**, *22* (23), 6402–6408. <https://doi.org/10.1021/cm102370a>.
- (169) Kasuya, A.; Sivamohan, R.; Barnakov, Y. A.; Dmitruk, I. M.; Nirasawa, T.; Romanyuk, V. R.; Kumar, V.; Mamykin, S. V.; Tohji, K.; Jeyadevan, B.; Shinoda, K.; Kudo, T.; Terasaki, O.; Liu, Z.; Belosludov, R. V.; Sundararajan, V.; Kawazoe, Y. Ultra-Stable Nanoparticles of CdSe Revealed from Mass Spectrometry. *Nat Mater* **2004**, *3* (2), 99–102. <https://doi.org/10.1038/nmat1056>.
- (170) Jadhav, A. A.; More, P. V.; Khanna, P. K. Rapid Microwave Synthesis of White Light Emitting Magic Sized Nano Clusters of CdSe: Role of Oleic Acid. *RSC Adv.* **2015**, *5* (94), 76733–76742. <https://doi.org/10.1039/C5RA14625A>.
- (171) Dolai, S.; Dutta, P.; Muhoberac, B. B.; Irving, C. D.; Sardar, R. Mechanistic Study of the Formation of Bright White Light-Emitting Ultrasmall CdSe Nanocrystals: Role of Phosphine Free Selenium Precursors. *Chem. Mater.* **2015**, *27* (3), 1057–1070. <https://doi.org/10.1021/cm5043638>.
- (172) Lysova, I.; Anton, H.; Dmitruk, I.; Mely, Y. Tuning Luminescent Properties of CdSe Nanoclusters by Phosphine Surface Passivation. *Methods Appl. Fluoresc.* **2016**, *4* (4), 044009. <https://doi.org/10.1088/2050-6120/4/4/044009>.
- (173) Talapin, D. V.; Rogach, A. L.; Kornowski, A.; Haase, M.; Weller, H. Highly Luminescent Monodisperse CdSe and CdSe/ZnS Nanocrystals Synthesized in a Hexadecylamine–Trioctylphosphine Oxide–Trioctylphosphine Mixture. *Nano Lett.* **2001**, *1* (4), 207–211. <https://doi.org/10.1021/nl0155126>.
- (174) Kodama, K.; Iikubo, S.; Taguchi, T.; Shamoto, S. I. Finite Size Effects of Nanoparticles on the Atomic Pair Distribution Functions. *Acta Crystallogr A* **2006**, *62* (Pt 6), 444–453. <https://doi.org/10.1107/S0108767306034635>.
- (175) Xia, Y.-S.; Zhu, C.-Q. Aqueous Synthesis of Luminescent Magic Sized CdSe Nanoclusters. *Materials Letters* **2008**, *62* (14), 2103–2105. <https://doi.org/10.1016/j.matlet.2007.11.027>.
- (176) Williamson, C. B.; Nevers, D. R.; Nelson, A.; Hadar, I.; Banin, U.; Hanrath, T.; Robinson, R. D. Chemically Reversible Isomerization of Inorganic Clusters. *Science* **2019**, *363* (6428), 731–735. <https://doi.org/10.1126/science.aau9464>.
- (177) Abe, S.; Čapek, R. K.; De Geyter, B.; Hens, Z. Tuning the Postfocused Size of Colloidal Nanocrystals by the Reaction Rate: From Theory to Application. *ACS Nano* **2012**, *6* (1), 42–53. <https://doi.org/10.1021/nn204008q>.
- (178) Jasieniak, J.; Bullen, C.; van Embden, J.; Mulvaney, P. Phosphine-Free Synthesis of CdSe Nanocrystals. *J. Phys. Chem. B* **2005**, *109* (44), 20665–20668. <https://doi.org/10.1021/jp054289o>.

- (179) Protière, M.; Nerambourg, N.; Renard, O.; Reiss, P. Rational Design of the Gram-Scale Synthesis of Nearly Monodisperse Semiconductor Nanocrystals. *Nanoscale Research Letters* **2011**, *6* (1), 472. <https://doi.org/10.1186/1556-276X-6-472>.
- (180) Brennen, C. E. *Cavitation and Bubble Dynamics*; Cambridge University Press: Cambridge, 2013. <https://doi.org/10.1017/CBO9781107338760>.
- (181) Frenette, L. C.; Krauss, T. D. Uncovering Active Precursors in Colloidal Quantum Dot Synthesis. *Nature Communications* **2017**, *8* (1), 2082. <https://doi.org/10.1038/s41467-017-01936-z>.
- (182) Evans, C. M.; Evans, M. E.; Krauss, T. D. Mysteries of TOPSe Revealed: Insights into Quantum Dot Nucleation. *J. Am. Chem. Soc.* **2010**, *132* (32), 10973–10975. <https://doi.org/10.1021/ja103805s>.
- (183) Ruberu, T. P. A.; Albright, H. R.; Callis, B.; Ward, B.; Cisneros, J.; Fan, H.-J.; Vela, J. Molecular Control of the Nanoscale: Effect of Phosphine–Chalcogenide Reactivity on CdS–CdSe Nanocrystal Composition and Morphology. *ACS Nano* **2012**, *6* (6), 5348–5359. <https://doi.org/10.1021/nn301182h>.
- (184) Bredol, M.; Kaczmarek, M. Potential of Nano-ZnS as Electrocatalyst. *J. Phys. Chem. A* **2010**, *114* (11), 3950–3955. <https://doi.org/10.1021/jp907369f>.
- (185) Mahvelati-Shamsabadi, T.; Goharshadi, E. K. Photostability and Visible-Light-Driven Photoactivity Enhancement of Hierarchical ZnS Nanoparticles: The Role of Embedment of Stable Defect Sites on the Catalyst Surface with the Assistant of Ultrasonic Waves. *Ultrasonics Sonochemistry* **2017**, *34*, 78–89. <https://doi.org/10.1016/j.ultsonch.2016.05.021>.
- (186) Mansur, H. S.; Mansur, A. A. P.; Soriano-Araújo, A.; Lobato, Z. I. P. Beyond Biocompatibility: An Approach for the Synthesis of ZnS Quantum Dot-Chitosan Nano-Immunoconjugates for Cancer Diagnosis. *Green Chem.* **2015**, *17* (3), 1820–1830. <https://doi.org/10.1039/C4GC02072C>.
- (187) Premkumar, S.; Nataraj, D.; Bharathi, G.; Ramya, S.; Thangadurai, T. D. Highly Responsive Ultraviolet Sensor Based on ZnS Quantum Dot Solid with Enhanced Photocurrent. *Scientific Reports* **2019**, *9* (1), 18704. <https://doi.org/10.1038/s41598-019-55097-8>.
- (188) Nath, S. S.; Ganguly, A.; Gope, G.; Kanjilal, M. R. ZnS Quantum Dots Based Voltage-Sensing Light-Emitting Device. *IEEE Sensors Letters* **2018**, *2* (3), 1–4. <https://doi.org/10.1109/LENS.2018.2862915>.
- (189) Mohammed, A. F.; Salah, W. R. Synthesis of ZnS Quantum Dots for QDs-LED Hybrid Device with Different Cathode Materials. *J. Phys.: Conf. Ser.* **2018**, *1032*, 012010. <https://doi.org/10.1088/1742-6596/1032/1/012010>.

- (190) Wang, G.; Huang, B.; Li, Z.; Lou, Z.; Wang, Z.; Dai, Y.; Whangbo, M.-H. Synthesis and Characterization of ZnS with Controlled Amount of S Vacancies for Photocatalytic H<sub>2</sub> Production under Visible Light. *Scientific Reports* **2015**, *5* (1), 8544. <https://doi.org/10.1038/srep08544>.
- (191) Hu, J.-S.; Ren, L.-L.; Guo, Y.-G.; Liang, H.-P.; Cao, A.-M.; Wan, L.-J.; Bai, C.-L. Mass Production and High Photocatalytic Activity of ZnS Nanoporous Nanoparticles. *Angewandte Chemie International Edition* **2005**, *44* (8), 1269–1273. <https://doi.org/10.1002/anie.200462057>.
- (192) Reber, J. F.; Meier, K. Photochemical Production of Hydrogen with Zinc Sulfide Suspensions. *J. Phys. Chem.* **1984**, *88* (24), 5903–5913. <https://doi.org/10.1021/j150668a032>.
- (193) Zhang, J.; Yu, J.; Zhang, Y.; Li, Q.; Gong, J. R. Visible Light Photocatalytic H<sub>2</sub>-Production Activity of CuS/ZnS Porous Nanosheets Based on Photoinduced Interfacial Charge Transfer. *Nano Lett.* **2011**, *11* (11), 4774–4779. <https://doi.org/10.1021/nl202587b>.
- (194) Zhou, R.; Guzman, M. I. CO<sub>2</sub> Reduction under Periodic Illumination of ZnS. *J. Phys. Chem. C* **2014**, *118* (22), 11649–11656. <https://doi.org/10.1021/jp4126039>.
- (195) Li, C.; Shen, G.; Zhang, R.; Wu, D.; Zou, C.; Ling, T.; Liu, H.; Dong, C.; Du, X.-W. Zn Nanosheets Coated with a ZnS Subnanometer Layer for Effective and Durable CO<sub>2</sub> Reduction. *J. Mater. Chem. A* **2019**, *7* (4), 1418–1423. <https://doi.org/10.1039/C8TA10799H>.
- (196) Hao, X.; Wang, Y.; Zhou, J.; Cui, Z.; Wang, Y.; Zou, Z. Zinc Vacancy-Promoted Photocatalytic Activity and Photostability of ZnS for Efficient Visible-Light-Driven Hydrogen Evolution. *Applied Catalysis B: Environmental* **2018**, *221*, 302–311. <https://doi.org/10.1016/j.apcatb.2017.09.006>.
- (197) Yu, X.; Yu, J.; Cheng, B.; Huang, B. One-Pot Template-Free Synthesis of Monodisperse Zinc Sulfide Hollow Spheres and Their Photocatalytic Properties. *Chemistry – A European Journal* **2009**, *15* (27), 6731–6739. <https://doi.org/10.1002/chem.200900204>.
- (198) Wang, X.; Shi, J.; Feng, Z.; Li, M.; Li, C. Visible Emission Characteristics from Different Defects of ZnS Nanocrystals. *Phys. Chem. Chem. Phys.* **2011**, *13* (10), 4715–4723. <https://doi.org/10.1039/C0CP01620A>.
- (199) Li, L. S.; Pradhan, N.; Wang, Y.; Peng, X. High Quality ZnSe and ZnS Nanocrystals Formed by Activating Zinc Carboxylate Precursors. *Nano Lett.* **2004**, *4* (11), 2261–2264. <https://doi.org/10.1021/nl048650e>.
- (200) Joo, J.; Na, H. B.; Yu, T.; Yu, J. H.; Kim, Y. W.; Wu, F.; Zhang, J. Z.; Hyeon, T. Generalized and Facile Synthesis of Semiconducting Metal Sulfide Nanocrystals. *J. Am. Chem. Soc.* **2003**, *125* (36), 11100–11105. <https://doi.org/10.1021/ja0357902>.

- (201) Srivastava, B. B.; Jana, S.; Karan, N. S.; Paria, S.; Jana, N. R.; Sarma, D. D.; Pradhan, N. Highly Luminescent Mn-Doped ZnS Nanocrystals: Gram-Scale Synthesis. *J. Phys. Chem. Lett.* **2010**, *1* (9), 1454–1458. <https://doi.org/10.1021/jz100378w>.
- (202) Yu, K.; Hrdina, A.; Zhang, X.; Ouyang, J.; Leek, D. M.; Wu, X.; Gong, M.; Wilkinson, D.; Li, C. Highly-Photoluminescent ZnSe Nanocrystals via a Non-Injection-Based Approach with Precursor Reactivity Elevated by a Secondary Phosphine. *Chem. Commun.* **2011**, *47* (31), 8811–8813. <https://doi.org/10.1039/C1CC12237A>.
- (203) Saeboe, A. M.; Nikiforov, A. Yu.; Toufanian, R.; Kays, J. C.; Chern, M.; Casas, J. P.; Han, K.; Piryatinski, A.; Jones, D.; Dennis, A. M. Extending the Near-Infrared Emission Range of Indium Phosphide Quantum Dots for Multiplexed In Vivo Imaging. *Nano Lett.* **2021**, *21* (7), 3271–3279. <https://doi.org/10.1021/acs.nanolett.1c00600>.
- (204) Kress, S. J. P.; Antolinez, F. V.; Richner, P.; Jayanti, S. V.; Kim, D. K.; Prins, F.; Riedinger, A.; Fischer, M. P. C.; Meyer, S.; McPeak, K. M.; Poulikakos, D.; Norris, D. J. Wedge Waveguides and Resonators for Quantum Plasmonics. *Nano Lett.* **2015**, *15* (9), 6267–6275. <https://doi.org/10.1021/acs.nanolett.5b03051>.
- (205) Doucet, M.; King, S.; Butler, P.; Kienzle, P.; Parker, P.; Krzywon, J.; Jackson, A.; Richter, T.; Gonzales, M.; Nielsen, T.; Ferraz, L. R. *SasView (Version 5.0.1)*; 2020.
- (206) Doucet, M.; King, S.; Butler, P.; Kienzle, P.; Parker, P.; Krzywon, J.; Jackson, A.; Richter, T.; Gonzales, M.; Nielsen, T.; Ferraz, L. R. *Sasmodels (Version 1.0.1)*; 2020.
- (207) Teixeira, J. Small-Angle Scattering by Fractal Systems. *J Appl Cryst* **1988**, *21* (6), 781–785. <https://doi.org/10.1107/S0021889888000263>.
- (208) Kline, S. R. Reduction and Analysis of SANS and USANS Data Using IGOR Pro. *Journal of Applied Crystallography* **2006**, *39* (6), 895–900. <https://doi.org/10.1107/S0021889806035059>.
- (209) NIST IGOR/DANSE. SasView Fractal Core Shell Model [http://www.sasview.org/docs/user/models/fractal\\_core\\_shell.html](http://www.sasview.org/docs/user/models/fractal_core_shell.html).
- (210) King, S.; Kienzle, P. Polydispersity & Orientational Distributions <http://www.sasview.org/docs/user/qtgui/Perspectives/Fitting/pd/polydispersity.html>.
- (211) Larson-Smith, K.; Pozzo, D. C. Scalable Synthesis of Self-Assembling Nanoparticle Clusters Based on Controlled Steric Interactions. *Soft Matter* **2011**, *7* (11), 5339–5347. <https://doi.org/10.1039/C0SM01497D>.
- (212) Biswas, S.; Kar, S.; Chaudhuri, S. Optical and Magnetic Properties of Manganese-Incorporated Zinc Sulfide Nanorods Synthesized by a Solvothermal Process. *J. Phys. Chem. B* **2005**, *109* (37), 17526–17530. <https://doi.org/10.1021/jp053138i>.

- (213) Sooklal, K.; Cullum, B. S.; Angel, S. M.; Murphy, C. J. Photophysical Properties of ZnS Nanoclusters with Spatially Localized Mn<sup>2+</sup>. *J. Phys. Chem.* **1996**, *100* (11), 4551–4555. <https://doi.org/10.1021/jp952377a>.
- (214) Chen, W.; Wang, Z.; Lin, Z.; Lin, L. Absorption and Luminescence of the Surface States in ZnS Nanoparticles. *Journal of Applied Physics* **1997**, *82* (6), 3111–3115. <https://doi.org/10.1063/1.366152>.
- (215) Busby, E.; Anderson, N. C.; Owen, J. S.; Sfeir, M. Y. Effect of Surface Stoichiometry on Blinking and Hole Trapping Dynamics in CdSe Nanocrystals. *J. Phys. Chem. C* **2015**, *119* (49), 27797–27803. <https://doi.org/10.1021/acs.jpcc.5b08243>.
- (216) Boles, M. A.; Ling, D.; Hyeon, T.; Talapin, D. V. The Surface Science of Nanocrystals. *Nature Materials* **2016**, *15* (2), 141–153. <https://doi.org/10.1038/nmat4526>.
- (217) Hendricks, M. P.; Campos, M. P.; Cleveland, G. T.; Plante, I. J.-L.; Owen, J. S. A Tunable Library of Substituted Thiourea Precursors to Metal Sulfide Nanocrystals. *Science* **2015**, *348* (6240), 1226–1230. <https://doi.org/10.1126/science.aaa2951>.
- (218) Chang, J.; R. Waclawik, E. Colloidal Semiconductor Nanocrystals: Controlled Synthesis and Surface Chemistry in Organic Media. *RSC Advances* **2014**, *4* (45), 23505–23527. <https://doi.org/10.1039/C4RA02684E>.
- (219) Phillips, C. L.; Glotzer, S. C. Effect of Nanoparticle Polydispersity on the Self-Assembly of Polymer Tethered Nanospheres. *J. Chem. Phys.* **2012**, *137* (10), 104901. <https://doi.org/10.1063/1.4748817>.
- (220) Peng, S.; Wen, Z.; Ye, T.; Xiao, X.; Wang, K.; Xia, J.; Sun, J.; Zhang, T.; Mei, G.; Liu, H.; Xu, B.; Li, X.; Chen, R.; Xing, G.; Wang, K.; Tang, Z. Effective Surface Ligand-Concentration Tuning of Deep-Blue Luminescent FAPbBr<sub>3</sub> Nanoplatelets with Enhanced Stability and Charge Transport. *ACS Appl. Mater. Interfaces* **2020**, *12* (28), 31863–31874. <https://doi.org/10.1021/acsami.0c08552>.
- (221) Samuel, B.; Mathew, S.; Anand, V. R.; Correya, A. A.; Nampoore, V. P. N.; Mujeeb, A. Surface Defect Assisted Broad Spectra Emission from CdSe Quantum Dots for White LED Application. *Mater. Res. Express* **2018**, *5* (2), 025009. <https://doi.org/10.1088/2053-1591/aaaa83>.
- (222) Monreal, R. C.; Apell, S. P.; Antosiewicz, T. J. Quantum-Size Effects in Visible Defect Photoluminescence of Colloidal ZnO Quantum Dots: A Theoretical Analysis. *Nanoscale* **2018**, *10* (15), 7016–7025. <https://doi.org/10.1039/C8NR00534F>.
- (223) Norberg, N. S.; Gamelin, D. R. Influence of Surface Modification on the Luminescence of Colloidal ZnO Nanocrystals. *J. Phys. Chem. B* **2005**, *109* (44), 20810–20816. <https://doi.org/10.1021/jp0535285>.

- (224) Joo, S.-Y.; Park, H.-S.; Kim, D.; Kim, B.-S.; Lee, C. G.; Kim, W.-B. An Investigation into the Effective Surface Passivation of Quantum Dots by a Photo-Assisted Chemical Method. *AIP Advances* **2018**, *8* (1), 015017. <https://doi.org/10.1063/1.5009788>.
- (225) Gayou, V. L.; Salazar Hernández, B.; Delgado Macuil, R.; Zavala, G.; Santiago, P.; Oliva, A. I. Structural Studies of ZnS Nanoparticles by High Resolution Transmission Electron Microscopy. *Journal of Nano Research* **2010**, *9*, 125–132. <https://doi.org/10.4028/www.scientific.net/JNanoR.9.125>.
- (226) Kim, S.; Kim, T.; Kang, M.; Kwak, S. K.; Yoo, T. W.; Park, L. S.; Yang, I.; Hwang, S.; Lee, J. E.; Kim, S. K.; Kim, S.-W. Highly Luminescent InP/GaP/ZnS Nanocrystals and Their Application to White Light-Emitting Diodes. *J. Am. Chem. Soc.* **2012**, *134* (8), 3804–3809. <https://doi.org/10.1021/ja210211z>.
- (227) Jang, E.; Kim, Y.; Won, Y.-H.; Jang, H.; Choi, S.-M. Environmentally Friendly InP-Based Quantum Dots for Efficient Wide Color Gamut Displays. *ACS Energy Lett.* **2020**, *5* (4), 1316–1327. <https://doi.org/10.1021/acsenerylett.9b02851>.
- (228) Yong, K.-T.; Ding, H.; Roy, I.; Law, W.-C.; Bergey, E. J.; Maitra, A.; Prasad, P. N. Imaging Pancreatic Cancer Using Bioconjugated InP Quantum Dots. *ACS Nano* **2009**, *3* (3), 502–510. <https://doi.org/10.1021/nn8008933>.
- (229) Brunetti, V.; Chibli, H.; Fiammengio, R.; Galeone, A.; Malvindi, M. A.; Vecchio, G.; Cingolani, R.; Nadeau, J. L.; Pompa, P. P. InP/ZnS as a Safer Alternative to CdSe/ZnS Core/Shell Quantum Dots: In Vitro and in Vivo Toxicity Assessment. *Nanoscale* **2012**, *5* (1), 307–317. <https://doi.org/10.1039/C2NR33024E>.
- (230) Tessier, M. D.; De Nolf, K.; Dupont, D.; Sinnaeve, D.; De Roo, J.; Hens, Z. Aminophosphines: A Double Role in the Synthesis of Colloidal Indium Phosphide Quantum Dots. *J. Am. Chem. Soc.* **2016**, *138* (18), 5923–5929. <https://doi.org/10.1021/jacs.6b01254>.
- (231) Buffard, A.; Dreyfuss, S.; Nadal, B.; Heuclin, H.; Xu, X.; Patriarche, G.; Mézailles, N.; Dubertret, B. Mechanistic Insight and Optimization of InP Nanocrystals Synthesized with Aminophosphines. *Chem. Mater.* **2016**, *28* (16), 5925–5934. <https://doi.org/10.1021/acs.chemmater.6b02456>.
- (232) Laufersky, G.; Bradley, S.; Frécaut, E.; Lein, M.; Nann, T. Unraveling Aminophosphine Redox Mechanisms for Glovebox-Free InP Quantum Dot Syntheses. *Nanoscale* **2018**, *10* (18), 8752–8762. <https://doi.org/10.1039/C8NR01286E>.
- (233) Cao, F.; Wang, S.; Wang, F.; Wu, Q.; Zhao, D.; Yang, X. A Layer-by-Layer Growth Strategy for Large-Size InP/ZnSe/ZnS Core–Shell Quantum Dots Enabling High-Efficiency Light-Emitting Diodes. *Chem. Mater.* **2018**, *30* (21), 8002–8007. <https://doi.org/10.1021/acs.chemmater.8b03671>.
- (234) Reid, K. R.; McBride, J. R.; Freymeyer, N. J.; Thal, L. B.; Rosenthal, S. J. Chemical Structure, Ensemble and Single-Particle Spectroscopy of Thick-Shell InP–ZnSe Quantum Dots. *Nano Lett.* **2018**, *18* (2), 709–716. <https://doi.org/10.1021/acs.nanolett.7b03703>.

- (235) Wegner, K. D.; Dussert, F.; Truffier-Boutry, D.; Benayad, A.; Beal, D.; Mattera, L.; Ling, W. L.; Carrière, M.; Reiss, P. Influence of the Core/Shell Structure of Indium Phosphide Based Quantum Dots on Their Photostability and Cytotoxicity. *Front. Chem.* **2019**, *7*, 1–12. <https://doi.org/10.3389/fchem.2019.00466>.
- (236) Lim, J.; Bae, W. K.; Lee, D.; Nam, M. K.; Jung, J.; Lee, C.; Char, K.; Lee, S. InP@ZnSeS, Core@Composition Gradient Shell Quantum Dots with Enhanced Stability. *Chem. Mater.* **2011**, *23* (20), 4459–4463. <https://doi.org/10.1021/cm201550w>.
- (237) Nasilowski, M.; Spinicelli, P.; Patriarche, G.; Dubertret, B. Gradient CdSe/CdS Quantum Dots with Room Temperature Biexciton Unity Quantum Yield. *Nano Lett.* **2015**, *15* (6), 3953–3958. <https://doi.org/10.1021/acs.nanolett.5b00838>.
- (238) Kim, S.; Park, J.; Kim, T.; Jang, E.; Jun, S.; Jang, H.; Kim, B.; Kim, S.-W. Reverse Type-I ZnSe/InP/ZnS Core/Shell/Shell Nanocrystals: Cadmium-Free Quantum Dots for Visible Luminescence. *Small* **2011**, *7* (1), 70–73. <https://doi.org/10.1002/smll.201001096>.
- (239) Bang, E.; Choi, Y.; Cho, J.; Suh, Y.-H.; Ban, H. W.; Son, J. S.; Park, J. Large-Scale Synthesis of Highly Luminescent InP@ZnS Quantum Dots Using Elemental Phosphorus Precursor. *Chem. Mater.* **2017**, *29* (10), 4236–4243. <https://doi.org/10.1021/acs.chemmater.7b00254>.
- (240) Gary, D. C.; Glassy, B. A.; Cossairt, B. M. Investigation of Indium Phosphide Quantum Dot Nucleation and Growth Utilizing Triarylsilylphosphine Precursors. *Chem. Mater.* **2014**, *26* (4), 1734–1744. <https://doi.org/10.1021/cm500102q>.
- (241) Li, L.; Reiss, P. One-Pot Synthesis of Highly Luminescent InP/ZnS Nanocrystals without Precursor Injection. *J. Am. Chem. Soc.* **2008**, *130* (35), 11588–11589. <https://doi.org/10.1021/ja803687e>.
- (242) Lange, H.; Kelley, D. F. Spectroscopic Effects of Lattice Strain in InP/ZnSe and InP/ZnS Nanocrystals. *J. Phys. Chem. C* **2020**, *124* (41), 22839–22844. <https://doi.org/10.1021/acs.jpcc.0c07145>.
- (243) Feng, S.; Wu, J.; Hu, P.; Chen, Y.; Ma, B.; Peng, J.; Yang, J.; Jiang, H. Epitaxial Growth of Successive CdSe Ultrathin Films and Quantum Dot Layers on TiO<sub>2</sub> Nanorod Arrays for Photo-Electrochemical Cells. *RSC Advances* **2014**, *4* (24), 12154–12159.
- (244) Holec, D.; Zhang, Y.; Rao, D. V. S.; Kappers, M. J.; McAleese, C.; Humphreys, C. J. Equilibrium Critical Thickness for Misfit Dislocations in III-Nitrides. *Journal of Applied Physics* **2008**, *104* (12), 123514. <https://doi.org/10.1063/1.3033553>.
- (245) dos Santos, C. L.; Piquini, P. Diameter Dependence of Mechanical, Electronic, and Structural Properties of InAs and InP Nanowires: A First-Principles Study. *Phys. Rev. B* **2010**, *81* (7), 075408. <https://doi.org/10.1103/PhysRevB.81.075408>.

- (246) Chiu, Y.-J.; Jian, S.-R.; Liu, T.-J.; Le, P. H.; Juang, J.-Y. Localized Deformation and Fracture Behaviors in InP Single Crystals by Indentation. *Micromachines* **2018**, *9* (12), 611. <https://doi.org/10.3390/mi9120611>.
- (247) Wei, S.-H.; Zunger, A. Calculated Natural Band Offsets of All II–VI and III–V Semiconductors: Chemical Trends and the Role of Cation d Orbitals. *Appl. Phys. Lett.* **1998**, *72* (16), 2011–2013. <https://doi.org/10.1063/1.121249>.
- (248) Kim, Y.; Ham, S.; Jang, H.; Min, J. H.; Chung, H.; Lee, J.; Kim, D.; Jang, E. Bright and Uniform Green Light Emitting InP/ZnSe/ZnS Quantum Dots for Wide Color Gamut Displays. *ACS Appl. Nano Mater.* **2019**, *2* (3), 1496–1504. <https://doi.org/10.1021/acsanm.8b02063>.
- (249) Freund, L. B.; Suresh, S. *Thin Film Materials: Stress, Defect Formation and Surface Evolution*; Cambridge University Press, 2004.
- (250) Ryu, E.; Kim, S.; Jang, E.; Jun, S.; Jang, H.; Kim, B.; Kim, S.-W. Step-Wise Synthesis of InP/ZnS Core–Shell Quantum Dots and the Role of Zinc Acetate. *Chem. Mater.* **2009**, *21* (4), 573–575. <https://doi.org/10.1021/cm803084p>.
- (251) Verma, M.; Kaswan, A.; Patidar, D.; Sharma, K. B.; Saxena, N. S. Phase Transformation and Thermal Stability of ZnSe QDs Due to Annealing: Emergence of ZnO. *J Mater Sci: Mater Electron* **2016**, *27* (9), 8871–8878. <https://doi.org/10.1007/s10854-016-4912-8>.
- (252) Kole, A. K.; Kumbhakar, P. Cubic-to-Hexagonal Phase Transition and Optical Properties of Chemically Synthesized ZnS Nanocrystals. *Results in Physics* **2012**, *2*, 150–155. <https://doi.org/10.1016/j.rinp.2012.09.010>.
- (253) Qadri, S. B.; Skelton, E. F.; Hsu, D.; Dinsmore, A. D.; Yang, J.; Gray, H. F.; Ratna, B. R. Size-Induced Transition-Temperature Reduction in Nanoparticles of ZnS. *Phys. Rev. B* **1999**, *60* (13), 9191–9193. <https://doi.org/10.1103/PhysRevB.60.9191>.
- (254) Lu, Y.; Miller, J. D. Carboxyl Stretching Vibrations of Spontaneously Adsorbed and LB-Transferred Calcium Carboxylates as Determined by FTIR Internal Reflection Spectroscopy. *Journal of Colloid and Interface Science* **2002**, *256* (1), 41–52. <https://doi.org/10.1006/jcis.2001.8112>.
- (255) Prasad, S. G.; De, A.; De, U. Structural and Optical Investigations of Radiation Damage in Transparent PET Polymer Films. *International Journal of Spectroscopy* **2011**, *2011*, e810936. <https://doi.org/10.1155/2011/810936>.
- (256) Wade, L. G. IR: Characteristic Infrared Absorptions of Functional Groups. In *Organic Chemistry: International Edition.*; Pearson Education (US), 2013; pp 1251–1253.
- (257) Abfalterer, A.; Shamsi, J.; Kubicki, D. J.; Savory, C. N.; Xiao, J.; Divitini, G.; Li, W.; Macpherson, S.; Gałkowski, K.; MacManus-Driscoll, J. L.; Scanlon, D. O.; Stranks, S. D. Colloidal Synthesis and Optical Properties of Perovskite-Inspired Cesium Zirconium Halide

- Nanocrystals. *ACS Materials Lett.* **2020**, *2* (12), 1644–1652. <https://doi.org/10.1021/acsmaterialslett.0c00393>.
- (258) Wu, X.; Ossadnik, C.; Eggs, C.; Veprek, S.; Phillipp, F. Structure and Photoluminescence Features of Nanocrystalline SiO<sub>2</sub>/SiO<sub>2</sub> Films Produced by Plasma Chemical Vapor Deposition and Post-Treatment. *J. Vac. Sci. Technol. B* **2002**, *20* (4), 11.
- (259) Xie, Y. H.; Wilson, W. L.; Ross, F. M.; Mucha, J. A.; Fitzgerald, E. A.; Macaulay, J. M.; Harris, T. D. Luminescence and Structural Study of Porous Silicon Films. *Journal of Applied Physics* **1992**, *71* (5), 2403–2407. <https://doi.org/10.1063/1.351097>.
- (260) Shibata, N. S. N.; Ikoma, H. I. H. X-Ray Photoelectron Spectroscopic Study of Oxidation of InP. *Jpn. J. Appl. Phys.* **1992**, *31* (12R), 3976. <https://doi.org/10.1143/JJAP.31.3976>.
- (261) Jaiswal, A.; Sanpui, P.; Chattopadhyay, A.; Ghosh, S. S. Investigating Fluorescence Quenching of ZnS Quantum Dots by Silver Nanoparticles. *Plasmonics* **2011**, *6* (1), 125–132. <https://doi.org/10.1007/s11468-010-9177-0>.
- (262) Jana, S.; Baek, I. C.; Lim, M. A.; Seok, S. I. ZnSe Colloidal Nanoparticles Synthesized by Solvothermal Method in the Presence of ZrCl<sub>4</sub>. *Journal of Colloid and Interface Science* **2008**, *322* (2), 473–477. <https://doi.org/10.1016/j.jcis.2008.04.021>.
- (263) Li, Z.-J.; Hofman, E.; Blaker, A.; Davis, A. H.; Dzikovski, B.; Ma, D.-K.; Zheng, W. Interface Engineering of Mn-Doped ZnSe-Based Core/Shell Nanowires for Tunable Host–Dopant Coupling. *ACS Nano* **2017**, *11* (12), 12591–12600. <https://doi.org/10.1021/acsnano.7b06773>.
- (264) Hwang, I.; Seol, M.; Kim, H.; Yong, K. Improvement of Photocurrent Generation of Ag<sub>2</sub>S Sensitized Solar Cell through Co-Sensitization with CdS. *Appl. Phys. Lett.* **2013**, *103* (2), 023902. <https://doi.org/10.1063/1.4813445>.
- (265) Zhang, X.; Wang, D.; Beres, M.; Liu, L.; Ma, Z.; Yu, P. Y.; Mao, S. S. Zincblende-Wurtzite Phase Transformation of ZnSe Films by Pulsed Laser Deposition with Nitrogen Doping. *Appl. Phys. Lett.* **2013**, *103* (8), 082111. <https://doi.org/10.1063/1.4819271>.
- (266) Reiss, P. ZnSe Based Colloidal Nanocrystals: Synthesis, Shape Control, Core/Shell, Alloy and Doped Systems. *New J. Chem.* **2007**, *31* (11), 1843–1852. <https://doi.org/10.1039/B712086A>.
- (267) Reiss, P.; Protière, M.; Li, L. Core/Shell Semiconductor Nanocrystals. *Small* **2009**, *5* (2), 154–168. <https://doi.org/10.1002/sml.200800841>.
- (268) Kennedy, T.; Bezuidenhout, M.; Palaniappan, K.; Stokes, K.; Brandon, M.; Ryan, K. M. Nanowire Heterostructures Comprising Germanium Stems and Silicon Branches as High-Capacity Li-Ion Anodes with Tunable Rate Capability. *ACS Nano* **2015**, *9* (7), 7456–7465. <https://doi.org/10.1021/acsnano.5b02528>.

- (269) Bierman, M. J.; Jin, S. Potential Applications of Hierarchical Branching Nanowires in Solar Energy Conversion. *Energy Environ. Sci.* **2009**, *2* (10), 1050–1059. <https://doi.org/10.1039/B912095E>.
- (270) U.S. News & World Report. The Best Chemical Engineering Programs in America, Ranked <https://www.usnews.com/best-graduate-schools/top-engineering-schools/chemical-engineering-rankings> (accessed 2021 -06 -30).
- (271) Fleming, K. L.; Matthaei, J.; Pfaendtner, J. A New Graduate-Level Seminar to Prepare Students for the Next Step in Their Careers. *Chemical Engineering Education* **2015**, *49* (1), 8.
- (272) Li, D.; Agha, L. Big Names or Big Ideas: Do Peer-Review Panels Select the Best Science Proposals? *Science* **2015**, *348* (6233), 434–438. <https://doi.org/10.1126/science.aaa0185>.
- (273) Brezis, E. S.; Birukou, A. Arbitrariness in the Peer Review Process. *Scientometrics* **2020**, *123* (1), 393–411. <https://doi.org/10.1007/s11192-020-03348-1>.
- (274) Andersson, E. R.; Hagberg, C.; Hägg, S. Implicit Bias Is Strongest When Assessing Top Candidates. *bioRxiv* **2019**, 859298. <https://doi.org/10.1101/859298>.
- (275) About UW ADVANCE <https://advance.washington.edu/about> (accessed 2021 -06 -30).
- (276) NSF Award Search: Award # 0123552 - ADVANCE Institutional Transformation Award [https://www.nsf.gov/awardsearch/showAward?AWD\\_ID=0123552&HistoricalAwards=false](https://www.nsf.gov/awardsearch/showAward?AWD_ID=0123552&HistoricalAwards=false) (accessed 2021 -06 -30).
- (277) Implicit Bias - UCLA Equity, Diversity & Inclusion <https://equity.ucla.edu/know/implicit-bias/>.
- (278) The University of Arizona Commission on the Status of Women. Avoiding Gender Bias In Letter of Reference Writing.
- (279) Kuo, M. Consciously Combating Unconscious Bias <https://www.sciencemag.org/careers/2017/01/consciously-combating-unconscious-bias>.
- (280) Hagiwara, T. L. G., Nao. The Problem with Implicit Bias Training <https://www.scientificamerican.com/article/the-problem-with-implicit-bias-training/> (accessed 2021 -07 -01).
- (281) Dobbin, F.; Kalev, A. Why Diversity Training Doesn't Work: The Challenge for Industry and Academia. *Anthropology Now* **2018**, *10* (2), 48–55.
- (282) Equality and Human Rights Commission. *Unconscious Bias Training: An Assessment of the Evidence for Effectiveness Research Report 113*; 2018.

- (283) Bezrukova, K.; Spell, C. S.; Perry, J. L.; Jehn, K. A. A Meta-Analytical Integration of over 40 Years of Research on Diversity Training Evaluation. *Psychological Bulletin* **2016**, *142* (11), 1227–1274. <https://doi.org/10.1037/bul0000067>.
- (284) Chamorro-Premuzic, T.; Chamorro-Premuzic, T. Science explains why unconscious bias training won't reduce workplace racism. Here's what will <https://www.fastcompany.com/90515678/science-explains-why-unconscious-bias-training-wont-reduce-workplace-racism-heres-what-will> (accessed 2021 -07 -01).
- (285) Oswald, F. L.; Mitchell, G.; Blanton, H.; Jaccard, J.; Tetlock, P. E. Predicting Ethnic and Racial Discrimination: A Meta-Analysis of IAT Criterion Studies. *J Pers Soc Psychol* **2013**, *105* (2), 171–192. <https://doi.org/10.1037/a0032734>.
- (286) Quinn, D. M. Experimental Evidence on Teachers' Racial Bias in Student Evaluation: The Role of Grading Scales. *Educational Evaluation and Policy Analysis* **2020**, *42* (3), 375–392. <https://doi.org/10.3102/0162373720932188>.
- (287) Wiederhold, B. K. Connecting Through Technology During the Coronavirus Disease 2019 Pandemic: Avoiding “Zoom Fatigue.” *Cyberpsychology, Behavior, and Social Networking* **2020**, *23* (7), 437–438. <https://doi.org/10.1089/cyber.2020.29188.bkw>.
- (288) Bailenson, J. N. Nonverbal Overload: A Theoretical Argument for the Causes of Zoom Fatigue. *Technology, Mind, and Behavior* **2021**, *2* (1). <https://doi.org/10.1037/tmb0000030>.
- (289) Lorenz, T. How to Prevent ‘Zoombombing’ in a Few Easy Steps. *The New York Times*. April 7, 2020.
- (290) Bilimoria, D.; Buch, K. K. The Search Is On: Engendering Faculty Diversity Through More Effective Search and Recruitment. *Change: The Magazine of Higher Learning* **2010**, *42* (4), 27–32. <https://doi.org/10.1080/00091383.2010.489022>.
- (291) Beard, L.; Akpan, J.; Notar (Emeritus), C. E.; Beard, L. Rubrics 101: What, When and How. *American Journal of Educational Research and Reviews* **2019****105**, *4*. <https://doi.org/10.28933/ajerr-2018-12-1408>.
- (292) Quinn, D. M. How to Reduce Racial Bias in Grading. *Education Next*, 2020.

## VITA

Brittany Paige Bishop was born in Boston, Massachusetts, and grew up in Newton, Massachusetts. She graduated from Newton South High School in 2011 and went on to attend Case Western Reserve University, where she graduated cum laude with a B.S.E. in Chemical Engineering in 2015. Upon graduation, she attended the University of Washington for her graduate studies in Chemical Engineering. During her time at the University of Washington, she became a Clean Energy Institute Graduate Fellow in 2017 and a Clean Energy Institute Education and Training Fellow in 2018. She also dedicated a large portion of her time at the University of Washington to science education, communication, and engagement. She was heavily involved with K-12 education through the Clean Energy Institute, acted as a Chemical Engineering Representative on the Graduate and Professional Student Senate for 3 years, lobbied for clean energy and higher education policy at the university and state level, helped run the Distinguished Young Scholar's Seminar for 2 years, and engaged in diversity efforts through Women in Chemical Engineering and the Association of Chemical Engineering Graduate Students. In 2019, she was awarded the Jane and Joseph McCarthy Award for Excellence in Chemical Engineering Graduate Student Teaching and in 2020, she became a Christine Mirzayan Science and Technology Policy Graduate Fellow through The National Academies of Sciences, Engineering, and Medicine. In 2020, she was awarded the University of Washington Chemical Engineering Outstanding Service Award for impactful dedication and service by a graduate student to the community and field of Chemical Engineering. Brittany earned a Master of Science in Chemical Engineering in 2018 and earned her Ph.D. in Chemical Engineering while studying the synthesis, surface functionalization, and strain-engineering of fluorescent semiconductor nanomaterials under the supervision of Professor Vincent Holmberg.

## Publications Completed During Graduate School

- 1) **Bishop, Brittany P.**; Holmberg, Vincent C., Impact of Precursors and Surface Chemistry on InP Shell Growth in Strain-Engineered InP Spherical Quantum Wells. Submitted, 2021.
- 2) **Bishop, Brittany P.**; Wolf, Caitlyn; Pozzo, Lilo D.; Holmberg, Vincent C., Highly Repeatable One-Pot Synthesis of Monodisperse ZnS Nanocrystals with Broadband Near-UV and Visible Emission. Submitted, 2021.
- 3) **Bishop, Brittany P.**; DeForest, Cole A., A Decade with DYSS: Lessons Learned and Looking Forward. *Chemical Engineering Education* (2021), Submitted.
- 4) Kastilani, Ryan; **Bishop, Brittany P.**; Holmberg, Vincent C.; Pozzo, Lilo D., On-Demand Sonochemical Synthesis of Ultrasmall and Magic-Size CdSe Quantum Dots in Single-Phase and Emulsion Systems. *Langmuir* (2019), 35(50), 16583-16592.
- 5) Zhang, Mengying; **Bishop, Brittany P.**; Thompson, Nicole L.; Hildahl, Kate; Dang, Binh; Mironchuk, Olesya; Chen, Nina; Aoki, Reyn; Holmberg, Vincent C.\*; Nance, Elizabeth\*, Quantum Dot Cellular Uptake and Toxicity in the Developing Brain: Implications for Use as Imaging Probes. *Nanoscale Advances* (2019), 1, 3424-3442.

## Presentations Given During Graduate School

- 1) Bishop, Brittany P., *et.al.*, “Strain-Engineering in Inorganic Nanostructures with Visible/Near-Infrared Luminescence.” Nanocrystals Northwest Poster Session; Eatonville, WA, 2019.
- 2) Bishop, Brittany P., *et.al.*, “Strain-Engineering in Inorganic Nanostructures with Near-Infrared Luminescence.” International Conference on Energy Conversion and Storage Poster Session; Friday Harbor, WA, 2018.
- 3) Bishop, Brittany P., “New Materials for Improving Clean Energy Resources”. Ewha-Luce International Seminar Open Forum Presentation; Seoul, South Korea, 2018.
- 4) Bishop, Brittany P., *et.al.*, “Inorganic Fluorescent Nanomaterials for Imaging and Clean Energy Applications”. Ewha-Luce International Seminar Poster Symposium; Seoul, South Korea, 2018.
- 5) Bishop, Brittany P., “Nanomaterials: History & Today”. Seattle Pacific University: Natural Sciences Capstone Seminar Guest Lecture; Seattle, WA, 2018.

## **Awards and Fellowships**

Chemical Engineering Graduate Student Outstanding Service Award	<b>2020</b>
Christine Mirzayan Science and Technology Policy Graduate Fellowship	<b>2020</b>
Jane and Joseph McCarthy Award for Excellence in Chemical Engineering Graduate Student Teaching	<b>2019</b>
2018 - 2019 Exemplary Senator for Commitment and Service to the Graduate and Professional Student Senate (GPSS)	<b>2019</b>
2017 – 2018 Outstanding GPSS Senator on the Legislative Advisory Board	<b>2018</b>
Washington State Super STEM Advocate Award	<b>2018</b>
Clean Energy Institute (CEI) Education and Training Fellowship	<b>2018</b>
2018 Dorothy Bowers Science and Engineering as Art, third prize	<b>2018</b>
2017 Dorothy Bowers Science and Engineering as Art, first prize	<b>2017</b>
Clean Energy Institute (CEI) Graduate Fellowship	<b>2016</b>
2016 Dorothy Bowers Science and Engineering as Art, first prize	<b>2016</b>